Bridging Monte Carlo Worlds:

A New Framework for Accelerator Physics Simulations Applied on Shielding and Machine Protection Studies

Thèse n. ? 2024
présenté le 24 January 2024
à la Faculté des Sciences Physique
Laboratory of Particle Accelerator Physics
École Polytechnique Fédérale de Lausanne
Programme doctoral en Physique

pour l'obtention du grade de Docteur ès Sciences
par

André Donadón Servelle

acceptée sur proposition du jury:

Prof. Fréderic Mila, président du jury
Prof. Mike Seidel, directeur de thèse
Dr. Vasilis Vlachoudis, co-directeur de thèse
Dr. Tatsuhiko Ogawa, rapporteur
Dr. Roberto Versaci, rapporteur
Prof. Andreas Laeuchli, rapporteur

Lausanne, EPFL, 2024

L’inferno esiste solo per chi ne ha paura
— Fabrizio de André

To my family

Abstract

This thesis delves into the critical study of particle transport in matter, particularly emphasising its implications for machine protection at CERN's accelerator complex and facilities. To conduct studies of this nature, FLUKA and Geant4 stand out within a small group of general-purpose, multi-particle Monte Carlo codes, validated in energies reaching the multi-TeV. However, their structural differences and user interface philosophies present significant challenges in obtaining results with both codes for the same problems. Overcoming these challenges is crucial, considering the inherent limitations of MC codes due to their physical models and reliance on specific databases for particle transport calculations.

A significant contribution of this work is the development of "Moira", a new software that integrates the infrastructure of Geant4 with the capability to process FLUKA inputs. This novel Geant4 application allows for a unique comparison of results between the two codes, enabling simulations with equivalent characteristics, with the primary distinction being the physical models used.

Using "Moira", this thesis presents a series of simulations using alternative models to FLUKA's, to analyse shielding and machine protection studies, focusing mainly in scenarios covering sections that span hundreds of meter in the Large Hadron Collider. Doing these simulations with multiple physics models permit to obtain a better quantification of the systematic errors, and also contribute significantly to the development of Monte Carlo codes.

Key words: Particle Transport, Machine Protection, Monte Carlo codes, CERN, FLUKA, Geant4, Large Hadron Collider, n_TOF, CHARM, High-Energy Physics.

Contents

List of Figures

List of Tables

Introduction

[English]

The study of particle transport in matter has undergone significant evolution and found numerous applications throughout the history of science. It seeks to understand how the interaction of these particles can affect the objects that the beam passes through and, in turn, the consequences for the beam itself. Understanding these processes is essential for medical, space-related, and machine protection applications, among many others. Regarding the latter, at CERN, particularly in its accelerator complex and facilities, particles in a wide energy spectrum interact daily with the equipment they comprise, posing a potential risk to their proper functioning. In this context, one of the primary studies carried out is to understand the impact of these losses on the machinery, based on using the Monte Carlo method through specialised software that allows simulating events that could pose a danger to the integrity or operation of the machine.

The flagship software used at CERN for this purpose is FLUKA. This Monte Carlo code has been crucial for the construction of accelerators like the Large Hadron Collider and facilities such as n_TOF and CHARM. It continues to be essential for studying potential upgrades of these machines and the possible construction of other accelerators, including the Future Circular Collider and the Muon collider. The existence of a tool like FLUKA for conducting these types of studies is invaluable. However, currently, due to the extensive code infrastructure built around FLUKA to be able to produce these complex simulations, it is practically impossible to emulate them with other Monte Carlo software. On the other hand, only a handful of the few available Monte Carlo codes can carry out simulations where the particle energy reaches multi-TeV. One of the main codes in this category is Geant4, whose primary development centre is also located at CERN, like FLUKA. Despite the many differences between these codes, such as the way geometry is described, user interfaces, and, primarily, the different physical packages they provide, both are multi-purpose and multi-particle codes, suitable for studying practically the same problems.

The purpose of this thesis was to improve the quantification of systematic errors through the obtention of complementary results, associated primarily with machine protection, using hadronic and electromagnetic models, and cross-section databases alternative to FLUKA, specifically those provided by Geant4.

To achieve this, an initial software development stage was necessary to create what was preliminary called "Moira". This Monte Carlo software is based on the Geant4 infrastructure but has the capability to perform simulations with FLUKA inputs. In this way, Moira can take advantage of the complementary tools that FLUKA possesses and make them its own. The main goal of Moira is to allow the user to perform simulations that can be done with FLUKA, with the same simulation characteristics, with the only difference being that the physical packages used are those provided by Geant4. Finally, this new development is used to make comparisons between many scenarios of interest, mainly cases with energies in the range of multiple TeV in highly complex geometries.

Regarding this manuscript, the text will begin with a necessary introductory part, starting with a description of the radiation transport problem, the equation that describes the problem, and a detailed explanation of the main hadronic and electromagnetic interactions (Chapter 1). Chapter 2 details the main method used to solve the radiation transport problem, which is the aforementioned Monte Carlo method. This chapter introduces the method, the mathematical tools, and its main characteristics. Subsequently, in Chapters 3 and 4, a description of the Geant4 and FLUKA codes is presented, highlighting their main functionalities, emphasising their similarities and differences. Concluding the introductory part, Chapter 5 explains the need for using these codes for machine protection studies, introducing the synchrotron accelerators, with a main focus on the Large Hadron Collider, and the CERN accelerator complex and facilities. It also details the sources of particle losses in the accelerators, their consequences, and existing methods to mitigate them.

Chapters 6 and 7 showcase the novelty in this thesis. Chapter 6 presents the new framework developed, the reasons for its creation, its current state, and its plans for the short, medium, and long term. The 7th aims to use this novel code, presenting seven different results, ordered by their complexity, with the goal of determining results with multiple physics packages, accounting for the intrinsic systematic uncertainties.

1 An Introduction to the Radiation Transport Problem

As a preamble to this manuscript, this chapter will introduce the basics on radiation transport in matter. A brief historical account will be given, defining the concept of radiation. This is followed by an introduction to the radiation transport problem, including the governing equation and the physical interactions involved in particle transport. Particular emphasis is placed on electromagnetic, hadronic interactions, and their associated particle showers, along with a detailed examination of the unique characteristics of low-energy neutrons.

1.1 Brief Historical Overview of Radiation Transport

The term "radiation" has a relatively modern origin. In the early days of science, the term was used primarily to describe the emission of light or other forms of electromagnetic radiation, such as thermal radiation.

People were aware of the effects of radiation, such as heat and light, but they did not have a precise understanding of the underlying physical processes that produced these effects. Bridging this gap, the 19th century marked significant progress in the study of radiation. J. C. Maxwell's equations, published in the 1860s [1], described the behaviour of electric and magnetic fields and showed that light is a type of electromagnetic wave. This led to a deeper understanding of the nature of electromagnetic radiation and its role in the universe. In addition, the discovery by W. Herschel of infrared radiation [2] and the ultraviolet radiation by German physicist J. Ritter [3], led to the realisation there was a wider range of light spectrum invisible to the eyes.

Building upon these foundational discoveries, the late 19th and early 20th centuries witnessed a dramatic shift in the understanding of radiation, marked by the discovery of X-rays by W. Röntgen [4] and radioactivity by A. Bequerel and M. Curie [5, 6]. These breakthroughs, along with the observation of various forms of radiation such as alpha particles (helium nuclei), beta particles (fast electrons), and gamma rays (high energy photons), which had distinct properties and produced different effects on matter (see Fig. 1.1), played a crucial role in the development of nuclear physics.

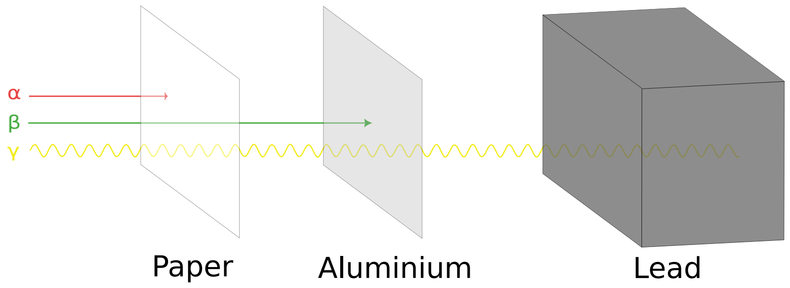

Figure 1.1: Penetration power of alpha, beta and gamma particles in different materials.

All these discoveries and advances in the understanding of physics culminated in the modern definition of "radiation". Today, this term is commonly used in a much broader sense, referring to:

**any emission and propagation of energy through space or matter,
whether in the form of electromagnetic waves or moving particles.**

1.2 The Radiation Transport Problem

The radiation transport problem, observed in a simplified scheme in Fig. 1.2, encompasses **(1) all situations where there is radiation**, including any kind of particle, such as:

- Photons (γ)
- Leptons: $e^{\pm}$, $\mu^{\pm}$, $\tau^{\pm}$, ν
- Hadrons: p, n, $\pi^{+,-,0}$, ($K^{+,-,0}$), ...
- Ions: (Z, A)

(2) emanating from a source, including:

- Radioactive sources
- Cosmic rays
- Colliding particle beams
- Synchrotron radiation

which **(3) propagates in an arbitrary geometry** composed of many structures defined by different materials and compounds. The radiation propagates in the geometry subjected to a number of relevant interaction mechanisms, affecting both radiation itself and the matter it encounters.

The effects on matter due to the passage of radiation are many, including:

- *Ionisation and excitation* of atoms or molecules in matter: The process generates an energy transfer from the radiation to the material.
- *Atom Displacement* due to nuclear interactions: The atoms in the material can displace from their normal lattice positions in matter, leading to the creation of defects and the

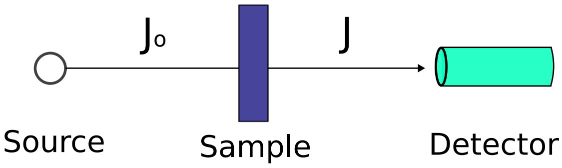

Figure 1.2: Illustration of an example of a radiation transport problem, exhibiting the variation of the initial flux (J_o), modified in an final flux (J) after the transport through a sample.

modification of material properties.

- *Production of Residual Nuclei*: Radioisotopes can be produced due to the nuclear interaction, whose type will depend of the material composition and decay chains. These residuals might be also radioactive.

And there are a variety of consequences on the radiation, for instance:

- *Energy loss, direction change and decrease in intensity* due to absorption and/or scattering of particles.
- *Creation of secondary radiation*: New particles can be created depending on the type of radiation, the material involved, and particle's energy. This could lead to the generation of "particle showers" (more details in Section 1.5).

Finally, one could have an **(4) interest in measuring/estimating/scoring** the mentioned effects.

There are many important fields of study and applications where the radiation transport in matter has relevance. To list a few:

- *Nuclear Reactor Design*: To calculate the distribution of neutron and gamma-ray fluxes within the reactor core, and to predict the behaviour of fuel rods and control rods.
- *Radiation Therapy*: To predict the distribution of radiation in tissue and to optimise the design of radiation therapy equipment, such as linear accelerators, for the treatment of cancer.
- *Space Science*: To understand space weather, studying the transport of energetic particles and electromagnetic radiation in the Earth's magnetic field and in interplanetary space.
- *Radiation and machine protection studies*: In particle accelerators, the transport of charged particles and high-energy photons produces intense radiation fields that can pose a hazard to the accelerator components and to personnel. To minimise this hazard, the study of radiation transport is used to predict the distribution of radiation in the accelerator environment and to design shielding and other protective measures (more details in Chapter 5).

1.3 The Radiation Transport Equation

To define the radiation transport equation (also known as Boltzmann equation), it is necessary to establish certain concepts and quantities:

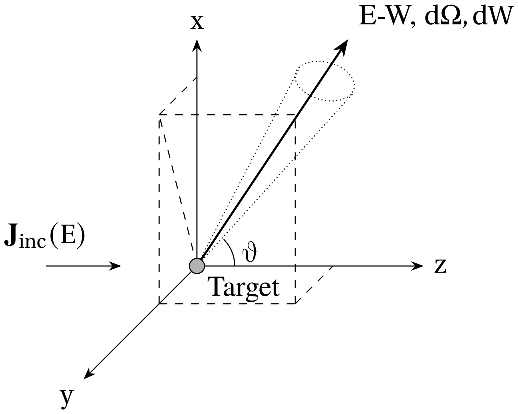

Figure 1.3: Schematic of the differential cross section.

Particle density - $n_i(\mathbf{r}, E, \Omega, t)$ -
Number of particles of species i per unit volume, unit energy, unit solid angle, at a time t.

Differential Cross section - $\frac{d^2\sigma(E,Z,A)}{d\Omega dW}$ -
Considering a flux of incoming particles J_{inc} interacting with a target (see Fig. 1.3), each type of particle can be subjected to a number of interaction mechanisms, characterised by a differential cross-sectional area, depending on the particle's energy (E) and the composition of the target (Z, A). This quantity expresses the likelihood of the incoming particles being scattered into a direction Ω with an energy loss W:

$$\frac{d^2\sigma(E,Z,A)}{d\Omega dW} = \frac{\dot{N}}{|\mathbf{J}_{inc}| d\Omega dW} \xrightarrow{[units]} \frac{Length^2}{Energy \times SolidAngle} \tag{1.1}$$

Where $\dot{N}$ is the rate of scattered particles.

Integrated Cross section - $\sigma(E, Z, A)$ -
Integrating the differential cross section (Eq. 1.1), the integrated cross section is obtained. It expresses the likelihood of an interaction to occurs:

$$\sigma(E,Z,A) = \int_{4\pi} d\Omega \int dW \frac{d^2\sigma}{d\Omega dW} \xrightarrow{[units]} Length^2 \tag{1.2}$$

Macroscopic Cross section - M σ -
If the material where the radiation is transported contains "M" scattering centres per unit volume, Mσ gives the probability of interaction per unit path length. It is known as the macroscopic cross-section.

Mean free path - λ -
The inverse of the macroscopic cross-section defines the mean free path ($\lambda = 1/M\sigma$). It represents the average distance travelled by a moving particle before it undergoes a change in direction or energy.

Given the relevant quantities, the **Transport Equation** can be defined:

The Transport Equation

The Transport or Boltzmann Equation is a balance equation determined by the time evolution of the particle density:

$$
\begin{aligned}
\int_V \mathrm{dr}\frac{\partial n_i(r,E,\Omega,t)}{\partial t} &= -\oint_S \mathrm{dA}\, j(r,E,\Omega,t)\cdot\widehat{a} && (1)\\
&\quad -M\int_V \mathrm{dr}\, n_i(r,E,\Omega,t)\, v(E)\sigma(E) && (2)\\
&\quad +M\int_V \mathrm{dr}\int \mathrm{dE}'\int \mathrm{d}\Omega'\, n_i(r,E',\Omega',t)\, v(E')\frac{\mathrm{d}\sigma}{\mathrm{d}\Omega''\,\mathrm{dW}''} && (3)\\
&\quad +M\int_V \mathrm{dr}\int \mathrm{dE}'\int \mathrm{d}\Omega\, \Sigma_j\, n_j(r,E',\Omega,t)\, v(E')\frac{\mathrm{d}\sigma_{sec,i}}{\mathrm{d}\Omega''\mathrm{dW}''} && (4)\\
&\quad +\int_V \mathrm{dr}\, Q_{source}(r,E,\Omega,t) && (5)
\end{aligned}
\tag{1.3}
$$

This is an integro-differential equation. The right hand side comprises two terms (1, 2) figuring the "destruction" of particles, and they contribute therefore negatively. Terms (3, 4, 5) represent the "creation" of particles, and contribute positively. They represent:

1. The net flux of *un-scattered particles* out of the volume V, expressed by the particle current density - j -, the unit normal vector - $\widehat{a}$ - and the surface element - dA -.
2. Particles *scattered out* of the infinitesimal volume.
3. The particles *scattered in* the volume from other states into the state of interest. The term $\frac{d\sigma}{d\Omega'' dW''}$ expresses the differential cross section for scattering from (E',Ω') to (E,Ω)
4. The *production of secondaries* of type "i" in the volume, due to interaction of other particles.
5. A *source of particles* in the volume.

There are many approaches to solve this equation, including:

- *Analytical solution*: only possible for very simple cases, where the geometries and/or the interaction models are restricted.
- *Spectral methods*: this method intends to approximate the equation in terms of "basis functions", easier to solve. As in the analytical case, this can only be applied for restricted cases.
- *Numerical quadrature integration*: these integration methods can be used for a general case, but they become inefficient for high-dimensional integral.

The only one method permitting to solve the transport equation in a general case with an arbitrary source of particles, an arbitrary geometry, and realistic interaction cross sections, is the **Monte Carlo method** (more details in Chapter Two).

1.4 Overview of Radiation Transport Interactions

This section describes the multiple interactions of particles with matter. It focuses on the electromagnetic processes involving electrons, positrons, and photons, the hadronic processes through a mostly qualitative description of inelastic interactions, and the unique characteristics of low-energy neutrons compared to other hadrons. Further details can be found in [7–9].

1.4.1 Electromagnetic Interactions

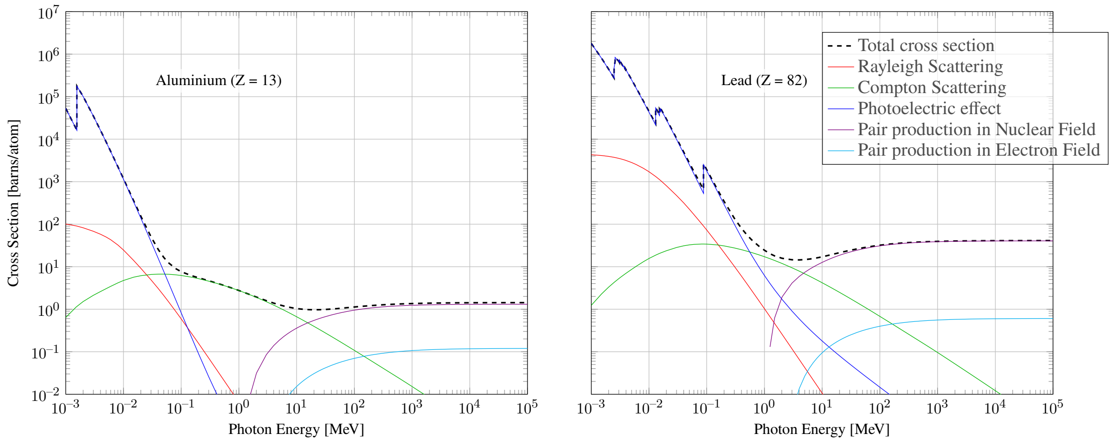

Figure 1.4: Cross section of photons interaction in Aluminium (left) and Lead (right). Data courtesy of NIST-XCOM database [10]

Photon Interactions

Depending on the photon energy and the material through which it passes, this particle will have a different probability of interacting in various ways. However, it is dominated by a particular process within a certain range of energies (see Fig. 1.4). The interactions are as follows:

- *Coherent scattering*[I]: The photon interacts with atomic electrons, changing its direction but without (or negligible) change in energy. Consequently, the energy deposited in the material is relatively insignificant compared to other processes. The cross-section of this interaction varies on the material with Z^2.
- *Photoelectric effect*: The photon is absorbed, and its energy is transferred to a bound electron, releasing it from its binding state. The final energy of the freed electron corresponds to the photon energy minus the binding energy, accompanied by atomic relaxation process if the electron is located in an inner shell. It is the dominant interaction for photons at lower energies (< MeV), and the cross-section scales with Z^{4-5} for different materials.
- *Incoherent scattering*[II]: The photon loses part of its energy and changes direction. The

---

[I] or Rayleigh scattering, named after Lord Rayleigh, who studied this process [11, 12].

[II] or Compton scattering, named after its discoverer [13].

lost energy is transferred to a free (or loosely bound) electron. Similar to the photoelectric effect, the scattering may lead to atomic relaxation depending on the electron binding energy. It is the dominant process at MeV energies, with a cross section scaling linearly with Z.

- e^-/e^+ *pair production*: When a photon interacts with the field of material nuclei, it can undergo the generation of a e^-/e^+ pair, splitting the energy of the incoming photon. Since only a negligible amount of energy is transmitted to the nucleus, the energy threshold for pair production is twice the $e^\mp$ rest mass ($m_e = 511\,{}^{keV}/_{c^2}$). This process can also occur in the field of an atomic e^- (with a lower cross section). However, the energy threshold required to conserve momentum in the process requires $4\,m_e$. Pair production scales quadratically with Z and it is the dominating process at high energies (i.e. > few MeV).

e^-/e^+ Interactions

- *Elastic Scattering*: Similar to coherent scattering observed in photons, in elastic scattering, the incoming electron or positron interacts with an atom, resulting in a change of direction, conserving energy. This interaction, however, has a minimal impact on the targeted atom. Notably, elastic scattering is a primary mechanism responsible for the angular deflection observed in the trajectories of these particles.
- *Inelastic Scattering*. In this process, $e^{-/+}$ losse(s) part of the energy transferred to the atoms in form of electronic excitation and ionisation. It is the dominant energy loss mechanisms at low-mid energies (< few MeV).
- *Bremsstrahlung*: A $e^{-/+}$ transported in matter accelerated by the electrostatic field of atoms leads to emission of radiation. The energy of the generated photon will be all or part of the energy of the $e^{-/+}$. This process is the dominant at high energies (> few MeV).
- *Positron annihilation*: A positron in a medium can interact with the electrons emitting, in most cases, two photons.

Charged Particles Transport

As a charged particle traverses a medium, it undergoes scattering by the atomic particles, analogously to the description for $e^{-/+}$ given above. Both scattering interactions can be collectively referred to as **Coulomb interactions**.

A particularity of charged particle transport in a medium lies in its notably large cross-section, which leads to multiple collisions during its path, with each collision resulting in a minor energy transfer. To account for this phenomenon, a statistical approach is utilised defining:

- *Electronic Stopping Power*: This parameter quantifies the mean energy loss per unit path length (${}^{dE}/_{dx}$) due to the interaction with atomic electrons.
- *Nuclear Stopping Power*: In this case, the energy loss arises from Coulomb collisions with nuclei. The energy losses due to nuclear collisions are generally much smaller compared to

electronic interaction, except in the case of low-energy heavy particles.

- *Multiple Coulomb Scattering*: In order to account for all the small deflections that occur in the collisions with nuclei, multiple Coulomb scattering theories treat it as net effect of these multiple events.

It is also very relevant to note that at high energies, charged particles lose energy through radiative losses, like the mentioned Bremsstrahlung in electrons case.

There is a value that defines the transition between collision stopping power and the radiative stopping power, named *Critical Energy* (E_c). This is the value at which these stopping powers are equal. Figure 1.5 shows the contribution of collision and radiative stopping power to the total, and the correspondent E_c for electrons in lead.

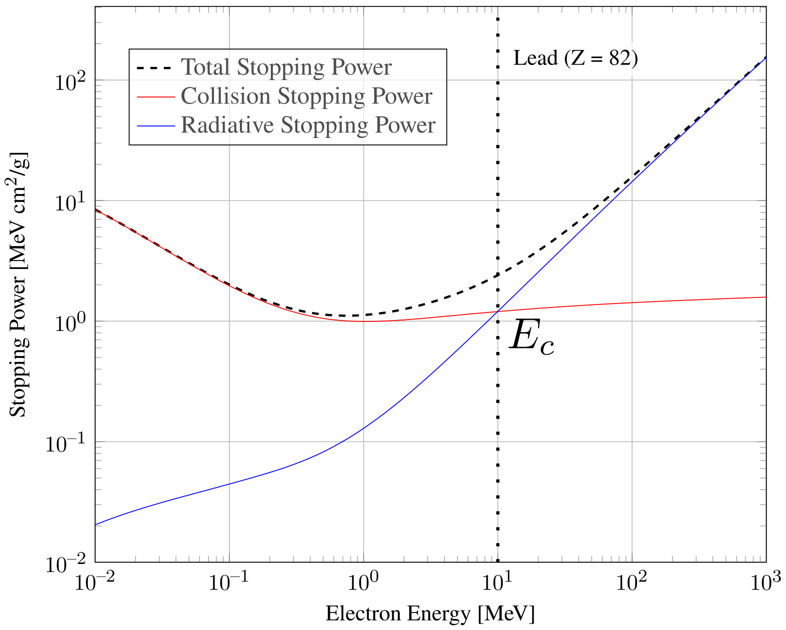

Figure 1.5: Comparison of collision and radiative stopping power of electrons in lead, illustrating the regions where each process dominates divided by the E_c. Data courtesy of NIST-ESTAR database [14]

1.4.2 Hadronic Interactions

Nuclear Interactions

Since nuclei are composed of nucleons (neutrons and protons), the interactions of hadron-nucleus (h-A) are strongly based on hadron-nucleon (h-N) interactions. Typically, these interactions are divided into elastic and inelastic:

- *Elastic Interactions*: These interactions are characterised by not producing new particles

	Particle	Rest mass [MeV/c²]	Mean life τ [s]	Main decay channel
–	γ	0	Stable	-
Leptons	e^-, e^+	0.511	Stable	-
	μ^-, μ^+	105.66	2.2×10^{-6}	$\mu^- \longrightarrow e^- \overline{\nu}_e \nu_\mu$ $\mu^+ \longrightarrow e^+ \nu_e \overline{\nu}_\mu$
Hadrons	p	938.27	Stable	-
	n	939.57	880	$n \longrightarrow p\ e^-\ \overline{\nu}_e$
	π^-, π^+	139.57	2.6×10^{-8}	$\pi^- \longrightarrow \mu^- \overline{\nu}_\mu$ $\pi^+ \longrightarrow \mu^+ \nu_\mu$
	π°	134.98	8.5×10^{-17}	$\pi^\circ \longrightarrow \gamma\gamma$

Table 1.1: Properties of most relevant particles for particle-matter interactions. The table lists their rest mass, mean life, and main decay channels. Table based on [7]

and by leaving the structure of both projectile target unchanged. There is no lower or upper energy limit for the projectile

- *Inelastic Interactions*: These involve the production of secondary particles and/or a change in the structure of the projectile/target. There is a minimum energy threshold below which these interaction cannot occur. Further details are provided in the following subsections and the reference [15].

Intermediate Energy Interactions: The Resonances Regime

As πs are the lightest hadrons (see Table 1.1), there is a range of low energies where only elastic interactions are possible. The first channel of inelastic nuclear interaction opens at 170 MeV, allowing for single π production from a π-N interaction:

$$\pi + \mathrm{N} \longrightarrow \pi' + \pi'' + \mathrm{N}'$$

For nucleon-nucleon (N-N) interactions, the channel opens at 290 MeV and becomes significant at energies above 700 MeV:

$$\mathrm{N}_1 + \mathrm{N}_2 \longrightarrow \mathrm{N}_1' + \mathrm{N}_2' + \pi$$

Typically, these two reactions are considered as generated from an intermediate state containing at least one resonance particle [III]. For instance, for single π production:

$$\mathrm{N}_1 + \mathrm{N}_2 \longrightarrow \mathrm{N}_1' + \Delta(1232) \longrightarrow \mathrm{N}_1' + \mathrm{N}_2' + \pi$$

$$\pi + \mathrm{N} \longrightarrow \mathrm{N}^*(1440) \longrightarrow \rho(770) + \mathrm{N}' \longrightarrow \pi' + \pi'' + \mathrm{N}'$$

In general, all these reactions at these energies can be included in the following forms:

$$\mathrm{h} + \mathrm{N} \longrightarrow \mathrm{X} \longrightarrow \mathrm{x}_1 + \ldots + \mathrm{x}_n$$

[III] Extremely short-lived particles ($\tau \propto 10^{-24}$s) typically formed as intermediate states in hadron inelastic interactions

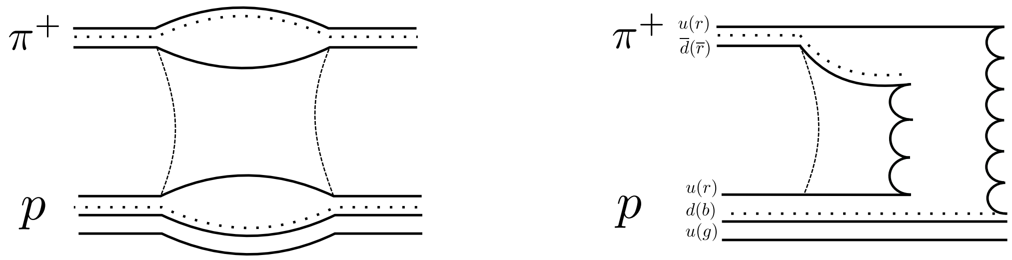

Figure 1.6: Schematic of the pomeron exchange elastic (left) and inelastic (right).

$$\mathrm{h} + \mathrm{N} \rightarrow \mathrm{X} + \mathrm{Y} \rightarrow \mathrm{x}_1 + ... + \mathrm{x}_n + \mathrm{y}_i + ... + \mathrm{y}_m$$

Where X and Y are real resonances or particles (n, p, π). This description is valid until a few GeV (below about 4 GeV), where the number of open channels grows enormously, the relevant resonances are not well known, and this treatment for nuclear interaction becomes impractical. For these reasons, different models based on interacting string are utilised at high-energy regime.

High Energy Interactions: The Strings Regime

In this model, the interacting hadrons are considered as "open strings", composed by quarks, antiquarks, or diquarks situated at the ends (Fig. 1.6). These models were conceived to describe the hadron-nucleus interactions at low transverse momentum (soft hadronic scale) following Regge's theory [16].

For instance, a π^+ particle, is depicted as a string with its valences quarks (u and $\bar{\mathrm{d}}$) at the ends. At high energies, the interaction with another hadron, such as a proton, is mediated by a Pomeron [IV] exchange, with a cylinder topology (see Fig. 1.6.i). In case there is a unitarity cut [V] on the Pomeron, two chains are generated as source of particle production (see Fig. 1.6.ii). The split of both hadrons due to the interaction produces a coloured separation for each particle, which is finally combined with the system of complementary colour of the other hadron, creating two new colourless chains.

Subsequently, these chains generated are materialised into hadrons, with the common assumption that the chains hadronisation does not depend on how they were originated (Chain universality).

Hadron-Nucleus Interactions Events Chain

Knowing the models involved in h-N interactions, the reactions during a h-A interaction are generally described with the following steps:

[IV] In particle physics, the Pomeron is a theoretical construct used to explain hadron interactions at high energies. It is conceptualised as the exchange of a colourless closed string.

[V] Method utilised on Feynman diagrams in scattering processes, isolating the intermediate states on the particles involved in the interaction.

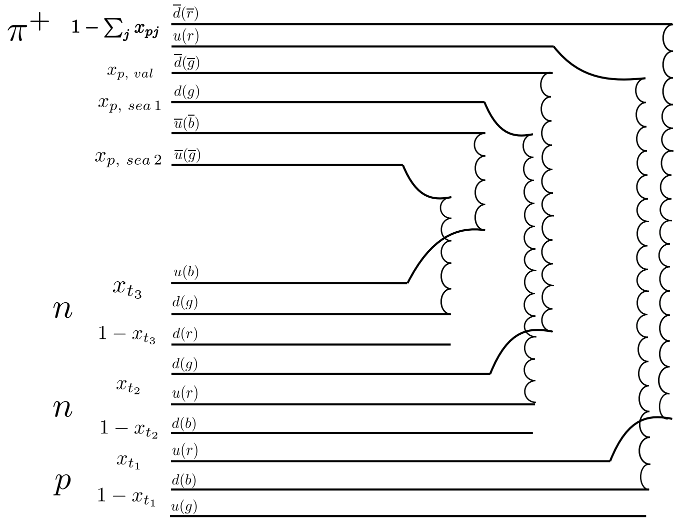

Figure 1.7: Diagram of a two-chain process in the DPM for $\pi^+ - A$ Glauber-Gribov cascade, featuring three collisions.

1. Glauber-Gribov Cascade for High-Energy Projectiles.
2. Generalised Intra Nuclear Cascade (GINC).
3. Pre-Equilibrium Emission.
4. Evaporations/Fragmentation/Fission and De-Excitation.

Glauber-Gribov Cascade.

In this context, an inelastic interaction is carried out by multiple interaction of the high energy projectile with n target nucleons. These n interactions generate 2n strings, where 2 of these strings are valence-valence strings between the valence (di)quarks of both projectile and target, and 2(n - 1) are sea-valence strings between the projectile quarks sea q-$\bar{q}$ and target valence (di)quarks (see Fig. 1.7).

Particles produced in the Glauber cascade can materialise either inside or outside the nucleus where the inelastic interaction took place. Particles that materialise within the nucleus are then included in the next phase of the process, specifically the Intra Nuclear Cascade (INC).

Generalised Intra Nuclear Cascade

This model is based on describing the nucleus as a group of non-interacting individual protons and neutrons (Fermi Gas [17]). The incident hadron is assumed as a free hadron, where free hadron-nucleon cross sections are used to define interactions with nucleons. It is a semi-classical description, since, even though, particles are point-like and follow classical trajectories, it incorporates the Pauli exclusion principle, used to restrict the generation of some of the particles that may be generated in the interactions.

There are multiple cascade models, whose applicability is in the range of hadrons from a few MeV

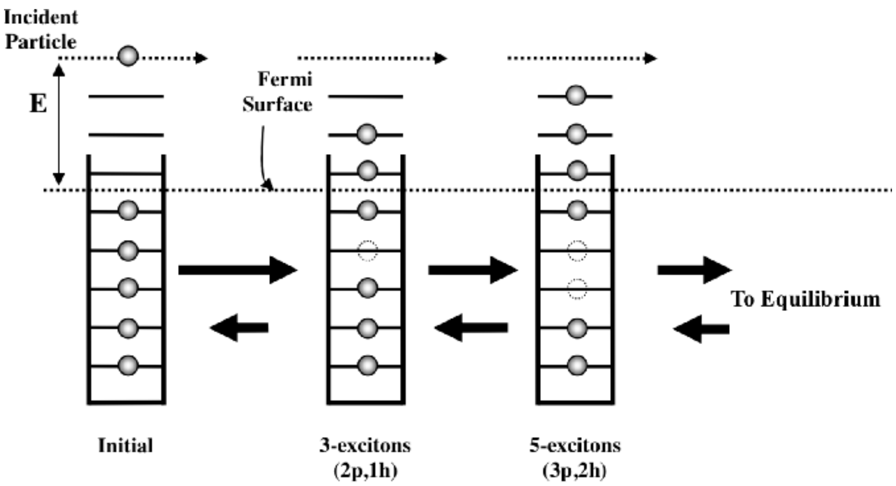

Figure 1.8: Illustration of pre-equilibrium process showing the process of excitons generation until reaching the equilibrium state. Solid lines represent single particle states in a potential well. Solid circles are the particles, while empty dashed circles are the holes. Courtesy [18].

to a few GeV. Normally, after the process generated by the cascade, where some of the produced particles will leave the nucleus, while others may re-interact with other nucleons. When their energy is below a few MeV, the step called *Pre-Equilibrium Emission* proceeds.

Pre-Equilibrium Emission

In this step, the remaining system of protons and neutrons is represented by particle-like and hole-like excitons [VI], and the remaining energy and momentum of the nucleus.

The process to reach equilibrium in a particular case is observed in Figure 1.8. When a hadron enters the target nucleus, it collides with one of the nucleons of the Fermi sea, thus producing an initial state with two particle-like excitons and one hole-like exciton, i.e., $n = 3$. Subsequent interactions produce changes in the number of excitons, being:

- $\Delta n = +2$ (New particle-hole pair).
- $\Delta n = -2$ (Annihilation of a particle-hole pair).
- $\Delta n = 0$ (Modification of the exciton configuration without changing their number).

As the system accumulates a significant level of excitons and gradually loses memory of its initial state, it transitions to a new phase, the *De-Excitation*.

Final De-Excitation

In the final state of the nuclear interaction, what remains is the excited nucleus, whose energy will be dissipated through the following processes:

[VI] excitons are a pair of a particle excited into a higher energy state and a corresponding hole left in the lower energy state.

- **Evaporation**: Isotropic emission of nucleons and light ions. Greater emission of neutrons due to the effect of the Coulomb barrier on other charged particles.
- **Fragmentation and fission**: The breaking of the nucleus into smaller pieces due to high excitation energy, where distinct models are utilised depending on the nucleus mass number.
- **Gamma de-excitation**: When the nucleus energy is below the energy required to break the binding energy of the nucleons, emission of gamma rays is the last step for the de-excitation of the nucleus.

1.4.3 Low-Energy Neutrons

As previously shown in Table 1.1, one of the most relevant particles in the realm of particle-transport in matter is the neutron. This significance arises not only because it is one of the fundamental building blocks that, along with protons, forms the nuclei of atoms, but also due to its extended lifetime when free from the nucleus, approaching a value close to 15 minutes.

Additionally, as neutrons are electrically uncharged particles, they exclusively interact with atomic nuclei. This makes their transport significant even at extremely low energies (below eV), as processes such as neutron capture can yield particles with energies of up to several MeV (e.g., gamma rays).

It is typical to divide the neutron treatment according to their energy into two categories: high energy neutrons (> 20 MeV), where the hadronic models detailed above are employed, and low-energy neutrons (20 < MeV).

A fundamental characteristic of neutrons within materials at these low energies is their complex and intricate interaction cross-section. This cross-section depends on the properties of the medium through which the neutrons traverse, including parameters like atomic mass and temperature. As illustrated in Figure 1.9, several energy regions can be identified for these neutrons:

- Thermal (and epithermal) neutrons : They are named so because neutrons spectra in thermal equilibrium follow a Maxwell-Boltzmann distribution [20], with the peak energy depending on the target medium, which for instance, at room temperature, i.e. at 290 K, is located at 0.025 eV. This energy range encompasses thermal neutrons from µeV to 0.1 eV, and their cross-section is functionally described as inversely proportional to velocity ($^1/_v$). Elastic scattering and neutron capture are the most significant processes.
- Resonance neutrons: In this regime, the cross section exhibits prominent resonance peaks associated with specific energy levels of the traversed compound (Z, A+1). The energy range spans from 0.1 eV to ≃ MeV. Neutron capture and elastic scattering reactions are common in this region.
- Fast neutrons: Within the spectrum of "low-energy neutrons", those with energies of around MeV, reaching up to 20 MeV, are termed "fast" neutrons. Elastic scattering and non-elastic reactions are predominant in this energy range.

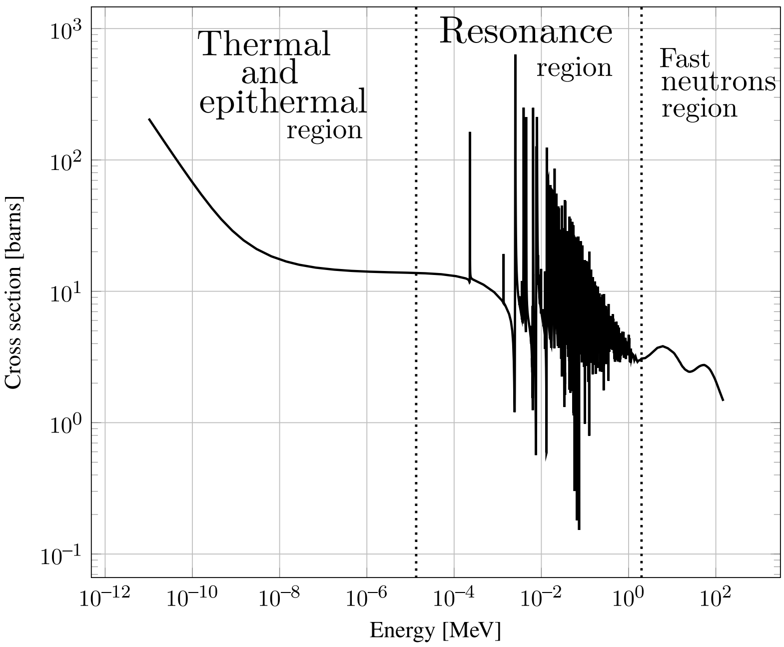

Figure 1.9: Total cross section of low energy neutrons in Cu-65. Data Courtesy of ENDF/B-VIII.0 [19]

The hadronic models exhibited previously (Sec. 1.4.2) do not well reproduce the complexity of these cross-sections. Thus, values are obtained from recognised data-bases, such as ENDF [19], JEFF[21], JENDL [22], among others.

1.5 Particle Showers

Concluding this chapter, a description of the development of high-energy EM and Hadronic shower in matter, including its coupling, permits to understand the complexity of their behaviours, and the importance at the moment of studying the consequences of particles transport in reigns of interest (more details in [7]).

1.5.1 EM Showers

As mentioned in section 1.4.1, high-energy electrons and positrons mainly lose energy through radiative losses (Bremsstrahlung), while high-energy photon interactions are dominated by e^-/e^+ pair production. When a high-energy (>few MeV) e^-, e^+, or photon is involved, a chain of these processes occurs, generating what is called an electromagnetic shower (illustration in Fig. 1.10).

The shower develops with a gradual loss of energy generation after generation, until the particles cross the "Critical Energy" (E_c), the energy at which bremsstrahlung and ionisation cross-sections are equal. Beyond this energy, the shower cannot develop further.

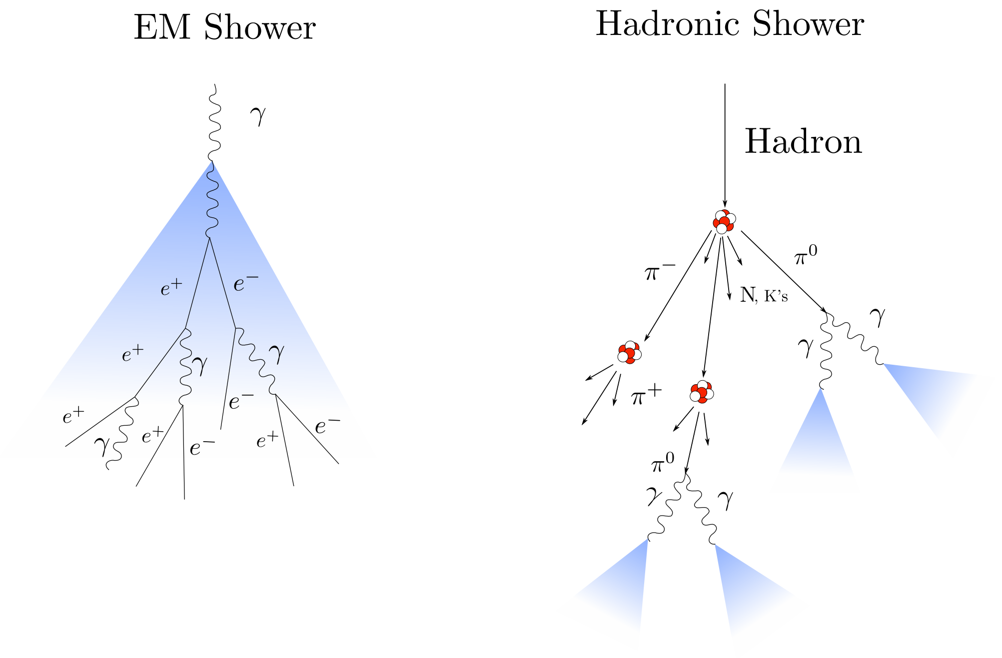

Figure 1.10: Illustration of EM shower (i) and Hadronic Shower (ii), exhibiting also the coupling due to π° decay.

Regarding the shower's depth, it can also be estimated by first defining the radiation length (X_0). This parameter is associated with the passage of high-energy e^-, e^+, and photons in matter in the following way:

- e^-/e^+: The average distance over which it loses all but $^1/_e$ of its energy via bremsstrahlung.
- γ: $^7/_9$ of the mean free path for pair production.

An approximated expression of X_0 for a single nucleus material (more details [23]]) expresses:

$$X'_0 = X_0 \times \rho = \frac{716.4A}{Z(Z+1)\ln(287/\sqrt{Z})} \xrightarrow{\text{[units]}} \text{Mass/Length}^2 \tag{1.4}$$

Where:

- ρ: Density of the material.
- Z and A: Atomic and mass numbers.

Thus, from a simplified model (more details [24]), the shower depth (X) can be estimated:

$$X \propto X_0 \times \log\left(^{E_0}/_{E_c}\right) \tag{1.5}$$

where E_0 is the initial energy of the incident particle.

1.5.2 Hadronic Showers

Beginning from an initial inelastic nuclear interaction generated by a high-energy hadron, the outcomes of this interaction are high-energy secondary products. These particles, mainly consisting of π, protons and neutrons, re-interact with other nuclei, creating a chain reaction known as hadronic shower.

Since the shower develops through nuclear inelastic interaction, the depth is defined by the inelastic scattering length (λ_{ine}), which scales with the mass number as follows:

$$\lambda_{\text{ine}} \propto A^{1/3} \tag{1.6}$$

This indicates that the hadronic showers are generally longer than electromagnetic ones:

$$\frac{\lambda_{\text{ine}}}{X_0} \propto A^{4/3} \tag{1.7}$$

Although most of the energy is subdivided among the secondary particles produced in each generation until the energy falls below the π production energy, a portion of the initial energy goes also to the nuclei as binding energy or is transferred to recoils. Additionally, less energetic particles are produced during the equilibrium phase, via evaporation, gamma de-excitation, and Fermi break-up.

1.5.3 Showers Coupling

In both cases, showers initiated by a hadron or an EM particle, are capable of generating a shower of the other type. In the hadronic case, the generation of π° is the main source of EM showers, due to their most common decay channel via two energetic photons (see Table 7.1), and because they carry about 1/3 of the energy in each nuclear interaction. Furthermore, the energy dissipated by the EM component increases with the initial energy of the hadron and becomes dominant at very high energies , because the initial energy requires more inelastic interactions to be deposit, resulting in a higher yield of π° in the process.

Electromagnetic shower can generate hadronic showers through electro-nuclear and photo-nuclear interactions. However, the energy transfer is significantly lower compared to the opposite case, due to the smaller cross-sections and the lower energy of the secondary hadrons generated. Nonetheless, this coupling may be relevant in certain applications, such as the impact of hadron production in lepton accelerators, i.e. machines where leptons, such as e^- are accelerated.

2 The Monte Carlo Method for Radiation Transport

In this chapter, the Monte Carlo (MC) method for particle transport is introduced. It provides a brief historical account of its development from its beginning to the present, followed by an explanation of the most relevant concepts of the method. These include the Central Limit Theorem, random and pseudo-random numbers, and sampling techniques essential for its operation. The chapter concludes by outlining the situations where this method is applicable, its limitations, and the reasons necessitating the diversification of these codes to overcome their intrinsic limitations.

2.1 Brief History of the Monte Carlo Method

To understand the MC method, a famous example cited by Stan Ulam in his autobiography helps to clarify ideas [25]. If one wishes to estimate the chances of winning a solitaire game (assuming the deck is perfectly shuffled before starting the game), the problem can be solved using elementary probability theory. However, this approach can be relatively tedious.

Another approach is simply to play the game many times (or program a computer for this purpose). Then, considering there are N repetitions of the game, where the cases of ending up victorious are n, the probability of winning can be estimated in the following way:

$$p = \lim_{N \to \infty} {}^{n}/_{N} \tag{2.1}$$

This example allows for a preliminary definition of the MC method:

"A stochastic approach to obtain outcomes for
both probabilistic and non-probabilistic problems".

Calculating the chances of winning the solitaire game is an example of a probabilistic problem. For a non-probabilistic problem, the needle experiment of Compte de Buffon serves as a classic example [26]. In this experiment, Compte de Buffon throws multiple needles of length L randomly (or as much random as he could!), onto a horizontal plane ruled with straight lines a distance d

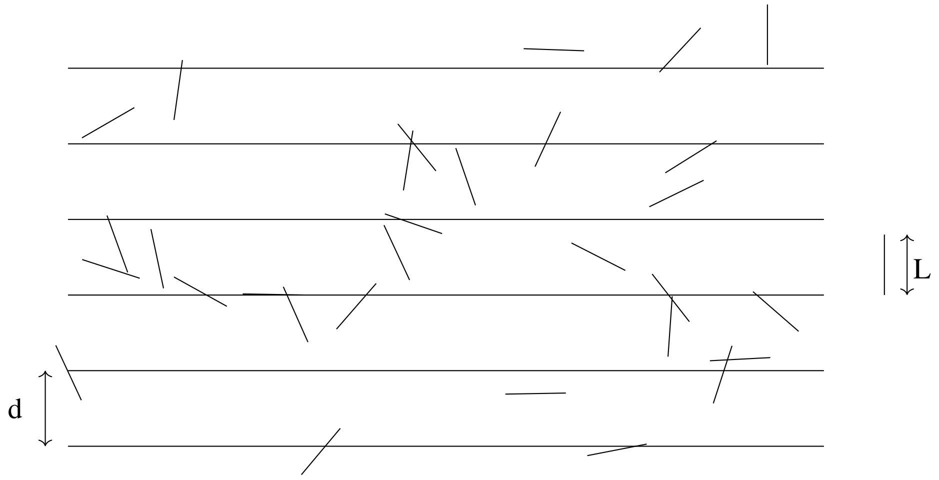

Figure 2.1: Illustration of Buffon's needle problem

apart (with d > L). Figure 2.1 illustrates the experiment. He then calculates the probability - p - that the needle will intersect the lines, obtaining:

$$p = \frac{2L}{\pi d} \tag{2.2}$$

From the results above (Eq. 2.1), it is easy to observe that the value of π can be estimated as follows:

$$\pi \approx \frac{2L}{d} \times {}^{n}/_{N} \tag{2.3}$$

Over the years, the theory of probability evolved, and the MC method found applications in various fields of knowledge, including particle transport in matter. One of the pioneers in applying the MC method for this purpose, albeit without formal publication, was Enrico Fermi in the 1930s, when he conducted numerical experiments to understand neutrons transport. These first attempts ended up in creation of an analogue machine called the "Fermi's Trolley" or the FERMIAC [27, 28].

The foundational work on the MC method in particle transport was laid by Ulam, Metropolis and Von Neumann in the 1940s during the times of the Manhattan Project. In 1949, they published the first paper on the use of MC method [29], defining it as:

> **"A statistical approach to the study of differential equations, or, more generally, of integro-differential equations that occur in various branches of the natural sciences."**

In this paper, they describe how to use this method for the study of particle transport, and the computational procedure. It is fundamental to note that the development of computers was in its nascent stages during those years, in machines like the ENIAC [30], enabling the execution of such studies, despite significant limitations in computing power. These limitations gradually reduced , but they continue to pose a considerable challenge today.

The concept of MC method applied to radiation transport in matter is detailed in the following sections, starting with a basic introduction to probability theory, which is fundamental for understanding all the necessary concepts.

2.2 Basics on Probability and Statistics for Monte Carlo Method

Many concepts are needed to understand **The Monte Carlo Method**:

Random variable
A random variable, denoted as X, describes the outcome of an event (e.g. experiment) where the value cannot be predicted with certainty. What is known about X includes:

- The possible values: $X \in [X_{min}, X_{max}]$.
- The probability density function (defined below).

Independent random variables
Two random variables, X and Y, are considered independent if "the knowledge of X does not provide any information to predict Y". More formally:

$$P(Y=y|X=x)=P(Y=y) \tag{2.4}$$

where P(B | A) expresses the probability of B given ("|") A.

The Probability Density Function (PDF) - p(x) -
The PDF describes the likelihood of an outcome for a random variable. It has the following properties:

- $p(x) \geq 0$ for all x
- $\int dx\, p(x) = 1$
- $\int_a^b dx\, p(x) = P(a < X < b)$

Where P(a < X < b) denotes the probability of being an outcome $x_1 \in [a, b]$

The Cumulative Distribution Function (CDF) - $F_x(y)$ -
The CDF of a random variable X, evaluated at x, expresses the probability of obtaining a value less than or equal to x.

$$F_x(y) = P(x \leq y) = \int_{-\infty}^{y} p_x(t)dt \tag{2.5}$$

The Expectation value - $\langle . \rangle$ -

The **expectation value** measures the average value of a random variable X:

$$\langle x \rangle = \int_{-\infty}^{\infty} dx\, x p(x) \tag{2.6}$$

The Variance - σ^2 - *and the Standard Deviation* - σ -

σ^2 and σ measure the square and the average deviation from $\langle x \rangle$ correspondingly:

$$\sigma^2(X) = \langle (X - \langle X \rangle)^2 \rangle = \langle X \rangle^2 - \langle X^2 \rangle \tag{2.7}$$

Estimator

An estimator can be defined as a function that "produces values looking to estimate a quantity"

A useful example will clarify the concept of the estimator. The function $\overline{x} = \frac{1}{N}\sum_{n=1}^{N} x_i$ is an estimator of the expectation value (or mean):

$$\langle \overline{x} \rangle = \int dx_i \frac{1}{N} \sum_{n=1}^{N} x_i p_{x_i} = \frac{1}{N} \int dx_i \sum_{n=1}^{N} x_i p_{x_i} = \frac{1}{N} \sum \int dx_i x_i p_{x_i} = \frac{1}{\cancel{N}} \times \cancel{N} \langle x \rangle$$

$$\boxed{\langle \overline{x} \rangle = \left\langle \frac{1}{N} \sum_{n=1}^{N} x_i \right\rangle = \langle x \rangle} \tag{2.8}$$

This result is essential, and the reasons will be explained in the next section.

Even more important is the result for the variance of this estimator:

$$\mathrm{Var}\,(\overline{x}) = \left\langle \left(\left(\frac{1}{N} \sum_{n=1}^{N} x_i - \left\langle \frac{1}{N} \sum_{n=1}^{N} x_i \right\rangle \right) \right)^2 \right\rangle = \frac{1}{N^2} \left\langle \left(\left(\sum_{n=1}^{N} x_i - \left\langle \sum_{n=1}^{N} x_i \right\rangle \right) \right)^2 \right\rangle = \frac{1}{N^2} \mathrm{Var} \left(\sum_{n=1}^{N} x_i \right)$$

Finally, considering that the random variables x_i are independent, the Variance is linear. Thus,

$$\frac{1}{N^2} \mathrm{Var} \left(\sum_{n=1}^{N} x_i \right) = \frac{1}{N^2} \sum_{n=1}^{N} \mathrm{Var}(x_i) = \frac{\cancel{N}}{N^{\cancel{2}}} \mathrm{Var}(x)$$

Obtaining the fundamental result:

$$\boxed{\mathrm{Var}\,(\overline{x}) = \frac{\mathrm{Var}(x)}{N}} \tag{2.9}$$

It expresses that the precision of the estimator $\overline{x}$ increases when the number of samples N increases.

2.3 The Central Limit Theorem

Having introduced the necessary elements for understanding probability theory, the next step is to detail its most crucial theorem, which justifies the MC method. This theorem is the **Central Limit Theorem**, which specifies:

Central Limit Theorem
If $x_1, x_2, .., x_n$ are n values of X sampled from a PDF p(x) with mean ($\langle X \rangle = \mu$) and standard deviation σ, both finite, the CLT states that the estimator:

$$\bar{x} = \frac{1}{n} \sum_{i=1}^{n} x_i$$

$\bar{x}$ is a random variable following a **Gaussian distribution** with the same mean $\langle \bar{x} \rangle = \mu$ a and standard deviation $\sigma/\sqrt{n}$. Taking the limit for large n, it comes $\langle \bar{x} \rangle = \langle x \rangle$. This result can be extended to an arbitrary function f(x), obtaining:

$$\overline{f(x)} = \frac{1}{n} \sum f(x_i)$$

$\overline{f(x)}$ is also a random variable, following a Gaussian distribution with mean $\langle \overline{f(x)} \rangle = \langle f(x) \rangle$ and $\mathrm{Var}(\overline{f(x)}) = \mathrm{Var}(f(x))/n$.

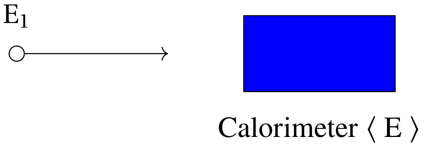

Figure 2.2: Particle with E_1 energy impinges onto a detector, where all the energy is deposited.

To understand the implications, consider the following example: a detector capable of measuring the energy of the particles (basically a calorimeter, see Fig. 2.2). The particles are emitted from a source, with random energy in a range of $[E_{min}, E_{max}]$ with equal probability (p(x) is a uniform distribution). The particles deposit all their energy in the material, and the detector estimates their energy using the mean estimator. The measured $\bar{E}$ is a random variable (as explained in the CLT), and it follows a certain distribution that depends on the number of particles emitted by the source and used to estimate the average $\langle E \rangle$, i.e., being $\langle E \rangle = \frac{1}{N} \sum E_i$:

- $N = 1$: $\langle E \rangle = E_1$. It follows a uniform distribution within the range $[E_{min}, E_{min}]$.

- N = 2: $\langle E\rangle = \frac{1}{2}\sum_{i=1}^{2} E_i$. Resulting in a triangular distribution.
- N = 3: $\langle E\rangle = \frac{1}{3}\sum_{i=1}^{3} E_i$. The distribution begins to resemble a Gaussian.
- N = 10: $\langle E\rangle = \frac{1}{10}\sum_{i=1}^{10} E_i$. It now closely coincide a Gaussian distribution.

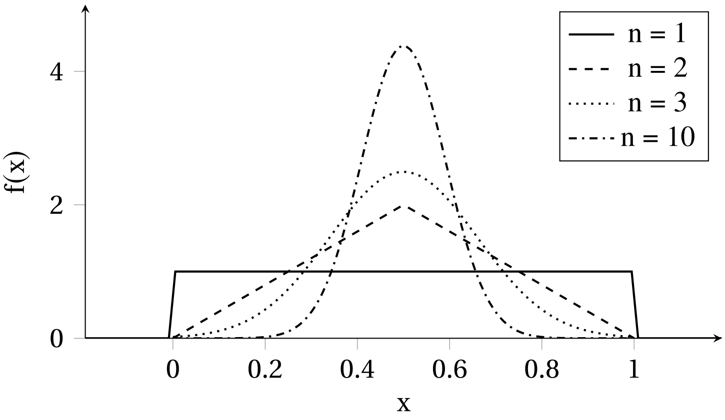

Figure 2.3: PDFs for various values of n. As n increases, the distribution approaches a Gaussian distribution (as the CLT predicts).

These results obtained were due to being sampling from a uniform distribution. Other distributions would emerge at lower N values, but the CLT ensures that with a sufficiently large values of N, the distribution of the means will tend to a Gaussian distribution.

The obtained results are attributable to sampling from a uniform distribution. While other distributions might manifest at lower N if sampling initially from another distribution, the CLT asserts that, as N becomes sufficiently large, the distribution of the means will converge towards a Gaussian distribution. Furthermore, the variance (or error) of this distribution decreases as N is increased, allowing for a precision modulated at discretion.

2.4 Random and Pseudo-Random Numbers

MC methods heavily rely on random number generation. Randomness is exploited throughout the entire process of simulating the particle histories, used to select interaction types and step lengths sampling through the interaction cross-sections. They are also essential for tracking particles, for sampling energy loss, and for determining changes in direction from differential cross sections, among others, which are necessary to estimate desired physical observables.

Although, ideally, the numbers utilised should be obtained from random processes, in practice, pseudo-random numbers are employed. These pseudo-random numbers are uniformly distributed numbers obtained from a deterministic algorithm (which means that actually they are not truly random). Nonetheless, they pass all the tests to consider them as random [31]. In general, it is better to use pseudo-random numbers because they allow reproducibility in the simulations, which is useful for tasks such as code debugging. The process to generate these numbers typically involves providing a seed (or several seeds) value/s, such as X_1, from which the sequence begins. Then, starting from X_1, X_2 can be calculated, and so on.

One simple example is the linear congruence, where $X_{n+1} = \mathrm{mod}(aX_n + c, m)$, and the values of a, c, m are carefully chosen to obtained numbers according to the criteria of randomness [32].

2.5 Random Sampling and Sampling Techniques

The importance of the use of random numbers in MC methods has been underlined. The generation of these random values from a given distribution is referred to as *sampling* or *random sampling*.

For the uniform distribution of pseudo-random numbers, generators detailed in the previous section suffice. Although, when one needs to sample from arbitrary distributions, various techniques are available, often based on the use of the uniform distribution. Two of the most well-known techniques are **inverse sampling** and **rejection sampling**.

The *inverse sampling* method operates as follows:

Consider one wants a random variable, X, with a CDF of F_X:

1. Using a uniform random generator, u ~ Unif (0,1)
2. Let $X = F_X^{-1}(u)$

And X follows the CDF of F_X.

An example with an important result will clarify the method. Sampling from an exponential distribution is fundamental in particle transport for step lengths and distances to decay. Using the inverse sampling method:

$$p(x) = e^{-x/\lambda}, x \in [0, \infty]$$

Normalising the CDF:

$$F(t) = \int_0^t \frac{e^{-x/\lambda}}{\lambda} = 1 - e^{-t/\lambda}$$

Sampling a $\xi \in [0, 1)$:

$$\xi = F(t) = 1 - e^{-t/\lambda}$$

And solving for t:

$$t = -\lambda \ln(1 - \xi) = -\lambda \ln(\xi) \Rightarrow \boxed{t = -\lambda \ln(\xi)}$$

The last step follows from the fact that $1-\xi$ is distributed equally to ξ.

As previously mentioned, this result is fundamental for determining the step length during particle transport, because path lengths to the next interaction follow an exponential distribution, where λ denotes the mean free path of a specific interaction.

To prove this, let n particles per unit time and surface enter normally on a material of width ds and N scattering centres per unit volume, with a cross sectional area σ (Fig. 2.4).

1. Number of particles that interact is given by $dn = nN\sigma ds$.
2. The interaction probability is $\frac{dn}{n} = N\sigma ds$.
3. p(s) is the distribution of path lengths to the next interaction.

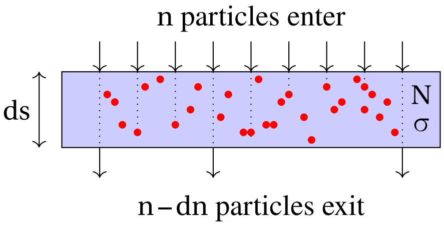

Figure 2.4: Illustration of flux of n particles per unit of time, impinging onto a material with N scattering centres, and σ cross-section.

Then, the probability p(s) of an interaction occurring after a particle has been transported a distance s is:

$$p(s) = \left[1 - \int_0^s ds' p(s')\right] N\sigma = \int_s^\infty p(s') ds' (N\sigma)$$

For clarification:

- $\int_0^s ds' p(s') N\sigma$: the probability of interaction between 0 and s
- $\int_s^\infty ds' p(s') N\sigma$: the probability of interaction between s and infinity
- $\int_0^s ds' p(s') N\sigma + \int_s^\infty ds' p(s') N\sigma = 1$

And finally, the solution to this equations is:

$$\boxed{p(s) = \frac{1}{\lambda} e^{s/\lambda}} \longrightarrow \lambda = 1/N\sigma \tag{2.10}$$

The inverse technique is particularly useful when the distributions can be inverted and the CDF calculated analytically. In case it is needed another approach, there is the *rejection technique* which proceeds in the following way:

1. Let f(x) be a normalised distribution from which one wants to sample.
2. Let g(x) be another normalised distribution that can be sampled, where $Cg(x) \geq f(x)$ (C a constant), for all $x \in [x_{min}, x_{max}]$.
3. Generate two uniform pseudo-random number, $\xi_1 \in [0, 1)$ to sample from g(x), and ξ_2.
4. The random value is accepted as sampled from f(x) if $\xi_2 < f(x)/Cg(x)$, otherwise ξ_1 and ξ_2 are re-sampled.

It is common to choose a uniform rectangular distribution to define g(x).

2.6 Basic Components of a Monte Carlo Code

There are some basic ingredients that a MC code for particle transport must include to be considered as one:

- *Geometry Description Package*. Every MC code has a particular manner to describe the geometry inside which the particles will be transported. Depending on the type of description, a custom *Geometry navigator* is also necessary to locate particle positions in the geometry and compute distances to geometry boundaries.
- *Physics Interactions*. The particles must have associated interactions defining how they behave when moving through matter. Depending of the MC code, it may include particles and interactions to emulate all major interactions (as in the case of a general-purpose code), or it may be restricted to a subset (e.g., the PENELOPE code, which simulates only e^-, e^+, γ) [33].
- *Particles source*. The code must provide a way to define the source of particles that will be transported.
- *Scoring Methods*. The previous three features enable a simulation to run, but the code remain meaningless without a way to extract information. It must provide methods to obtain, or "score" relevant quantities (e.g., Energy deposited, Fluence, Flux, etc) in volumes and surfaces correspondingly.
- *Biasing Techniques*. Many MC codes allow for the application of *variance reduction techniques*. These techniques distort probability distributions by applying modified distribution $p'(x)$ instead of the natural one $p(x)$. They are typically used to enhance rare events in a simulation, focusing on these specific cases, allowing a reduction in CPU time.
- *Transport and Production Cuts*. These parameters act as thresholds for particle transportation or generation. Transport cuts terminate particle trajectories when their energy falls below a predefined value, while production cuts specify the minimum energy at which secondary particles are produced. These cuts are crucial for controlling the simulation's precision and computational efficiency.
- *Fields*. The code may include options to define magnetic, electric and/or gravitational fields.

2.7 Basic Flow Diagram of a Monte Carlo Simulation of Radiation Transport

A schematic and simplified algorithm of a MC simulations for particle transport typically involves the following steps:

- Initialisation: Define the source of particles, geometries, materials and the required scoring.
- Main Loop: Iteratively perform the following steps for a large number (N) of primary particles (particles emerging from the source):
  1. *Initialise Particle State*: Set the initial position and momentum of the source particle.
  2. *Interaction Definition*: Determine the integrated cross-sections for each type of interaction based on the particle's current energy, material, and type.
  3. *Mean Free Path Calculation*: Evaluate the mean free path $\lambda(E)$.
  4. *Step length Sampling*: Randomly sample the step length to the next interaction while simultaneously accumulating contributions to estimators.
  5. *Energy loss and direction change sampling*: Sample energy loss and/or changes in particle direction based on the differential cross-section for the specific interaction. Again, accumulate the contributions to estimators.
  6. *Secondary particle generation*: Add any generated secondary particles to the particle stack, if applicable.
  7. *Survival check*: Check if the primary particle survives the current interaction. If it does survive, update its energy and direction and return to step 3. If not, return to step 2 (or step 1 if there are no more particles in the stack).

2.8 Assumptions and Limitations of Monte Carlo Method

In the previous sections, the MC method for radiation transport and its capabilities were detailed. Considering the strengths expressed, it is important to summarise the assumptions made when performing a simulation to ensure that the particular problem intended to be addressed will be feasible with MC simulations:

1st Assumption: *The Medium is Homogeneous.*
In a homogeneous material, its density and composition are uniform at every point. Other assumptions related to the medium include it typically being isotropic and amorphous. Exceptions exist, such as in the case of using crystals to channel charged particles [34], and scenarios involving non-isotropic magnetic or electric fields.

2nd Assumption: *The Material is not Affected by Previous Particles*[I].
This does not imply that the material is unaffected in reality, but rather that the potential effect of one particle on the material will not be considered for subsequent simulated particle. This

---

[I] Common, but not general assumption, since it is not considered in codes like McCARD [35], utilised for nuclear reactors simulations limitation may affect the simulation accuracy, for example, in cases where damage or significant defects are created in the material, and accounting for them would be necessary during the transport of upcoming particles.

3rd Assumption: *The Particles do not Interact with each other.*
In a MC transport code, particles are tracked individually. It is essential to note that primary particles from the source do not interact with each other, nor with any potential secondary particles generated during transport. Some physical effects, such as the collective effects of beams in accelerators at high energies, cannot be replicated using this type of codes.

4th Assumption: *The Transport Process is Markovian* [II].
A process is considered Markovian if the future evolution of the system is determined only by its current state and not by its history. In particle transport terms, the fate of a particle does not depend on its past history but only on its current energy, position, and direction. The random motion of a Brownian particle in a fluid is an example of a non-Markovian process. In this case, the particle's motion is influenced by the thermal fluctuations in the surrounding fluid, resulting in correlated changes in direction and speed. Consequently, the particle's motion cannot be described as a series of independent events.

5th Assumption: *Semi-classical representation of particles*
Assuming particles point-like and following classical trajectories is critical to highlight, as it delimits the energy range within which particles can be transported while maintaining a physically consistent situation.The Heisenberg uncertainty principle establishes that it is impossible to precisely know both position and momentum simultaneously. The particle's de Broglie wavelength must be significantly smaller than typical inter-atomic distances for that assumption to hold. Fig. 2.5 exhibits their wavelength expressed as:

$$\lambda_{dB} = \frac{hc}{\sqrt{E_k\,(E_K + 2m_0c^2)}}$$

where:

- E_k is the particle's kinetic energy
- m_0 is the rest mass
- h is the Planck constant
- c is the speed of light

2.9 Systematic Uncertainties of Monte Carlo Method

In preceding sections, the discourse was centred on uncertainties in statistical scenarios and their management through MC simulations. Although MC simulations inherently cannot produce exact outcomes, their associated statistical error or uncertainty can be progressively mitigated by increasing the number of primary particles.

[II] This assumption is in fact a consequence of the 2nd and 3rd, but it is added for clarity.

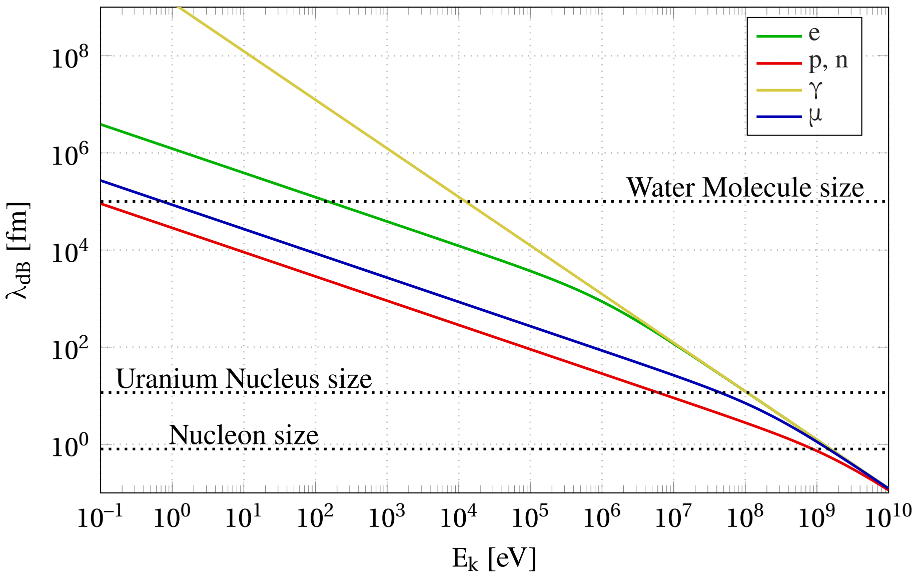

Figure 2.5: De Broglie Wavelength (λ_{dB}) as a function of particle energy (E_k) for various particles, illustrating the range of applicability of MC simulations.

In contrast, this section introduces a different kind of uncertainty, the systematic ones, which do not arise from stochastic fluctuations. Instead, these uncertainties arise from multiple origins, some due to an incomplete understanding or oversimplifications of the problem. An example includes the presence of materials in the geometry with insufficiently known properties or where the geometry cannot be precisely replicated.

Excluding user errors, systematic errors might still emerge from bugs in the simulation code or from implementation-related issues. For instance, the **Transport Algorithm** might inaccurately deposit the energy of particles during a step, or there could be poor handling of boundary conditions. The most appropriate way to evaluate an algorithm's quality is through benchmarks at the macroscopic level, using large geometries.

Despite these sources of uncertainties are important, the most crucial ones are intrinsic to the definition of a MC code for particle transport: the **Physics Models** utilised, and the **Cross-Section Databases**. These characteristics must be tested at a microscopic level, for example, by simulating particle transport in thin layers.

Numerous physics models have been developed to emulate interactions observed in nature. While some are more accurate, others are applicable only within specific energy or material (Z, A) ranges. The existence of multiple models stems from the fact that no single model currently encapsulates every aspect of the physical realm. Some models may be more suitable in certain regimes, whereas others might be better for different particle types, energies or materials. Moreover, even when the cross-section data is derived from experiments or theoretical models, it still carries an inherent uncertainty. This can lead to significant deviations from experimental observations or practical expectations. For instance, if one aims to create a gamma treatment and the absorption cross-section has a non-negligible uncertainty, the treatment will not only fail its objective but could also cause harm to the patient.

Consequently, several pivotal questions central to this thesis emerge:

- Is simulating with only one MC code sufficient?
- How can one trust the results obtained from a MC code?
- Would it be advantageous to utilise at least a second code?
- What if simulations run with two codes yield drastically different results?

The answers to these questions determine the applicability of a code to a specific problem. For instance, using the a MC code dedicated to EM particles to simulate transport hadrons in matter would be clearly erroneous. A subtler situation might involve physics models that have not undergone rigorous testing or validation within certain energy ranges.

However, if one possesses a MC code with physics models validated against experimental results and cross-section databases, trust in the simulation's accuracy increases. Nevertheless, the "perfect" code remains elusive. Models are never entirely accurate, and cross-section databases always come with inherent uncertainties. Hence, relaying on a second code (or even multiple codes), equipped with distinct physics models that are also benchmarked and validated, along with different cross-sections databases, can lead to more robust and reliable conclusions, since the complementary results allow for a better quantification of the systematic errors.

In the previous statement, the potential discrepancies between geometry descriptions are not considered. These differences between codes might have an impact if, for example, cases involve a geometry or materials more detailed in one code than in the other.

This leads to the central point of this thesis. The primary aim has been to develop a new simulation framework facilitating simultaneous simulations with two distinct MC codes, FLUKA and G4, presented in the next two chapters. In this framework, discrepancies in setup description between the two simulations is either non-existent or minimal, ensuring an equivalent comparison focused mainly on the selected physics.

While this might sound unprecedented, numerous studies have drawn comparisons between MC codes [36–39]. However, none have been performed with the mentioned codes applied on shielding and machine protection studies involving highly intricate geometries at energies spanning from GeV to multi-TeV with totally equivalent simulation characteristics.

3 Geant4

In this chapter, G4, one of the most widely used MC codes for radiation transport in matter within the scientific community, will be introduced. Each section will be dedicated to a specific aspect of this software, particularly focusing on the functionalities it offers to users and how these can be accessed.

The chapter will begin by briefly recounting the history of G4, exploring its origins and evolution. The philosophy regarding its application by users will also be analysed. In addition, the hierarchical description used to geometry definition will be detailed, accompanied by a review of the physical processes and models included in G4.

Later on, the functionalities of G4 will be explored, including discussions on biasing techniques, fields, cuts, and scoring options. The chapter will conclude by enumerating the available graphical interfaces, which greatly facilitate and enhance the use of this powerful MC simulation tool.

3.1 A Historical Overview of the Geant4 Toolkit

Figure 3.1: Geant4 Logo as of version 11 (Latest release: 11.2.0. Date: 08-12-2023)

Geant4 (GEometry and Tracking 4) is a general-purpose MC software package that offers a toolkit for simulating the passage of particles through matter [40–42]. Originating from two independent research centres: the European Organisation for Nuclear Research (CERN)[I] [43] and

---

[I] Centre Européen pour la Recherche Nucléaire

The High Energy Accelerator Research Organisation (KEK)[II] [44] in 1993, the G4 project aimed to improve the FORTRAN-based Geant3 simulation programme by adopting modern computing techniques [45]. Geant3 encountered two primary limitations:

1. Its complex structure, shaped by historical reasons, made it unfeasible to introduce new features or correct bugs, highlighting the constraints of FORTRAN and/or old programming methodologies.
2. A decreasing workforce at CERN underscored the challenges of having centralised support.

In 1994, the two groups merged their activities and submitted a formal proposal, RD44, to create a new object-oriented (OO) programme designed for advancements in subatomic physics research [46]. The initiative attracted a large international collaboration of physicist programmers and software engineers from institutes and universities around the world. Over time, it expanded to include scientists from fields such as nuclear, accelerator, space, and medical physics.

The R&D phase was completed in December 1998 with the delivery of the first production release [47]. The collaboration was subsequently renamed G4, and a formal Memorandum of Understanding (MoU) was signed by many of the participating organisations in RD44. This MoU outlines the programme's management, maintenance, and user support, emphasising its ongoing development and refinement.

Since its initial release, G4 has undergone several enhancements. A significant update came in 2016 with version 10.0, which incorporated a major restructuring of the code to incorporate multi-threading support [48]. This restructuring enabled G4 to take advantage of modern multi-core processors, dramatically increasing the speed and efficiency of the simulations.

Although originally G4 was primarily developed for high-energy physics applications, such as detectors designing [49–51], the code evolved to include a variety of different fields. It is now utilised in diverse sectors, including space applications, medical science, among many more [41, 52–54].

3.2 Geant4's Design Philosophy and User Roles

The idea behind the G4 project was to develop a more flexible code, making an OO system, highly modular and customisable, providing a much easier way to address potential bugs in the code and to add new features. This facilitates better collaboration with the project and offers users a simpler approach to create, extend, and modify the toolkit for their purposes.

While higher flexibility might be an advantage and an evolution from its predecessor, one important drawback is the responsibility placed on the user to effectively make use of the toolkit. This can be clarified by understanding how simulations are conducted with the G4 toolkit.

[II] 高エネルギー加速器研究機構 (Kō Enerugī Kasokuki Kenkyū Kikō)

The G4 collaboration identifies two types of G4 users: The **end user**, and the **application programmer**. While the following description is a simplification, it helps clarify the distinctions ([55, p. 11] for more details). Commonly, when software is acquired, it is already compiled; the user provides an input (e.g. a text file detailing simulation preferences) to receive an output (e.g. energy deposited in a specific region of the geometry). However, this is not the case with G4. Here, the user requires some C++ programming, and G4 knowledge, to create the **application** that will essentially conduct the simulation. This application must include code related to the geometry description, the physics used, the participating particles, the primary particles generator, and other requirements such as scoring relevant quantities, fields, etc. The user in charge of this task is termed application programmer. Conversely, if a user has an already established application and it merely wishes to modify certain simulation parameters (e.g., energy or type of source particles), this aligns more with the initial description. Such a user referred to as end user.

The primary feature offered by the G4 toolkit to end users for parameters control is the **macro file** [56, p. 48]. This file consists of **User Interface (UI) commands**. Many UI commands, like *gps* (generic particle source [56, p. 24]), are standard in the G4 toolkit, allowing users to set particle type, direction, energy, etc. Although, adhering to the philosophy of affording users flexibility, application programmers can introduce additional UI commands to provide control over other parameters to end users.

G4 also supports two persistent formats for defining simulation geometry:

- The Geometry Description Markup Language (GDML) [57]: An XML-based language designed as an application-independent format for describing geometries.
- TextGeom [58]: A feature dedicated to importing G4 geometry setups from a plain text description.

3.3 Fundamentals of Geant4 Geometry: Solids, Volumes, and Hierarchical Description

In order to define the geometry (called "Detector" in G4 documentation [56, p. 9]), three fundamental concepts must be understood: **Solid**, **Logical Volume**, and **Physical Volume**.

Solids represent geometrical primitives. These are purely geometrical representations with no associated physics. The user defines their shape, and size. A wide array of solids is available, ranging from basic shapes like cylinders, cubes, boxes, and spheres to more intricate forms like toruses, twisted boxes, and tessellated solids [56, p. 122]).

Logical volumes associate physical attributes to solids. While these volumes have yet to become part of the simulation geometry, they are no longer just abstract concepts. Their size and shape are predetermined by the solid's information, but acquiring physical properties such as material composition, fields (magnetic, electric, and/or gravitational), and other user-specific details (via

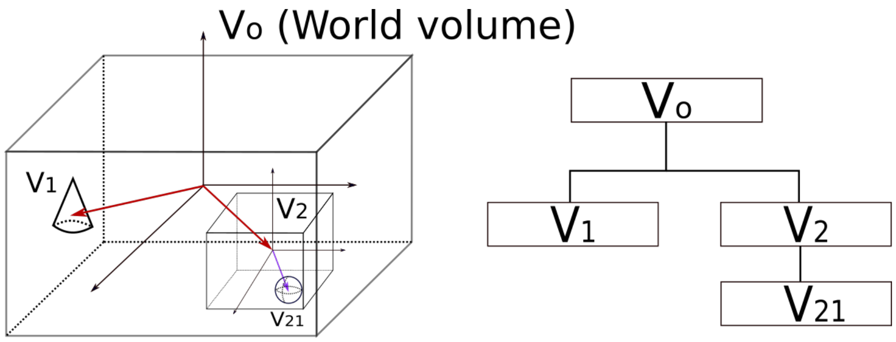

Figure 3.2: Illustration of G4 hierarchical description. Four volumes V_0, V_1, V_2, and V_{21} are used to define the simulation geometry (left) and the hierarchy among them (right)

G4UserLimits [56, p. 291]) used to impose limits on particle tracking, such as the step size, kinetic energy, and other parameters.

Another important concept, though not compulsory in a G4 simulation, are the **Regions**. Useful in scenarios with complex geometry setups, regions are essentially groups of two or more logical volume sharing physical properties. Two crucial attributes include fields and production cuts. In this context, if a user wishes to assign the same properties to numerous logical volumes, it can simply be attributed to the region, eliminating the need to assign it to each logical volume individually,

Lastly, there is the concept of **Physical Volume**. In this case, users define the spatial positioning of the logical volumes, specifying their position, and rotation. Physical volumes represent the final stage in defining simulation geometry. An important aspect is the hierarchical placement, illustrated in Fig. 3.2. The first volume a user must define is the "world volume" (root volume of the hierarchy). This unique volume contains all other volumes. The world volume sets the global coordinate system, centred within itself. From this "world volume" concept, the mother-daughter volume relationship can be defined. To position two volumes V_1 and V_2, users need to be associate them with another volume (V_0). Consequently, V_1 and V_2 are placed relative to V_0, meaning V_0 is the mother volume of V_1 and V_2, becoming them daughter volumes of V_0. However, V_2 can also function as the mother volume of another volume, V_{21}. This forms a **"Geometrical Hierarchy"** in geometry definition. It should be noted that the mother-daughter volumes association exists between logical volumes.

3.4 Overview of Physics in Geant4

In G4, physics processes are not pre-defined; users are required to explicitly declare them. For example, if the simulation needs to include protons, the user must specifically declare this. Therefore, it is mandatory to define all the necessary particles and associate them with the desired processes: decay, electromagnetic, hadronics, etc., that will be involved. The previous statement underscores the G4 philosophy of leaving the final decision to the users. It offers high flexibility in defining the physics but also places the responsibility on the user to do so "properly". By "properly", it is meant that users should understand the objectives of the simulations, where might be more interest e.g. in reducing computation time even if it compromises accuracy, or in solely utilising EM particles. Thus, G4 offers an atomistic, rather than an integral approach to physics, providing numerous independent processes, physics models, cross-section data that the users can select and even modify at will.

In G4 terms, users must define the "physics list". This list contains information about, particles, processes, and if required, production cuts. G4 allows for a physics list to be modular, by the use of "physics constructors" [56, p. 300]. This latter feature enables the grouping of particles and their processes construction based on the physics domain. The G4 toolkit includes many pre-defined physics constructors in the G4 toolkit, such as G4EmStandardPhysics, G4DecayPhysics, etc. When registering to the modular physics list, these constructors automatically define all the electromagnetic particles and their processes using a specific physics model, and all particles with lifetime decay, correspondingly. Of course, it is also possible to define a custom physics constructor.

Another significant approach relies on pre-packaged physics lists [56, p. 300]. These lists are used for G4 validation and testing, ensuring a consistent physics set. There is a naming convention for these physics lists:

[String]_[Cascade]_[Neutron]_[EM]

Where (see Fig. 3.3):

- String are the hadronic string models at high energies:
  - Quark Gluon String model (QGS) [59], [60, p. 260]
  - Fritiof String model (FTF) [61, 62], [60, p. 277]
    - Precompound model for de-excitation [63], [60, p. 335] (FTF**P**, QGS**P**)
- Cascade are the hadronic cascade models at low-mid energies:
  - Bertini Cascade model (BERT) [64], [60, p. 307]
  - Binary Cascade model (BIC) [65], [60, p. 313]
  - Liège Cascade model (INCLXX) [66], [60, p. 325]
- Neutron to provide High Precision neutron model at low energies. (HP option)
- EM are the electromagnetic packages:
  - Standard Physics: EM0, EMV, EMX, EMY, EMZ. [67] [68, pp. 21–25]
  - Livermore models (LIV). [68, p. 25]
  - PENELOPE models (PEN). [69], [68, p. 26]
  - And more: WVI, GS, SS. [68, pp. 26–27]

The G4 collaboration recommends FTFP_BERT (which includes the EM0 electromagnetic package) as a viable option for high energy physics experiments [40], [68, p. 7] (all details of this physics list and EM package in Appendices A & B). However, there are many other options

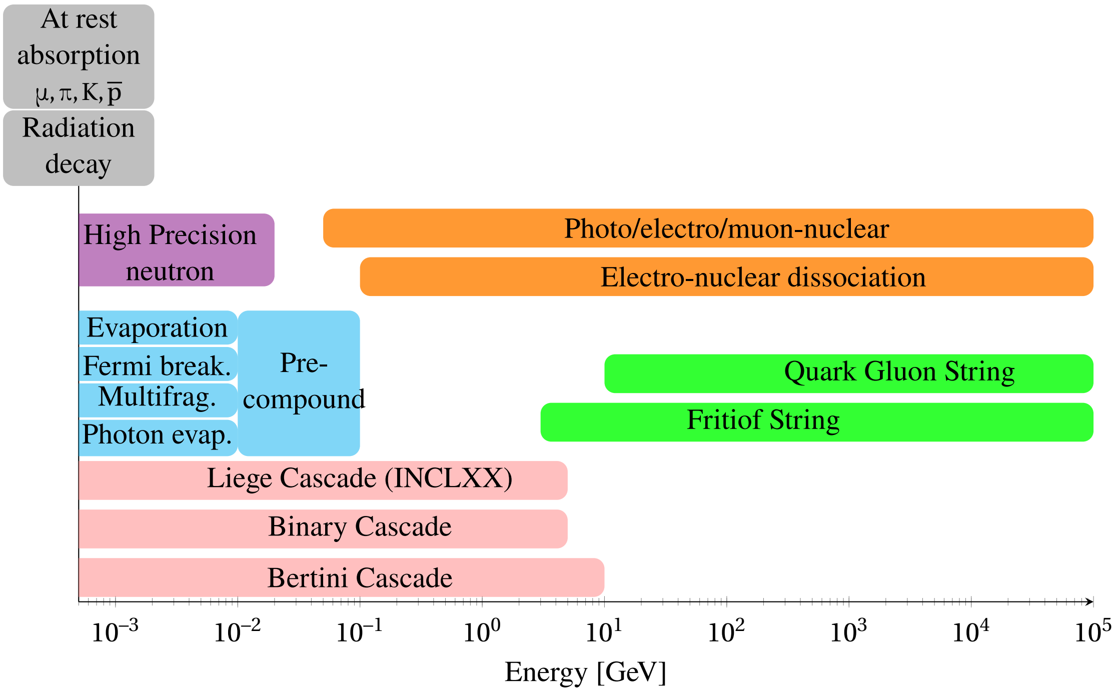

Figure 3.3: Main Hadronic interaction models included in the G4 toolkit

available by the G4 collaboration, which are described in Appendices C & D. The differences in the range of applicability of the hadronic models for many pre-packaged physics lists are illustrated in Fig. 3.4.

3.5 Variance Reduction Techniques in Geant4

Among the various biasing options provided by the G4 toolkit for users, the following are particularly noteworthy for users (more details in [56, p. 77] & [56, p. 85]):

Geometry-Based Biasing

The G4 toolkit offers tools dedicated to the implementation of geometry-based biasing, such as importance biasing and weight window (WW) techniques. To benefit from these techniques, users must incorporate a way to store the correspondent values (via G4VIStore/G4VWeightWindowStore interface) for volumes in the geometry. Additionally, users has also to define a "Sampler" (via G4VSampler interface) where particle sampling is adjusted to apply the aforementioned techniques.

While there is no UI command provided by default, application developers can establish for end-users.

Physics-Based Biasing

Figure 3.4: Overlap between string and cascade models main G4 physics lists

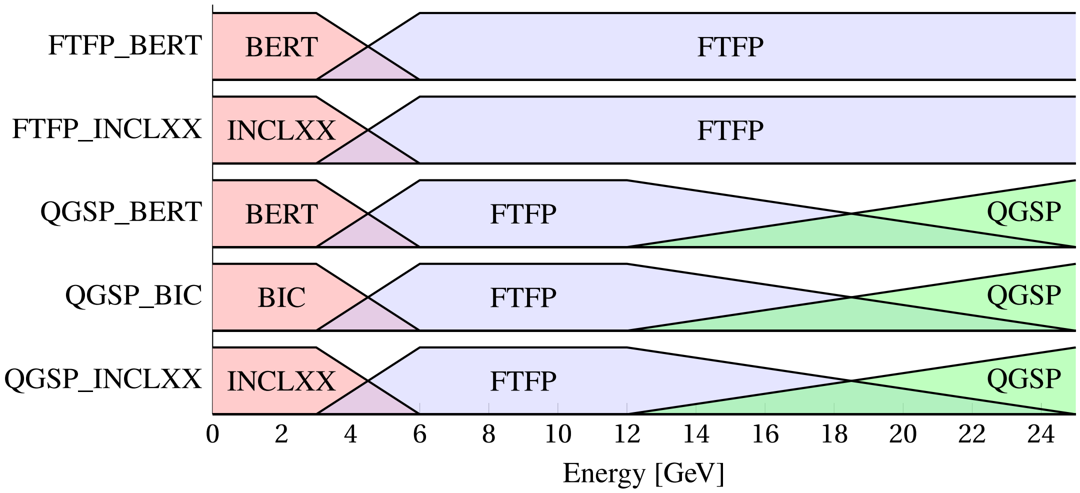

Primary Particle Biasing

The General Particle Source (GPS) allows users to generate primary particles for simulation. A wide array of parameters, including particle type, energy, angle, and more, can be adjusted. Furthermore, GPS enables particle source biasing, assigning more importance to some positions, angular distributions or energy distributions. (UI commands provided)

Radioactive Decay Biasing

There is a variety of radioactive decay biasing, including limitations on which radionuclides can be generated, decay time biasing, and forced selection of rare decay channels (branching fraction biasing). Another option is nuclear splitting, where multiple copies of nuclei are generated with an appropriate weights. Most of these techniques have UI commands implemented for end-users.

Cross-Section Biasing

G4 provides mechanisms to artificially enhance/reduce cross-section values. There are options for hadronic interactions controlled with the BiasCrossSectionByFactor in G4HadronProcess (no UI command included) and for electromagnetic ones (including UI commands).

Leading Particle Biasing

A Hadronic leading particle biasing technique exists. After an interaction, the system retains only the most energetic particle and a single particle (picked randomly) from each particle species. To use this method, the "SwitchLeadBiasOn" environmental variable has to be activated. (No UI command)

User Defined Event Biasing: G4WrapperProcess and Generic Biasing Scheme

The G4WrapperProcess permits users to wrap an existing process, offering a non-invasive way to alter characteristics of an existing process.

Although, even more important is the new scheme introduced after the G4 version 10.0 (see [56, p. 93]), termed "Generic Biasing". This scheme provides an easy infrastructure, benefiting from the OO approach, to define physics-based biasing (modifying existing physics processes, like interaction occurrence and/or final state production). It also includes non-physics-based (geometric) biasing, to implement techniques such as those discussed earlier. (No UI command).

3.6 Fields in Geant4

G4 permits propagating particles in various types of fields, including magnetic, electric, gravitational, and a combination of these three (more details in [56, p. 164]).

The toolkit comes with several built-in fields:

- Magnetic:
  - Uniform, Quadrupole, Sextupole fields.
  - Line Current: Magnetic field of a line current.
  - DELPHI: Field of the DELPHI detector, part of the Large electron-positron collider (LEP) [70]
  - Harmonic Polynomial: Magnetic field parameterised by harmonic polynomial up to 3rd order.
- Electric: Uniform.
- Gravity: Uniform.

However, in line with its flexible design, users can create custom fields according to their requirements.

For the integration of the field's equation of motion, G4 provides multiple methods to solve these differential equations, including multiple Runge-Kutta methods [71, 72] (4th/5th order RK Dormand Prince being the default), Bogacki-Shampine, FSAL, Helix, among others. Users can also adjust the integration accuracy, setting the position error for an integration step and establishing limits on the relative error of the position/momentum inaccuracy.

Most of the mentioned capabilities can only be profited by the application developer. Just for some simple cases, there are user commands implemented, such as the definition of a uniform magnetic field in the whole simulation geometry.

3.7 Transport and Production Cuts in Geant4

G4, by default, offers the option to apply production cuts to photons, electrons, positrons and protons[III] (more in [56, p. 285]). Notably, there is no transport (or "tracking") cut applied to the particles. This means that if a particle is transported, it will not be stopped until its energy is completely depleted.

Regarding production cuts, in contrast to other MC codes where these cuts are set by energy cut-offs, G4 requests a distance, or range cut-off. This value is internally translated to the corresponding energy for the considered material.

By default, G4 establishes a cut-off value for all particle types at 0.7 mm. Users have the flexibility to adjust this default value. They can also specify the cut-off for individual particles throughout the entire geometry or set it per region (all these options have UI commands).

Even though there are no tracking cuts by default, G4 provides a feature (via G4UserLimits) to define constraints in step length, track length, time of flight, kinetic energy, and remaining range. In this way, it is a feasible to associate transport cuts, for a specific particle type within a designated region.

3.8 Scoring in Geant4

As previously mentioned, to perform a MC simulation for particle transport in matter, if the user provides the geometry, physics, and particle source, the code will conduct the simulation "silently". G4 naturally adheres to this procedure. Consequently, users must initiate some actions to extract information from that simulation. For this purpose, G4 offers the following options:

- Built-in UI scoring commands (more in [56, p. 201]): G4 offers three ways to perform scoring using a command-based approach:
  - Defining a 3D mesh: In this method, users can create a mesh in a cubic or cylindrical shape, independent of any existing volume in the geometry.
  - Assigning scorers to a logical volume: Given a logical volume in the geometry, quantities (e.g., total energy deposited) can be obtained from it. This information will be assessed individually for each physical volume created from the logical volume.
  - Scoring probe: These refer to small cubic volumes that can superimpose the primary geometry.

  For all the above methodologies, it is feasible to assign an arbitrary number of scorers ("primitive scorers"), where only one specific quantity is accumulated. These scorers can be extended to the list of scorers already included in the toolkit. This list includes, deposited energy (already mentioned), deposited dose, track length, and several others. Each of these

---

[III] In cases where a hadron undergoes elastic scattering off a nucleus, the nucleus will only form a new track if its kinetic energy exceeds a specified threshold value.

scorers can be assigned a specific "filter" to refine the extracted information. For instance, it can be set to score only charged particles or exclusively neutrons, and can even be tailored based on the kinetic energy ranges of the particles, among other criteria.

- Sensitive detectors (more in [56, p. 182]) : This term is employed when a logical volume becomes "sensitive" to the passage of particles (through the association with G4VSensitiveDetector). Contrary to the previous method, sensitive detectors necessitate user implementation. These detectors can contain numerous quantities to score (via association to G4VHits). Although, what is offered by sensitive detectors can be done with the features of the first method, it is notable that they can be memory-demanding when saving result data. Hence, in scenarios with a "relatively high" number of scorers, users are recommended to generate their own sensitive detector.
- User Hooks (more in [56, p. 299]): Within the G4 toolkit, there are user-focused functions where the user has the ability to extract information from the last step (via G4UserSteppingAction) or the total track of it (via G4UserTrackingAction). Practically all the information that can be extracted from the particle being transported can be obtained at these points, providing a powerful tool for users who require more direct access to particle information.

3.9 GUIs for Geant4

G4 provides to the users some interfaces to run simulations with UI commands. These commands are submitted and processed sequentially (G4 User Interface Session [56, p. 44]). There are also interfaces dedicated to the visualisation of the Geometry, with some of them also incorporated into the Interface Sessions.

The available interface sessions are:

- Command-line terminal.
- Xm, Qt, Win32: These are variations of the mentioned terminal using Motif, Qt, Windows widgets.
- GAG: a fully graphical user interface and its network extension GainServer, which operates on a client/server type [73].

The G4 visualisation system was conceived to address a diverse set of requirements:

1. Quick response to study geometries, trajectories and hits.
2. High-quality outputs suitable for publications.
3. Flexible camera controls for debugging complex geometries.
4. Tools that highlight volume overlap errors in detector geometries.
5. Interactive selection features to get more details about visualised objects.

No single graphics system can ideally cater to all these requirements. This is the reason behind G4's visualisation strategy, centred around an abstract interface that supports a diverse family of graphics systems. The visualisation system handles a variety of graphical technologies simultaneously and interchangeably, allowing the user to choose the visual representation most appropriate to their requirements.

Among the mentioned drivers, some of them are supported by the G4 toolkit, and can be compiled and operated directly within G4. Examples include OpenGL [74], QT [75], OpenInventor [76], RayTracer and ASCIITree. However, drivers like HepRepFile [77], DAWN, VRML2FILE [78] and gMocren [79] require users to supply a file produced by G4 to achieve the desired visualisation.

4 FLUKA

After discussing G4 in the previous chapter, this one will cover the MC code FLUKA. It outlines FLUKA's evolution up to the present, its structure, and user interface philosophy. This chapter then details the FLUKA's geometry and provides a description of its physics models, biasing techniques, fields, transport and production cuts, as well as the available scoring options.

The chapter concludes by presenting important tools that enhance FLUKA usage, such as the FLAIR graphical interface, the FLUKA Elemental Data Base, Line Builder, and SixTrack, which are crucial for conducting simulations in particle accelerator geometries.

4.1 Brief History of FLUKA

FLUKA (FLUktuierende KAskade)[I] [80–82] is a general-purpose MC code designed for the transport and interaction of hadrons, leptons, and photons in any material. It covers a wide energy range from keV [II] to cosmic ray energies.

FLUKA was first developed in the 1960s by J. Ranft at CERN, who was tasked with simulating hadron cascades, creating what is considered the first generation of FLUKA codes.

The second generation of FLUKA, developed by the leading of G. Stevenson during the 1980s, focused on reformulating the hadron interaction model, among many other implementations.

[I] Fluctuating cascade

[II] With the exception of neutrons, tracked down to thermal energies

Figure 4.1: FLUKA.CERN logo as of version 4-3 (Latest release: 4-3.4. Date: 29-09-2023)

The third generation of FLUKA was conceived by A. Ferrari and A. Fassò. Over a six-year period, FLUKA transitioned from a code specialised in high-energy accelerator shielding to a multi-purpose, multi-particle code. It has been successfully applied in a wide range of fields and energies, including neutrino physics [83], machine and radiation protection studies [84], radiotherapy and dosimetry [85], and many more applications [86–88].

In August 2019, the agreement between CERN and INFN (Istituto Nazionale di Fisica Nucleare), which had collaborated on FLUKA for 15 years, concluded. Since September 1^{s}t, 2019, CERN has established a multilateral collaboration (FLUKA.CERN) with CERN SY & HSE-RP and ELI-Beamlines. This marked the beginning of the new fourth generation of FLUKA, developed by the FLUKA.CERN collaboration (Logo exhibited in Fig. 4.1).

4.2 The Philosophy of FLUKA and its Simulation Methodology

The philosophy behind FLUKA authors was not to create a toolkit for particle physics simulations but to develop a code that incorporates the best available physics. Furthermore, FLUKA includes a wide range of features, including beam definition, scoring, biasing techniques, auxiliary tools, and more. Generally, FLUKA users are viewed as "end-users", using G4 terminology. For the majority of applications, users do not need to write any programming code. Instead, they can define the geometry, scoring, and other simulation characteristics using an ASCII file (the FLUKA input file ".inp"). This file comprises "FLUKA CARDs" (which are sequences of option lines) that the user must provide as an argument to the FLUKA executable.

Although this covers the majority of use cases, FLUKA also includes some flexibility for situations where the options provided are insufficient. In these cases, a set of user interface routines (written in Fortran 77) is available for users with special requirements.

4.3 The FLUKA “Combinatorial Geometry” Description

The Combinatorial Geometry (CG) description is used in FLUKA. Unlike G4’s description, the FLUKA one is "flat", meaning there are no hierarchies between the different region of the geometry (see Fig. 4.2). This description involves three fundamental concepts: **Bodies**, **Zones**, and **Regions**.

Bodies: These include convex solid bodies, representing finite portions of space completely delimited by surfaces up to the second degree. Cylinders, spheres, and cones are examples of such bodies. In addition, infinite cylinders and planes are also permitted (and are even recommended for improved performance). Although defining bodies is the initial step in constructing the simulation geometry, bodies alone are insufficient for fully defining the geometry. To complete the simulation geometry, regions must be defined.

Regions (and zones): These are crafted by combining bodies through Boolean operations. By

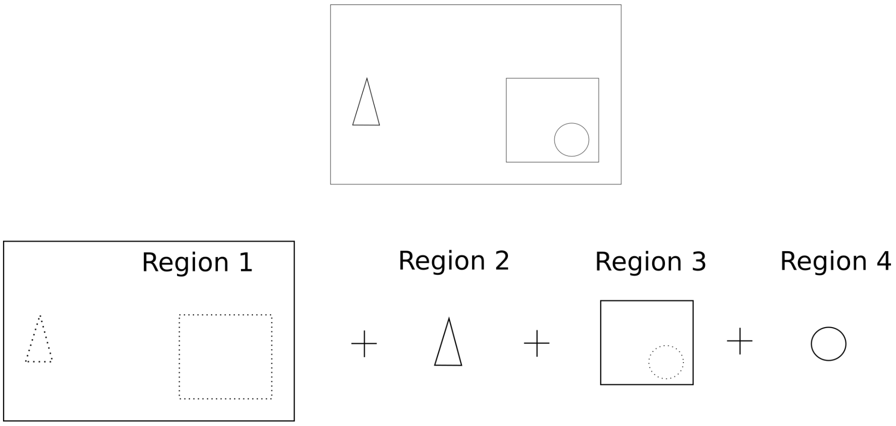

Figure 4.2: Based on Figure 3.2, looking a cross section of the geometry in 2D. In FLUKA, there is not hierarchy between the Regions. Thus, for each space, a Region has to be defined to occupy all part of the geometry.

Figure 4.3: Main FLUKA hadronic interactions models

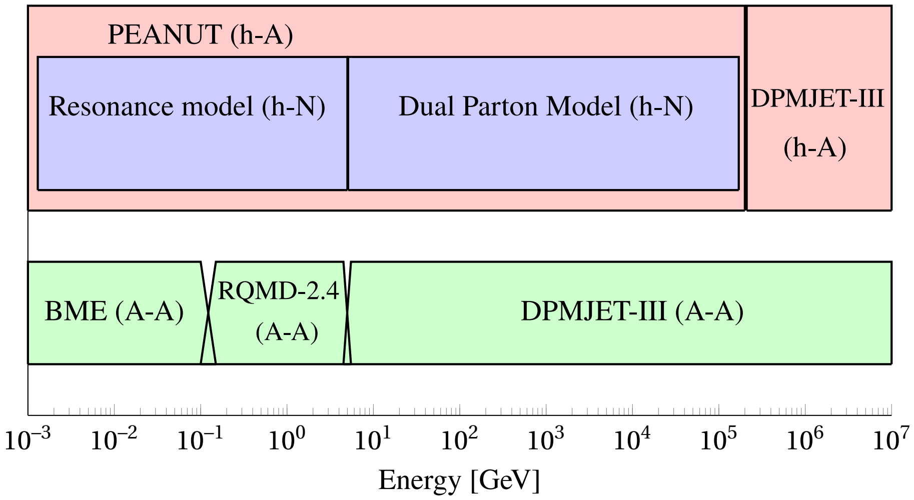

employing intersection operations, zones can be created. These zones are then combined to create regions through union operations. Upon creating a region for the FLUKA geometry, it is mandatory to assign it an homogeneous material that meets all necessary requirements.

A fourth concept, although not always obligatory, is notably practical: **Lattices**.

Lattices: These involve repetitions of existing regions. For instance, in a simulation comprising numerous identical detectors with intricate geometries, one can define a "prototype", and utilise FLUKA's lattice capabilities to replicate it across all desired locations.

4.4 Overview of Physics in FLUKA

FLUKA provides users with a comprehensive package of physics models for both hadronic and electromagnetic interactions. This package composed by various models and cross-sections includes:

Hadronic Interactions

Inelastic Models:

The FLUKA code makes use of the PEANUT (FLUKA PreEquilibrium Approach to Nuclear Thermalisation) [89] for **h-A** interactions up to ≅ 20 TeV. These interactions rely on the **h-N** interaction models, where for all hadron with momentum ranging from 5 GeV/c to 20 TeV/c, the Dual Parton Model (DPM) [15, 90, 91] is applied. For momentum below 5 GeV/c, the Resonance production and decay model [15] is used.

Beyond 20 TeV DPMJET-III is the model utilised up to 10^5 TeV for h-N interactions. It is also the model for high energy **Inelastic A-A** interaction. As the following bullet list summarises:

- DPMJET-III [92, 93] is the method for particle energies exceeding 5 GeV/N.
- For energies between 125 MeV/N and 5 GeV/N, Relativistic Quantum Molecular Dynamics Model (RQMD)-2.4 [94, 95] is the method of choice. There is an overlap with DPMJET-III from 4.5 to 5.5 GeV/N, range where the two methods have comparable performance.
- Boltzmann Master Equation (BME) [96] is the method for energies below 125 MeV/N. There is an overlap with RQMD-2.4 from 0.1 to 0.15 GeV/N, range where both methods are applicable and yield similar results.

Subsequent to inelastic interactions, equilibrium processes such as evaporation, fission, Fermi break-up, and gamma de-excitation are simulated with intrinsic FLUKA models.

Regarding inelastic cross sections, these are calculated using a combination of tabulated data and parameterised fits.

The elastic interactions:

The elastic interactions are based on a phase-shift analysis, fits of experimental differential data and eikonal approximation. These processes are based on parameterised N-N cross sections and tabulated N-A cross sections.

FLUKA has also implemented **γ-nuclear** interactions:

- The reaction cross section are obtained from four different sources:
  - Giant Dipole Resonance [6, 60] MeV
  - Quasi-deuteron and Delta resonance [60 MeV, 300 MeV]
  - Delta resonance [300 MeV, 0.7 GeV]

  - Vector Meson Dominance above 0.7 GeV
- The reaction outcome is determined by the INC, pre-equilibrium and evaporation stages.

Muon-nuclear and electro-nuclear reactions are also implemented through the use of virtual photons, thus based on photon-nuclear interaction.

Electromagnetic Interactions

The electromagnetic interactions in FLUKA are defined for e^-, e^+ and γ in the EMF package. The rest of charged particles share the same approach for multiple scattering and ionisation as $e^{+/-}$.

γ:

- e-/e+ pair production: FLUKA model with Landau-Pomeranchuk-Migdal (LPM) suppression effect at high energies. Actual (correlated) angular distribution of electrons and positrons.
- Compton and Rayleigh scattering : The model transforms the Compton interaction of a photon with a bound electron in motion to the simpler case of an interaction with an electron at rest. This allows to describe the scattering process itself based on the Klein-Nishina (KN) cross section. Effects due to the motion and binding of the atomic shell electrons emerge naturally and result in scattering suppression for low momentum transfers due to energy conservation and Doppler broadening. Compton effect with Doppler broadening using a fit of the Compton profiles. Both scattering account for atomic bonds through use of inelastic Hartree-Fock form factors.
- Photoelectric effect: Accounting of actual photo-electron angular distribution according to the fully relativistic theory of Sauter. Interactions sampled separately for each component element and for each edge. The edge fine structure is taken into account. Parameterisations/tabulations for photoelectric cross sections including all known edges up to Z = 100 and down to a few eV. Optional emission of fluorescence photons and approximate treatment of Auger electrons for all K and most L lines.

e^-/e^+:

- Multiple Coulomb Scattering: Original algorithm based on Molière multiple-scattering theory.
- Bremmsstrahlung:
  - Differential cross section from Berger-Seltzer database
  - Considered LPM suppression effect and the Ter-Mikaelyan polarisation effect.
- Ionisation: Delta-ray generation through Bhabha and Moeller scattering formulation.
- Positron annihilation: In flight and at rest based on Heitler model.

FLUKA Neutronics at Low Energies

Since version 4.3, FLUKA has incorporated two methods for handling neutronics at low energies: Groupwise and Pointwise [97].

The **Groupwise** approach employs grouped data for neutron transport calculations, offering fast calculations and a small memory footprint, making it suitable for certain applications. However, it may not accurately reproduce self-shielding effects, offers limited angular distributions, and lacks detailed representations of recoils and other particle emissions.

Conversely, the **Pointwise** approach uses a continuous scatter plot of energy and cross-section pairs. This method provides precise tracking of cross-section variations, accurately reproduces angular distributions, and handles all final states effectively. Despite these advantages, it requires more time and memory for calculations.

Users can choose the approach that best fits their neutron transport simulation needs based on these characteristics.

4.5 Variance Reduction Techniques in FLUKA

FLUKA provides a variety of biasing techniques for users [98, sec. 7.19]. These techniques can be divided into non-physics and physics biasing methods:

- **Non-physics**:
  - Region importance biasing (BIASING CARD [98, sec. 7.22.6]).
  - Weight windows (WW-FACTO, WW-THRES, WW-PROFI CARDs [98, sec. 7.22.9(4-6)]).
- **Physics**:
  - Leading particle Biasing for EM and for Hadronic called "Multiplicity tuning" (EMF-BIAS[98, sec. 7.22.19], BIASING CARDs).
  - Lifetime biasing and mean free path biasing (LAM-BIAS CARD [98, sec. 7.22.38]).
  - Low energy Neutrons absorption and down-scattering biasing (LOW-BIAS, LOW-DOWN CARDs [98, sec. 7.22.(39-40)]).

Moreover, FLUKA offers user routines [98, sec. 13.2.2(2-3)] to allow further customisation of biasing:

- Modification of biasing weight on a region-dependent basis (ubsset.f).
- Permits to apply importance biasing on every particle step (usimbs.f).
- Directing emitted neutrinos in decays (udcdrl.f).

4.6 Fields in FLUKA

FLUKA allows the transportation of particles in either electric or magnetic fields (only one type at a time).

Since FLUKA version 4-2.0, the following fields CARDs are included:

- Electric: Homogeneous (restricted to vacuum material) (ELCFIELD CARD [98, sec. 7.22.17]).
- Magnetic (applicable in any material):
  - Analytical fields including Constant, dipolar, quadrupolar, sextupolar, octupolar and decapolar (MGNFIELD [98, sec. 7.22.49], MGNCREATe [98, sec. 7.22.47]) CARDs.
  - Bilinear and Trilinear interpolation: In this mode, users provide a 2D or 3D field map, interpolating the magnetic field for each spatial point based on the provided map values (MGNDATA CARD [98, sec. 7.22.48]).
  - A combination of both analytical and interpolated fields.

If the CARDs options are insufficient, user routines [98, sec. 13.2.10] are available to define more complex scenarios. For instance, "magfld.f" is designated for magnetic fields, while "elefld.f" is for electric fields.

Moreover, users have the liberty to fine-tune the tracking accuracy. This feature permits to set the maximum angle subtended by a single step from the origin along curved path, or by defining the maximum permissible error in geometry intersections.

4.7 Transport and Production Cuts in FLUKA

FLUKA employs an energy scheme to dictate the transport and production cuts for particles. Users can specify a kinetic energy (or momentum) value to determine whether a particle with energy below this value will be killed (transport cut), or whether a delta ray (e^-, e^+, gamma) will be produced by an electromagnetic particle (e^-, e^+), μ, or charged hadron (production cuts).

The energy thresholds cards for these processes are the following ones:

- Transport threshold for e^-, e^+, and γ (EMFCUT CARD [98, sec. 7.22.20])
- Transport threshold for hadrons, μs, and ions (PART-THR CARD [98, sec. 7.22.56])
- Delta ray production threshold for e^- and e^+ (EMFCUT CARD)
- Delta ray production threshold for μ and charged hadrons (DELTARAY CARD [98, sec. 7.22.56])

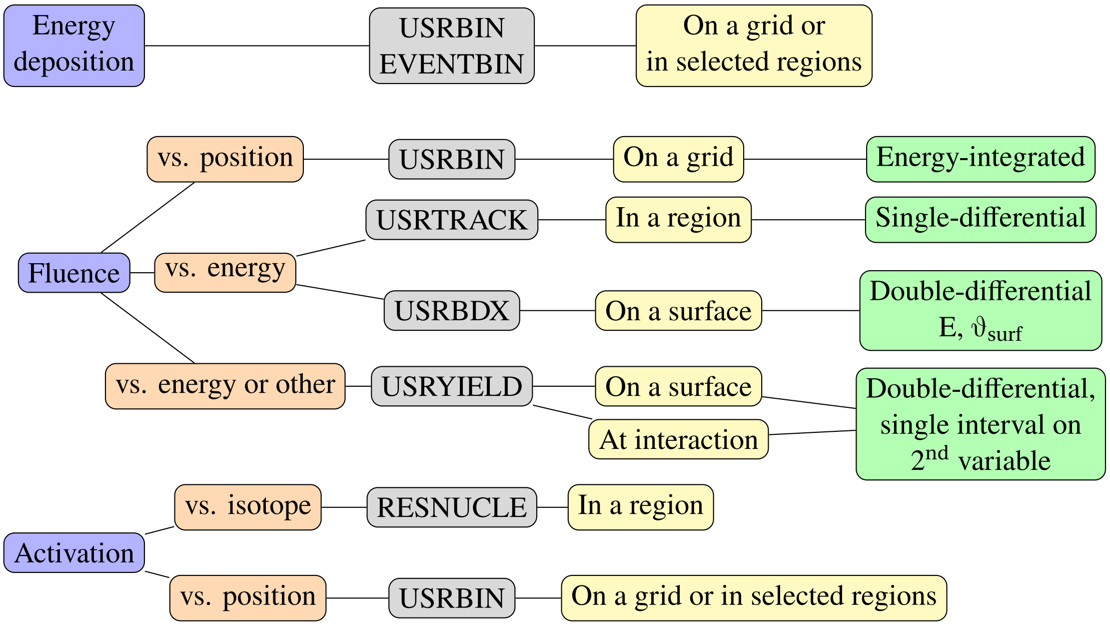

Figure 4.4: Diagram of FLUKA estimators

4.8 Scoring in FLUKA

FLUKA provides multiple predefined estimators for users, enabling them to extract information from simulations. This scoring, covering most common needs, is activated through the aforementioned CARDs. These are depicted in the diagram of figure 4.4. The most relevant can be summarised as follows:

- USRBIN: A user-specified regular mesh for scoring various quantities in space such as energy, fluence, dose, and more. The available shapes include Cartesian, cylindrical, or "per region" [98, sec. 7.22.87].
- USRTRACK: Serves for estimating track-length fluence, scoring single-differential fluence ($d\varphi/dE$) of a specific type or family of particles within a designated region. [98, sec. 7.22.92]
- USRBDX: Estimates boundary crossing fluence (or current), scoring double-differential fluence ($d^2\varphi/dEd\Omega$) of a type or family of particles on a designated surface. [98, sec. 7.22.86]
- USRYIELD: Permits to score double-differential particle yield on a given surface, generally with respect to energy and angle[III]. It can be used around either an extended or a point target. [98, sec. 7.22.93]
- Some more "special" scoring options:
  - DETECT: Suitable feature to analyse response from single-events. It scores energy deposition on an event-by-event basis, being, in this context, an "event" defined as energy deposited in one or more detector regions by a primary particle and its descendants [98, sec. 7.22.14].
  - EVENTBIN: Analogous to USRBIN, but binning output is provided after each event

---

[III] Other more peculiar quantities can be utilised

  instead of the average over particle histories.[98, sec. 7.22.24]
  - RESNUCLEi: Mainly utilised for scoring residual nuclei and/or activation on a region [98, sec. 7.22.64].
  - USERDUMP: Enables users to dump specific information, such as particle trajectories, local energy depositions, continuous energy depositions, of each primary particle history [98, sec. 7.22.84].

In cases where the provided options are insufficient, FLUKA offers a wide variety of user routines for those who need them. The most significant ones include:

- mgdraw.f: Activated by the USERDUMP card, this routine allows users to create their own routines for dumping and extracting information about trajectories, secondary particles, boundary-crossing events, energy depositions, etc [98, sec. 13.2.12].
- usrrnc.f: This routine is called when there is a residual nuclei created [98, sec. 13.2.31].
- mdstck.f: Invoked after a nuclear interaction where a minimum of one secondary is generated [98, sec. 13.2.11].
- usrmed.f: Routine activated each time a particle is set to be transported through any material tagged by the user [98, sec. 13.2.29].

4.9 GUIs for FLUKA: Flair

Flair (FLUKA Advanced Interface) [99] is a graphical user-friendly interface originally developed for FLUKA. This GUI was initially created to overcome the difficulties associated with the input syntax and logical errors in the FLUKA code. Moreover, it provides a comprehensive environment to facilitate the user's work. Among all the features included in the FLAIR interface, the users can:

- Build the input file.
- Visualise, debug, and modify the geometry.
- Manage simulations runs.
- Post-process output files.
- Plot results.

Starting from version 3, Flair has evolved to serve as an interface for multiple MC simulation codes, offering easy integration of other simulation packages, such as G4, PENELOPE, MCNP [100] and PHITS [101]. The G4, i.e. Moira, integration will be explained in Section 6.4.8.

4.10 FLUKA Elements Data Base

The FEDB [102] is a compilation of FLUKA models representing accelerator components typically utilised in various CERN machines, including the Proton Synchrotron (PS), Super Proton Synchrotron (SPS), the LHC, among others. These models contained within the FEDB encompass a range of devices, such as collimators, magnets (see Fig. 4.6), masks, and dumps.

Figure 4.5: Flair logo as of version 3.3 (Latest release: 3.3-0.3 Date: 13-12-2023)

The primary benefit of organising these models in a database is the uniformity it provides in the utilisation of accelerator components across various studies and by multiple users. By having a shared repository of accelerator components, users can ensure they are operating with consistent definitions and models, as their colleagues in the field. Moreover, the database enables updates to be quickly disseminated, such as modifications to material definitions or changes in design, which can greatly enhance the accuracy and dependability of simulations.

Another benefit of the FEDB is the capability to track the development of specific designs and compare various technical solutions easily. This feature enables users to observe how designs have progressed over time and evaluate the benefits of different approaches. With this information readily available, users can make informed decisions about the optimal designs for their simulations without needing to create models from scratch.

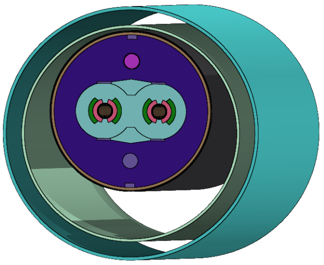

Figure 4.6: FEDB model of a superconducting bending magnet in the LHC accelerator

4.11 Line Builder

The Line Builder (LB) [102] is a powerful tool that offers a convenient and efficient way to define complex geometries for accelerator beam lines in FLUKA. It allows the assembly of FLUKA geometries of beam lines by taking the accelerator lattice sequence, magnet strengths, and optical parameters as input, and providing a FLUKA input file with the required beam line as output (see Fig. 4.7).

Instead of manually specifying element positions, the LB emphasises defining the properties and parameters of individual elements, such as magnets and collimators. These definitions are stored in the FEDB mentioned above, promoting reuse and consistency across different studies.

This software is frequently used at CERN for radiation and machine protection studies in various accelerators, including the PS, the SPS, the LHC, among others.

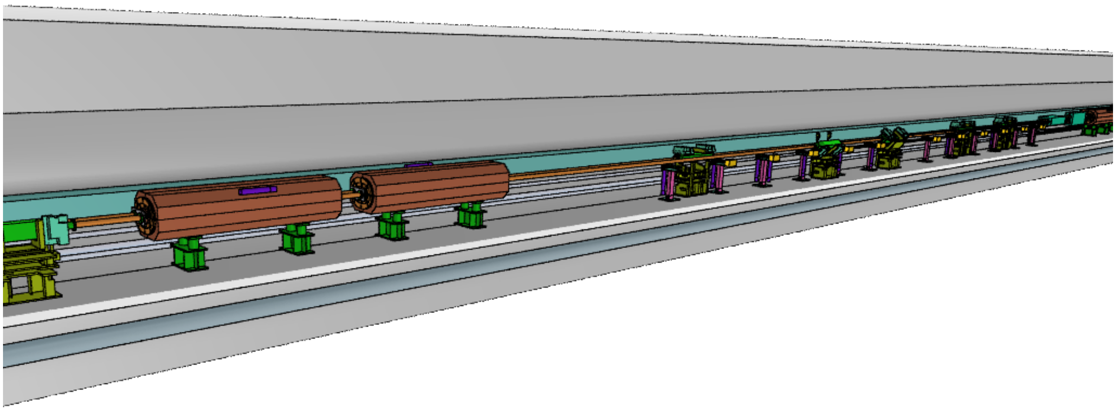

Figure 4.7: Flair image of a LHC section created by LB

4.12 SixTrack - FLUKA Coupling

SixTrack [103] is a particle tracking code used to simulate charged particle beams in accelerators. It is widely used in accelerator physics and beam dynamics research.

The SixTrack - FLUKA coupling [104] refers to the integration of Six Track and FLUKA, where SixTrack is used to model the beam dynamics and FLUKA utilised to model the particle interactions with matter (Fig. 4.8). This coupling allows for a more comprehensive and accurate simulation of accelerator beam-lines, as it combines the strengths of both codes.

With SixTrack, the user can model the beam dynamics including beam-beam interactions, space charge effects, and external field effects. FLUKA, on the other hand, provides a detailed simulation of the interactions between charged particles and matter, including energy loss, multiple scattering, and radiation processes. By coupling these two codes, the user can obtain a more complete and accurate simulation of the beam-line, including both the beam dynamics and the particle interactions with matter.

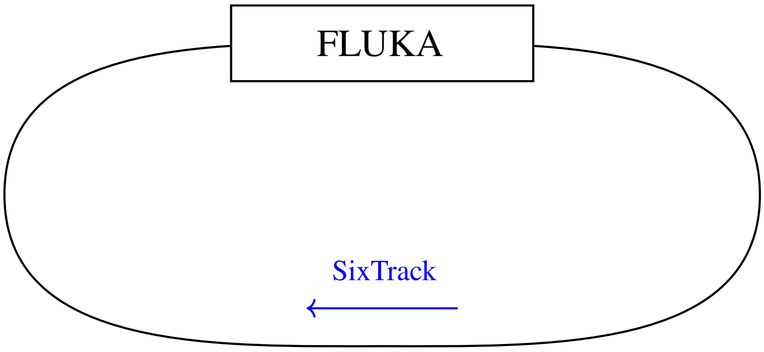

Figure 4.8: SixTrack - FLUKA coupling simplified representation.

5 Particle Transport and Machine Protection in Beam Facilities

In any facility where a particle beam is utilised, understanding the impact that radiation on both people and environment (radiation protection studies), as well as on machinery (machine protection studies) is crucial. Comprehending how particle transport affects the materials composing the machine and surrounding areas is key to implementing measures that mitigate environmental consequences and prolong the lifespan of the equipment.

Concerning machine protection, risks of undesirable outcomes arise from the energy stored in the beam and the power transferred from the particle beam to the machine components. Evaluating these factors allows for an assessment of the system's hazard risk by estimating the **consequences** of an incident and its **probability** of occurrence. This estimation aids in understanding the necessary machine protection measures for specific circumstances.

This chapter introduces in its first section concepts essential for understanding synchrotron accelerators, particularly the LHC. It also details the main elements of the LHC, its operation, and the upgrades it has undergone toward the future High Luminosity LHC. Regarding machine protection studies, the types of losses that a beam can experience, the consequences these can have on the equipment, and the types of protection that the LHC employs to detect and address them will be described.

The chapter will conclude explaining the importance of using MC particle transport simulations for such studies and the scenarios where they are crucially needed. Even though, the chapter should be self-contained, the appendix E is a good source of information related to beam dynamics.

5.1 Synchrotron Accelerators: a focus on the LHC

Although most of the following concepts can be applied for any facility employing a particle beam, the focus will be on synchrotron particle accelerators, specifically the LHC. Introducing quantitative values permits better assimilation and sets the stage for referencing the LHC in subsequent sections.

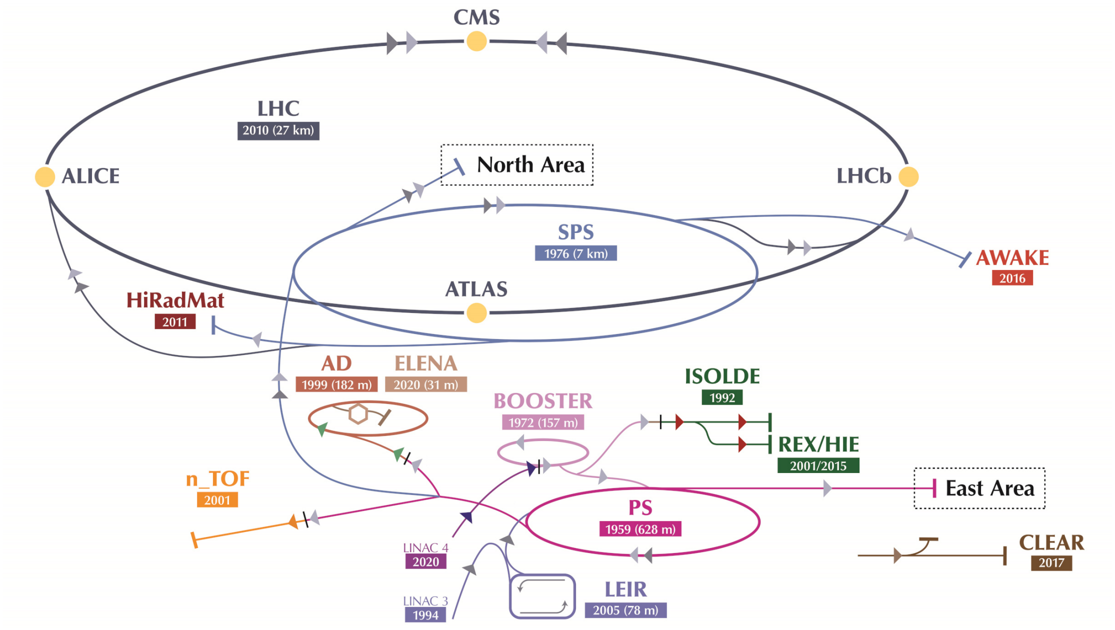

Figure 5.1: CERN accelerator complex as in 2024. Courtesy [105].

The LHC is a synchrotron, a type particle accelerator in which particles travel in a closed circular path inside a beam pipe under ultra-high vacuum ($\approx 10^{-12}$ bar). Many devices are utilised for the purpose of accelerating these particles. the most relevant could be listed as follows:

- Magnets: They ensure the particles follow the intended path, including:
  - Bending magnets: These are dipole magnets, utilised for curving the trajectory of the particles through the accelerator. The LHC contains 1232 SC and 44 warm bending magnets.
  - Focusing magnets: These are quadrupole magnets, needed to focus the particle beam. They are generally arranged in cells of Focusing (F), and Defocusing (D) magnets, interspersed by drift spaces (O), denominated "FODO" cells. The combination of these focusing and defocusing magnets in the FODO lattice helps stabilise the beam throughout its path in the accelerator, ensuring it remains constrained within the desired limits. The LHC hosts 392 SC and 48 warm quadrupole magnets.
- Radio-frequency cavities: 16 SC cavities are utilised for the purpose of accelerating the particles through the production of an oscillating voltage.

Commonly, in synchrotrons, an injection system introduces particles from a preceding accelerator, and an extraction system sends them to another accelerator, a different facility for experiments, or to a dump (see Fig. 5.1). Depending on the accelerator, it may or may not incorporate experiments into the chain of devices. For the LHC, the 26,658.833 m long accelerator comprises 8 arcs and 8 insertion regions (IR) composing eight octants each centred at the IR (observe Fig. 5.2). These octants consist of:

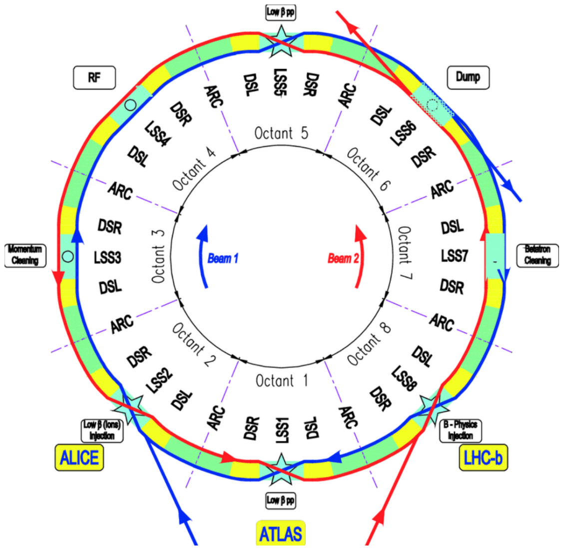

Figure 5.2: LHC layout. Courtesy [106].

- **Long-Straight-Section (LSS):** Approximately 530 m sections designated for experimental or utility insertions.
- **Dispersion Suppressor (DS) regions:** These transition regions lie between the LSS and the arcs, one on each side of the LSS. They are composed of SC dipoles and quadrupoles, disposed in a manner to minimise the beams dispersion.
- **The ARCs:** Comprising 23 cells, each containing a periodic structure of dipole magnets, quadrupole magnets and other multipolar magnets.

To better understand the distinct regions of the LHC, it is helpful to explore the operation of a synchrotron, with a particular focus on the LHC itself.

A typical operation cycle in the LHC involves:

1. *Before Injection in LHC*. As shown in Fig. 5.1, the journey begins at the Linear Accelerator 4 (LINAC4), where negative hydrogen ions (H^{-}) are accelerated, reaching an energy of 160 MeV, before being transferred to the Proton Synchrotron BOOSTER. The particles arriving at the BOOSTER are already protons because the ions are stripped of the two electrons during the injection. Subsequently, as seen in Fig. 5.1, the protons are sent either to the ISOLDE or the PS accelerator at an energy of 2 GeV. The PS has two transfer lines:
    - the PS East Area, where many facilities, such as the IRRAD and CHARM, are irradiated with a beam at 24 GeV.
    - There is trifurcation of the protons in the Antiproton Decelerator (AD), the n_TOF facility, and the SPS accelerator. Being the latter the last stage before reaching the LHC.

   Finally, the particles are accelerated in the SPS from 24 GeV to an energy of 450 GeV, transferred whether to the North Area or to the LHC, entering clockwise in IR2 (Beam 1) and anti-clockwise in IR8 (Beam 2).

2. *An LHC Nominal Fill*: Typically, what is obtained during a proton injection cycle in the LHC, the process of colliding particles, and finally concluding in the dump has the following steps and is schematically shown in Fig. 5.3:
   - *Injection*: In this initial stage, protons are injected into the accelerator. They are injected in bunches, with a design intensity of 1.15×10^{11} protons. Additionally, a maximum of 2808 bunches can be injected. The bunches are injected sequentially, as shown in the mentioned figure 5.3, where the proton intensity in Beam 1 and Beam 2 shows a step-like function.
   - *Ramp*: Here, the magnets increase their strength, resulting in an increase in the energy of the already injected protons thanks to the RF cavities located in IR4. This phase continues until the desired maximum energy is reached, which in the LHC's design is 7 TeV.
   - *Squeeze*: After reaching the desired energy, the beams are then "squeezed", narrowing the beams to increase the chances of collision when they are brought together.
   - *Adjust*: This involves fine-tuning the positions of the beams to ensure they are correctly aligned for optimal collisions.
   - *Stable beam*: This is when the conditions are right for collisions to occur. The beams are brought into collision at the LHC's four main experiment sites, IR1, IR2, IR5, and IR8, where the detectors ATLAS, ALICE, CMS, and LHCb are hosted, respectively. This phase can last several hours, typically around 10 hours, if the conditions in the accelerator and the beams are correct.
   - *Beam dump and ramp down magnets*: When beam quality significantly deteriorates or an unexpected event occurs, the particles are extracted in IR6 to impact a dump primarily composed of a high-density block of concrete and graphite. This is followed by the ramping down of the magnets' strength in preparation for the next injection cycle.

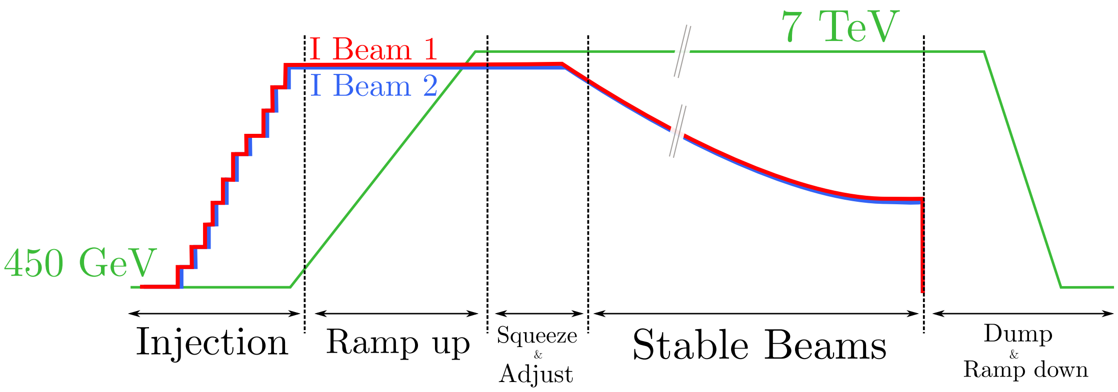

Figure 5.3: LHC nominal fill, exhibiting the different stages during the process of filling the accelerator with the beams.

Even though the total energy storage in the LHC is huge, it is comparable to the energy stored in

16 kg of chocolate [I]. The critical factor is the rate at which this energy can be released, which for the LHC is in the order of μs. Taking this into consideration, it is imperative understanding how the particles might behave if they escape the accelerator, the potential damage they could cause to equipment, and the strategies to minimise their impact.

5.1.1 High Luminosity LHC

One of the fundamental characteristics that defines the LHC is that it is a **collider**, meaning that it is not only used to store particles circulating within it for acceleration but also for their collision. These events occur at IP1, 2, 5, 8, where particle detectors are used to characterise the collision debris.

Since its start up in 2008, the LHC has undergone several upgrades with the goal of optimising various parameters that define it. Among the most relevant are the energy of the particles, the number of bunches, the quantity of particles per bunch (Intensity), and the emittance. The main reason, given that the LHC is a collider, is to maximise the collision rate, or a related parameter, the **Luminosity**:

Luminosity - L -
The Luminosity is a parameter that provides a measure of the collision rate at a given point in the machine:

$$\mathrm{L} = \frac{1}{\sigma}\frac{\mathrm{dN}}{\mathrm{dt}} \xrightarrow{\text{[units]}} \frac{1}{\mathrm{cm}^2}\frac{1}{\mathrm{s}} \tag{5.1}$$

where:

- $\frac{\mathrm{dN}}{\mathrm{dt}}$: Number of collisions per unit of time
- σ: The cross section of the process to occur.

In the case of Gaussian beams, such as in the LHC, this parameter can be expressed in terms of beam parameters:

$$\mathrm{L} = \mathrm{f}\frac{\mathrm{n_b}\,\mathrm{N_b^2}}{4\pi\sigma_x\sigma_y} \tag{5.2}$$

Where:

- $\mathrm{n_b}$: Number of bunches.
- $\mathrm{N_b}$: Number of particles per bunch.
- f: Revolution frequency.
- $\sigma_{x,y}$: Betatronic rms size.

A related parameter is the **integrated luminosity**, a value used to characterise the performance of

---

[I] Milk chocolate has - 520 calories per 100 g , then being the LHC beam energy 350 MJ, which is 16 kg of chocolate.

			LHC		HL-LHC
	Design	Run I	Run II	Run III	Run IV-..
		2009-2013	*2015-2018*	*2022-2025*	*2028-2040*
E [TeV]	7	3.5-4	6.5	6.8	6.8-7
N_b	2808	1380	2556	2748	2748-2808
$I_b [\times 10^{11} p]$	1.15	1.55-1.65	1.2	1.8	2.0-2.2
E_s [MJ]	362	140	315	539	600-700
B_s [ns]	25	50	25	25	25
ε_n [µm rad]	3.75	2.5	2.0	1.8-2.5	2.5-3.0
L_{int} [$^{1}/_{fb}$]	66 ^{II}	30	200	450	3000-4000

Table 5.1: Overview of proton beam specification in LHC Runs. The table includes beam energy (E), # bunches per beam (N_b), bunch intensity (I_b), stores beam energy (E_s), bunch spacing (B_s), normalised emittance (ε_n) and integrated luminosity (L_{int})

colliders:

$$L_{int} = \int L dt \xrightarrow{[\text{units}]} \frac{1}{fb} \tag{5.3}$$

Table 5.1 displays, among all the mentioned parameters, L_{int}, indicating its evolution during the various upgrades and the extent to which it is intended to increase during this new High-Luminosity (HL) phase [107]. This increase is accompanied by a simultaneous rise in beam intensity, consequently resulting, potentially, in higher beam losses.

5.2 Beam Losses

A particle is considered lost when it deviates excessively from the designed trajectory and is no longer transported correctly.

Beam losses can be categorised in two types:

- *Regular beam losses*: These are continuous losses characterised by a low intensity and slow drop, spanning over minutes or even hours (low rate). Regular beam losses can arise from a variety of reasons, including the losses from the beam halo, collisions debris, machine errors (e.g. magnetic field errors, radio-frequency (RF) noise) and both elastic and inelastic interactions with the residual gas.
- *Accidental beam losses*: These are infrequent losses that occur rarely. The intensity loss is significant and rapid $O(ns-ms)$, often requiring a beam refill. The most common causes of accidental losses include hardware failure in the accelerator (for instance, a magnet malfunction) and unidentified falling objects (UFOs). The latter refers to µm-sized dust particles that drop into the beam's path, provoking intense interaction between the beam particles and the object.

5.3 Consequences of Beam Losses

Uncontrolled energy or power release can result in serious consequences. Among them:

1. **Radiation Damage to Accelerator Components (Microscopic Defects)**: Radiation interactions may induce defects in the material's structure, altering its properties, (e.g. electrical, thermal). Particles can also affect the material's lattice structure by breaking chemical bonds or displacing the atoms due to inelastic interaction.
2. **Damage or Deformation of Accelerator Components (Macroscopic Effects)**: The particle impact on materials results in energy deposition, increasing lattice vibrations and heating the material. This can lead to phase transitions (like melting or sublimation) or generate mechanical stress in the material.
3. **Quenches in Superconducting Magnets**: A quench refers to the transition from a superconducting state to normal conducting one. Several factors determine the minimum energy density needed to induce a quench. Including beam loss duration, superconductor material, coil geometry, operating temperature, and magnet current. The energy deposition to lead a quench is $\mathrm{O(mJ/cm^3)}$, significantly less than the damage threshold of accumulated dose in coils ($\approx$ few tens of MJ). For the case of continuous regular beam losses on the magnet, there is also a limitation in terms of the balance between deposited power and cooling, being this value $\approx$ tens of $\mathrm{mW/cm^3}$. It is crucial to prevent quenches, considering the potential damage to machine components and the extended downtime required for repairs.
4. **Residual Activation**: Inelastic interactions of high-energy protons losses can generate radioactive nuclei within the affected equipment. These activated materials emit beta and gamma radiation during and after beam operations. This may necessitate access restrictions or a cool-down period to mitigate the radiation's impact on personnel and the environment.
5. **Effects on Electronics**: Electronics exposed to radiation fields can experience single-event effects, where a solitary particle induces a change in a circuit element. Prolonged exposure can also degrade electronics through accumulated displacement damage and/or the dose deposited by charged particles.

5.4 Protection Devices

Having listed the potential consequences of beam losses in the equipment, it is necessary to explore the avenues to protect the accelerator from these effects. There are two distinct protective measures:

- *Active protection*: This is based on the constant monitoring of beam and machine parameters, providing online measurements of important quantities such as beam position with Beam position Monitors (BPMs), Beam loss rate with Beam Loss Monitors (BLMs), power failures of magnets with Fast Magnet Current Change Monitors (FMCMs), and many more.

The operation is straightforward. In any monitored parameter goes beyond a predefined safety range, the dump system is activated, and the beam is extracted from the accelerator onto the beam dump.

- *Passive protection*: There may be cases where the active system is not fast enough to ensure the total safety of the equipment. In these instances, considerations are made within the accelerator's collimation system where beam absorbers and collimators are utilised for specific failure cases. For instance, during the injection of high-intensity beam into a synchrotron, if the kicker magnet fail to inject the beam correctly, an absorber must be strategically placed to deposit the beam energy.

5.4.1 The Beam Loss Monitoring System

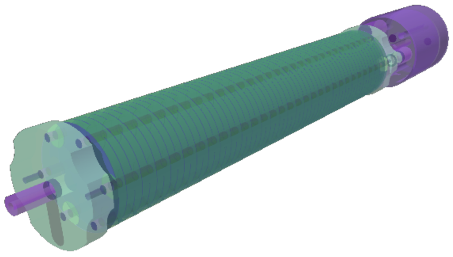

Figure 5.4: Flair image of BLM Ionisation Chamber.

The Beam Loss Monitoring (BLM) system is an integral part of protecting particle accelerators like the LHC. Its primary function is to detect beam losses and prevent damage to the machine components from the resultant energy deposition. The BLM system operates rapidly, with reaction times as short as 40 µs, to detect losses promptly and prevent downtime or equipment damage.

Comprising thousands of detectors distributed across the accelerator, the BLM system predominantly uses Ionisation Chambers (IC), exhibited in Fig. 5.4. These ICs are calibrated to provide a current signal corresponding to the intensity of the particle shower within the chamber. The derived signal indicates the intensity and location of beam losses, helping in discerning the loss mechanism and optimising collimator settings and control.

Beyond machine protection, the BLM system serves as a powerful diagnostic tool tracking beam losses along the beam-line. Its large dynamic range, measuring currents from pA to µA (up to 10^6 - 10^8 orders) allows it to register even minor losses, providing valuable information about the accelerator's operational efficiency.

If the BLM system detects beam loss exceeding set thresholds, it activates a beam abort. This emergency procedure involves the rapid extraction and safe disposal of the beam, stopping further losses and protecting the machine from damage. It is crucial the BLM system covers the entire accelerator, ensuring no part of it is left unmonitored.

5.4.2 Collimation System

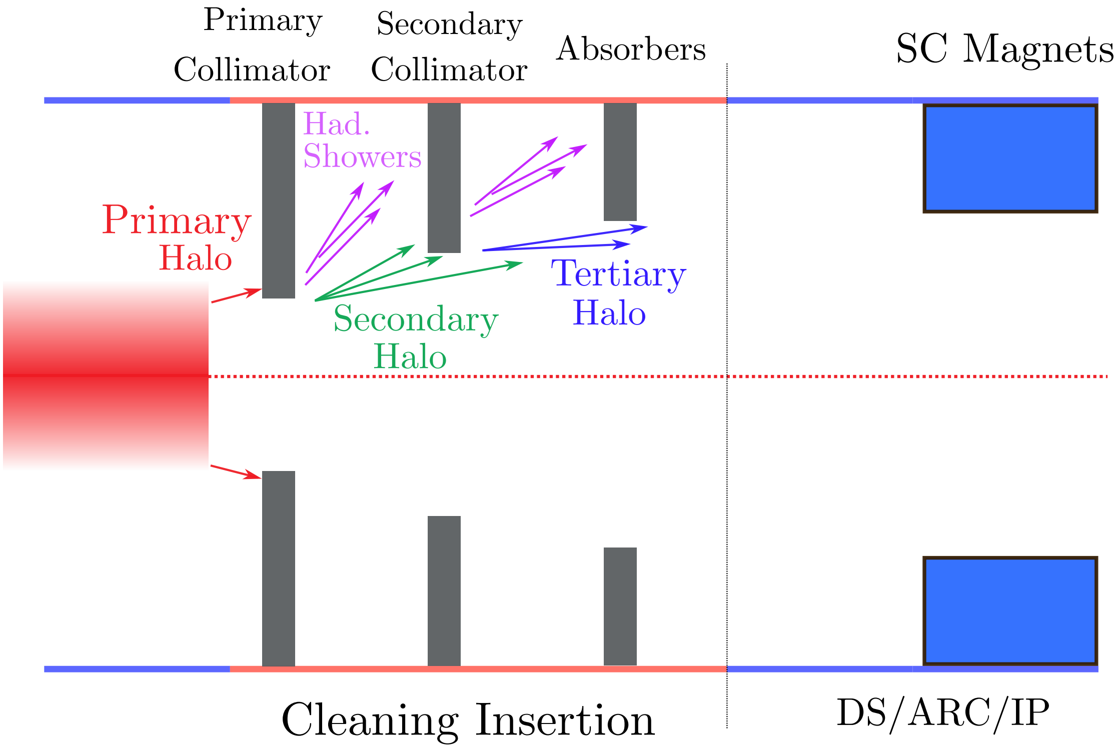

Figure 5.5: Hierarchical working principle of the LHC collimation system.

Within the LHC, there are two regions of great importance for ensuring its performance and protection. These are the Betatron Cleaning Insertion (IR7) and Momentum Cleaning Insertion (IR3). They are responsible for intercepting particles with significant deviations in transverse oscillations and momentum, respectively.

To achieve this, both areas have a collimation system consisting of a hierarchy of collimators, schematically showed in Fig. 5.5. It begins with primary Target Collimator Primary (TCP) collimators made of carbon fiber-reinforced carbon (CFC), strategically positioned near the circulating beam to intercept particles from the primary halo. Next are the secondary collimators (TCS), of the same composition as the primaries, which absorb the particles scattered by the primary collimators and the showers generated by the interaction of the primary halo with the TCPs. Finally, the remaining particles are intercepted by the Tungsten Shower Absorbers (TCLA). These components work harmoniously together to ensure that these particles do not pose a real danger to the accelerator's operation.

It is worth noting how efficient this collimation system has been, which demonstrated during Run

I, II, and currently Run III, where no magnet quench occurred due to halo-induced issues.

However, the significant increase in luminosity expected for the HL-LHC (see Table 5.1) requires studies to predict the potential for quench under these new circumstances, as well as the impact in terms of accumulated dose on the magnets that are part of the accelerator.

5.5 Role of Monte Carlo Transport Codes for Machine Protection

After having understood the impact of high-energy losses, the development of beam losses during transport through matter, and methods to protect equipment from these losses, one might wonder:

"Why use a MC code for particle transport in machine protection?"

While it is simple to calculate analytically quantities as the energy deposited by a pencil beam at 7 TeV/c proton pencil beam in a copper block and predict the temperature increase in the material, in real-world scenarios where the distribution of impacting particles, the generated shower, and the details of the material and geometry are important, accurate calculation of quantities of interest needs MC codes like FLUKA or G4.

The mentioned relevant quantities can be divided in the short-term and long-term effects on the equipment.

- *Short-Term effects*. These effects are observed in an accelerator, for instance, as quenches and (explained in Sec. 5.3). These consequences are almost immediate in the event of a beam loss, and the quantities to investigate the potentiality of these cases involve calculating the energy and/or power deposition in the region of interest for the specific situation.
- *Long-Term effects*. These effects include damage to the structure of the material (see Sec 5.3). The two most important quantities to calculate here are the dose accumulated and the displacement per atom over a period of time. Both provide values that, depending on the time and material type, may indicate relevant degradation or structural damage, factoring into the planning of the expected lifetime of the devices.

The results obtained from simulations allows to conclude whether the situation of study requires mitigation strategies. This procedure was conducted during previous runs of the LHC I, II and III, e.g. studying the effect of the collision debris in Point I and Point V [108], as well as in the collimation system in point VII [109]. It is currently applied to predict the impact of beam loss impact in future accelerators and experiment, such as the High-Luminosity LHC (HL-LHC) [110], the Future Circular Collider (FCC) [111], and the Muon Collider [112].

6 The Moira Framework

6.1 The Concept of Moira

In the previous chapter, the multiple differences and similarities between the FLUKA and G4 MC codes were detailed. Both being multi-purpose and multi-particle codes allow the simulation of a large number of scenarios where the transport of radiation in matter is of particular interest. As previously explained, the use of multiple MC codes, rigorously tested, is important to obtain a better assesment of the sysmatic errors in the results. Therefore, the use of both FLUKA and G4 is always of great interest in the scientific community. The challenge lies in the difficulty, and in many cases, the impossibility, of performing simulations with both codes while ensuring that these simulations are **equivalent**. Among the challenges in achieving this equivalence there is:

1. *Difficulty due to different ways of using the codes*: Considering a simulation with one of the two codes, performing an analogous one with the counterpart may require arduous work for the user. A complex geometry, a magnetic field not included in the range of options, an uncommon biasing, and may require a lot of work to be implemented. A clear example is the FLUKA inputs obtained from the use of the mentioned LB. Extensive geometries, with multiple magnetic fields defined in detail to simulate sections of the LHC, are generated for an exclusive FLUKA format. Trying to carry out a simulation with G4 would require a titanic task on the part of the user.
2. *The impossibility of performing some simulations*: Although some simulations could require a great effort to be carried out with both codes, some are simply unrealisable (at least considering their current state). For example, performing a simulation with electric fields in materials other than vacuum in FLUKA is currently impossible, while as mentioned in previous sections, G4 even allows electromagnetic and gravitational fields.
3. The fact that simulations are equivalent implies that both simulations are defined with the same characteristics (or as close as possible), with analogous fields, transport and production thresholds, same geometry, etc. Finally, hadronic and electromagnetic physics must be applicable and validated in the energy range of interest.

This new development, tentatively called "Moira" [113], emerges to reduce (if not eliminate) the aforementioned limitations. Moira is a code created to provide the user with the capabilities of the G4 toolkit, but structured with the usage philosophy provided by FLUKA. Moira seeks to solve the three mentioned challenges, enabling the execution of simulations with G4 that are feasible with FLUKA[I].

6.2 Motivations Behind the Development of Moira

There are two main reasons that drive the development of Moira:

- *Reducing reliance on a single MC code*: As mentioned before, conducting simulations with multiple MC codes, tested their validity in specific scenarios of interest, increases the credibility of the obtained results. So far, the SY-STI-BMI[II] section has primarily relied on FLUKA for their studies, which has been successful in predicting various particle loss impacts in multiple facilities and accelerators at CERN. However, to further enhance their capabilities, the group aims to utilise G4, which offers multiple physics lists, allowing for a wider range of simulation scenarios.
- *Laying the foundation for the fifth version of FLUKA.CERN*: Similar to the transition from the old Geant3 code to G4, the FLUKA.CERN's current version faces several limitations, primarily due to the Fortran77 standards:
  - Variables and functions have cryptic names due to the six-character limitation.
  - The overuse of COMMON blocks[III] poses risks and limitations.
  - The code structure is rigid, following the fixed-format layout of Fortran77, which restricts code formatting and syntax flexibility compared to modern programming languages.

  Additionally, a significant portion of the code consists of duplicated, obsolete, or inactive parts, making it challenging to improve, incorporate external contributions, debug, and maintain in the long term. The objective is to follow a process of modularisation through the use of OO programming, to assure a better maintenance and enhancement of FLUKA physics performance, the code long-term maintainability, and facilitate the incorporation of further implementation developed by the collaboration and by external contributors.

These reasons have led to the development of Moira, which can be defined as:

"An application based on the G4 toolkit, offering a FLUKA-like experience".

Moira represents an initial step in a medium to long-term plan toward a new generation of FLUKA. This endeavour is particularly interesting because the same motivations that led to the creation of

---

[I] NB: But not necessarily the other way around!

[II] The author of this manuscript is a member of the specified section at CERN

[III] In Fortran77 a COMMON block is a shared piece of memory utilised to pass information between program units without using arguments

G4 are now facilitating the evolution of FLUKA through the G4 toolkit.

6.3 Moira Development Plan Towards a New FLUKA.CERN Generation

The development plan is guided by a series of objectives, which could necessitate multiple years of effort to reach a stage where a new version is ready to supplant the existing fourth generation of FLUKA:

- *Translating FLUKA Functionalities into Moira*: One by one, all functionalities provided by FLUKA, such as geometry description, scoring types, transport thresholds, fields, etc., will be incorporated into Moira. This allows users to replicate FLUKA simulations using G4. Access to these functionalities in Moira should be through one or more command(s) that can be translated from the FLUKA format to Moira, enabling a FLUKA input to be run with Moira (G4).
- *Extending Flair to include Moira*: In previous sections, Flair's capabilities for FLUKA were discussed, providing features for editing inputs, generating geometry, visualising and debugging, running simulations, processing results, and plotting. Incorporating Moira within Flair will provide users with multiple functionalities to conduct simulations. Anticipating details from next section, Flair will act as a bridge between the codes, providing equivalent commands for both codes. This facilitates the automatic conversion of FLUKA input to Moira inputs, or directly conducting G4 simulations with FLUKA inputs, with Flair silently performing the conversion.
- *Incorporating FLUKA's physics models into Moira*: Initially, Moira will rely on G4's physics models. Gradually, FLUKA's hadronic and electromagnetic models will be added to Moira.
- *Release of the new FLUKA.CERN generation*: Upon completion of the previous equivalent, and when results from Moira are consistent with the latest FLUKA v4, Moira will be released as the new generation of FLUKA.CERN, FLUKA v5.

6.4 Current Status of Moira

The following section outlines the current status (as of 2024-03-27) of Moira [IV], covering the most relevant topics. This description is not intended to be a detailed manual for usage or a technical specification of the code implementation. Instead, it presents a summary of the code's current state with a moderate level of detail. Additionally, it includes an example that offers a general overview of Moira's usage and capabilities available to users.

[IV] Disclaimer: Readers should be aware that the evolution of this code is so rapid that the description provided here may not fully represent the current state of the code at the time of reading.

6.4.1 The ASCII Input Files

Emulating the FLUKA usability, Moira, instead of creating a G4 application (since Moira is actually one), requires ASCII files to run. Currently, Moira requires two types of files to conduct simulations:

- The typical **".macro"** file, which consists of UI commands necessary for the simulation. Moira allows the use of default G4 commands and also includes those created to mimic FLUKA functionalities.
- A file that describes the simulation geometry. Two options are available to the user:
  - An extended version of the "textgeom" format, named **".moira"**. This format permit the use of FLUKA's CG along with the G4's hierarchical description.
  - GDML files, which are also supported by Moira for geometry description, allowing only the G4 description.

6.4.2 Geometry Description

The strategy for enabling a G4 application to utilise a CG description like FLUKA is based on extending the standard G4 geometry to include a new "FLUKA solid" named "G4Zone", designed to function equivalently to FLUKA zones. This FLUKA solid, as the FLUKA original zones, are described as intersection of finite and infinite quadratic surfaces. The main features required include:

- Employing the Flair-Geoviewer library, the Flair plugin that permits the geometry editing and visualisation in the GUI. In Moira, it is crucial for defining bodies and zones, as well to compute the particle transport through the geometry.
- The G4Zones are defined by keeping a list of what the user required to delimit the space (Bodies).
- The analogue FLUKA regions are described by linking a list of G4Zones.
- Including a custom-built external navigator equivalent to FLUKA's, allowed since the release of G4 version 10.6 [114].

Each G4Zone has a one-to-one representation between G4Zone, logical volume, and physical volume, thereby simplifying the hierarchical representation to ensure every physical volume is contained within a logical (mother) volume. In addition, the space must be entirely filled by G4Zones, like happens in FLUKA. It is needed to have proper functioning of the navigator.

This framework enables all simulation regions to emulate the FLUKA-style representation. However, it also permits for both representations to coexist and be utilised simultaneously.

Figure 6.1 illustrates a cubic world volume including two spherical volumes: One with FLUKA bodies, and the other with complex figures of order higher than two. Moira supports such configurations by employing the external navigator in the first region and G4's default navigator for the second. Regarding the G4 Textgeom format, it has been extended to include equivalent

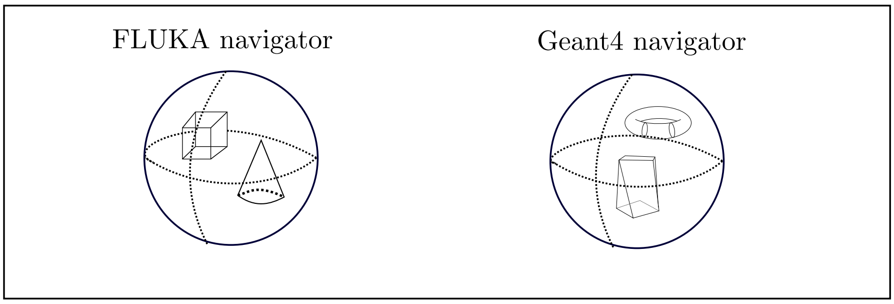

Figure 6.1: Illustration of Moira capability to use both navigators simultaneously in a simulation. The FLUKA navigators is called where only convex geometries are permitted, and the G4 default one, where complex geometries such as tori and twisted parallelepipeds are included.

descriptions with the following tags:

- **:BODY** ⟶ Analogous to FLUKA bodies.
- **:CELL** ⟶ Equivalent to FLUKA regions.
- **:LATTICE** ⟶ Corresponds to FLUKA lattices.

In this way, a bi-univocal correspondence between FLUKA and Moira geometries is achievable when the CG approach is employed. For instance, the basic template provided by Flair shows a copper cylinder surrounded by a vacuum sphere (Fig. 6.2). Figure 6.3 shows the differences between the geometry defined with FLUKA input and its equivalent in Moira. Lastly, if the geometry is purely defined using the G4 description, it can be represented with a GDML file as well.

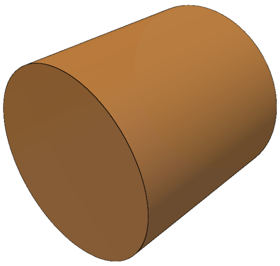

Figure 6.2: Basic copper target geometry. 3D visualisation with Flair

6.4.3 Scoring Status

From the options G4 provides for creating custom scoring, the use of "User Hooks", introduced in section 3.8, was considered the most appropriate for this development, due to the flexibility they offer. By utilising the "UserSteppingAction", "UserTrackingAction", among other user method.

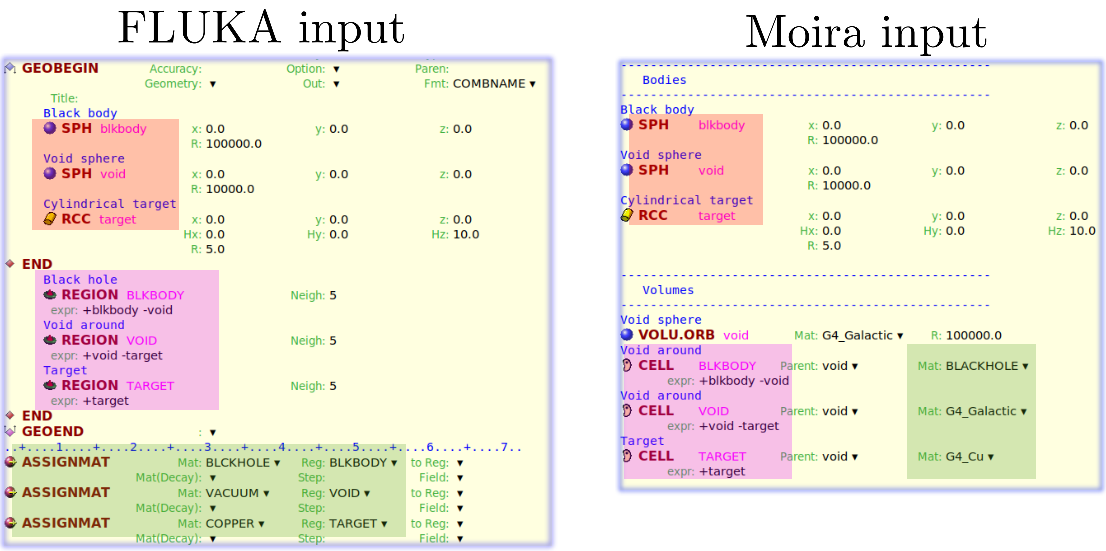

FLUKA input

```
GEOBEGIN          Accuracy:            Option: ▾           Paren:
                  Geometry: ▾          Out: ▾              Fmt: COMBNAME ▾
    Title:
  Black body
  SPH  blkbody        x: 0.0             y: 0.0            z: 0.0
                      R: 100000.0

  Void sphere
  SPH  void           x: 0.0             y: 0.0            z: 0.0
                      R: 10000.0

  Cylindrical target
  RCC  target         x: 0.0             y: 0.0            z: 0.0
                     Hx: 0.0            Hy: 0.0           Hz: 10.0
                      R: 5.0
END
  Black hole
  REGION  BLKBODY                      Neigh: 5
   expr: +blkbody -void
  Void around
  REGION  VOID                         Neigh: 5
   expr: +void -target
  Target
  REGION  TARGET                       Neigh: 5
   expr: +target
END
GEOEND                   : ▾
..+....1....+....2....+....3....+....4....+....5....+....6....+....7..
ASSIGNMAT          Mat: BLCKHOLE ▾    Reg: BLKBODY ▾   to Reg: ▾
              Mat(Decay): ▾           Step:             Field: ▾
ASSIGNMAT          Mat: VACUUM ▾      Reg: VOID ▾      to Reg: ▾
              Mat(Decay): ▾           Step:             Field: ▾
ASSIGNMAT          Mat: COPPER ▾      Reg: TARGET ▾    to Reg: ▾
              Mat(Decay): ▾           Step:             Field: ▾
```

Moira input

```
---------------------------------------------------
   Bodies
---------------------------------------------------
Black body
SPH     blkbody        x: 0.0          y: 0.0          z: 0.0
                       R: 100000.0

Void sphere
SPH     void           x: 0.0          y: 0.0          z: 0.0
                       R: 10000.0

Cylindrical target
RCC     target         x: 0.0          y: 0.0          z: 0.0
                      Hx: 0.0         Hy: 0.0         Hz: 10.0
                       R: 5.0

---------------------------------------------------
   Volumes
---------------------------------------------------
Void sphere
VOLU.ORB  void       Mat: G4_Galactic ▾    R: 100000.0
Void around
CELL    BLKBODY     Parent: void ▾       Mat: BLACKHOLE ▾
         expr: +blkbody -void
Void around
CELL    VOID        Parent: void ▾       Mat: G4_Galactic ▾
         expr: +void -target
Target
CELL    TARGET      Parent: void ▾       Mat: G4_Cu ▾
         expr: +target
```

Figure 6.3: FLUKA and Moira input files respectively, describing a copper cylinder

The necessary information is obtained to estimate the desired quantities making use of a fully custom scoring implementation with dedicated containers and histograming capabilities. Moira, emulating the functionalities of FLUKA, currently offers to users the following options:

- Region-based scoring: Moira provides the option to obtain different quantities (e.g., energy, fluence, and more) based on the regions that compose the geometry. This mimics FLUKA USRBIN card (in "per region" scheme).
- Single-differential scoring: It is also possible to perform single-differential scoring, including differential fluence ($\frac{d\varphi}{dE}$ -FLUKA USRTRACK card) in a given region.
- Double-differential scoring: Moira supports options equivalent to USRBDX and USRYIELD, allowing for double-differential fluence or current scoring on a surface, as well as double-differential yield of particles escaping from a surface with respect to various quantities.
- Mesh scoring: Similarly to USRBIN, it is possible in Moira to obtain energy density or fluence in a user-defined mesh, where the mesh can be described in Cartesian or cylindrical coordinates.
- Other "special" scoring cards from FLUKA have been included in Moira, such as DETECT, USERDUMP, and RESNUCLEi.

It is important to highlight the novel standalone analytical mesh scoring implementation included in Moira. Compared to the G4 built-in mesh, this custom implementation does not interfere with the step length taken by particles being transported through a region with mesh scoring. The results have shown a run-time performance improvement of about 40 to 100 times, and a notable reduction in RAM usage by an order of magnitude when compared with G4 implementation. This enhancement is crucial as it can lead to more efficient simulations, a key factor in MC particle transport simulations, where simulations often span days or even weeks. Such efficiency

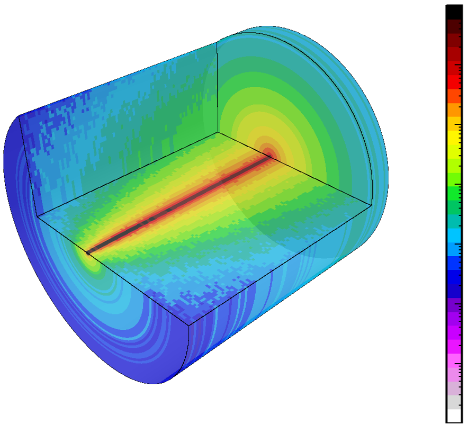

Figure 6.4: Energy deposited by a proton pencil beam at 10 GeV. Colorbar added for illustrative purpose, displaying from lower (white) to higher (black) energy.

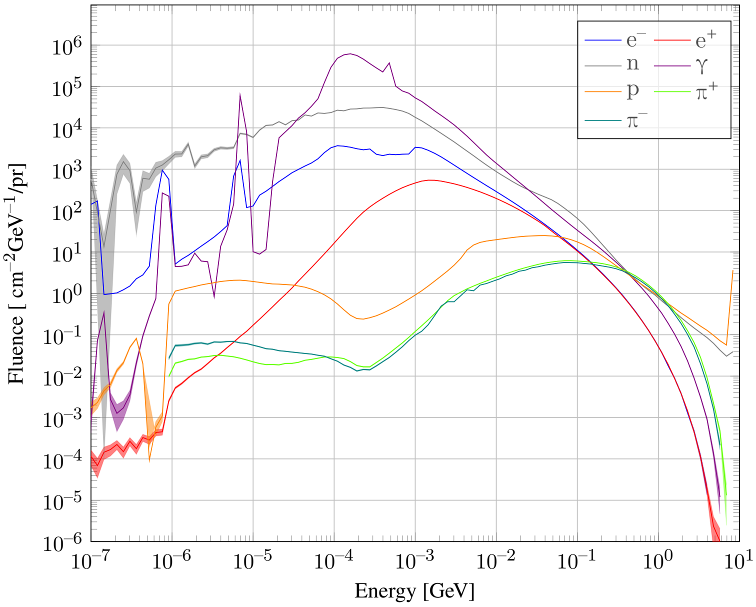

Figure 6.5: Fluence of multiple particles in a copper cylinder.

improvements could greatly reduce computational times, making long-term simulations more feasible and efficient. More details in [115].

To give an overview of the usage of the counterparts to USRBIN and USRTRACK in Moira, Figure 6.4 shows the energy deposited by a 10 GeV proton beam interacting with the copper block created in the previous section, while Figure 6.5 depicts the fluence of multiple particles in this cylinder.

The figure 6.6 illustrates the correspondence between FLUKA's CARDs and Moira's commands to obtain the results shown in the previous figures. Once again, there is a bi-univocal relationship

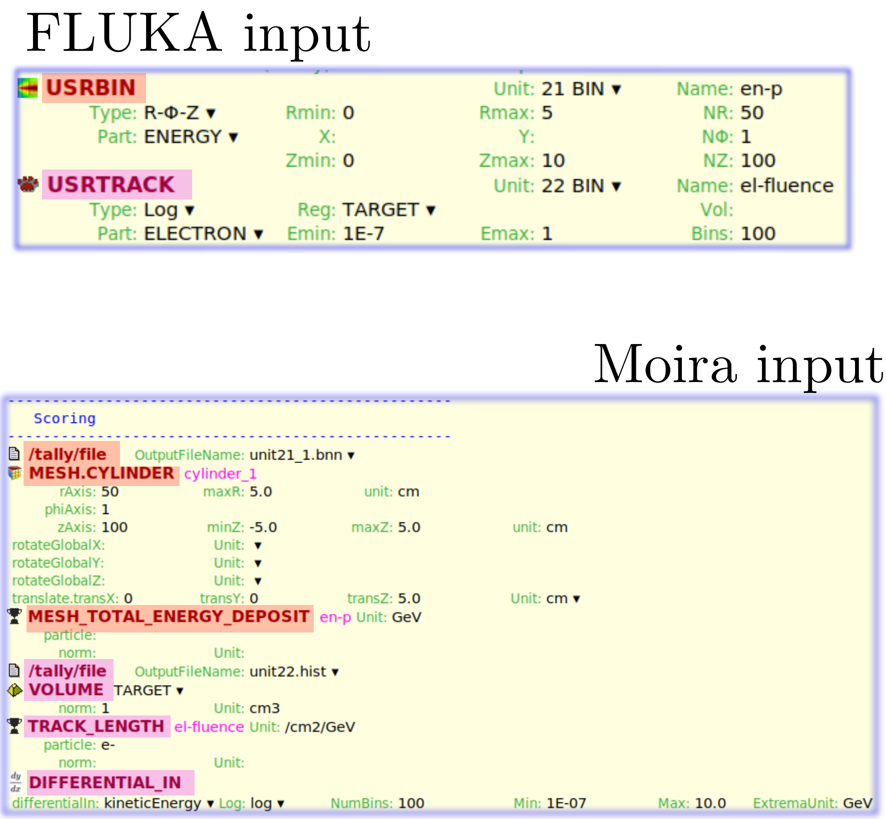

FLUKA input

```
USRBIN                                            Unit: 21 BIN ▾   Name: en-p
      Type: R-Φ-Z ▾       Rmin: 0                 Rmax: 5            NR: 50
      Part: ENERGY ▾         X:                      Y:              NΦ: 1
                          Zmin: 0                 Zmax: 10           NZ: 100
USRTRACK                                          Unit: 22 BIN ▾   Name: el-fluence
      Type: Log ▾          Reg: TARGET ▾                            Vol:
      Part: ELECTRON ▾    Emin: 1E-7              Emax: 1          Bins: 100
```

Moira input

```
----------------------------------------------------
  Scoring
----------------------------------------------------
/tally/file     OutputFileName: unit21_1.bnn ▾
MESH.CYLINDER cylinder_1
       rAxis: 50           maxR: 5.0           unit: cm
     phiAxis: 1
       zAxis: 100          minZ: -5.0         maxZ: 5.0           unit: cm
rotateGlobalX:             Unit:  ▾
rotateGlobalY:             Unit:  ▾
rotateGlobalZ:             Unit:  ▾
translate.transX: 0      transY: 0          transZ: 5.0           Unit: cm ▾
MESH_TOTAL_ENERGY_DEPOSIT en-p Unit: GeV
    particle:
        norm:              Unit:
/tally/file     OutputFileName: unit22.hist ▾
VOLUME TARGET ▾
        norm: 1            Unit: cm3
TRACK_LENGTH el-fluence Unit: /cm2/GeV
    particle: e-
        norm:              Unit:
DIFFERENTIAL_IN
differentialIn: kineticEnergy ▾ Log: log ▾   NumBins: 100        Min: 1E-07       Max: 10.0    ExtremaUnit: GeV
```

Figure 6.6: Scoring FLUKA and Moira input files to obtain energy deposited in a cylindrical mesh, and the fluence of e^-s in the copper cylinder.

between both inputs. The same applies to all the functionalities implemented so far in Moira and FLUKA.

6.4.4 Tracking Cutoffs Status

In Section 3.7, it was explained that G4 provides users with production cuts for electrons, positrons, photons, and protons. These cuts are employed in situations where particles produced by processes such as ionisation, bremsstrahlung, and pair production[V], cannot traverse a distance greater than that defined by the cuts (specified in terms of range/distance). If this occurs, the particle is not generated, and its energy is deposited on the spot. On the other hand, G4 does not offer transport cuts, hence particles are transported until their energy is depleted.

Moira incorporates the use of production cuts, following an energy-based scheme similar to FLUKA and most other MC codes, as well as transport cuts.

For the implementation of production cuts energy-based, a "trick" was utilised in Moira for

---

[V] Discrete processes like photoelectric effect, Compton scattering, and gamma conversion may also be included optionally.

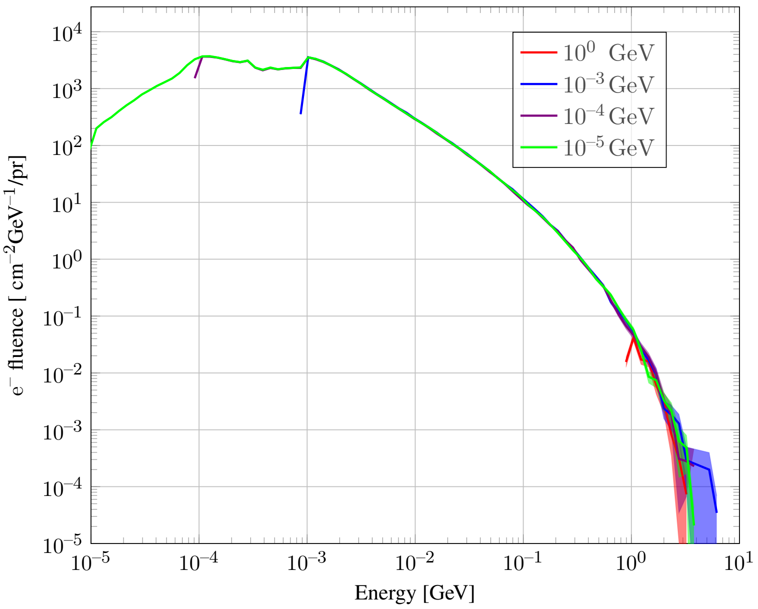

Figure 6.7: Fluence of electrons for different transport cuts

the current, probably temporary, implementation. The idea was to keep relying on the G4 implementation, i.e., internally provide the range cut to G4. When the user supplies to Moira the energy values, making use of G4 methods to obtain energy from range in a material for e-, e+ and photons, through utilising a simple bisection method the correspondent range can be obtained. It is natural to consider that this might be a temporary solution, because, even though, it works, G4 in fact, when the user provides a range for the production cuts, it finally utilises the energy!. Thus, current implementation in Moira is doing an unnecessary extra step. However, no straightforward solution has been found yet to skip this dispensable conversion.

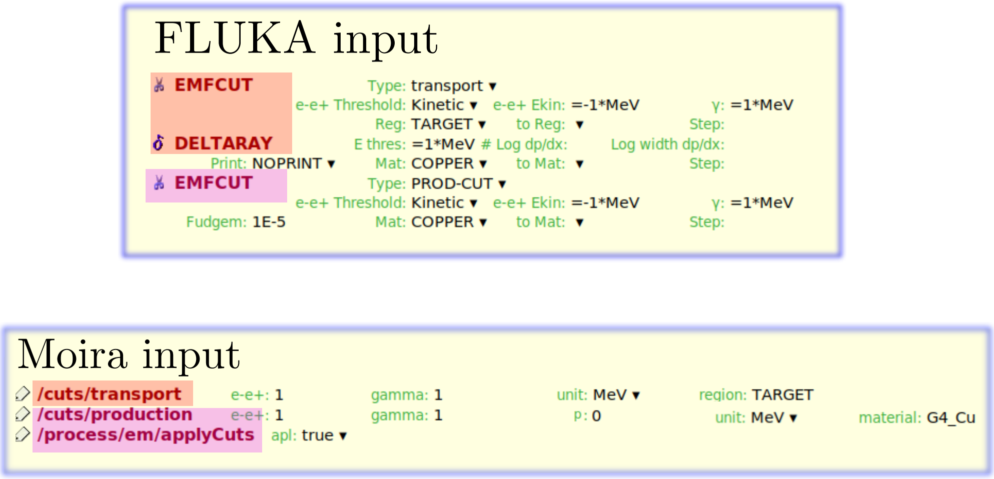
FLUKA input

```
EMFCUT                         Type: transport ▾
               e-e+ Threshold: Kinetic ▾   e-e+ Ekin: =-1*MeV          γ: =1*MeV
                          Reg: TARGET ▾       to Reg:  ▾            Step:
DELTARAY                  E thres: =1*MeV # Log dp/dx:        Log width dp/dx:
          Print: NOPRINT ▾        Mat: COPPER ▾       to Mat:  ▾            Step:
EMFCUT                         Type: PROD-CUT ▾
               e-e+ Threshold: Kinetic ▾   e-e+ Ekin: =-1*MeV          γ: =1*MeV
       Fudgem: 1E-5               Mat: COPPER ▾       to Mat:  ▾            Step:
```

Moira input

```
/cuts/transport       e-e+: 1        gamma: 1          unit: MeV ▾       region: TARGET
/cuts/production      e-e+: 1        gamma: 1            p: 0             unit: MeV ▾         material: G4_Cu
/process/em/applyCuts  apl: true ▾
```

Figure 6.8: Equivalent FLUKA and Moira inputs for imposing production and transport cuts on EM particles

Furthermore, to define the transport cuts, a new custom-process was defined in Moira for this purpose, a new one called "**transportcuts**". This process is invoked when a particle energy falls below the cut-off level set for the region within the geometry it occupies. In this situation, the particle is discarded, and its energy is deposited on the spot. There is a missing implementation here, since the described situation can be imposed to any type of particle. In FLUKA, if the particle is a hadron, heavy ion, muon or neutrino, the particle is ranged out if the cut-off is defined below 100 MeV.

A sample of the impact of different production and transport cuts can be observed in Figure 6.7. It exhibits the fluence of electrons, as the cuts are reduced for the already presented copper cylinder. While the comparison of both inputs is exhibited in figure 6.8.

6.4.5 Fields Status

Regarding fields, even though, all the infrastructure to enable electric, gravitational and magnetic fields [VI] has been implemented, Moira currently provides to users the possibility to make use of solely magnetic fields. These fields are implemented using G4's infrastructure introduced in Section 3.6, with capabilities to replicate any magnetic field in FLUKA, which include:

- **Analytical fields**:
  - Constant:

    $$\vec{B} = B\widehat{z}$$

  - Dipolar: Here, v is a normalised vector.

    $$\vec{B} = B\widehat{v}$$

  - Quadrupolar:

    $$\vec{B} = B\,(y\widehat{x} + x\widehat{y})$$

  - Sextupolar:

    $$\vec{B} = B\left(xy\widehat{x} + \frac{(x+y)(x-y)}{2}\widehat{y}\right)$$

  - Octupolar:

    $$\vec{B} = B\left[\left(\frac{y}{24}\left(\sqrt{3}x+y\right)\left(\sqrt{3}x-y\right)\widehat{x} + \frac{x}{24}\left(\sqrt{3}y+x\right)\left(x-\sqrt{3}y\right)\widehat{y}\right)\right]$$

  - Decapolar:

    $$\vec{B} = B\left(\frac{1}{6}xy(x+y)(x-y)\widehat{x} + \frac{1}{24}\left(x(x+\sqrt{3}y)(x-\sqrt{3}y)x - y(\sqrt{3}x+y)(\sqrt{3}x-y)y\right)\widehat{y}\right)$$

- **2D and 3D tabulated fields for numerical interpolation**: The idea is illustrated in Figure 6.9. When the particle is located between the square limited by the map, an interpolation in the following way is defined:

  $$\vec{B}_x = b_1 + (y-y_1)\,(b_2-b_1)$$

[VI] or a combination of two or three

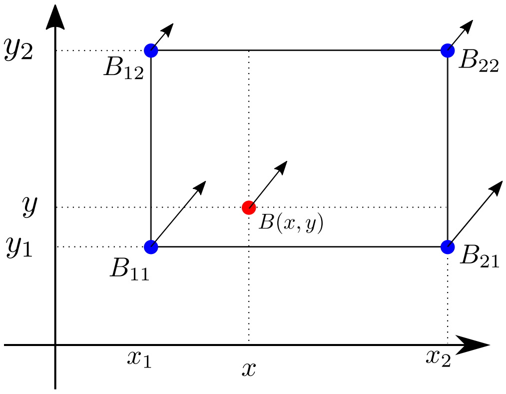

Figure 6.9: 2D interpolation of a field map.

Where:

$$b_1 = B_{11} + (x - x_1)(B_{21} - B_{11})$$

$$b_2 = B_{12} + (x - x_1)(B_{22} - B_{21})$$

Being analogous for $\vec{B}_y$.

- **A combination analytical + interpolated**: This option permits to utilise an analytical field in a part of the space, and an interpolation in the rest. Fig. 6.10 shows many of the magnets that the LHC hosts, including the warm dipole and quadrupole (MBW and MQW) and the superconducting magnets (MB and MQ). For instance, the MB field is described by a combination of fields, using an analytical dipolar field in the beam pipes, and the interpolated case for the rest of the magnet. Figure 6.12 exhibited the equivalent cards to include in the simulation this MB field.

Continuing with the copper cylinder example, applying a dipolar field with a strength of 20 T throughout its region demonstrate the effect on all electrons produced by the interaction of 100 protons with a kinetic energy of 10 GeV. The influence of the field on the electron trajectories is exhibited in Fig. 6.11.

6.4.6 Biasing Techniques Status

For the biasing techniques implemented in Moira at the moment, the "Generic Biasing" framework (discussed in 3.5) was utilised. The infrastructure provided by this scheme permitted, so far, the definition of multiple techniques, following the FLUKA methods implementation:

- **Importance Biasing (IB) and Weight Window biasing (WW)**: These technique are geometry-based. I.e., they act when a particle is crossing from a region to another (IB) or when they are in a given region (WW). In both cases, the objective is to increase/reduce the number of particles to transport in a region of the simulation.
  In the IB, when a particle is traversing the border of from region 1 to region 2, where a different "Importance" was assigned I_1 and I_2, depending of these values, different

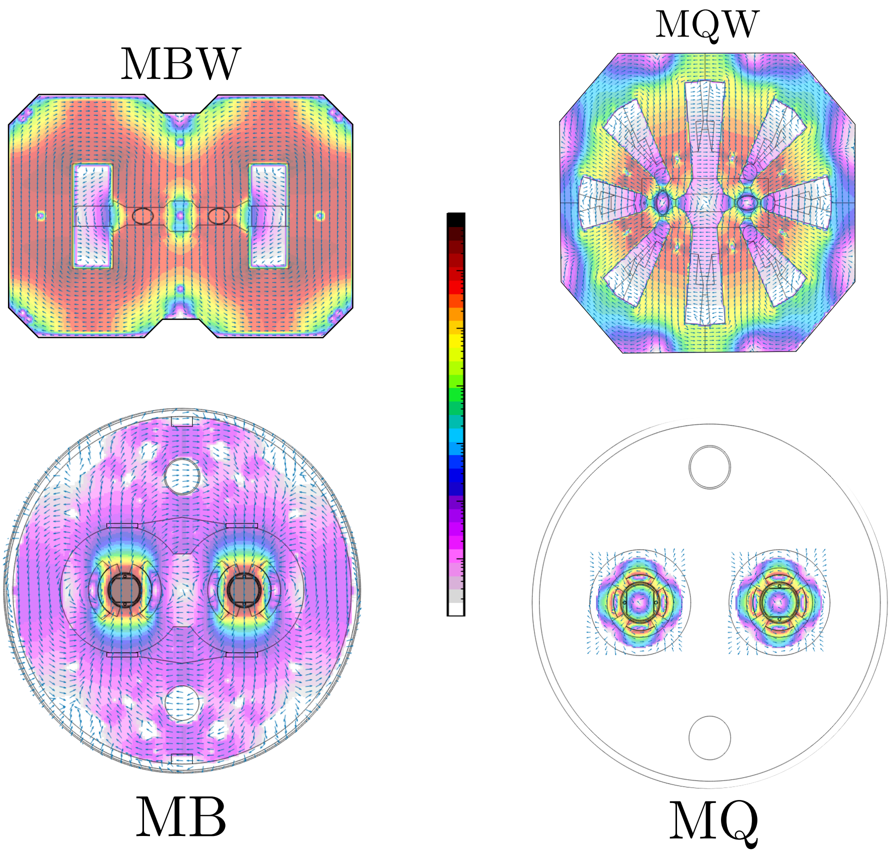

Figure 6.10: Dipole and quadrupole, Warm and SC, fields maps in Moira.

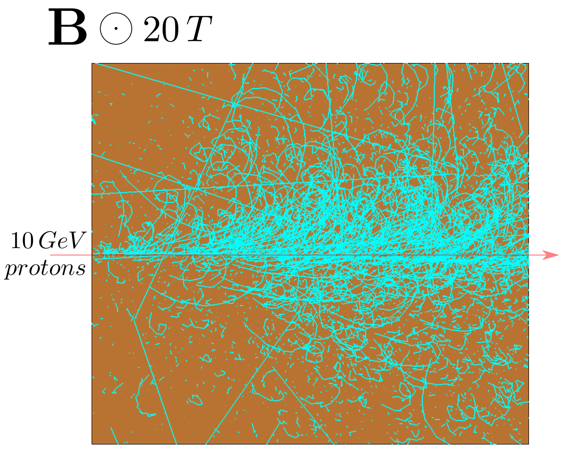

Figure 6.11: Electrons generated by the passage of primary protons and their curved trajectories due to the 20 T dipolar field.

algorithms are applied:

- If $I_2/I_1 > 1$: In this case, "surface splitting" is applied. The particle splits in $n = I_2/I_1$ identical particles, with a weight, being a fraction n of the initial weight.
- If $I_1/I_2 > 1$: In this situation, "Russian roulette" is applied. The particle is killed with a

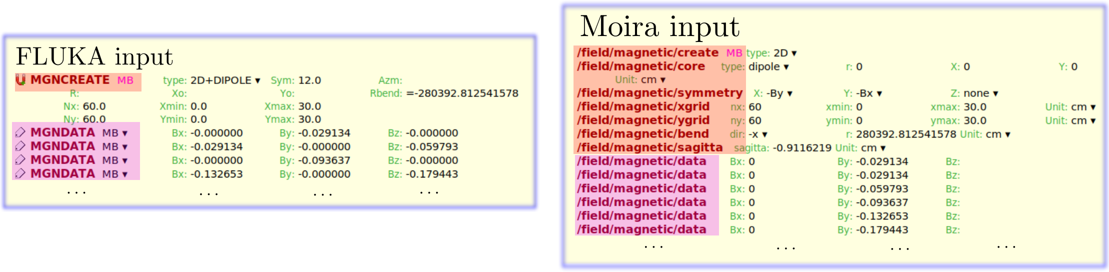

```
FLUKA input
MGNCREATE MB    type: 2D+DIPOLE ▾  Sym: 12.0          Azm:
       R:         Xo:              Yo:               Rbend: =-280392.812541578
      Nx: 60.0  Xmin: 0.0        Xmax: 30.0
      Ny: 60.0  Ymin: 0.0        Ymax: 30.0
MGNDATA MB ▾      Bx: -0.000000    By: -0.029134     Bz: -0.000000
MGNDATA MB ▾      Bx: -0.029134    By: -0.000000     Bz: -0.059793
MGNDATA MB ▾      Bx: -0.000000    By: -0.093637     Bz: -0.000000
MGNDATA MB ▾      Bx: -0.132653    By: -0.000000     Bz: -0.179443
   ...               ...              ...               ...
```

```
Moira input
/field/magnetic/create  MB type: 2D ▾
/field/magnetic/core       type: dipole ▾       r: 0              X: 0             Y: 0
       Unit: cm ▾
/field/magnetic/symmetry   X: -By ▾             Y: -Bx ▾          Z: none ▾
/field/magnetic/xgrid      nx: 60            xmin: 0           xmax: 30.0       Unit: cm ▾
/field/magnetic/ygrid      ny: 60            ymin: 0           ymax: 30.0       Unit: cm ▾
/field/magnetic/bend      dir: -x ▾             r: 280392.812541578 Unit: cm ▾
/field/magnetic/sagitta   sagitta: -0.9116219 Unit: cm ▾
/field/magnetic/data       Bx: 0               By: -0.029134     Bz:
/field/magnetic/data       Bx: 0               By: -0.029134     Bz:
/field/magnetic/data       Bx: 0               By: -0.059793     Bz:
/field/magnetic/data       Bx: 0               By: -0.093637     Bz:
/field/magnetic/data       Bx: 0               By: -0.132653     Bz:
/field/magnetic/data       Bx: 0               By: -0.179443     Bz:
   ...                        ...                 ...               ...
```

Figure 6.12: Input file in FLUKA and Moira to define the warm quadrupole field (MQW).

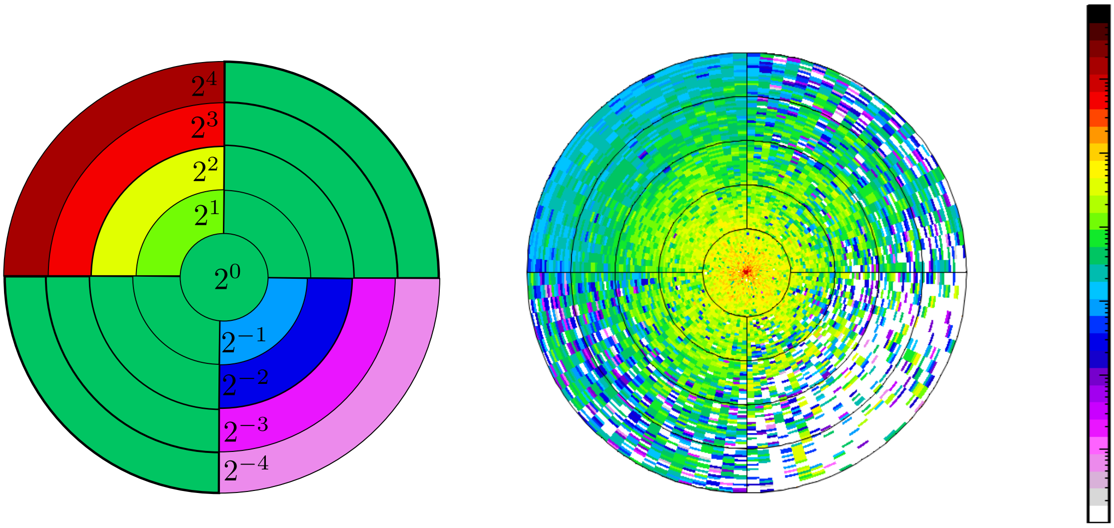

Figure 6.13: Electrons fluence in the four quadrants of copper cylinder.

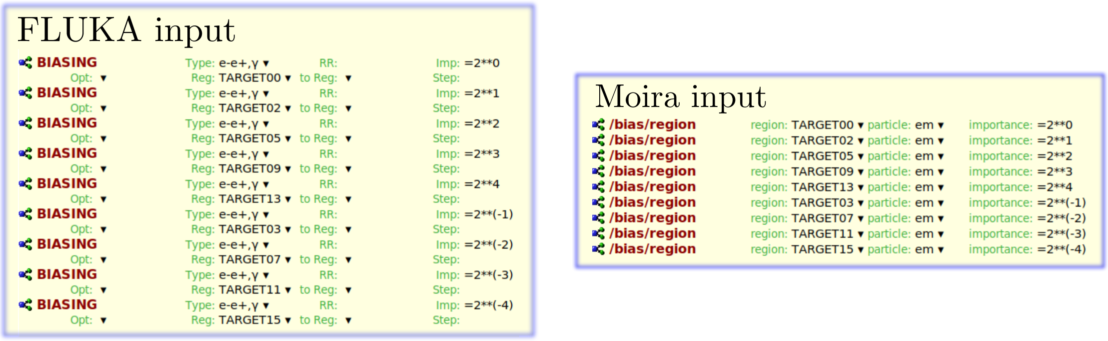

```
FLUKA input
BIASING               Type: e-e+,γ ▾           RR:              Imp: =2**0
       Opt: ▾          Reg: TARGET00 ▾  to Reg: ▾              Step:
BIASING               Type: e-e+,γ ▾           RR:              Imp: =2**1
       Opt: ▾          Reg: TARGET02 ▾  to Reg: ▾              Step:
BIASING               Type: e-e+,γ ▾           RR:              Imp: =2**2
       Opt: ▾          Reg: TARGET05 ▾  to Reg: ▾              Step:
BIASING               Type: e-e+,γ ▾           RR:              Imp: =2**3
       Opt: ▾          Reg: TARGET09 ▾  to Reg: ▾              Step:
BIASING               Type: e-e+,γ ▾           RR:              Imp: =2**4
       Opt: ▾          Reg: TARGET13 ▾  to Reg: ▾              Step:
BIASING               Type: e-e+,γ ▾           RR:              Imp: =2**(-1)
       Opt: ▾          Reg: TARGET03 ▾  to Reg: ▾              Step:
BIASING               Type: e-e+,γ ▾           RR:              Imp: =2**(-2)
       Opt: ▾          Reg: TARGET07 ▾  to Reg: ▾              Step:
BIASING               Type: e-e+,γ ▾           RR:              Imp: =2**(-3)
       Opt: ▾          Reg: TARGET11 ▾  to Reg: ▾              Step:
BIASING               Type: e-e+,γ ▾           RR:              Imp: =2**(-4)
       Opt: ▾          Reg: TARGET15 ▾  to Reg: ▾              Step:
```

```
Moira input
/bias/region     region: TARGET00 ▾ particle: em ▾    importance: =2**0
/bias/region     region: TARGET02 ▾ particle: em ▾    importance: =2**1
/bias/region     region: TARGET05 ▾ particle: em ▾    importance: =2**2
/bias/region     region: TARGET09 ▾ particle: em ▾    importance: =2**3
/bias/region     region: TARGET13 ▾ particle: em ▾    importance: =2**4
/bias/region     region: TARGET03 ▾ particle: em ▾    importance: =2**(-1)
/bias/region     region: TARGET07 ▾ particle: em ▾    importance: =2**(-2)
/bias/region     region: TARGET11 ▾ particle: em ▾    importance: =2**(-3)
/bias/region     region: TARGET15 ▾ particle: em ▾    importance: =2**(-4)
```

Figure 6.14: FLUKA and Moira biasing input files to define importance values in cylinder quadrants.

probability $(1 - {}^{I_2}/_{I_1})$. If it survives, its weight is increase by ${}^{I_1}/_{I_2}$.

On the other hand, the WW techniques, make use of these two algorithms, but defining a range of energies and weights where they are applied in a region. I.e. if a particle, for instance, an e^+ is a in a region 1, with energy E and weight w, where there is defined a window of $[w_1, w_2]$:

  - If $w > w_2$: "Surface splitting" is applied and the particle is replaced by two identical particles with $w/2$.
  - If $w < w_1$: "Russian roulette" is called, and the particle survives with a probability w/w_1. In case it happens, the new weight will be w_1.
- **Leading Particle Biasing**: This technique applies to e^-, e^+, and γ reducing the production of secondary particles following an electromagnetic interaction, thus preventing geometric progression in EM showers. Final state EM interactions end up in two particles. The idea is to retain one of these two particles, defining the probability of survival by their energy:
  - If E_1 and E_2 are the energy of the final state particles. Then, particle 1 will survive with a $p = \frac{E_1}{E_1+E_2}$.
  - If particle 1 survives, the second particle, of course, is killed, and the weight is redefined by $w = w_1/p$.
- **Multiplicity Tuning**: It is an analogous technique to Leading Particle Biasing exists, but applied to hadronic inelastic interactions. Currently, the implementation is different to the one in FLUKA. While in FLUKA the user defines a probability of survival to the secondary particles generated. In Moira, the most energetic particles is retained, while the rest of secondaries are subdivided in different particle types:
  - Mesons
  - Baryons
  - Gammas
  - π°
  - Leptons

  Then, randomly, only one of these particles is picked, and the weight is redefined, scaling it by the number of secondaries of the same type.
- **Interaction (or Mean Free Path) Biasing**: Users have the possibility to artificially decrease the mean free path for inelastic nuclear interactions. Despite some differences in the current implementation, e.g. FLUKA is material-based and Moira is region-based, and the cross section can be modified for any process in Moira, since it has to be defined explicitly, both achieve the same goal, modifying artificially the cross section of a process of interest, which might be useful to enhance reactions in some rare cases or thin/low density targets.

Employing the copper cylinder example once more (this time without the magnetic field used earlier) to exhibit the application of IB, the cylinder is subdivided into various regions, as indicated in Figure 6.13. The first quadrant is assigned an ascending importance with factors of 2, whereas in the third quadrant, a descending importance with the same factor is applied exclusively to electrons, positrons, and photons. The difference in electron fluence observe with respect to each quadrant is notable. Particularly, the difference in quadrant one and three, where this method is applied.

6.4.7 Radioactive Decay and Activation Status

One of the remarkable qualities of FLUKA is its capability for radiation protection and activation studies. Moira has incorporated all the necessary machinery for this purpose, offering the following features so far:

- Distinguishing between prompt radiation and radiation generated by radioactive decay: This distinction allows for the identification of the source of contributing particles during scoring. It also accounts for secondary particles generated from the decayed processes.
- Two modes of simulating radioactive decay, which can be activated on a per-volume basis, are available:
  - *Standard mode*: In this mode, the treatment provided by G4 is used, where radioactive nuclei are considered as any other unstable particle. This mode emulates the "analogue" mode provided by FLUKA.
  - *Activation calculations à la FLUKA*: This mode allows users to specify irradiation and cooling times, mirroring FLUKA's approach, enabling the use of multiple irradiation profiles and the option for negative cooling times.

The activation mode in Moira is implemented via a a new process called "MoiraActivation". Instead of relying on the default G4decay, this method utilises a different decay engine known as ActiWiz [116], which aims to solve the Bateman equations [117, 118]. ActiWiz is responsible for calculating the evolution of isotopic abundances throughout the decay chain. Irradiation profiles and cooling times are assigned a corresponding weights, and the decay products are ultimately introduced into the G4 transport framework as delayed particles.

6.4.8 Moira Integration within Flair

The benefits provided by the graphical interface Flair for performing simulations with FLUKA have already been mentioned in section 4.9. From the straightforward generation and editing of input files to structures run management, data processing, and visualisation of result, Flair is a powerful tool simulation management.

Presently, Flair's capabilities are not limited to FLUKA alone but have been extended to support other MC codes. In its preliminary phase, Flair is capable of handling input from codes such as PENELOPE, PHITS, MCNP, and, of course, G4 through Moira. Apart from the latter, detailed information about the current status of the other codes will not be given in this manuscript.

With Moira, users have access to all the functionalities mentioned earlier. In a way, Moira's integration with Flair is made possible by its design. Moira's objective is to replicate FLUKA's inputs and outputs process. Its input was constructed to be equivalent with FLUKA's, facilitating its importation into Flair. Flair enhances user experience with additional features. The title of this thesis captures its essence, positioning FLUKA and G4 as two distinct worlds within MC simulations, linked by Moira, the bridge that enables practical results. This link is strengthen

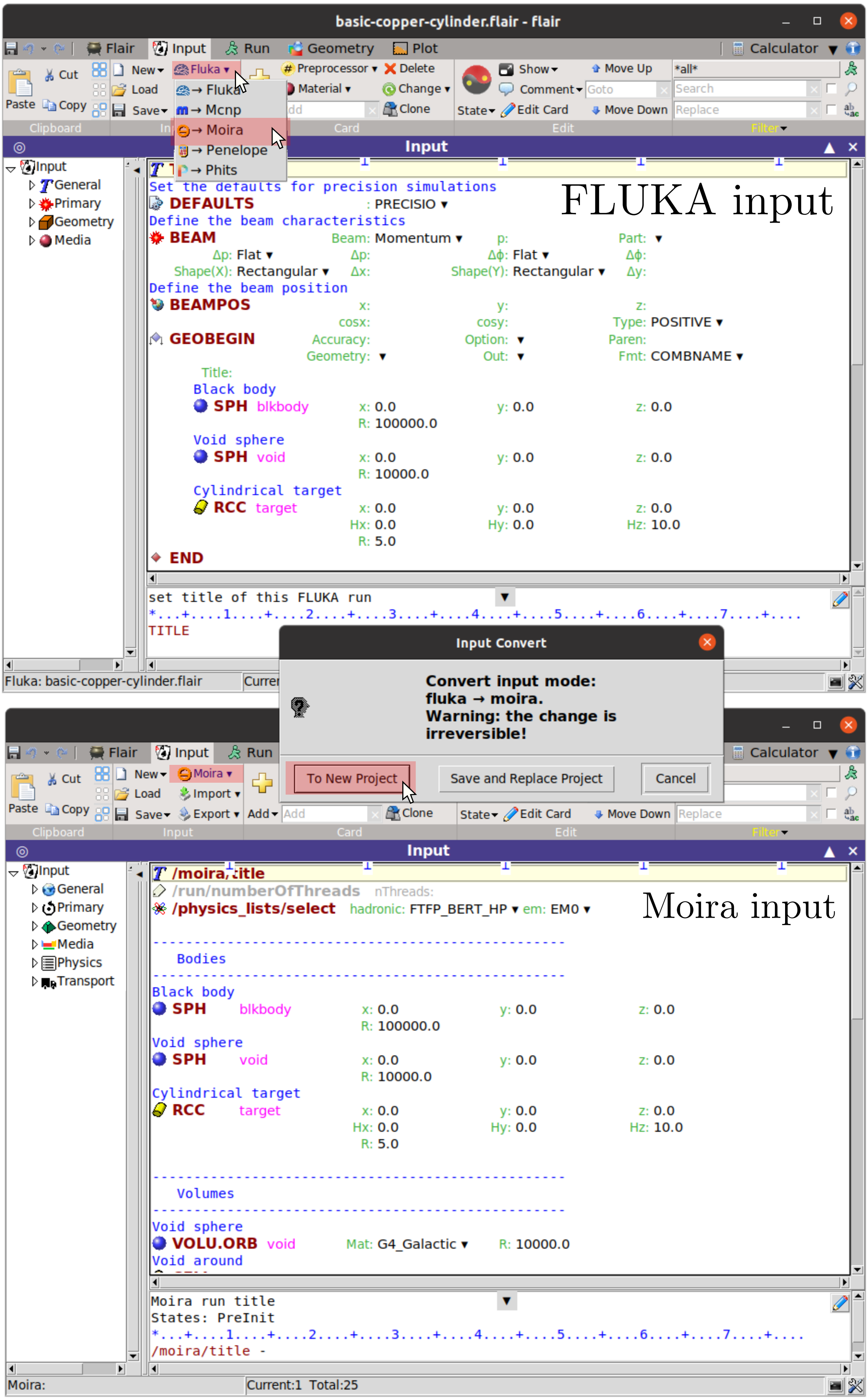

Set the defaults for precision simulations
DEFAULTS : PRECISIO
Define the beam characteristics
BEAM Beam: Momentum p: Part:
Δp: Flat Δp: Δϕ: Flat Δϕ:
Shape(X): Rectangular Δx: Shape(Y): Rectangular Δy:
Define the beam position
BEAMPOS x: y: z:
cosx: cosy: Type: POSITIVE
GEOBEGIN Accuracy: Option: Paren:
Geometry: Out: Fmt: COMBNAME
Title:
Black body
SPH blkbody x: 0.0 y: 0.0 z: 0.0
R: 100000.0
Void sphere
SPH void x: 0.0 y: 0.0 z: 0.0
R: 10000.0
Cylindrical target
RCC target x: 0.0 y: 0.0 z: 0.0
Hx: 0.0 Hy: 0.0 Hz: 10.0
R: 5.0
END

```
set title of this FLUKA run
*...+....1....+....2....+....3....+....4....+....5....+....6....+....7....+....
TITLE
```

Fluka: basic-copper-cylinder.flair

Convert input mode:
fluka → moira.
Warning: the change is irreversible!

/moira/title
/run/numberOfThreads nThreads:
/physics_lists/select hadronic: FTFP_BERT_HP em: EM0

```
--------------------------------------------------
    Bodies
--------------------------------------------------
```

Black body
SPH blkbody x: 0.0 y: 0.0 z: 0.0
R: 100000.0
Void sphere
SPH void x: 0.0 y: 0.0 z: 0.0
R: 10000.0
Cylindrical target
RCC target x: 0.0 y: 0.0 z: 0.0
Hx: 0.0 Hy: 0.0 Hz: 10.0
R: 5.0

```
--------------------------------------------------
    Volumes
--------------------------------------------------
```

Void sphere
VOLU.ORB void Mat: G4_Galactic R: 10000.0
Void around

```
Moira run title
States: PreInit
*...+....1....+....2....+....3....+....4....+....5....+....6....+....7....+....
/moira/title -
```

Moira: Current:1 Total:25

Figure 6.15: Conversion from FLUKA to Moira input in Flair

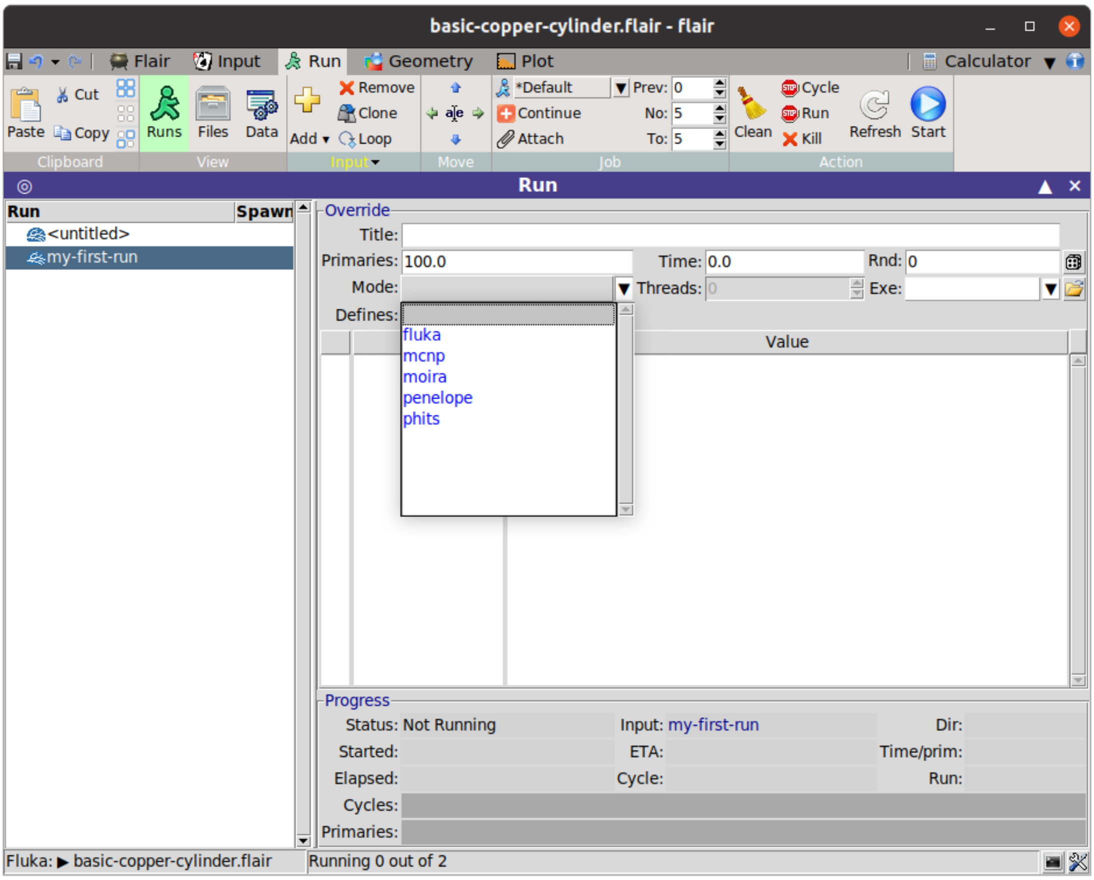

<untitled>
my-first-run

Prev: 0
No: 5
To: 5

Title:
Primaries: 100.0
Time: 0.0
Rnd: 0
Mode:
Threads: 0
Exe:
Defines:

fluka
mcnp
moira
penelope
phits

Status: Not Running
Input: my-first-run
Dir:
Started:
ETA:
Time/prim:
Elapsed:
Cycle:
Run:
Cycles:
Primaries:

Fluka: ▶ basic-copper-cylinder.flair
Running 0 out of 2

Figure 6.16: Run from FLUKA input with other MC codes using Flair

through Flair, which allows for the conversion of FLUKA inputs into Moira's format.

As shown in Fig. 6.15, Flair is equipped to transform FLUKA inputs to Moira and other mentioned MC codes. At this stage, Flair's conversion is unidirectional, from FLUKA to other MC code, with reverse conversion pending to be implemented. Although the latter will be necessary in the near future, the most fundamental aspect is the transition from FLUKA to other codes. As sections 4.10 & 4.11 detailed, all infrastructure for machine protection simulations, including the FEDB and LB, originally developed for FLUKA, are now accessible for Moira and other codes.

A final feature to highlight is that Flair not only allows the generation and manipulation of the input; as illustrated in Fig. 6.16, Flair also performs runs directly from the FLUKA input with other code. Flair operates by internally converting inputs under the hood, transparent to the user, and utilises the internally converted input for simulation [VII].

[VII] WARNING!: Since all features are in development status, it is recommended for users to perform the conversion to ensure the obtained results are correct.

6.4.9 G4-FLUKA Interface

Moving towards this new fifth generation of FLUKA, the capability to access FLUKA's physics models from Moira is a crucial step. The current state of FLUKA requires considerable effort to modernise the current code, ensuring its openness and facilitating future maintenance.

In an important initial move towards this fifth generation, an interface has been developed allowing any G4 (including Moira), to independently access FLUKA's hadronic h-A (PEANUT) and the A-A (BME/RQMD/DMPJET) inelastic interactions.

This interface is a standalone code that isolates the FLUKA h-A and A-A interaction modelling, providing as output the cross-sections for inelastic scattering and the final states of the nuclear interactions. It permits to be utilised in two ways:

- Event generator at the interaction level: The user, providing the type of particle, energy and target nucleus, can obtain the interaction cross section and final states, such as secondaries spectra and residual nuclei distributions. It is a powerful tool for comparing different cross sections and physics models.
- FLUKA physics list in G4: It is the possibility for G4 users to make use of a custom G4 physics list including the FLUKA inelastic interactions. This physics lists so far is composed by the following constructors:
  - FLUKA hadron inelastic interactions
  - Geant4 neutron HP
  - FLUKA ions inelastic interactions
  - G4 elastic interactions
  - G4 EM Livermore package

The objective is to progressively replace the G4 physics by the FLUKA ones, until complete a full FLUKA physics list. As an example of a result obtained with the FLUKA physics list, Figure 6.17 exhibits the fluence of neutrons due to the interaction of 20 GeV protons on lead, comparing FLUKA v4, FTFP_BERT_HP and the described FLUKA physics list in Moira. Further details can be found in [119].

6.5 Conclusions

This sixth chapter introduced the development of an innovative framework for conducting MC simulations, provisionally named Moira. Moira enables simulations in the FLUKA format using the G4 code, along with various alternative hadronic and electromagnetic models.

The current status of this code was highlighted, with a focus on the comparison between using FLUKA and this new development. The discussion also included the options currently available to users, encompassing scoring, fields, biasing, cuts, and other functionalities.

Moreover, the extension of the Flair graphical interface to incorporate other MC codes represents a significant advancement. It allows users to access comprehensive options for input generation,

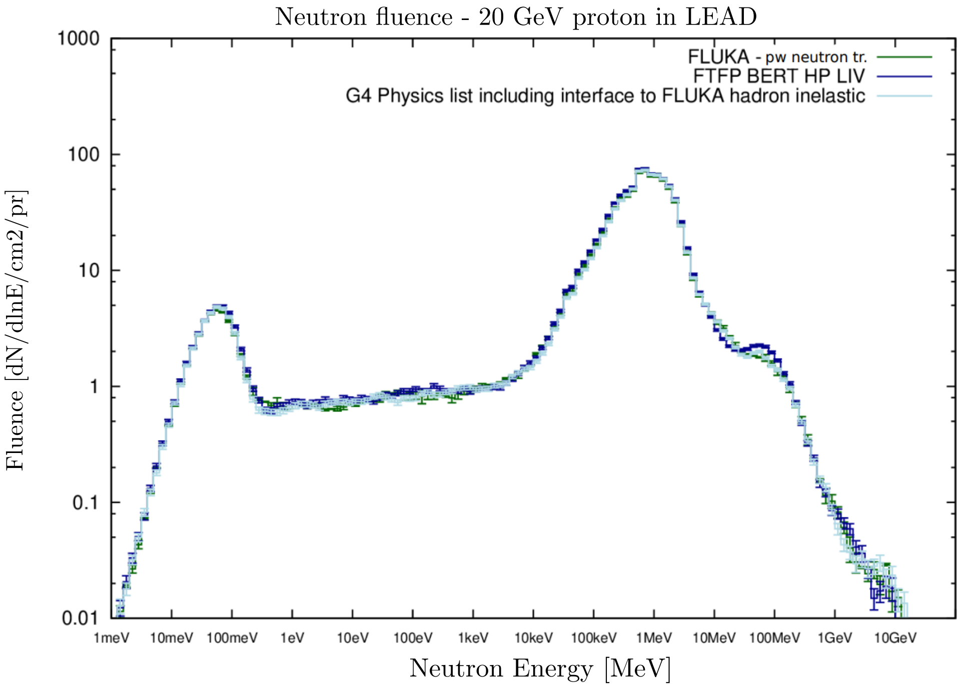

Figure 6.17: Comparison of neutrons fluences between FLUKA v4, a prepackaged G4 physics list, and the FLUKA physics list. Courtesy of G. Hugo.

geometry editing, and simulation execution. This development greatly facilitates the execution of equivalent simulations across different codes, particularly between FLUKA and G4, enabling studies at energies beyond the TeV range.

6.6 Next Steps

- Transition to a purely GDML format. Initially, as described in section 6.4.2, Moira was built using TextGeom for the input associated with the geometry. Due to the lack of maintenance and updates of this feature by the G4 collaboration, it was considered more convenient for long-term stability of Moira to transition to the exclusive use of GDML as Moira's standard format. GDML has been continuously maintained by the G4 collaboration throughout the different releases.
- Generate a simplification of the input by reducing it to a single one, as is done in FLUKA.
- Continue with the implementation of FLUKA v4 features such as missing scoring capabilities, more biasing options, voxel geometries, among many more. At the same time, continue maintaining what has already been done and debug existing features.
- Proceed with the modularisation of the FLUKA v4 components by rewriting them in C++, allowing them to be used in both FLUKA v4 and Moira (FLUKA v5). This step is fundamental for the transition from one generation to the other, simplifying the possibility of continuing with the development of the new code, without causing inconveniences in

subsequent versions of FLUKA v4 and facilitating the comparison of results between both codes.
- Create a users' guide.
- The realisation of an internal release in the collaboration to extend its use, motivating the exposure of bugs, errors, and deficiencies in the code.
- Complete the integration into FLUKAVAL [120], the validation framework for FLUKA, used for testing FLUKA versions with potential for release. This framework simulates a large number of test cases and compares them with previous versions to ensure the good quality of the version that seeks to be released. The integration of Moira into FLUKAVAL is crucial to evaluate the results of FLUKA v5 and v4.

6.7 Acknowledgements

Immense gratitude is extended to Vasilis Vlachoudis, Gabrielle Hugo, Francisco Ogallar, Ivan Sharankov, and Chris Theis for their invaluable contributions to the development of Moira. Without their support and work, this thesis would not have been possible.

7 Validation Studies with Moira

After listing the current status regarding the development of Moira, it is time to present a variety of studies conducted over the past years, which will help verify the advantages of having this innovative MC particle transport framework available.

While acknowledging the importance of having a tool that allows for obtaining inputs from FLUKA to G4 in a practically automatic way, the focus of the upcoming sections is on proofing the significance of carrying out these studies, as well as all similar studies, with multiple Monte Carlo codes, particularly for machine protection studies.

The order presented in the sections was considered based on the complexity of the geometry used. It will begin by showing cases with simple geometries where the existence of Moira may not provide complete justification of its utility, advancing to cases with more complex geometries, where the absence of Moira would lead to these studies being practically unfeasible.

These simulations were also selected due requests to the FLUKA.CERN collaboration, and others based on recent studies conducted by this section using FLUKA, taking advantage of the available results in some cases, and the participation of the authors of those studies to provide support in the execution and analysis of the results.

The version of FLUKA.CERN used for all seven studies was 4-2.2. In the case of G4 it was the 11.0. In addition, the first two studies, which were requested to the collaboration, used Shielding-EM0 and FTFP_BERT-EM0 for the first and second studies, respectively. For the remaining five studies, results were obtained using EM0 package and five different hadronic physics lists:

- FTFP_BERT_HP (G4 Default)
- FTFP_INCLXX_HP
- QGSP_BERT_HP
- QGSP_BIC_HP

  - QGSP_INCLXX_HP [I]

The choice of these physics lists is due to a trade-off between:

1. The pre-packaged physics lists available in G4.
2. The time required to conduct simulations; repeating simulations with different physics lists increases enormously the time needed to obtain results with all of them.
3. Conducting as many permutations of hadronic models in G4 as possible while always using the High-Precision neutron package. This way, the study covers both string models (FTF, QGS) and the three cascade models (BERT, BIC, INCLXX) [II]

More detail about these physics models in appendices A & D.

[I] Reduced to "FBERT", "FINCLXX", "QBERT", "QBIC", "QINCLXX" when text space requires.

[II] Binary cascade in conjunction with FTFP is not currently available as a physics list for users. It would be beneficial to construct it in the future to enable testing with Moira.

7.1 SATIF-15 Workshop: Particle Production Inter-Comparison

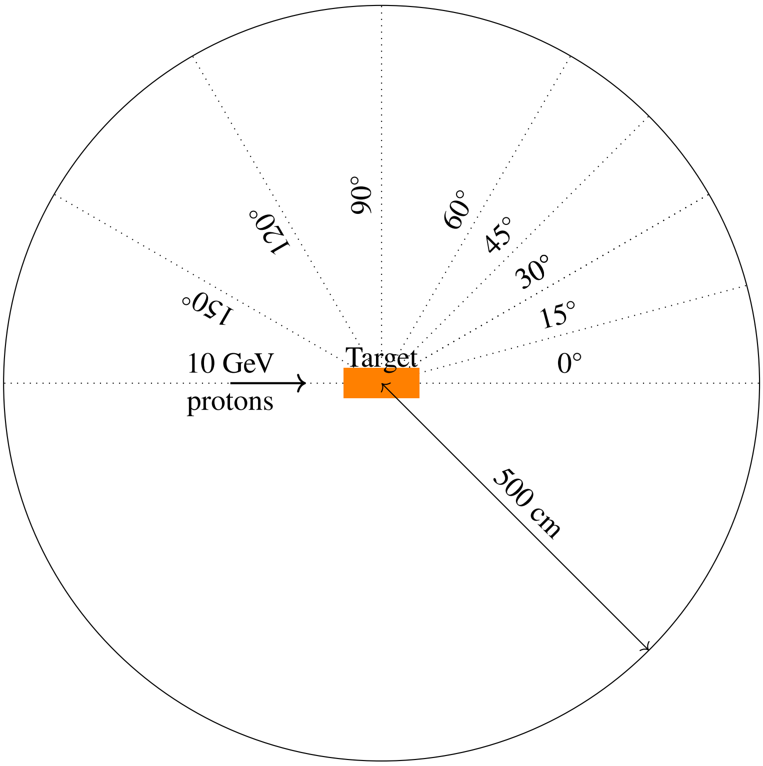

Figure 7.1: Illustration of particle production problem for SATIF15

The Shielding Aspects of Accelerators, Targets and Irradiation Facilities (SATIF) workshops have been held regularly since 1994, occurring biennially and alternating between the United States, Europe, and Asia. These workshops serve as a platform for experts in accelerator shielding and related fields to discuss crucial aspects of modelling and design. Beyond organising these events, the SATIF group also plays a pivotal role in coordinating analysis and suggesting action items.

The primary objectives of the SATIF workshops encompass several key areas. They aim to promote the exchange of information among experts, creating a collaborative environment where knowledge and insights can be shared. These workshops offer a unique opportunity for professionals to learn from one another and remain informed about the latest advancements.

Moreover, the SATIF workshops seek to identify areas where international cooperation could yield fruitful results. By identifying mutual challenges and potential solutions, experts can establish collaborations that transcend geographical boundaries. Such global cooperation enhances the collective expertise, promoting progress in accelerator shielding and its associated fields.

Since SATIF-12, an inter-comparison problem of particle production in thick targets, lead by Dr. Hideo Hirayama, involved multiple MC codes, including FLUKA, G4, PHITS, MARS, and MCNP. The purpose was to examine the observed differences among them [121–123].

In 2022, from September 20th to 23rd, the SATIF-15 workshop took place [124]. As in the four previous occasions, this particle production study was conducted. The FLUKA.CERN collaboration participated by providing results from FLUKA and G4, taking advantage of the development of Moira.

The inter-comparison problem, schematically shown in Figure 7.1 aims to compare the spectra of different particles resulting from the interaction of 10 GeV protons on a target made up of three different materials. In more detail, the specific scenarios examined were:

- Incident particle: Pencil beam of protons with 10 GeV.
- Target materials and their sizes.
  - Al: length 40 cm, diameter 4.0 cm and density 2.7 $\mathrm{g\,cm^{-3}}$.
  - Cu: length 16 cm, diameter 1.6 cm and density 8.63 $\mathrm{g\,cm^{-3}}$.
  - Au : length 10 cm, diameter 1.0 cm and density 19.3 $\mathrm{g\,cm^{-3}}$.
- Quantities to be calculated:
  1. Neutron, proton, π^+, π^- and photon spectrum above 20 MeV in particles/MeV/sr/proton at 0°, 15°, 30°, 45°, 60°, 90°, 120°, 150° with angular width ± 0.5°.
  2. Angular integral spectrum in particles/MeV/proton
  3. Energy integral fluence for (1) and (2) in particles/proton

Although previously was mentioned that this study employed multiple MC codes, this manuscript will exclusively present the results obtained with FLUKA and G4 for the Items (1), (3.1) and (3.2). Readers interested in observing the entirety of the outcomes should consult the SATIF-15 proceedings [III].

7.1.1 Results

Starting presenting the result of the last Item (3.2), namely, the particle production per primary particle, it is interesting how these results demonstrates notable differences between codes, even for such a simple problem.

Table 7.1 displays the number of neutrons, protons, π^+, π^-, and photons generated per primary particle, i.e., per 10 GeV proton transported in Al, Cu, and Au targets. Based on the results from this table, several conclusions can be inferred. There is a tendency in G4 to produce a higher number of neutrons ($\approx$ a 1.80 ratio in Au) and protons ($\approx$ a 1.56 ratio in Au). For the cases of charged π, the differences are less pronounced, except for positive π in copper, with a ratio of roughly 0.48, i.e. FLUKA yields twice as many π^+ as G4. FLUKA also exhibits a higher tendency for photon production across all three material types. Considering the photon generation in this context stems from the decay of π°, it suggests that FLUKA produces a higher amount of these π

[III] Note: As of 2024-03-27, the SATIF-15 proceedings have not been published.

Table 7.1: Number of particles type generated per primary proton. Statistical errors in results are defined by ±1 of the last digit.

	Al		Cu		Au	
	Geant4	FLUKA	Geant4	FLUKA	Geant4	FLUKA
n	2.36	1.53	2.11	2.69	6.73	3.64
p	1.51	1.33	1.85	1.46	2.41	1.54
π^+	0.591	0.598	0.586	1.22	0.526	0.520
π^-	0.505	0.496	0.530	0.496	0.536	0.492
γ	2.22	2.85	2.90	3.71	2.72	3.41

compared to G4 (remember Table 1.1).

These results permits to reflect about the potential consequences of high differences in particle production depending on the code. if one of them produces, for instance, double the number of neutrons, like the Au case in this study, two essential considerations arise. In the context of radiation shielding, where the SATIF workshop is focused, such information is vital due to the penetrating capabilities of neutrons. Overestimating radiation levels could lead to unnecessary and expensive protective measures. Conversely, underestimating this radiation can pose risks to the equipment and personnel in the respective facility.

The results from Item (3.1) also provide insights on each code's behaviour concerning particle production at different angles under this context. Table 7.2 lists the integrated fluence (particles/sr/primary) of the five particle species for the scenarios explained.

Observable trends can be identified for all particles. Their fluence decreases as the observation angle widens. The maximum fluence is observed at 0°, while the minimum appears at 150°. This phenomenon is due to the momentum imparted by the beam, leading to particle clustering in the direction of 0°.

Furthermore, fluence values typically increase with denser target materials, except at 0° and 15°. This behaviour can be attributed to the interaction probabilities of the 10 GeV proton during inelastic interactions and the consequent generation of secondary particles. The increased interaction probability and higher absorption in denser materials contribute to the observed trend.

Figures 7.2 provide a more direct impression of the results expressed in the tables. These figures display the G4/FLUKA ratio of integrated fluence against scattering angles for all particle types.

Regarding the observed differences between G4 and FLUKA, these figures reveal a general agreement between the codes for charged π, though differences become more pronounced at higher densities and larger scattering angles. Similar trends emerge for photons, with production variations mainly appearing at 0° and angles surpassing 90°. For protons and neutrons, the deviations are more substantial, growing with the scattering angle. Differences of up to a factor

Table 7.2: Fluence Energy Integrated (above 20 MeV) [particles/sr/primary]

Particle	Angle	Al		Cu		Au	
		Geant4	FLUKA	Geant4	FLUKA	Geant4	FLUKA
n	0	7.66	5.16	6.22	4.49	4.76	3.62
	15	1.04	0.889	1.30	0.986	1.69	1.21
	30	0.546	0.440	0.778	0.554	1.19	0.828
	45	0.376	0.277	0.576	0.377	0.964	0.632
	60	0.293	0.188	0.473	0.273	0.843	0.501
	90	0.199	0.0992	0.352	0.162	0.703	0.343
	120	0.151	0.0663	0.282	0.116	0.611	0.267
	150	0.121	0.0537	0.228	0.0961	0.513	0.228
p	0	1136	1054	984	931	652	544
	15	0.871	0.834	0.958	0.822	0.950	0.758
	30	0.334	0.345	0.407	0.380	0.480	0.402
	45	0.191	0.194	0.250	0.226	0.328	0.253
	60	0.133	0.117	0.186	0.144	0.268	0.167
	90	0.0767	0.0481	0.121	0.0657	0.204	0.0828
	120	0.0460	0.0265	0.0791	0.0384	0.148	0.0499
	150	0.0219	0.0150	0.0383	0.0214	0.0751	0.0271
π^+	0	1.74	2.16	1.45	2.02	1.00	1.84
	15	0.778	0.760	0.748	0.725	0.625	0.642
	30	0.248	0.224	0.251	0.213	0.225	0.190
	45	0.0947	0.0908	0.0979	0.0873	0.0921	0.0803
	60	0.0444	0.0458	0.0469	0.0444	0.0458	0.0419
	90	0.0157	0.0180	0.0169	0.0177	0.0185	0.0168
	120	0.00880	0.0106	0.00953	0.0104	0.0114	0.00982
	150	0.00583	0.00714	0.00630	0.00686	0.00769	0.00623
π^-	0	1.40	1.40	1.26	1.36	0.980	1.28
	15	0.671	0.600	0.687	0.593	0.648	0.568
	30	0.212	0.197	0.225	0.196	0.227	0.194
	45	0.0802	0.0827	0.0873	0.0835	0.0904	0.0854
	60	0.0374	0.0419	0.0413	0.0427	0.0448	0.0450
	90	0.0135	0.0163	0.0155	0.0167	0.0191	0.0177
	120	0.00785	0.00948	0.00917	0.00960	0.0126	0.00990
	150	0.00529	0.00614	0.00618	0.00604	0.00909	0.00587
γ	0	10.7	21.7	7.23	16.6	2.10	5.57
	15	2.52	2.98	4.54	5.74	3.09	4.70
	30	0.683	0.704	0.950	0.952	1.37	1.57
	45	0.296	0.320	0.333	0.338	0.473	0.516
	60	0.160	0.185	0.168	0.179	0.211	0.225
	90	0.0691	0.0907	0.0722	0.0847	0.0847	0.0856
	120	0.0424	0.0612	0.0455	0.0569	0.0564	0.0532
	150	0.0316	0.0485	0.0342	0.0448	0.0404	0.0359

Figure 7.2: Ratio of integrated fluence between G4 and FLUKA for all particles and materials considered.

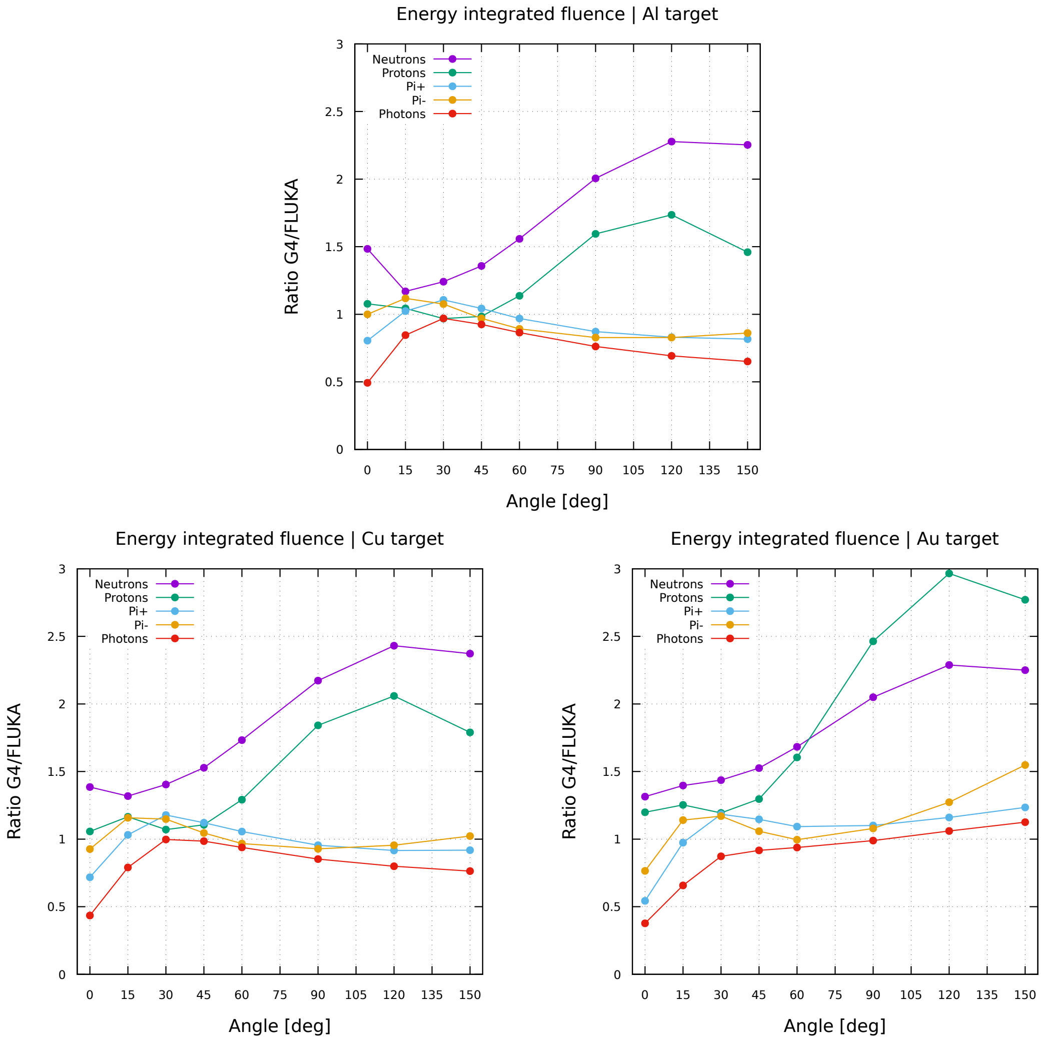

of 2.5 for neutrons (in Cu) and up to 3 for protons (in Au) are evident.

Finally, the copper target results of Item (1) are displayed in Figures [7.3 - 7.7]. Readers interested in the results for other materials can find the remaining plots in the SATIF-15 proceedings [125]. These figures present spectra of neutrons, protons, π^+, π^-, and photons. The previously observed results can be further understood in detail based on the plots shown here.

For charged π, as expected from prior data, both codes are generally in agreement, excepting the spectrum at 0°, where in both π^+ and π^- scenarios, the functional curve shape exhibits a noticeable shift.

For photons, a considerable agreement is observed between both codes, showing an overproduction of photons by FLUKA compared to G4, particularly noticeable at 0°. This was noticed in the

Table 7.3: Average CPU time per primary for each material and code

	FLUKA [s]	G4 (Shielding) [s]
Al	3.0×10^{-3}	3.0×10^{-3}
Cu	6.5×10^{-3}	6.5×10^{-3}
Au	1.75×10^{-2}	3.5×10^{-2}

previous results, indicating, as already said, a tendency in FLUKA to produce more neutral π compared to G4.

The most significant variations appear in the spectra for neutrons and protons. In both cases, as the angle widens, a "shoulder" around 1 GeV emerges, distinguishing the G4 spectrum from FLUKA's. This variance seems rooted in a specific "feature" of G4's physics models; in other MC codes (although not shown in this manuscript), the results align more with FLUKA, without the pronounced "shoulder" at larger angles. The differences in the spectral shapes at 0° are evident, moreover it is particularly striking the peak near 10 GeV in the neutron spectrum, which FLUKA does not exhibit.

To conclude the results of this study, it is crucial to observe the CPU time that was necessary to produce these simulations. Table 7.3 shows the average time required per primary particle transported for each code in the three simulated cases. Similar times are observed for the Al and Cu target cases, but the Au case shows a difference of double the time for G4 compared to FLUKA. While the time seems negligible for transporting each particle, since they are on the order of milliseconds, for the presented results about 10^7 particles were transported, leading to total times ranging from hours to several days. In this case, a difference of double the time may not be dramatic, but under other circumstances, it is by no means negligible.

7.1.2 Conclusions

In this section, the first study carried out with Moira was presented, whose results were shown at an international workshop, SATIF-15.

Although the complexity of the simulation was not such as to justify the existence of Moira, it nonetheless provides an initial taste of the possibilities that Moira offers. The problem does not appear complex, but it may require considerable time for a user to carry out a simulation of these characteristics in any MC code, more particularly with G4. Moira, based on FLUKA input, allowed the results to be obtained automatically through Flair, with identical characteristics and without potential user errors.

Several discrepancies were observed in the reported values, including:

- Higher production of π° in FLUKA compared to G4, inferred from the differences shown in photon generation.

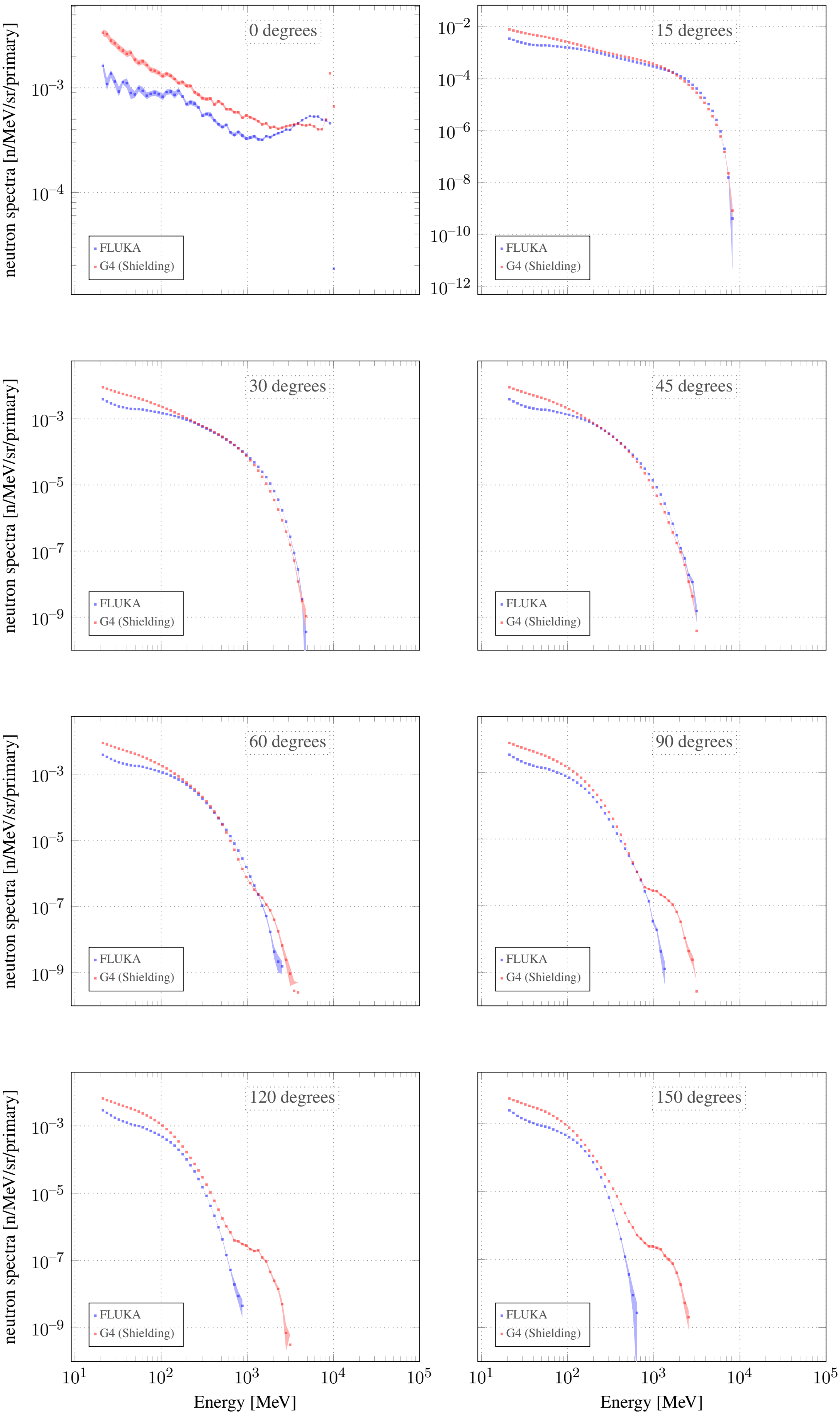

Figure 7.3: Neutron fluence across all considered scattered angles for Cu target case.

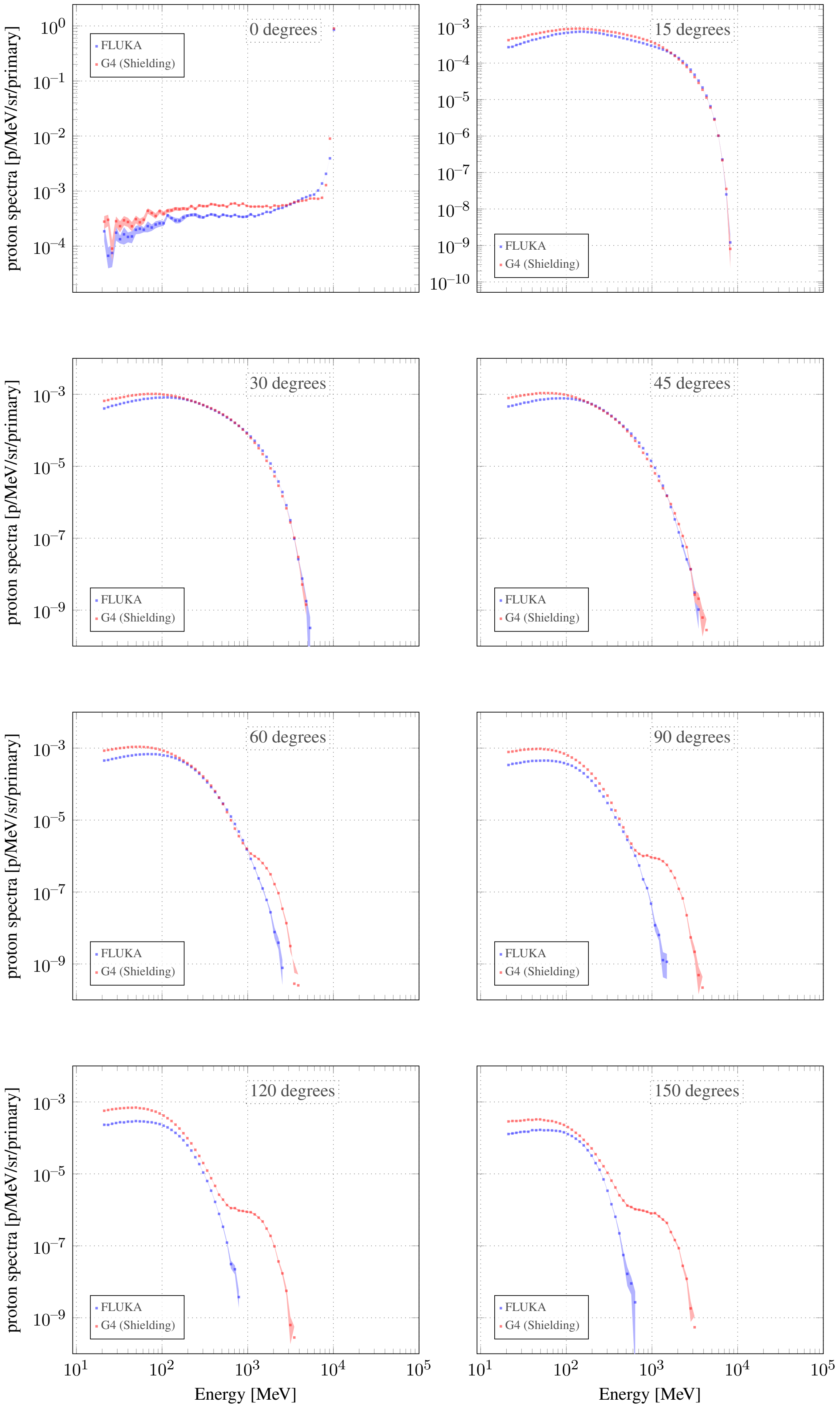

Figure 7.4: Proton fluence across all considered scattered angles for Cu target case.

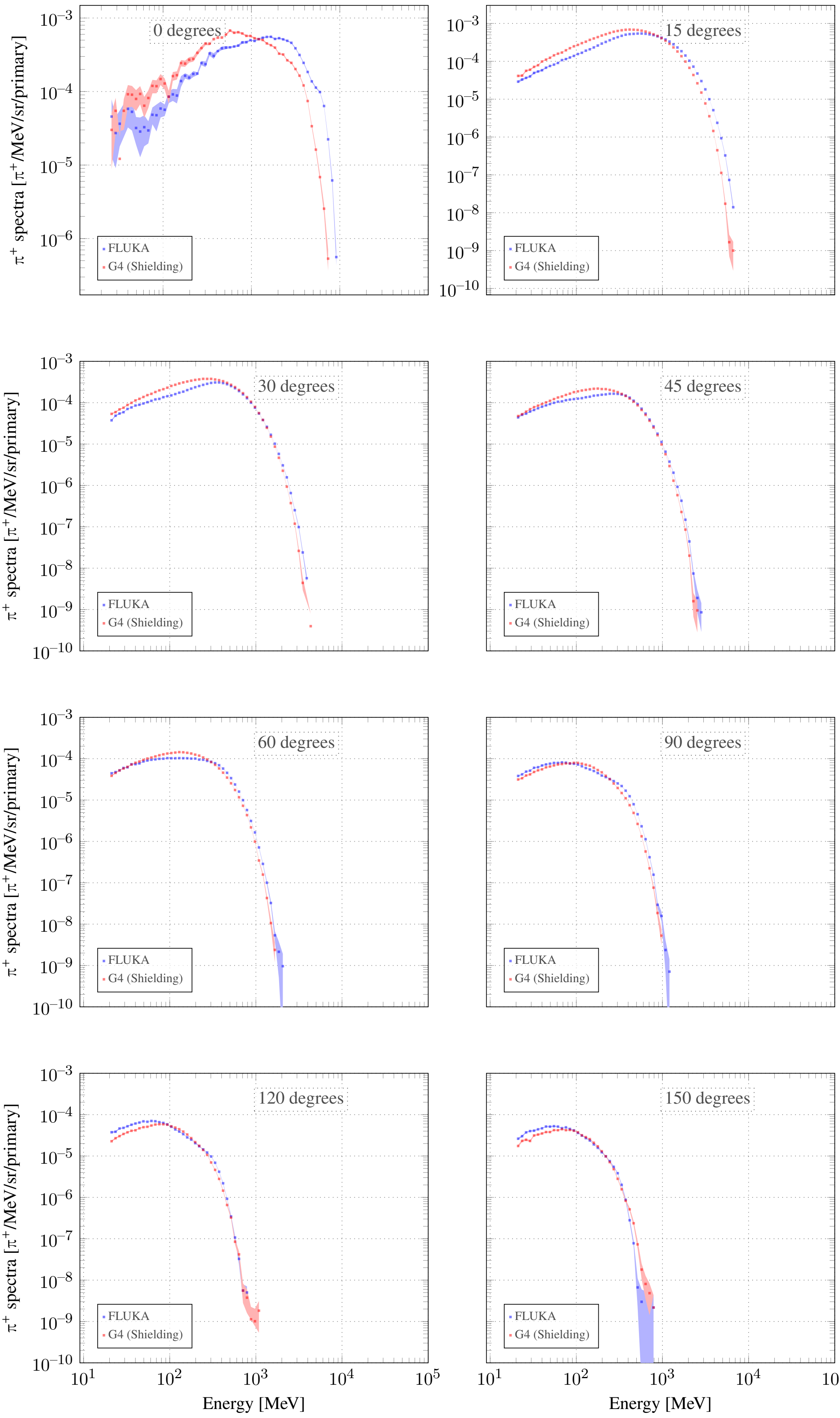

Figure 7.5: π^+ fluence across all considered scattered angles for Cu target case.

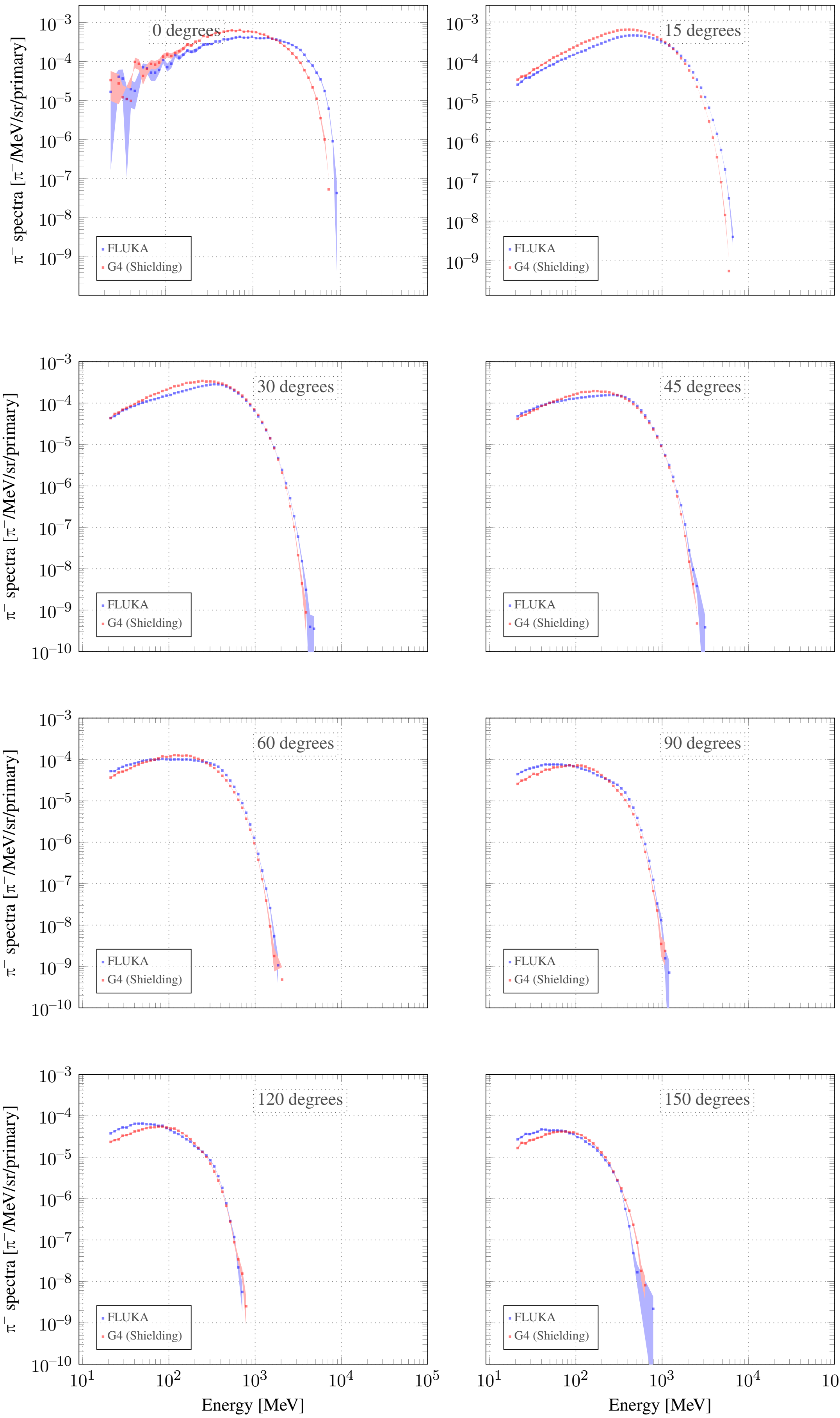

Figure 7.6: π^- fluence across all considered scattered angles for Cu target case.

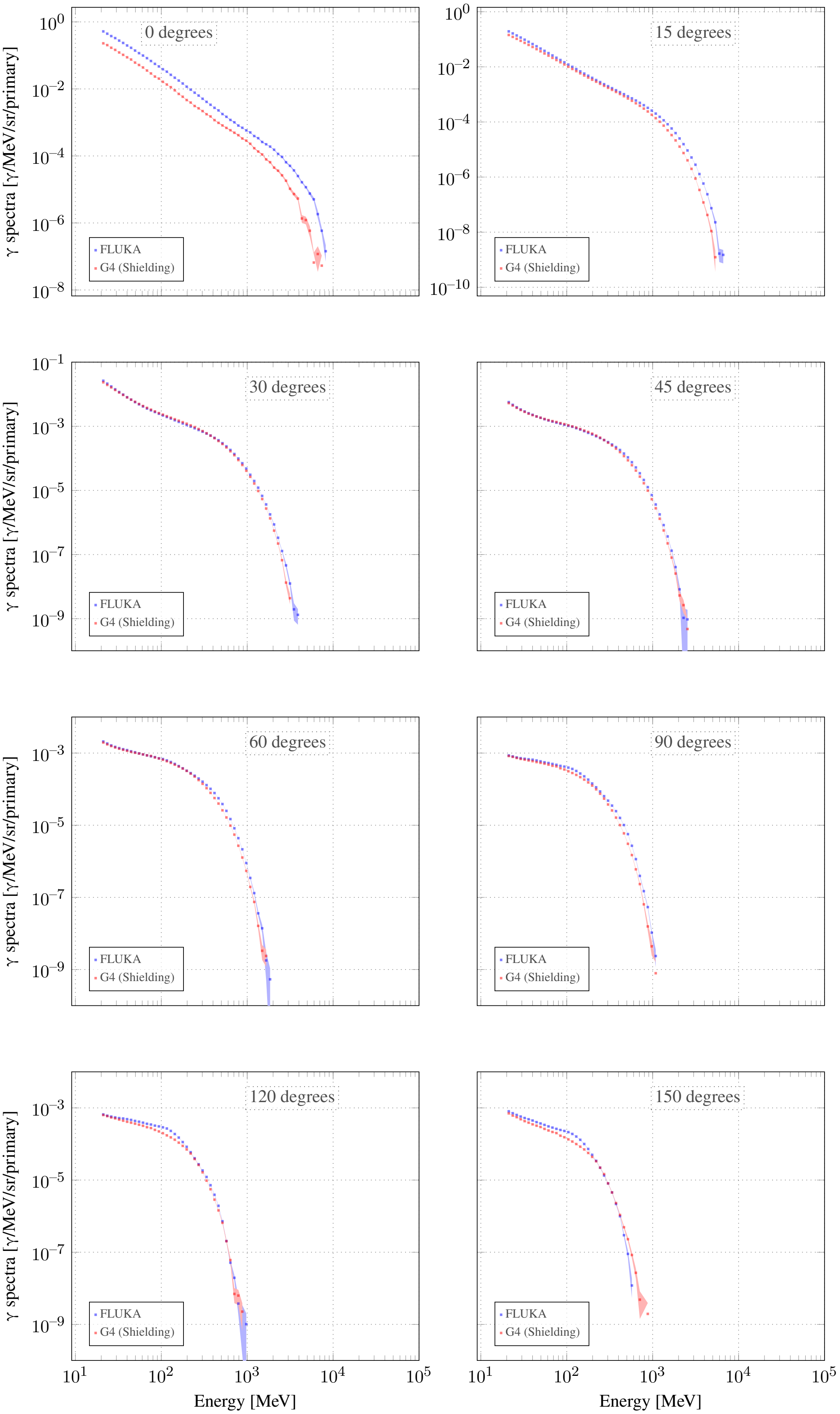

Figure 7.7: γ fluence across all considered scattered angles for Cu target case.

- Notable discrepancies in the production of protons and neutrons in the forward direction. The appearance of a "shoulder" in G4 for large angles in the case of protons and neutrons.

Unfortunately, the findings cannot be contrasted with experimental results, which could give more credibility to one code over another. However, the results exhibit the non negligible differences between codes, and how the systematic uncertainties are expressed by the range of values provided by the MC codes.

7.1.3 Next Steps

- Participation in SATIF-16 [126]: The 16th edition of this workshop will take place at the National Laboratories of Frascati of INFN on May 28-31, 2024. The FLUKA.CERN collaboration has already been contacted to repeat the results shown in this section, again providing simulations made with the latest version of FLUKA at that time and with G4 (Moira).
- Find the source of the "shoulder" in p and n fluence: There might be a doubt that this peculiar behaviour observed in the fluence of protons and neutrons is due to some bug in Moira's code when performing scoring. Although the potential for this to be the case is low since this is not observed in other particles, a way to verify this fact, and at the same time check the proper functioning of Moira, is to perform simulations with the "FLUKA Physics List" presented in Sec. 6.4.9. Being the same hadronic physics of FLUKA v4, if all characteristics of the simulation are equivalent in Moira and FLUKA, the results should also be the same. Therefore, it is a very efficient way to verify any discrepancy in the results, particularly in these studies where there are only inelastic hadronic interactions.

7.1.4 Acknowledgements

The author would like to express sincere gratitude to Dr. Hideo Hirayama for leading this important study and for granting the opportunity to be a part of it. Special thanks are also extended to Vasiliki Kouskoura for her generosity in providing the FLUKA results.

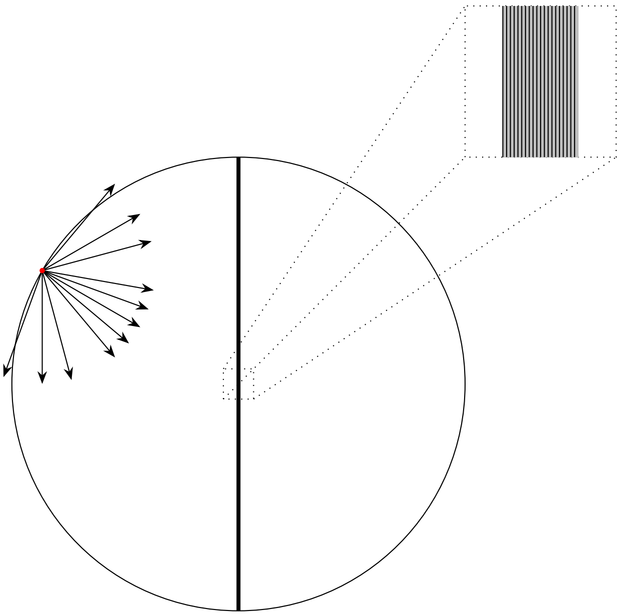

Figure 7.8: Schematic of simulation geometry. In the centre of the sphere the target emulating the space shielding, and a particles emitted from the surface of the sphere is sampled utilising a cosine-law angular distribution. This emission produces an isotropic flux on the target.

7.2 Space-Shielding Radiation Dosage

The NASA Artemis program [127, 128] aims to continue what was initiated decades ago with the Apollo project [IV], i.e., sending astronauts to the lunar surface and establishing a continuous presence on the satellite.

To achieve this mission, numerous studies are being conducted, including understanding the impact of absorbed doses within spacecraft due to radiation in the interstellar medium.

To analyse these radiation levels in early phases of spacecraft design studies, the ShielDose-2 (SD-2) code [129, 130] is widely used. This code calculates the absorbed dose as a function of the thickness of the aluminium shielding protecting the spacecraft, for a given fluence of electrons or protons in the interstellar medium. SD-2 is extensively used by NASA due to its rapid computation capability and reliable results. Despite this, there is a lack of information about SD-2 regarding the range of applicability concerning shielding thickness and result precision.

In response to this situation, at the request of the Artemis program, the NASA Engineering and Safety Centre (NESC) initiated a two-phase study in order to:

1. Better understand and document the capabilities and limitations of the SD-2 code.
2. Recommend alternative tools in case SD-2 cannot be applied.

[IV] The program's name is derived from Artemis, the Greek goddess of the moon and twin sister to Apollo

As part of the findings from Phase 1 [131], it was deemed necessary to conduct a study using multiple MC codes, including FLUKA, G4, MCNP, PHITS, among others, for result comparison. In this manuscript, only the results obtained from FLUKA and G4 (via Moira) will be presented to be compared with the SD-2 results.

The specific problem for this benchmark aims to compare the absorbed dose by an aluminium shielding at different thicknesses represented by multiple layers, for various energies of electrons and protons, with an emission that emulates the conditions of the spacecraft in orbit. In more detail, the specifications of the simulations were as follows:

1. Material: Aluminium.
2. Energies to simulate:
    - Electrons: 0.01, 0.1, 1, and 10 MeV.
    - Protons: 0.1, 1, 10, 100 MeV.
3. Cosine-law source to emulate the isotropic environment.
4. Continuous Slowing Down Approximation (CSDA) ranges values taken from SD-2 (see Table 7.4).
5. Geometry:
    - Disk radius = 100 × CSDA range.
    - Disk thickness:
        - 1.25 × CSDA range for electrons.
        - 1.0 × CSDA range for protons.
6. The number of layers = 50. This means that:
    - One layer thickness for electron cases is 0.025 of the CSDA range
    - One layer thickness for proton cases is 0.02 of the CSDA range
7. Score the energy depositions from electrons and from bremsstrahlung, separately.
8. Normalise the results to a unit incident current ($1\,\mathrm{cm}^{-2}$) of particles crossing into the plane aluminium medium (MeV/g)

Table 7.4: Electron and proton ranges in aluminium used in SD-2.

Electron [MeV]	**Range [g/cm^2]**	**Proton [MeV]**	**Range [g/cm^2]**
0.01	3.54×10^{-4}	0.1	2.63×10^{-4}
0.1	1.87×10^{-2}	1.0	3.95×10^{-3}
1.0	5.55×10^{-1}	10.0	1.71×10^{-1}
10.0	5.86	100.0	1.00×10^{1}

7.2.1 Methodology

The simulation geometry and particle source modelled can be observed in figure 7.8. The approach to achieve an isotropic fluence on the target was carried out by modifying the emission

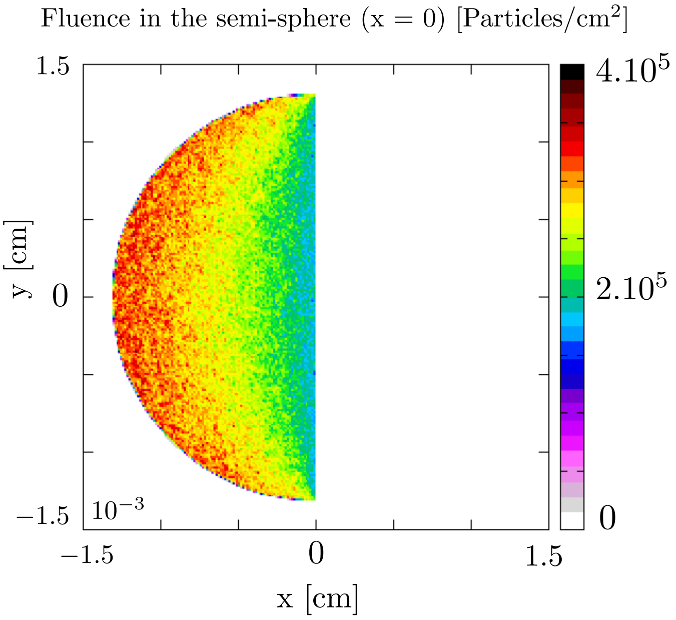

Figure 7.9: Fluence in the semi-sphere (x projection)

of a spherical source with a cosine-law to just half of it, that is, emitting from a semi-sphere. It's not difficult to see that at the centre of the semi-sphere, where the target is located, since the fluence on the sphere at every point was isotropic, it must be isotropic on this plane as well. Figure 7.9 aims to show this fact, displaying the fluence in the semi-sphere. A proof with geometric arguments is presented in the appendix F.

Having presented the emission methodology, the studies for each type of source can now be exhibited.

7.2.2 Results

Electrons Source

Given the requirement to distinguish between the dose due to electrons and the dose due to bremsstrahlung, it is necessary to define correctly what each case refers to and how the results were obtained:

- Electrons with bremsstrahlung (Case 0): This is the default case. No modifications or biasing are applied to obtain this result. Here, the absorbed dose by aluminium will include contributions from all generated particles.
- Electrons without bremsstrahlung (Case 1): In this situation, during the simulation, when a photon is generated, it is discarded. Information about the photon (energy, position, direction) is stored in an output file, and its energy is not considered when discarding it.
- Bremsstrahlung (Case 2): Using the photon dumped obtained in Case 1, these particles are

> simulated, and all secondary particles that are generated are also considered to be due to bremsstrahlung. It is important to note that the weight of these photons had to be adjusted so that their contribution aligns with the simulation carried out in Case 1, i.e., the results are normalised by electrons on the aluminium target.

Figure 7.11 displays these three results overlaid in four plots (except for energies of 0.01 MeV where the photons generation was very low) for FLUKA, G4 (via Moira), and SD-2.

Firstly, the results make sense considering the physics of the problem. The stopping power of electrons in aluminium (see Fig. 7.10) explains why at lower energies the energy deposition is higher, resulting in less variation for photons with higher energies in the first aluminium layers (almost constant stopping power), and a significant increase in photon generation. This is more evident due to the statistical improvement as energy increases. Additionally, the contribution of dose from photon generation due to bremsstrahlung is clearly observed, matching almost perfectly among the three study cases for deeper layers. Regarding the study's purpose, FLUKA and G4 show a significant agreement in all three simulations and for all four considered energies. Meanwhile, SD-2 demonstrates notable results, although the range of applicability is slightly lower than the one obtained with the MC codes. SD-2's results stand out considering the difference in computation time compared to FLUKA and G4, where the first provides results immediately, and the others, as observed in Table 7.5, taking into account that 10^7 of particles where transported to reach the observed statistical uncertainties in the results, it can require CPU times going up to several hours or even days.

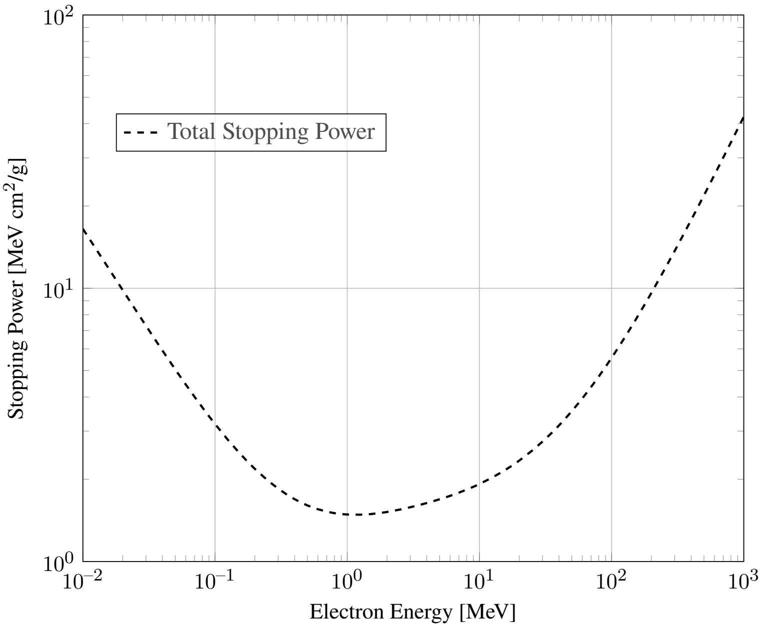

Figure 7.10: Total stopping power of electrons in aluminium. Data courtesy of NIST-ESTAR database [14]

Lastly, a more in-depth analysis is needed to understand why, at 0.1 MeV, G4's results do not seem to match the bremsstrahlung dose and total dose that well. Additionally, the reason for the bremsstrahlung statistics being lower than FLUKA's results needs to be investigated.

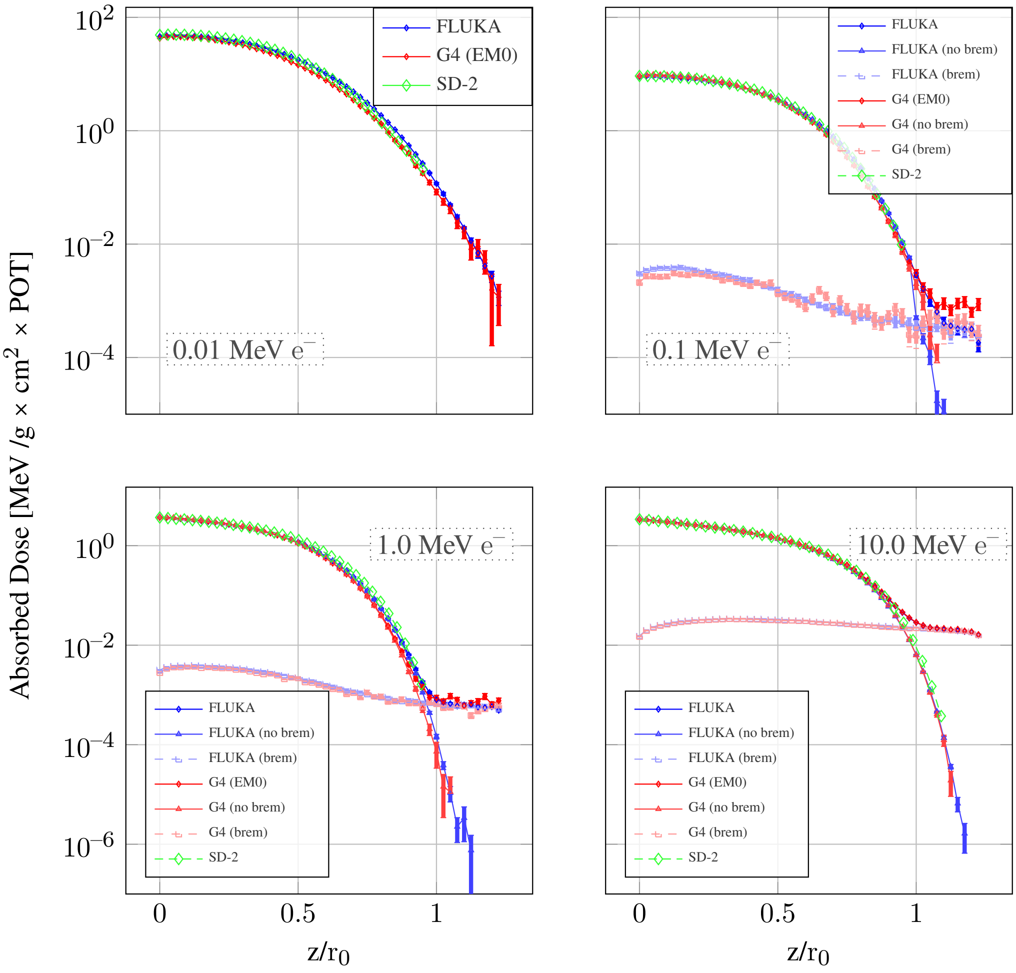

Figure 7.11: Absorbed dose in electron source case vs distance normalised by the CSDA range for each energy (r_0).

Table 7.5: Average CPU time per primary for each electron energy and MC code.

	FLUKA [s]	G4 (FTFP_BERT-EM0) [s]
0.01 MeV	3.5×10^{-4}	1.3×10^{-4}
0.1 MeV	9.0×10^{-4}	2.5×10^{-4}
1.0 MeV	4.3×10^{-3}	4.3×10^{-4}
10.0 MeV	3.2×10^{-2}	3.5×10^{-3}

Protons Source

In this case, bremsstrahlung is not considered. Therefore, the results only account for the dose due to the proton source and all secondary particles generated by their transport through the layers of aluminium, i.e. only the case 0 from the previous study. The results are presented in Figure 7.13.

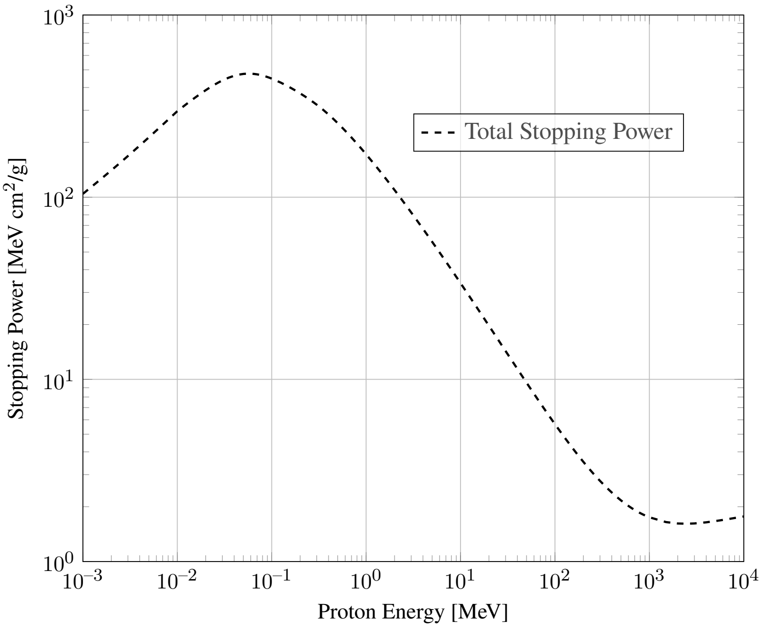

Figure 7.12: Total stopping power of protons in aluminium. Data courtesy of NIST-PSTAR database [14]

Similar to the results with electrons, the obtained outcomes are physically reasonable when considering the stopping power of protons in aluminium (see Fig. 7.12), where there is a peak near 0.1 MeV of energy and a gradual decrease down to 1 GeV. Once again, the improvement in agreement between codes at higher energies is noteworthy. Particularly interesting is the observation that at 0.1 MeV, G4 exhibits a sudden decrease in dose beyond the layer of 0.7.

The following points should be taken into consideration:

- Neither FLUKA nor G4 were used in the proton simulations with a single-scattering treatment for charged particles. This could explain all or part of why the results at 1 MeV, and especially 0.1 MeV, show worse "performance".
- In the G4 simulations, the default electromagnetic package (EM0) was used. As explained in the previous point, this package lacks single-scattering for energies below 100 MeV and also provides relatively lower precision compared to other packages, such as EMZ, Penelope, Livermore.

Once again, the performance of SD-2 is remarkable, showing great agreement (particularly with FLUKA) over a range that practically covers up to the last aluminium layer, perhaps with slightly less precision in the last layers. This could be valid to state, as the explanation provided earlier requires simulations with FLUKA and G4 using the single-scattering treatment to gain deeper insight into the reasons for these discrepancies. Nevertheless, SD-2 demonstrates noteworthy results, considering again CPU time required (see Table 7.6), and consistent with what has been observed in these studies, proving to be a powerful tool for conducting preliminary studies for space shielding applications. Concluding this section, it is interesting to observe the differences in CPU time between FLUKA and G4 in the already mentioned Tables 7.5 & 7.6. These results expose faster simulations in FLUKA for the cases with lower energies, while the other three cases G4 required much less time, being differences of one order of magnitude in some cases.

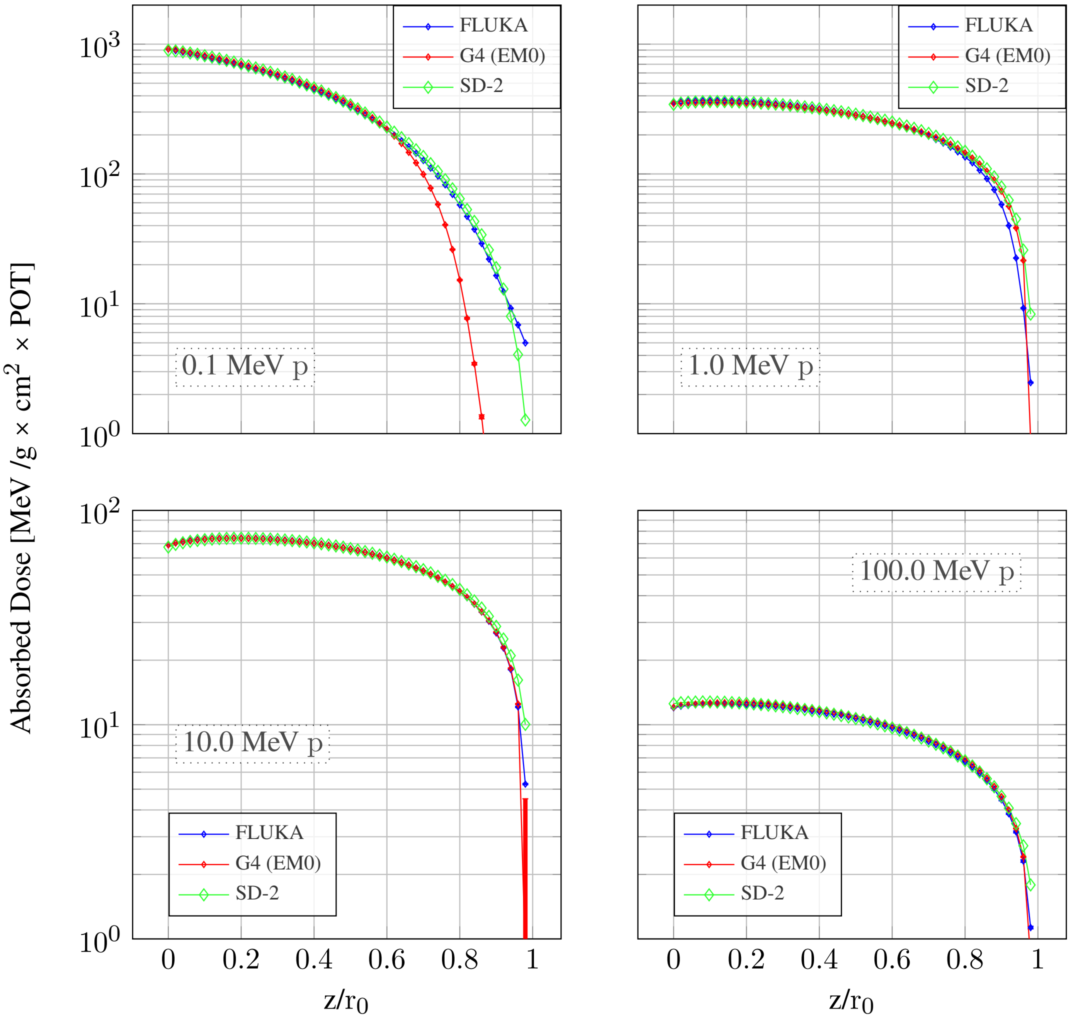

Figure 7.13: Absorbed dose in proton source case vs distance normalised by the CSDA range for each energy (r_0).

Table 7.6: Average CPU time per primary for each proton energy and MC code.

	FLUKA [s]	G4 (FTFP_BERT-EM0) [s]
0.1 MeV	5.5×10^{-5}	1.0×10^{-4}
1.0 MeV	9.0×10^{-4}	2.5×10^{-4}
10.0 MeV	5.0×10^{-2}	2.0×10^{-3}
100.0 MeV	4.5×10^{-1}	1.5×10^{-2}

7.2.3 Conclusions

As in the SATIF-15 simulations presented in the previous section, the characteristics of this study may not justify the creation of Moira, in the same way, it again demonstrates the powerful tool it is for potentially centralising these types of comparisons between MC codes, greatly facilitating obtaining these results. Regarding the results obtained in the different studies:

- A great performance of SD-2 is observed considering CPU time and the results compared to what was obtained with the MC codes, although there were certain discrepancies mainly in deeper layers of the shielding. In any case, SD-2 proves to be a great tool for obtaining first estimates of shielding space dosage.
- About FLUKA-G4, generally good agreement was obtained between both codes, except in the results of protons at low energies. Complementary studies using electromagnetic models in G4 that include single-scattering could show if this treatment is necessary to reduce these differences.

7.2.4 Next Steps

- Extending the energy range of the simulations is in process to obtain results at 5 keV of energy for electrons and 10 keV for protons. This will allow for a more extensive comparison in the energy range that showed lower performance.
- At the same time, the realisation of the same simulations already carried out with aluminium, but with two other materials that SD-2 allows to obtain results: Teflon and z93-paint [132].

7.2.5 Acknowledgements

Big gratitude to Insoo Juu and the Artemis project for allowing me to be part of these studies. Also, many thanks to Ruben Garcia Alia for entrusting me with this task, and a big apology for not being able to fully complete the last phase. Finally, big thanks to Francesc Salvat Pujol for all the insightful discussions and for taking care, along with Stefano Marin, of the last phase of these studies.

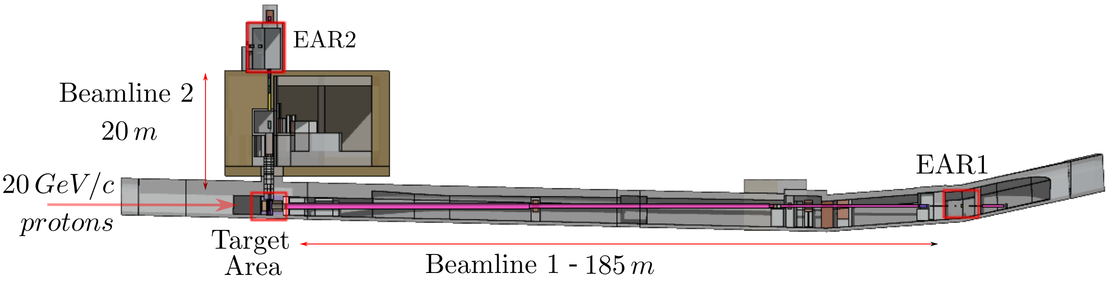

Figure 7.14: Flair image showcasting side view of n_TOF facility

7.3 Neutron Flux Benchmark in EAR1 at the Neutron Time of Flight Facility

From this point to the end of this chapter, the results presented already have a more novel character. The geometries used in all cases are so complex that for a G4 user, it would necessarily demand a time frame that could reach years to be completed. Moira provides the opportunity to obtain input almost instantly, with an **equivalent** simulation in terms of geometry, transport, production cuts, magnetic fields, scoring, and more. The only difference between simulations are the physical models used in each case.

It is worth starting with an introduction to the Neutron Time of Flight facility (n_TOF) [133]. This facility is located at the CERN laboratory. Its main function is to measure the cross-sections of neutron-induced reactions for various samples of interest, covering an energy range from meV to GeV. The facility underwent a series of improvements and expansions since its construction in 2000, leading to the current situation that can be seen in the Figure 7.14. In this figure, three main regions can be observed:

- The neutron spallation target: n_TOF is powered by the Proton Synchrotron, delivering pulses of up to 10^{13} protons at a momentum of 20 GeV/c. These protons impact on a lead target, from which, through the spallation mechanism and the use of various moderators, neutrons in the aforementioned energy range are obtained.
- Experimental area 1 (EAR1) [134]: As the name suggests, this was the first experimental area built at the facility. It is located at the same depth as the target, after approximately 185 m of beamline, occupying an area with a length of about 8 m. Depending on the measurement of interest, various detectors are used to study the different reactions produced by neutrons in the sample.
- Experimental area 2 (EAR2) [135]: After more than a decade of unprecedented measurements of cross-sections, this new area was built, located 20 m above the lead target. This extension aimed to increase the neutron flux from spallation, allowing the use of low-mass samples (less than mg), as well as highly radioactive samples and/or samples with very small cross-sections.

The construction and eventual changes to n_TOF have always been accompanied by studies conducted with MC simulations. These aim to determine the characteristics of the neutron beam generated in the facility, whose information is crucial when planning experiments.

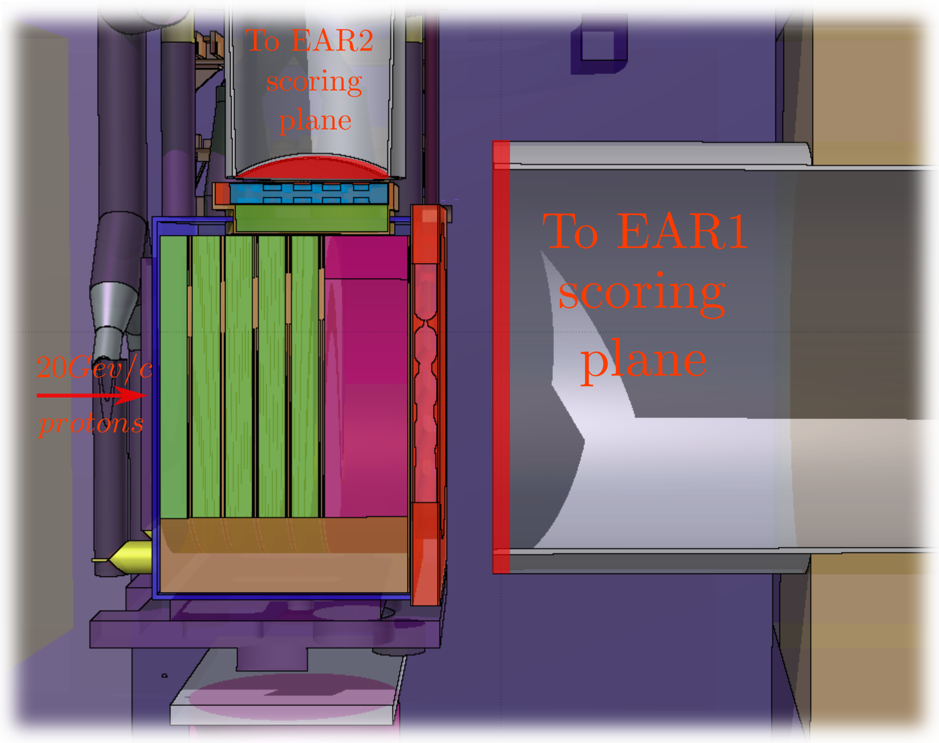

Figure 7.15: n_TOF's Target area. Scoring planes to EAR1 and EAR2 are displayed.

The facility's geometry was developed from the beginning in the FLUKA format, reaching a high level of detail. It was updated over the years in response to upgrades. For simulations, before the implementation of the point-wise treatment, neutrons were transported with FLUKA at energies greater than 20 MeV. Below this energy, neutron transport was handled by MCNP, as its performance with point-wise treatment was superior compared to FLUKA's group-wise treatment [136].

G4 was also the other code used. Although with less detailed geometry than FLUKA, MC simulations involving EAR2 were performed, obtaining results in good agreement with the FLUKA-MCNP coupling [137]. The results that will be presented in this section seek to continue what was done with G4, for the n_TOF phase 4 [138].

The results to be presented aim to benchmark the neutron flux in EAR1, showing what was obtained with FLUKA using the novel point-wise treatment, Moira with multiple physics lists incorporated the thermal neutrons treatment (registering G4ThermalNeutrons), and experimental results [139].

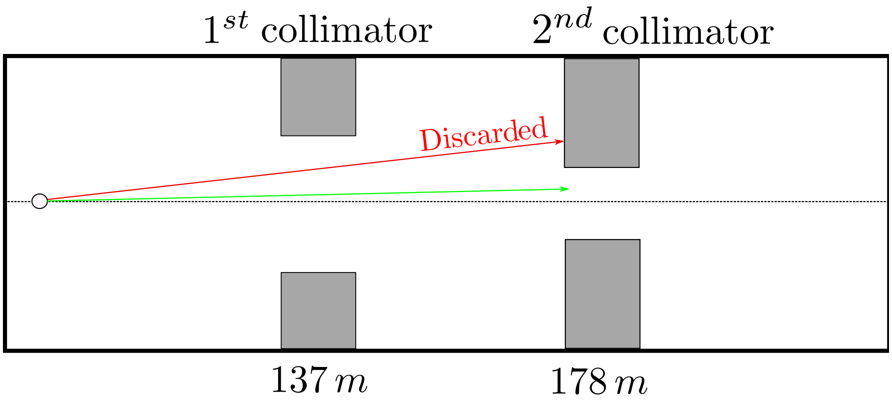

Figure 7.16: Simplified schematic of neutron optics transport from target area to EAR1.

In this context, the "Neutron Flux" will be defined as the number of neutrons integrated over the total spatial profile of the beam reaching the experimental area.

7.3.1 Simulation Methodology

The simulations to obtain the particle flux in both experimental areas (although only EAR 1 will be presented in this manuscript) were carried out in two steps:

1. Neutron generation: The first step was based on transporting the particles in the target area geometry using MC codes. In each simulation, where both FLUKA and G4 were included, a 20 GeV/c proton beam (PS beam) was used, producing the desired neutrons through spallation process in the lead target. The neutrons were transported until they reached one of the two regions shown in figure 7.15. Upon reaching one of these regions, the neutron's transport was stopped, with its position, energy, time, weight, and direction stored for use in the subsequent step.
2. Optics transport to EARs: The stored information was used to transport the neutrons heading to EAR1 or EAR2, depending on whether they reached scoring plane 1 or 2. If one had wanted to carry out the full transport with an MC code to one of the experimental areas, the required time would have been much longer [V]. Therefore, with this information, an optical transport with a dedicated software [136] was performed from the scoring plane to the corresponding experimental area. Oversimplifying the picture, this transport essentially propagates the neutrons in a straight line, depending on their initial direction. Additionally, the low energetic ones are influenced by the gravity, following a parabolic path. As figure 7.16 shows, neutrons intercepted by a collimator are discarded, while the remaining ones are used to calculate the final neutron flux in the experimental area, with EAR1 shown in figure 7.17.

[V] Each particle bunch comprises 10^{13} particles, typically resulting in the generation of approximately 300 neutrons per proton. Being 10^{6} the average number of neutrons arriving in EAR1, there is factor 8-9 of difference!.

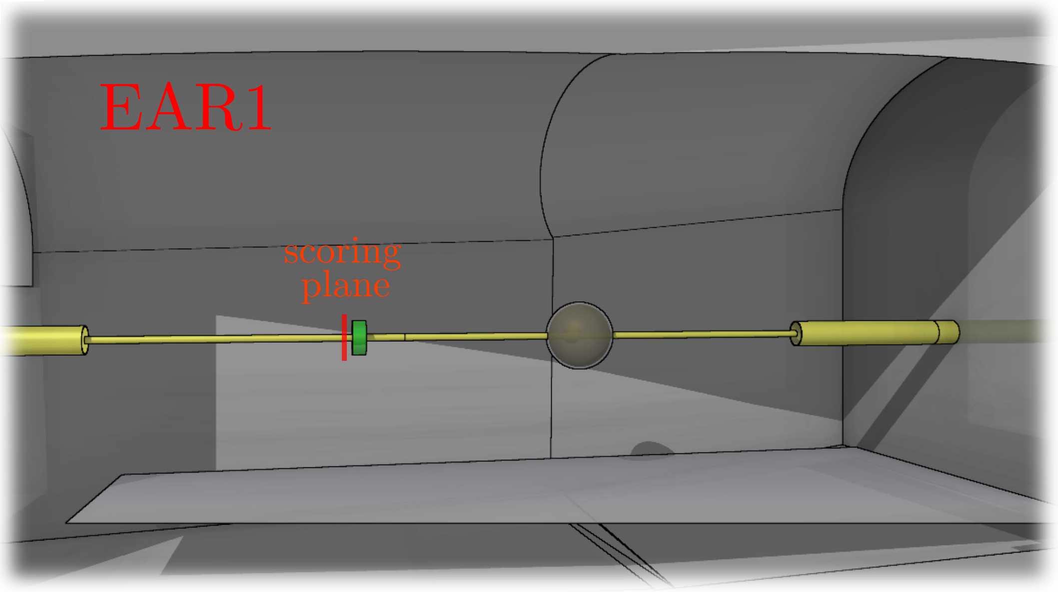

Figure 7.17: n_TOF experimental area 1, exhibiting the plane where neutron flux scoring/measurement occurs

7.3.2 Results

The neutron flux in EAR1 and their counts at the target area's scoring plane, as shown in figures 7.18 and 7.19 respectively, reveal a generally reasonable alignment between the various results. Variations in estimation, over or under, are noted, particularly at medium energy levels [1 - 10^7] eV, being the cascade models the ones that produce these differentiations. The BERT cascade tends to overestimate flux by 20%, while BIC cascade and FLUKA models align more closely with experimental data. The Liege cascade (INCLXX), however, underestimates by about 20%. All simulations successfully replicate the dips due to neutron-aluminium interactions in the beamline.

In the [10^{-2} - 1] eV range, FLUKA closely matches experimental data, while all G4 simulations exhibit similar results. It is also observed in the neutrons counts, where all the models have a similar cruve, until ≈ 2.10^{-1} eV, where the thermal neutrons treatments produces significant deviations, with great increase of counts in G4 and a peak shift to ≈ 5.10^{-2} eV compared to FLUKA's 7.10^{-2} eV. This results indicated major differences in the thermal neutrons treatment or potential definition deficiencies in the moderator material (e.g. Boron-10 concentration) of the n_TOF target.

At higher energies [10^7 - 10^9] eV, BERT and BIC models demonstrate superior performance. In contrast, FLUKA and INCLXX, especially between [10^7 - 2.10^8] eV, show significant deviations from experimental findings. These differences underscore the variability inherent in model-based studies. The target's scoring plane counts reflect a functional curve shape similar to EAR1's final flux, indicating that these outcomes are predominantly influenced by the chosen cascade models.

FLUKA [s]	FBERT[s]	QBERT[s]	QBIC[s]	FINCLXX[s]	QINCLXX[s]
0.5	12	11	11	9	8

Table 7.7: Average primary particles transport time per model in EAR1 n_TOF study

Finally, Table 7.7 reveals a much lower performance in average time for transporting a primary from G4, being around 20 times slower than FLUKA. Since the main interest of these simulations were related to neutron transport, it is easy to presume that the reason might be coming from the HP treatment, but more investigation is required to a conclusive argument.

7.3.3 Conclusion

This study served as the perfect opportunity to demonstrate Moira's ability to produce relevant results in scenarios with highly complex geometries. The neutron flux results highlighted the necessity of conducting simulations using multiple codes or physical models, as they yield diverse values with varying performances depending on factors such as the energy range. The data obtained from the simulations provide a degree of confidence regarding the range of real flux values that will be observed in n_TOF samples, as evidenced when compared to experimental measurements.

Regarding Moira's performance, its capability to support users requiring simulations with complex geometric inputs from FLUKA is noteworthy. However, a detailed analysis of the reason behind the high CPU time required for these simulations is necessary.

7.3.4 Next steps

- Performing these simulations with the FLUKA physics lists would provide another interesting comparison, which should agree with FLUKA at high energies (> 20 MeV), but follow the trends of G4 at low energies.
- The integration of FLUKA's point-wise treatment into Moira is expected. This new addition is highly significant, not only for the future generation of FLUKA.CERN, but also because it should potentially improve the results in G4 for low energies, and radically reduce the CPU time for simulations.

7.3.5 Acknowledgements

Practically the entire credit for these simulations and their subsequent analysis is given to Jose Antonio Pavon Rodriguez. The author of this manuscript contributed mainly in the conversion of the input, the generation of the scoring, and the addition of the treatment of thermal neutrons in G4. Thus, total thanks to Jose and his supervisors, Marta Sabate Gilarte and Jose Antonio Cortes Giraldo, and the n_TOF collaboration, for giving me the opportunity to contribute to this study.

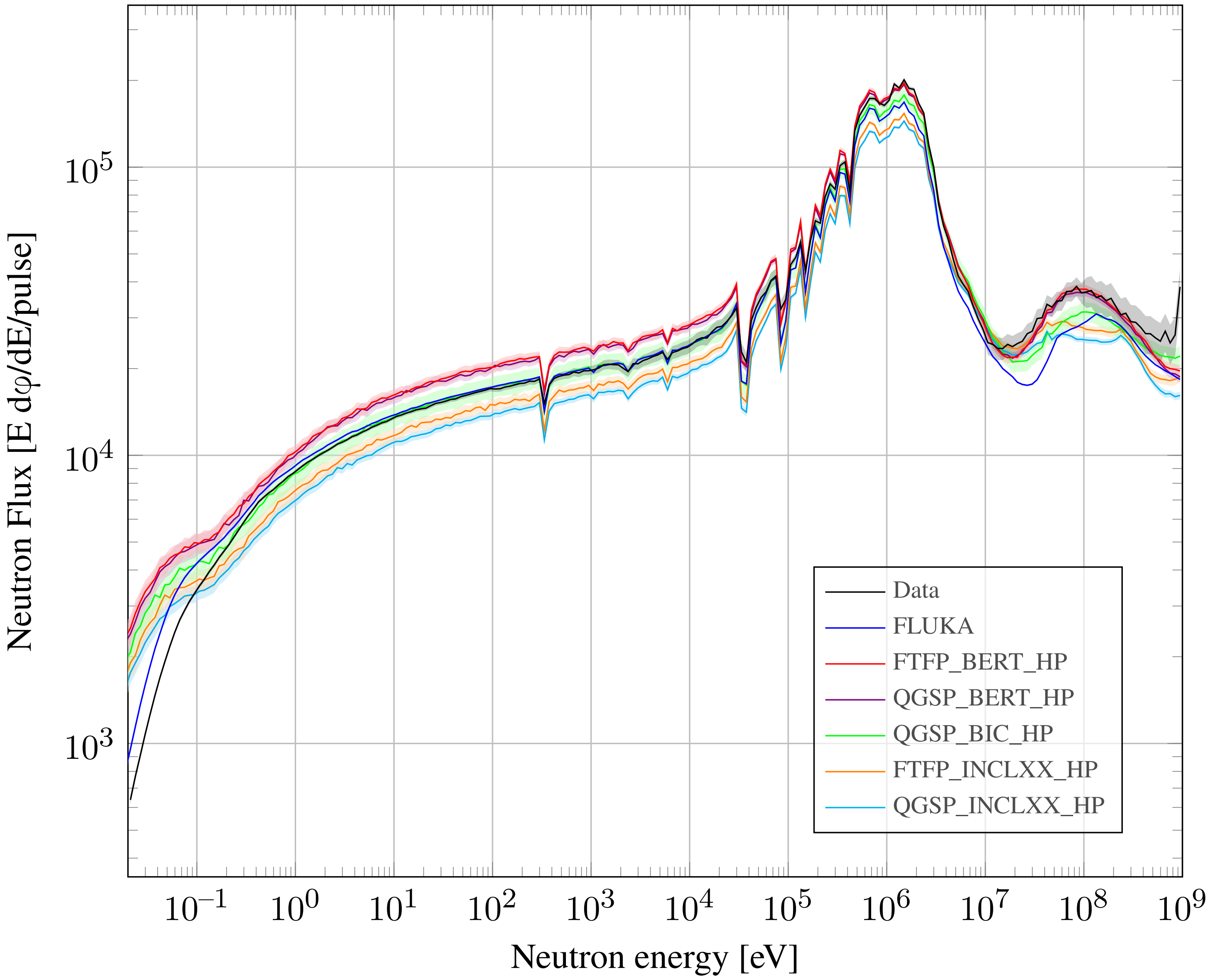

Figure 7.18: Neutron fluxes in EAR1 n_TOF

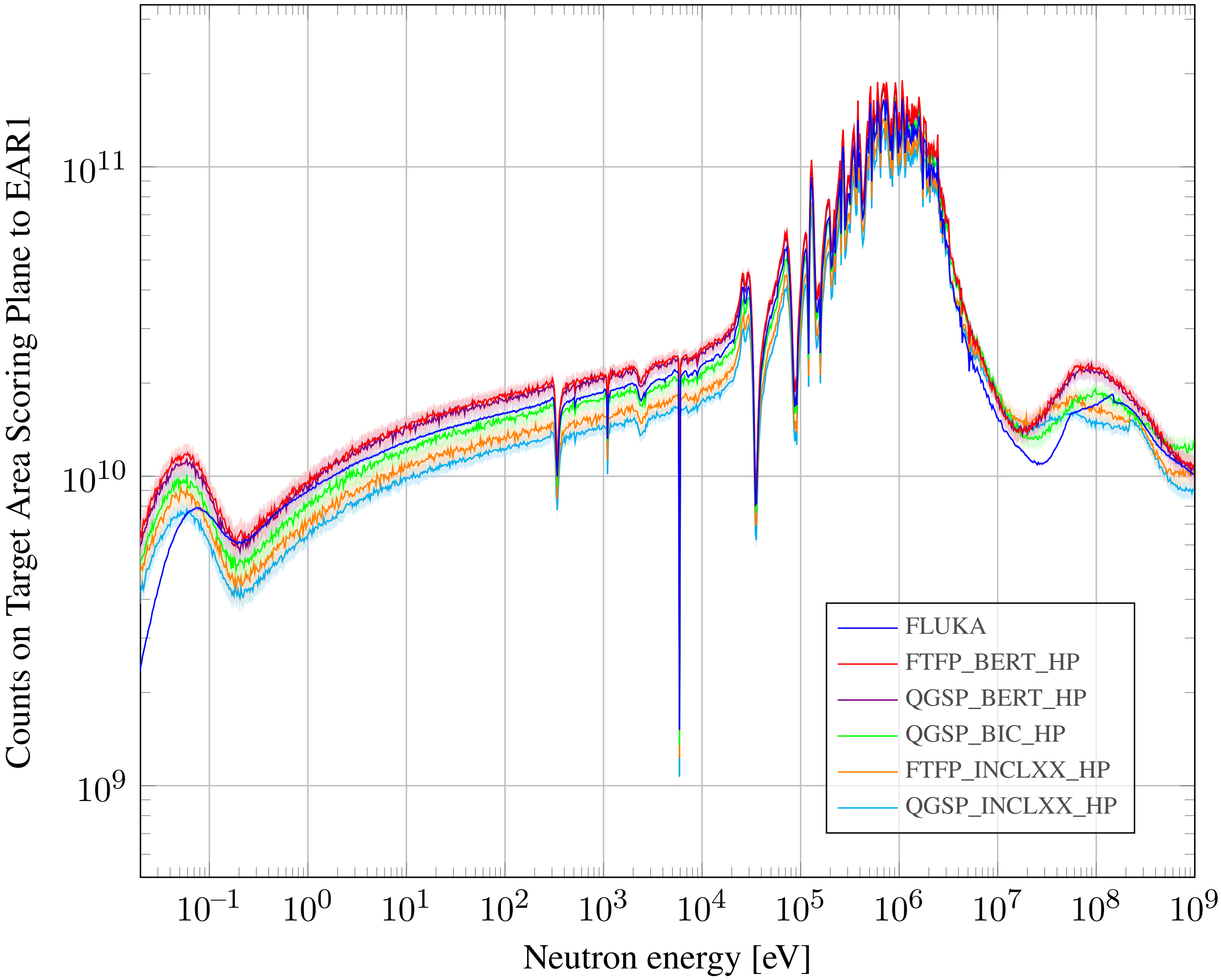

Figure 7.19: Counts in target scoring plane to EAR1

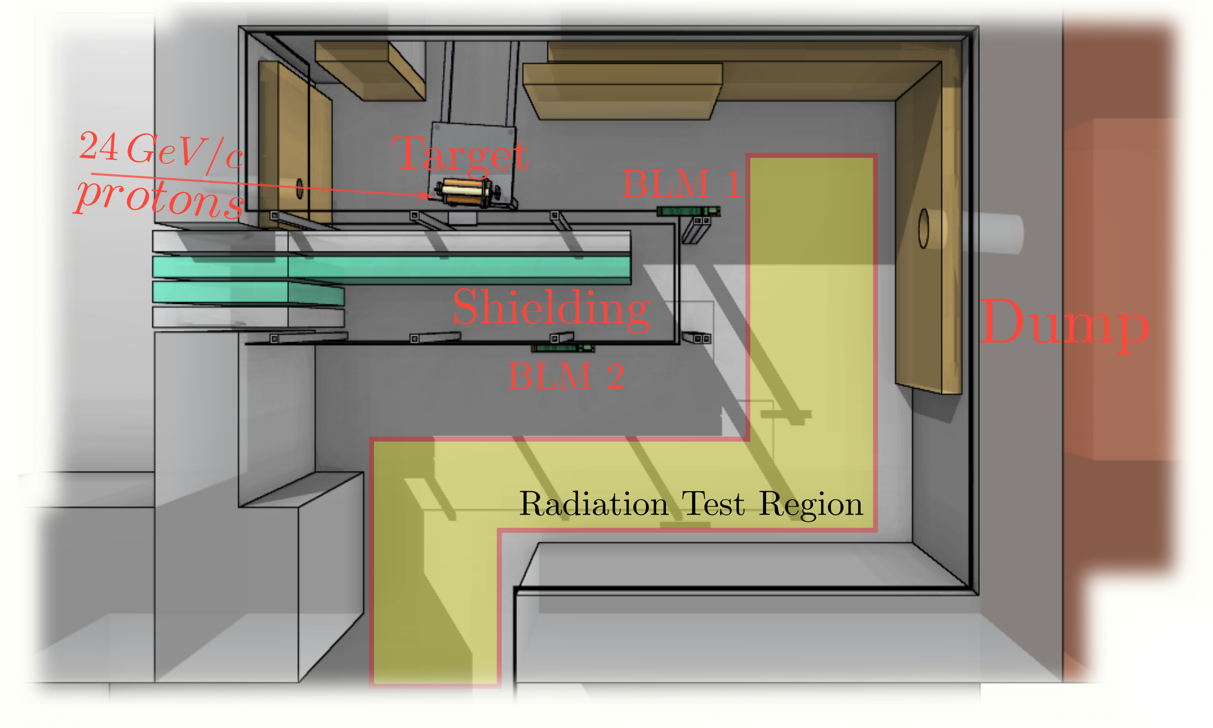

Figure 7.20: CHARM facility experimental area

7.4 Systematic Error Estimation through BLM Benchmark at the CHARM Facility

In the previous section, where the n_TOF facility was studied, the impact that Moira can have on the field of MC simulations for radiation transport was demonstrated. The geometry modelling of the mentioned facility was done for FLUKA with a high level of detail, which took several years to develop. Attempting to emulate this with G4 would require a similar amount of time, and there would be no guarantee that the geometry achieved would be identical to that created in FLUKA. Moira, through the use of the Flair interface, not only allows for the automatic generation of this input but also provides simulations with a level of fidelity that is difficult to match. Continuing along this line of complex geometries, although somewhat smaller than that of n_TOF, this section will complement a study carried out by Daniel Prelipcean at the CHARM facility [140, 141], characterising the systematic error of the simulation results through the benchmark with BLMs measurements.

7.4.1 Description of the CHARM Facility

CHARM [142, 143] is a flexible irradiation infrastructure designed to test electronics and systems in a carefully characterised mixed radiation field. This facility is unique in its ability to replicate

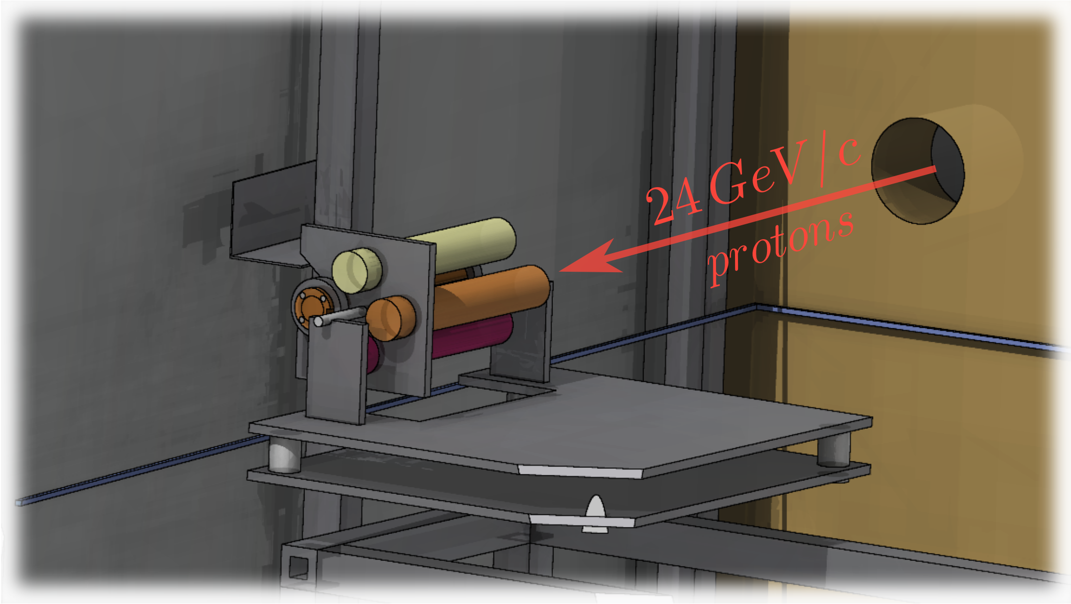

Figure 7.21: CHARM target table.

controlled environments such as space, the atmosphere, or complex accelerator setups.

Figure 7.20 provides an overhead view of CHARM. Protons at 24 GeV/c, supplied by the CERN PS accelerator, impact one of three possible target materials:

- Copper (Cu).
- Aluminium (Al).
- Aluminium with holes[VI] (Al_h).

These materials were selected due to their different densities, which have a direct effect on the generated radiation. The target consists of a 50 cm long cylinder with a diameter of 8 cm (fig. 7.21).

Another important factor contributing to radiation in the area is the shielding configuration, consisting of four movable blocks with dimensions of $20 \times 214 \times 350\,\mathrm{cm}^3$. These blocks are placed between the target and various test locations and can be combined in different ways. The outer blocks are made of concrete (C), and the inner blocks are made of stainless steel (S).

To properly define each configuration (target and shielding), an acronym is used, defined by the combination of both, i.e., [material][shielding], where:

- material: Cu, Al, Alh.
- shielding: Four characters (each of which will be "C," "S," or "O" to refer to the absence of

---

[VI] Aluminium with half density

shielding) defined based on the distance of the block from the target.

For example, the configuration shown in figure 7.20 is specified as CuCSOO, indicating that the target is copper, and the shielding blocks are used as follows:

1. Concrete
2. Stainless Steel
3. (empty)
4. (empty)

The figure also shows the test positions and the two BLMs used for the presented comparisons. BLM1 is highly irradiated because it is situated in an area where it is not protected by the shielding blocks. In contrast, the level of irradiation of BLM2 will depend on the shielding utilised due to its position. However, as will be observed, this BLM is always less irradiated than BLM1 for each shielding configuration.

7.4.2 Simulations for BLMs systematic errors estimation

The simulations conducted in this section are based on assessing the systematic errors of each simulation of each physics packages doing a BLM benchmarks for the two BLMs included in CHARM, using multiple shielding and target configurations. These selections were made due to the availability of experimental results obtained during the period of 2015-2018.

The methodology utilised to obtain this estimation is simply based in calculating the ratio between simulations and measurement for each configuration. Finally, by averaging all these ratios for each material, a systematic error can be estimated for the physics package.

7.4.3 Results

The figure 7.22 shows comparisons of BLM1 and BLM2 for various shielding configurations.

It is evident, and observed in both BLMs, that the absorbed dose depends on the material of the target. The dose decreases as a function of density, noting this fact in both measurements and all the simulations carried out.

Regarding the different shielding configurations, a noticeable decline in the dose is observed, with BLM1 showing a relatively constant dose. As previously mentioned, this BLM is positioned where the impact of the protection is almost insignificant. A potential increase in the dose in cases with protection could be explained by the possibility of back-scatter due to the shielding blocks.

When comparing the results, the relationships between FLUKA and G4 in BLM1 indicate that FLUKA tends to consistently overestimate the dose by approximately 20-30% compared to G4. The results from G4 show behaviour similar to that of FLUKA and the data, not exceeding in

Table 7.8: BLM Ratios (Data/Sim.) Average

	FLUKA	FBERT	QBERT	QBIC	QINCLXX	FINCLXX
			BLM1			
Cu	1.00	1.11	1.17	1.19	1.01	1.03
Al	1.17	1.19	1.42	1.45	1.09	1.34
Al_h	0.68	0.72	0.94	0.95	0.70	0.89
			BLM2			
Cu	0.79	0.80	0.84	0.92	0.94	0.98
Al	0.79	0.93	1.01	1.16	1.08	1.39
Al_h	0.59	0.63	0.70	0.80	0.71	1.00

most of them a difference of 50% between Moira-Data and Moira-FLUKA. Among the G4 models, there is a tendency, also observed in the upcoming sections, for the FTFP string model to produce more dose in the BLMs compared to QGSP. This is more clearly observed in BLM1, where the incidence of cascade models is reduced due to minimal transport of particles after the inelastic interaction in the target. This is evident from the ratios between these models of 30-40%, indicating greater agreement between FLUKA and FTFP physics lists.

Although a tendency of all simulations to closely align with the measurements is observed, there are certain specific cases that merit attention. The BLM2-CuOOOC shows a peculiar result. As expected, with a shielding block between the target and the detector, a reduction in the absorbed dose is observed in the measurements. However, this is not replicated in any of the simulations. In fact, there appears to be no reduction (or increase) in the dose, as if the shielding had no impact. This suggests that, since this result is consistent across all models, there might be a deficiency in the definition of the geometry/material, possibly involving errors in the definition/position of the shielding/target/BLM, among many other possibilities. It is certain that this problem also influences other results where the last shielding block is used. The most evident cases are BLM2-CuCSSC, where there is an increase in the dose in most simulations compared to the case with less shielding CuCSSO.

Table 7.9: Sysmatic error estimation for each physics package and material

	FLUKA	FBERT	QBERT	QBIC	QINCLXX	FINCLXX
Cu	20%	20%	25%	20%	10%	10%
Al	20%	20%	45%	45%	10%	40%
Al_h	40%	30%	20%	20%	30%	15%

Based on the obtained simulations, it is possible to estimate a value of the systematic uncertainty comparing with the measurements. Table 7.8 displays in the first section the average value of the ratios for each type of material in each simulated model, providing a way to quantify the uncertainties of the results obtained from each of these models. These information is useful for the calculation of other quantities of interest in this facility, such as the fluence, dose, etc. From these benchmarks, it is possible to have an associated systematic error for each physics package.

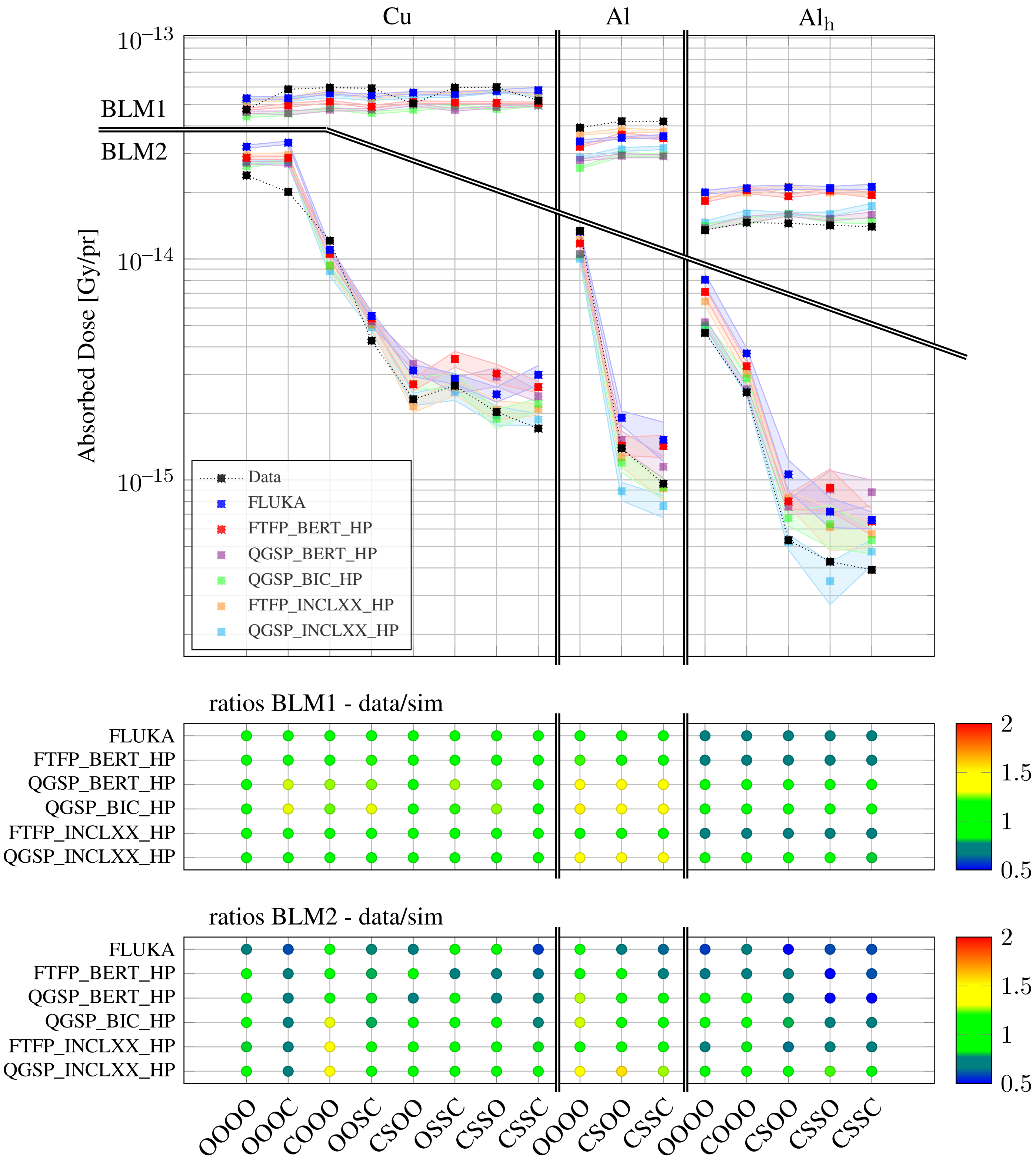

Figure 7.22: BLMs benchmark CHARM

Thus, rounding up values to 5% multiples, the uncertainty for each simulation, taking the worst result with respect to BLM1 or BLM2 in each case, is exhibited in Table 7.9.

Regarding the time efficiency of each code for conducting these simulations, Table 7.10 shows the average time required for the transport of a primary particle. An average value is estimated for all the shielding cases, as they did not vary among themselves by more than 10% of the values shown in the table.

It is noteworthy to observe that in this study, the simulations with Moira marked a difference of 60% between the slowest model (FBERT) and the fastest (QINCLXX), while FLUKA required the least amount of time, being two to three times faster than the models used in G4.

Table 7.10: Average CPU time per primary particles transported in CHARM facility study.

	FLUKA [s]	FBERT [s]	QBERT [s]	QBIC [s]	FINCLXX [s]	QINCLXX [s]
Cu	0.80	2.5	2.0	2.0	1.5	1.5
Al	0.45	1.5	1.5	1.5	1.0	1.0
$\mathrm{Al_h}$	0.40	1.5	1.5	1.5	1.0	1.0

7.4.4 Conclusions

Comprehensive simulation results were compared with experimental data, allowing for the inference of various facts:

- The calibration of the systematic error obtained for each physics package permits in the future produce results in the context of radiation to electronics.
- The G4 models showed a high degree of agreement, being on the same level as FLUKA.
- Depending on the model, a better agreement with the experimental data is obtained for different targets, e.g., FLUKA & FTFP matched better with Cu & Al, while QGSP matched better with $\mathrm{Al_h}$. This suggests that, given a particular circumstance such as the target material, it might be more convenient to use one model over another, as it better fits experimental results.
- Not relying on a single code allows for the suggestion of potential errors in the input, as observed in cases where concrete is used in the 4^{th} Shielding. If a simulation carried out with two or more MC codes shows similar behaviour, but differs from experimental results, and assuming the experimental results were measured correctly, it is reasonable to consider that there might be some error in the input, e.g., in the simulation geometry.

7.4.5 Next Steps

- Investigate the source of the peculiar result observed when using the 4^{th} shielding.
- Continue with a study already initiated to understand the contribution of each type of particle to the dose absorbed by the BLMs. The approach used is based on recording the

information of the particles that enter the detectors and then, with a second simulation, determining the contribution of each particle type. This result is itself interesting, but it is also relevant to compare the amount and type of particles that reach the detectors and their contribution to the total absorbed dose.

- Use the FLUKA physics list to corroborate results. This attempt has already been made, but a series of bugs in this implementation limited the conclusion of these simulations. Overcoming these limitations is key to continuing on the right path towards the development of FLUKA v5.
- Extend the use of this input in the Radiation to Electronics (R2E) team. The result presented in this section is just one of many studies carried out by the original author. Moira is already capable of conducting many of the simulations regularly done in the R2E team, such as energy deposited, dose, etc., but still requires the implementation of more scoring options, e.g., high energy hadron fluence, low-energy neutrons, among others.
- Complement these results performing the simulations with the PHITS MC code.

7.4.6 Acknowledgements

Great thanks to the original author of this study, Daniel Prelipcean, for the support in realising this section, providing the FLUKA results and input. He also contributed in the analysis of these complementary results, and review the presented text.

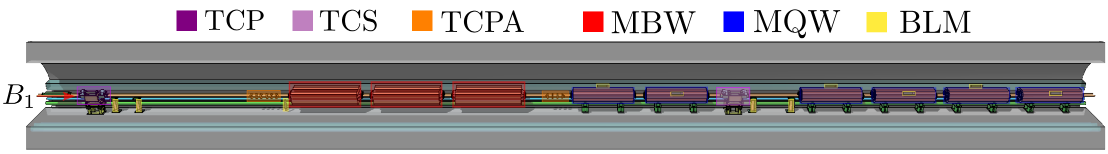

Figure 7.23: Layout of the IR3 section under study.

7.5 Absorbed Dose on IR3 Warm Magnets during HL-LHC era

Within the study of the impact of lost protons at the LHC during the HI-Lumi phase, this section continues the simulations carried out by Andreas Waets in 2021 [144] analysing the consequences of these losses on the warm magnets located in the momentum cleaning insertion region (IR3) of the LHC. The results to be presented are the first in this text to provide a foundation for machine protection studies at multi-TeV energies and complex geometries, using alternative physical models to FLUKA.

7.5.1 IR3: Geometry of Interest

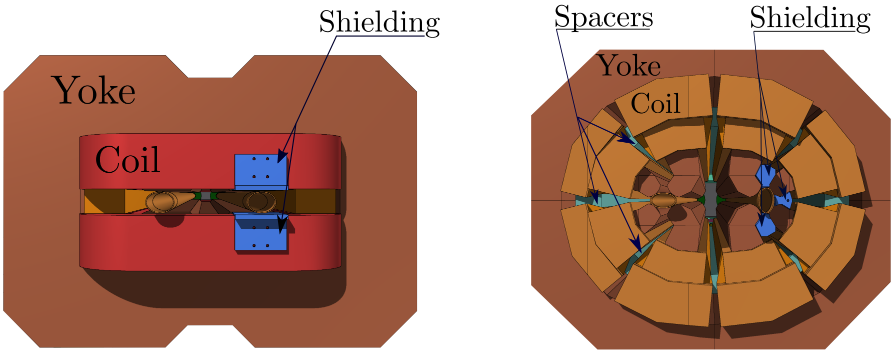

Figure 7.24: Front view of MBW and MQW respectively, exhibiting the main parts of their structure.

For the present study, Figure 7.23 shows the length of the IR3 LSS section used for this simulation and the devices that compose it. As observed, it is composed of the following features:

- ≈ 55 m of IR3 LSS.
- One TCP collimator, one TCS collimator, and two TCPA absorbers.
- Magnets:
  - Three MBW warm dipole magnets:
    - [C6, B6, A6] located at ≃ [–165, –161, –157] m w.r.t. IP3.
  - Six MQW quadrupole magnets:
    - [E5, D5, C5, 5, B5, A5] located at ≃ [–150, –147, –138, –135, –131, –127] m w.r.t. IP3.
- 11 BLMs:

- [TB6L, EB6L, TC6L, QF5L, QE5L, TC5L, TB5L, QD5L, QC5L, QB5L, QA5L] located at ≈ [-175.9, -174.7, -167.1, -150.6, -146.8, -142.6, -140.6, -138.6, -134.8, -131.06, -127.26] m w.r.t. IP3.

7.5.2 Studies & Methodology

The simulations aim to calculate the absorbed dose in the dipole (MBW) and quadrupole (MQW) magnet coils, including their plastic spacers essential for holding the MQW magnet coils (see Fig. 7.24). This assessment focuses on evaluating the magnets' performance during the 12-year operational period of the HL-LHC.

Previous preliminary studies [104, 145] had already provided results justifying the installation of additional protection for these magnets to reduce the impact of radiation on them. Thus, during the LS2, the following protections were added to the magnets (see Fig. 7.25):

- MBW (C6, B6, A6): W shielding between the aperture and return coils.
- MQW (E5, D5): W/Cu pieces of variable total length inserted in the yoke.
- MQW (C5, 5, B5, A5): W front shielding + W/Cu inserts (similar to E5, D5).

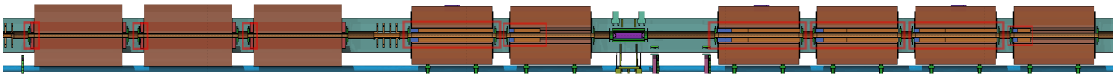

Figure 7.25: Magnets cross-section showing the added shielding after the LS2.

In this study, a more detailed analysis was sought of the potential damage that the mentioned materials (coils and spacers) would experience during the HL-LHC era. Additionally, the study aims to analyse whether extra front shielding is necessary for MQ.(D5, E5).

For the simulations, a primary particle source was used with an impact input from the TCP collimator, based on simulations with the SixTrack-FLUKA coupling, using the collision configuration in the LHC for 2017 and 2018 [146].

Firstly, a BLM benchmark was conducted, scaling the results from FLUKA and Moira with experimental data from 2017 and 2018, using the least squares fit method. This scaling factor, which represents the number of lost protons for 2017 and 2018, allows estimating the "IR3/IR7" loss ratio, utilised to predict the amount of lost protons in IR3 during HL-LHC scenario. Finally, by obtaining the maximum dose peaks in the coils and spacers of the various magnets, it is possible to infer the dose absorbed by them during HL-LHC, both with and without shielding.

Before showing the results, it is essential to detail all the considerations and assumptions used in this study:

1. Even though the energy of the protons for HL-LHC are expected to be at 7 TeV, the simulations were performed at 6.5 TeV. i.e., the energy deposited per primary particle or

the dose per primary particle obtained in the simulation at 6.5 TeV is considered not to vary significantly with the result at 7 TeV.

2. Results will only be accounted for when the beam is at a stable, flat top energy level. This implies that contributions from any other beam state will be excluded in the results.
3. Contributions due to ion beams (lead) will not be considered.

7.5.3 Results

In Figure 7.26, the absorbed dose by the mentioned 11 BLMs in the studied IR3 region is presented. The values are scaled with the results observed in Table 7.12 to compare with the data from 2017. The case for 2018 is also shown in the table, which is necessary to obtain an estimated value of losses in HL-LHC. However, the 2018 benchmark will not be shown because it does not provide extra information.

Firstly, it is noteworthy that there is a difference in the factor obtained when using the least squares fit method, which represents the number of lost protons. There is a clear dependence of this factor on the high-energy physics used in G4 because the values obtained with FTFP ($\approx 10^{14}$) are lower than those obtained with QGSP ($\approx 8.53 \times 10^{13}$). It is important to note that QGSP results in approximately 16% fewer losses compared to the use of the FTFP model and likewise with FLUKA.

All BLMs follow the functional form of the experimental data. Although the results show cases where they differ by up to a factor of 2 from the measurements, what is obtained for all the physics lists used demonstrates the level of confidence a user can have in Moira and the physics provided by G4, at least for machine protection studies.

In general, FLUKA shows the best performance in estimating the dose values in BLMs, except for BLM.TB5L. This particular BLM overestimates the experimental results by 40% with FLUKA, while for the QGSP physics lists, there is an underestimation of 25% and 15% for FTFP ones. Taking into consideration the accumulated dose when coils and spacers start to show a damage exhibited in Table 7.11, the previous result can be of significance when observing the values in the graphs for the accumulated dose in the MBW coils (Fig. 7.27), and the MQW spacers (Fig.

Table 7.11: Accumulated Dose limits for MBW and MQW

Element	Dose Limits [MGy]		
	Beginning of Damage *No bubbles, variation in properties*	Moderate Damage *Bubbles formation, properties reduction*	Failure on Component *Extensive Bubbles, properties loss*
MBW Coils	50-75	75-90	> 90
MQW Coils	10-50	50-75	> 75
MQW Spacers	5-10	10-15	> 15

7.28) and coils (Fig. 7.29).

The mentioned graphs allow obtaining, thanks to the fact of simulating with multiple MC codes, a results expressed by a range of values, which translates into a quantification of systematic errors.

A widespread reduction can be seen when the protection for the magnets was installed (represented by the black cross bars in the graphs), ranging from half to a third of what was obtained for the case with shielding in the dipole magnets. Similarly, there is a reduction of 25% for MQ.(E5, D5) in their coils, while for the remaining quadrupoles, the impact on coils and spacers is almost negligible, with the exception of MQ.C5 in FLUKA.

Before conducting a more in-depth analysis of other missing contributions to these final results, what is presented in the figures indicates that the addition of the shielding detailed earlier might not have been necessary at all, since the only case where the limit is reached is in the MQW.C5 coils with FLUKA. It is generally wise to consider the worst-case scenario when it comes to protecting critical equipment that also affects the functionality of an accelerator. Therefore, it is reasonable in this case, to exercise caution by adding these additional protective elements to ensure complete certainty that potential damage will not occur during the period of use of these devices. However, the results obtained indicate that there may be cases where this extra shielding is unnecessary, thereby avoiding a decrease in the costs required for the proper functioning of the facility in question. Having said that, it is worth adding that certain contributions, by no means irrelevant, were not taken into account for the final results obtained. As mentioned above, the following assumptions were made for the simulations:

- The equivalence between results with 6.5 TeV and 7 TeV protons: Using 7 TeV protons certainly generates an increase in the dose. However, this increase is likely marginal, since the centre-of-mass energy for a fixed nucleus and one of these protons does not vary significantly.
- Ramp and injections accounts for an increase of an additional 5-20% to the dose [144]
- Ions run: Based on Run 2 BLM data from 2017, 2018, the Pb ion contribution to the total dose is 40-50% at BLMs associated to IR3 warm magnets [147]
- Among other additional contributions due to Crystal collimation for ions in HL, modifications in configuration/operations, etc.

Taking these factors into account, it is reasonable, as was done originally when this study was performed with FLUKA, to consider that a factor of 2 could be applied to encompass all these additional contributions. In this way, the coils of MQ.E5, and the coils and spacers of MQ.C5 are already exceeding or approaching the damage limit in the case without shielding. Considering this extra factor, the added shielding proves to be sufficient to withstand damage in all the elements studied here for all the physical models contemplated.

Concerning the CPU times (Table 7.13), it is interesting to observe a worse performance for FLUKA in this study, with a difference above ≈ 40% comparing with Moira simulations.

Figure 7.26: BLMs benchmark IR3

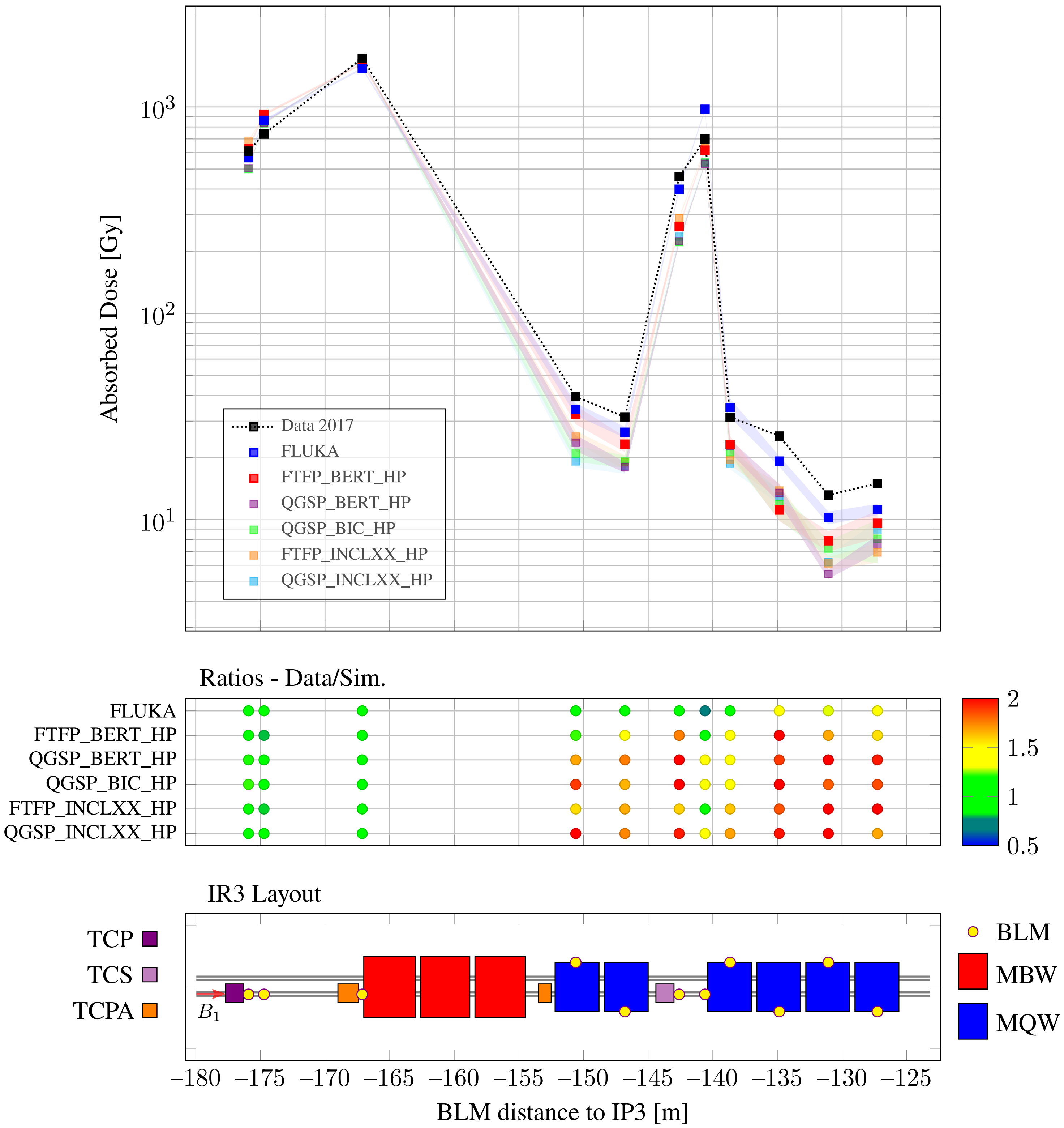

7.5.4 Conclusions

The results of the first simulations of machine protection studies at TeV energies in highly complex geometries using hadronic models alternative to FLUKA's were presented. This is a milestone in itself, but several inferences were also made from the results:

- Although overall FLUKA's results in the BLM benchmark show the best performance compared to experimental data, the results obtained with G4 are up to the task, with values always within a factor of 2 difference and a functional form totally compatible with that obtained with FLUKA.
- The curious fact that G4, in the initial result without the extra contributions, does not predict the need for shielding for MQW.C5 is a key result. It is important to put this result in context. What this shows is that, if finally the shielding was not necessary for the magnets to function correctly during the HL-LHC era, it implies an unnecessary but reasonable expense in the face of the potential danger of an accelerator malfunction, which could lead to much greater complications, or a stoppage of the machine. Certainly in this case FLUKA shows the most "conservative" result, and therefore, the most appropriate for the circumstances of machine protection, but it could happen that in a situation the results showed that G4 predicts a potential danger, and not FLUKA. This shows the fundamental importance of having other physical models with which to compare results, to verify that what is obtained with one is consistent with others, and that the confidence in what these simulations predict allows for the prevention of future dangers and/or expenses that could be reduced.
- Given the assumption of adding a factor of 2 that included all the extra contributions, the shielding was shown to be necessary for all models. On the other hand, the results also predict that there would be no need to add more shielding for the MQW.(D5, E5) magnets.

7.5.5 Next Steps

- Carrying out simulations with the FLUKA physics list will allow for a comparison of the already obtained results, providing information regarding MQW.C5, and also with the aim of Moira becoming FLUKA v5 in the future.
- It would be interesting to carry out a similar analysis using the results being obtained during Run III. A different BLM benchmark could be obtained, with which to make a new estimation of losses in IR3 for the HL-LHC phase.

7.5.6 Acknowledgement

Immense gratitude is extended to Andreas Waets, the original author of this study, for his invaluable assistance in the development of this section. His contributions included providing the FLUKA results and input, as well as playing a significant role in analysing the results and reviewing the text presented here.

Table 7.12: Estimation ratio of losses IR3/IR7 for HL-LHC

	2017 ($\times 10^{13}$)	**2018** ($\times 10^{13}$)	**HL-LHC** ($\times 10^{16}$)
Protons lost in IR7	160	450	10
Protons lost in IR3			
FLUKA	10.00	8.30	
FTFP_BERT_HP	10.10	8.45	Estimated losses:
QGSP_BERT_HP	8.52	7.06	$\boxed{1.0}$
QGSP_BIC_HP	8.53	7.06	
FTFP_INCLXX_HP	10.00	8.33	
QGSP_INCLXX_HP	8.36	6.94	
Ratio IR3/IR7			
FLUKA	0.06	0.02	
FTFP_BERT_HP	0.06	0.02	Assuming: **0.1**
QGSP_BERT_HP	0.05	0.02	
QGSP_BIC_HP	0.05	0.02	
FTFP_INCLXX_HP	0.06	0.02	
QGSP_INCLXX_HP	0.05	0.02	

	FLUKA [s]	FBERT [s]	QBERT [s]	QBIC [s]	FINCLXX [s]	QINCLXX [s]
No Shielding	100	70	70	70	65	65
Shielding	110	80	75	75	70	70

Table 7.13: Average CPU time per primary particles transported in IR3 study.

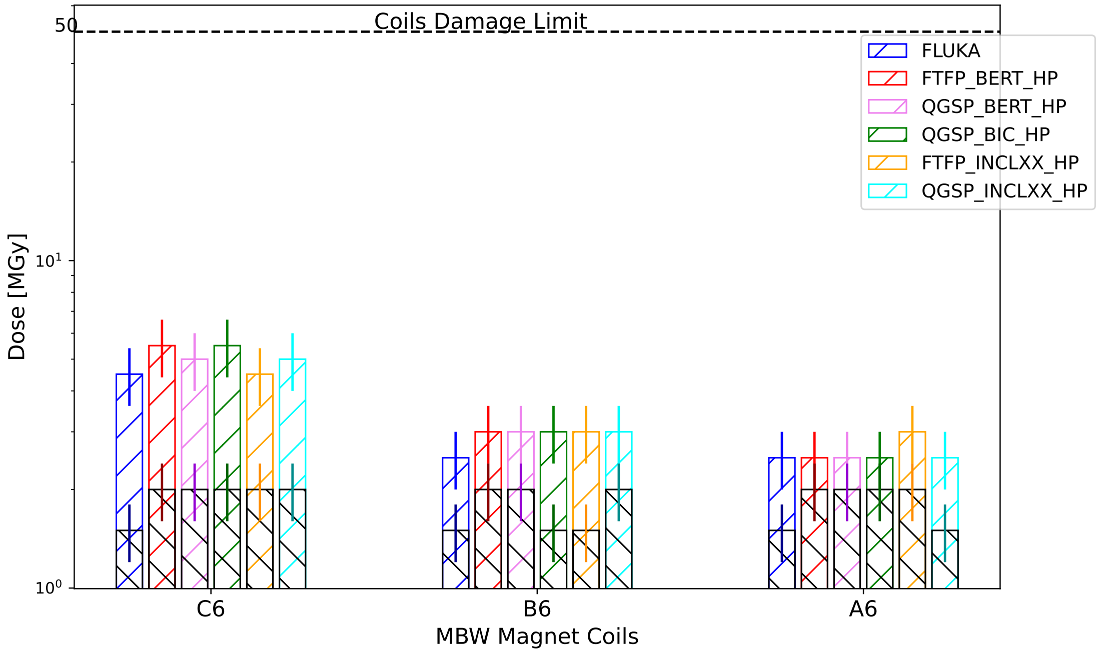

Figure 7.27: Accumulated dose on dipole magnets coils. The different physics packages are expressed with the exhibited colours, while the relevant reduction due to the shielding is observed in the bars in black, producing a cross with the case without the shielding.

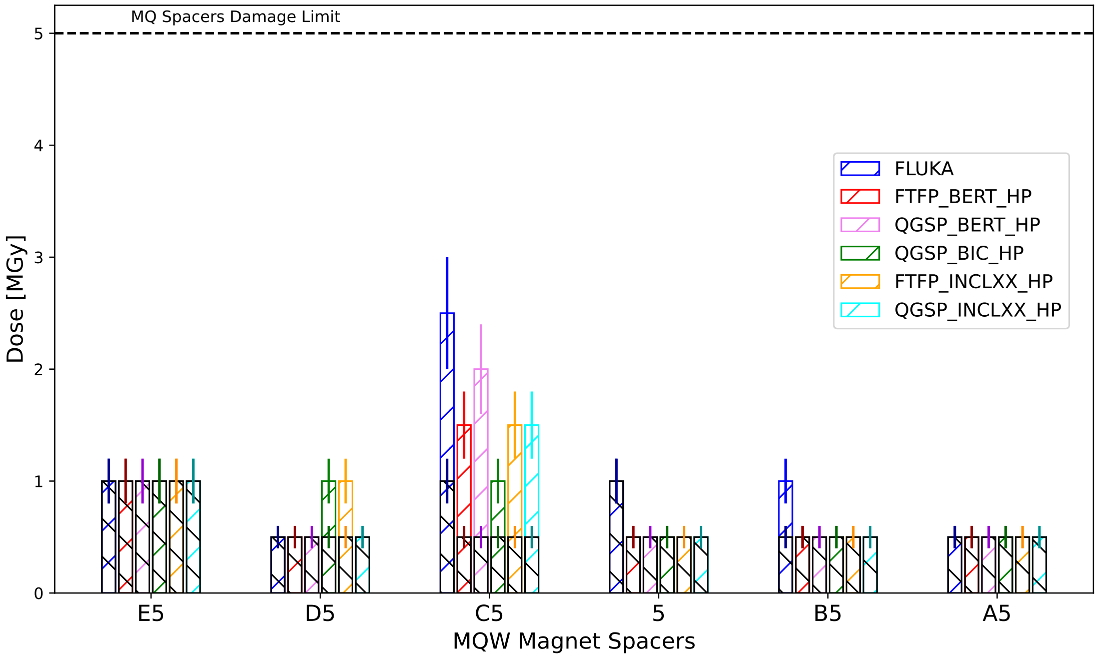

Figure 7.28: Accumulated dose on quadrupole magnets spacers. No shielding in colours, and with shielding in black, producing a cross for comparing.

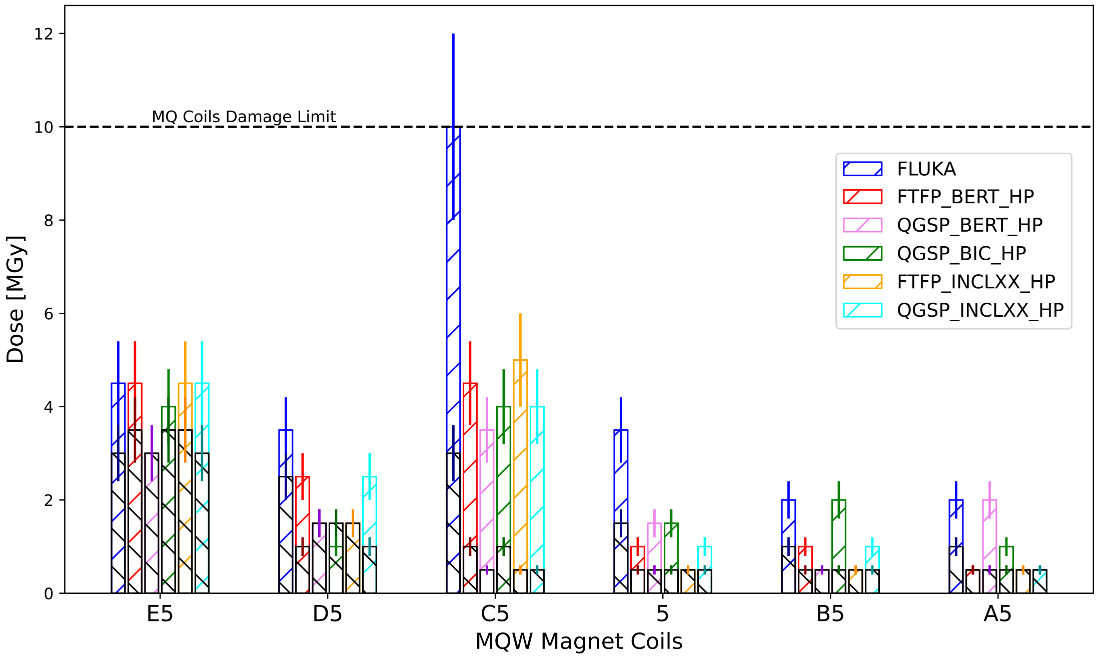

Figure 7.29: Accumulated dose on quadrupole magnets coils. No shielding in colours, and with shielding in black, producing a cross for comparing.

7.6 The BGV Instrument and its Impact on IR4 SC Magnets

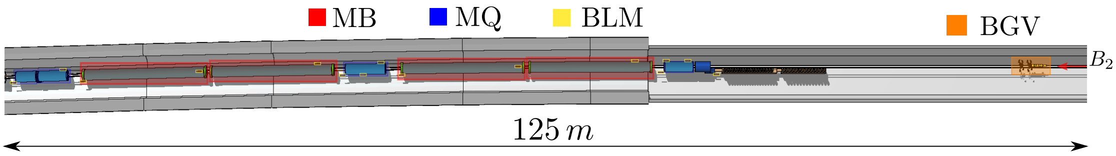

Figure 7.30: Layout of IR4 section under study, created with Flair.

Of all the devices hosted by the LHC, some are dedicated to measuring beam properties such as position, intensity, emittance, among others. The Beam Gas Vertex (BGV) monitor is intended to measure the transverse beam profile through inelastic collisions caused by the passage of bunches traversing a gas to get injected into the chamber. In this section, following the study performed by Daniel Prelipcean [148] the impact of the radiation generated by the BGV during Run II will be assessed, enabling an estimation of its effects during the HL-LHC era.

7.6.1 The BGV Instrument

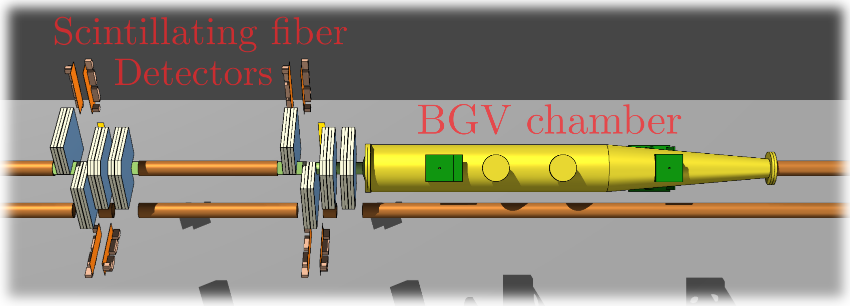

Figure 7.31: Flair figure of BGV detector.

The BGV monitor, schematically represented in Figure 7.31, is primarily based on the use of a gas chamber installed in one of the LHC beam pipes. In a non-invasive manner, part of the protons in the bunches generate an inelastic interaction with the injected gas (Neon), as they pass through the chamber. This interaction produces new particles, which are detected by detector modules positioned outside the vacuum beam pipe. With these detectors, it is possible to reconstruct the interaction vertex of particles and thus estimate the beam profile at the point in the LHC under consideration. In this case, the point is located at -220 m from IP4, on Beam 2, where a BGV demonstrator was installed as a test of its functionality for Run II.
The direct question arising from the above is:

**What impact do these losses have on the equipment,
particularly on the superconducting magnets in the vicinity of the BGV?**

This question will be evaluated in this section by comparing simulations with the measurement results obtained during Run II, estimating the impact that the radiation generated by the BGV would have on the HL-LHC stage regarding superconducting dipoles and quadrupoles, in terms of total absorbed dose and the risks of a quench occurring.

7.6.2 Geometry of Interest

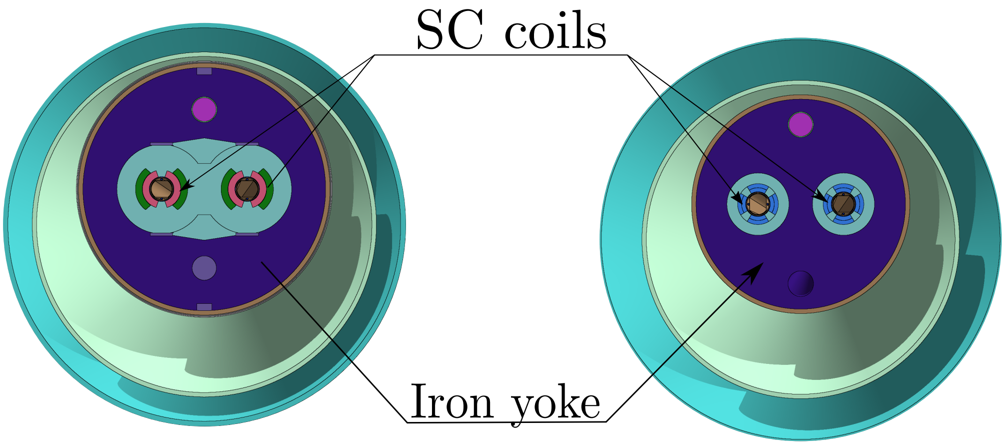

Figure 7.32: Front view of MB and MQ respectively, exhibiting the main parts of their structure.

Figure 7.30 shows the geometry considered for the studies. It consists of a section of the LSS of IR4, with the BGV located approximately -220 m from the centre of IR4. Furthermore, part of the DS adjacent to IR4 makes up this geometry, covering a total length of about 125 m.

In this way, the geometry in question can be specified, composed of the following relevant characteristics:

- Length: Approximately 125 m (comprising 50 m of LSS and 75 m of the adjacent DS).
- BGV Detector: Located at -220 m from IP4 (Source of proton losses).
- Magnets: Includes the following SC magnets:
  - Four MB SC Dipole Magnets:
    - [B9, A9, B8, A8] located at ≈ [−330.9, −315, 2, −291.8, −276.5] m w.r.t. IP4.
  - Four MQ SC Quadrupole Magnets:
    - [MC9, M9, M8, M7] located at ≈ [−346.5, −342.1, −303.8, −265.3] m w.r.t. IP4.
- A total of 17 BLMs:
  - [QF9, QD9, QC9, QB9, QA9, BA9, QF8, QD8, QC8, QB8, QA8, BA9, QF7, QE7, QC7, QB7] located at ≈ [-350.1, -347.0, -343.8, -341.0, -338.5, -324.1, -309.7, -306.6, -304.1, -301.9, -299.4, -285.0, -270.6, -267.5, -266.8, -264.2, -260.6] m w.r.t. IP4.

7.6.3 Studies & Methodology

The goal of the studies in this section, as previously mentioned, is to first benchmark the BLMs in the detailed geometry, where dose measurements in BLMs verify the reliability and scaling factors of the simulations carried out. With this result in hand, one is confident to estimate the impact of radiation on the magnets, initially for this same run, and ultimately to estimate the dose on the magnets for the time when the BGV is used in the HL-LHC stage.

To accurately estimate the absorbed dose in BLMs as well as in the magnets, it is essential to understand the factors that affect the radiation level rate ($^{dN}/_{dt}$). This rate is considered here to be proportional to the interaction rate (I_{col}) of inelastic collisions, which can be expressed in terms of the following factors:

$$\frac{dN}{dt} \propto I_{col} = \Theta(t; s_a, s_b) \cdot \sigma(E) \cdot f \cdot n(t) \tag{7.1}$$

Where:

- $\Theta(t; s_a, s_b)$: The integrated gas density profile in the BGV region [s_a, s_b] at time t.
- $\sigma(E)$: The inelastic cross section for p-Ne interactions at energy E for protons.
- f: The revolution frequency of the particles within the accelerator.
- $n(t)$: The total number of charges passing through the BGV chamber at time t.

The last two terms are specific accelerator configuration data. These can be seen in Table 7.14, which provides the values for total charges, beam energy, gas pressure in the BGV, and the revolution frequency for the LHC Run II and HL-LHC.

Table 7.14: Operating Parameters for LHC Run II and HL-LHC

	LHC Run II *(Measured)*	HL-LHC *(Projected)*
Total Charges (n)	3.00×10^{14}	6.35×10^{14}
Beam Energy (E)	6.5 TeV	7.0 TeV
Gas Pressure (p)	0.79×10^{-7} mbar	1.00×10^{-7} mbar
Revolution Frequency (f)	11245 Hz	11245 Hz
Total Usage Time	169 h	200 h

Concerning the cross-section, the inelastic cross-section is the one that contributes to the generation of radiation. To estimate it, the approach involves extrapolating the problem by considering p-p interactions, utilising the cross-section for this case, and then scaling it with the number of nucleons (A) relevant to the problem (see [149]), which is 20 for the neon injected into the BGV. This allows for the estimation of the radiation generated:

$$\sigma_{p-A} \approx \sigma_{p-N} \times A^{\alpha} \tag{7.2}$$

where α was obtained experimentally [149] with a value ≈ 0.71.

Then, being the nucleons in the neon basically a fixed target for the protons of the beam, the energy of the centre of mass can be approximated in the following way:

$$\sqrt{s_{p-p}} \approx (2mc^3 p_{lab})^{1/2} \tag{7.3}$$

Considering the energy value for a proton at 6.5 TeV resulting in $\sqrt{s} \approx 110$ GeV, and using a cross section of approximately 40 mb for p-p, interactions at 110 GeV, it is derived:

$$\sigma_{p-p}^{inel}(110\,\mathrm{GeV}) \approx 40\,\mathrm{mb} \Rightarrow \boxed{\sigma_{p-Ne}^{inel}(110\,\mathrm{GeV}) \approx 320\,\mathrm{mb}} \tag{7.4}$$

Regarding the factor associated with the density profile of neon gas (Θ), experimental determination of this distribution is not feasible. Thus, simulations were employed. The MOLFLOW+ software [150] was utilised to calculate this profile, which is illustrated in Figure 7.33. Based on the information provided by this simulation, the contribution can be estimated given the density of neon:

$$\boxed{\Theta(t; s_a, s_b) = \rho_{max} \int_{s_a}^{s_b} \frac{\rho(s)}{\rho_{max}} ds} \tag{7.5}$$

With this information, the results of absorbed doses in BLMs and magnets can be appropriately scaled to account for the radiation generated by inelastic interactions in the BGV gas.

7.6.4 Details about the Simulations

The process for generating primary particles was executed using the gas density profile described earlier. By obtaining the CDF, the position for generating p-Ne inelastic interactions was sampled, and the resulting secondary particles were stored in the stack for subsequent transport.

The previous method was employed in FLUKA to obtain particles for further transport. In Moira, secondary particles generated from inelastic interactions in FLUKA were utilised. This indicates that the initial inelastic interactions weren't modeled using G4's physics models. As a result, the benchmark was limited to energies up to 110 GeV, which is the maximum range for the secondary particles. Nevertheless, the results obtained with G4 remain valuable because the transported particles share identical properties with those transported using FLUKA, ensuring a completely **equivalent** benchmark between the two codes.

7.6.5 Results

The Figure 7.35 displays the absorbed dose by the 17 BLMs in the geometry of interest, as well as the ratios between the various physical models used and the experimental data obtained during LHC Run II.

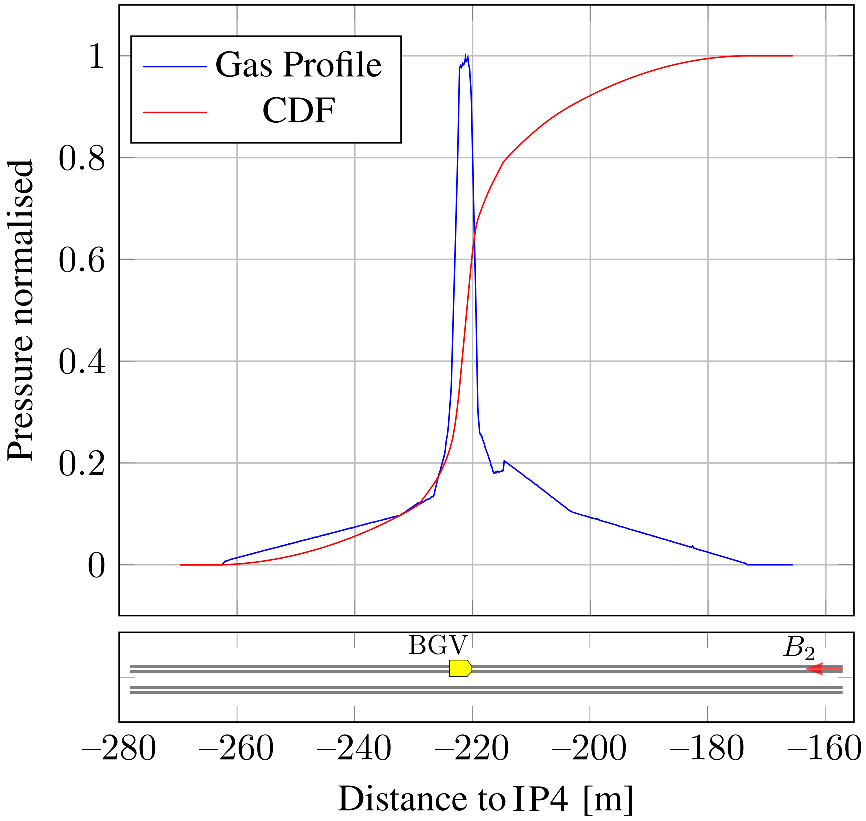

Figure 7.33: Pressure/Density profile of the BGV and its CDF utilised for p-A interaction.

A remarkably similar performance is observed for all the results, with the dose in all BLMs differing by no more than a factor of two. This disagreement is particularly notable in cases at BLM.(QF7, BA9, QA8, QC8). Unlike the more distant BLMs, where radiation is relatively low and the measured and simulated results have higher uncertainty, the mentioned BLMs and the differences between measurements and simulations suggest that some geometric details or simplifications in the particle sampling method may lead to these discrepancies.

Nevertheless, the results are sufficiently robust to conclude that the doses and heat loads on the magnets are within a factor of less than 2 for the results presented in Figure 7.34. The studies were primarily conducted on a limited range of magnets, specifically, the closest magnets to the BGV, MB.(A8, B8), MQ.(M7, M8). These magnets were selected because they are the most irradiated. Furthermore, the figures depict nearly identical outcomes since the quantity scored primarily involved energy or energy weighted by the material density, which in this case, was the coil material. The goal of the graphs is to evaluate the potential for quench occurrence (heat loads) and dose accumulation in the magnets during the period when the BGV was used in Run II and to estimate its contribution to the HL-LHC stage.

The results indicate a strong agreement among all models, especially for the predominantly irradiated magnets. The low statistical significance in the results for less irradiated magnets hinders a direct comparison among the physical models. Still, it does allow for conclusions about the impact of these losses generated by the BGV. A maximum peak (D_p) of approximately $2\times10^{-1}\,\mathrm{kGy\,h^{-1}}$ in dipoles and $1\times10^{-1}\,\mathrm{kGy\,h^{-1}}$ in quadroples is observed. Considering that the limit for accumulated dose is around 15 MGy for dipoles and 25 MGy for quadrupoles [39] and that the BGV was used for approximately 169 hours, the estimated dose is **35 kGy** and **18 kGy** respectively; orders of magnitude below the limits. This is even more conservative if considering the extra factor of 2 mentioned earlier in the BLM benchmark.

Assuming, as done in the IR3 study, that the impact of particles at 6.5 TeV does not vary significantly for the case at 7.0 TeV, it is possible to scale the obtained results, taking into account the total number of particles for the HL-LHC. Therefore,

$$D_p \times \frac{n_{\text{HL-LHC}}}{n_{\text{RunII}}} \times 200\,\mathrm{h} \approx \begin{cases} \textbf{Dipoles:}\, 85\,\mathrm{kGy} \ll 15\mathrm{MGy} \\ \textbf{Quadrupoles:}\, 45\,\mathrm{kGy} \ll 25\mathrm{MGy} \end{cases} \tag{7.6}$$

In this case as well, far from causing concern for device functionality, even when considering the additional factor of 2, the dose is three orders of magnitude below values that could be considered risky.

On the other hand, the second figure allows to analyse the risk of a quench in the superconducting magnets. Quench limits are estimated to be around $40\,\mathrm{mW/cm^3}$ for quadrupoles and $13\,\mathrm{mW/cm^3}$ for dipoles [39]. The results for Run II show heat loads below **0.4 mW/cm**^{3} for the dipole magnets and below **0.2 mW/cm**^{3} for the quadrupole magnets. Both values are well below the mentioned limits and do not pose a danger of phase changes in the magnets, even when considering the additional factor of 2.

Then, concerning the risk of quenches in HL-LHC, as previously estimated, it is obtained:

- **Dipoles:** Estimated heat load for HL-LHC is $0.85\,\mathrm{mW/cm^3}$, which is significantly below the 13 mW/cm^3 quench limit.
- **Quadrupoles:** The heat load estimate for HL-LHC is $0.45\,\mathrm{mW/cm^3}$, well under the 40 mW/cm^3 quench limit.

Concluding that there is no risk of damage due to accumulated dose or quench for the studied superconducting magnets in the HL-LHC, with this result supported by all the physical models presented in this section.

Finally, Table 7.15 displays the average times required by each model for the transport of a primary particle. In this study, FLUKA showed a performance between 20% and 45% superior to that of the G4 models.

FLUKA [s]	FBERT [s]	QBERT [s]	QBIC [s]	FINCLXX [s]	QINCLXX [s]
450	650	650	600	550	550

Table 7.15: Average CPU time per primary particles transported in IR4 study.

Figure 7.35: Benchmark of BLMs in IR4

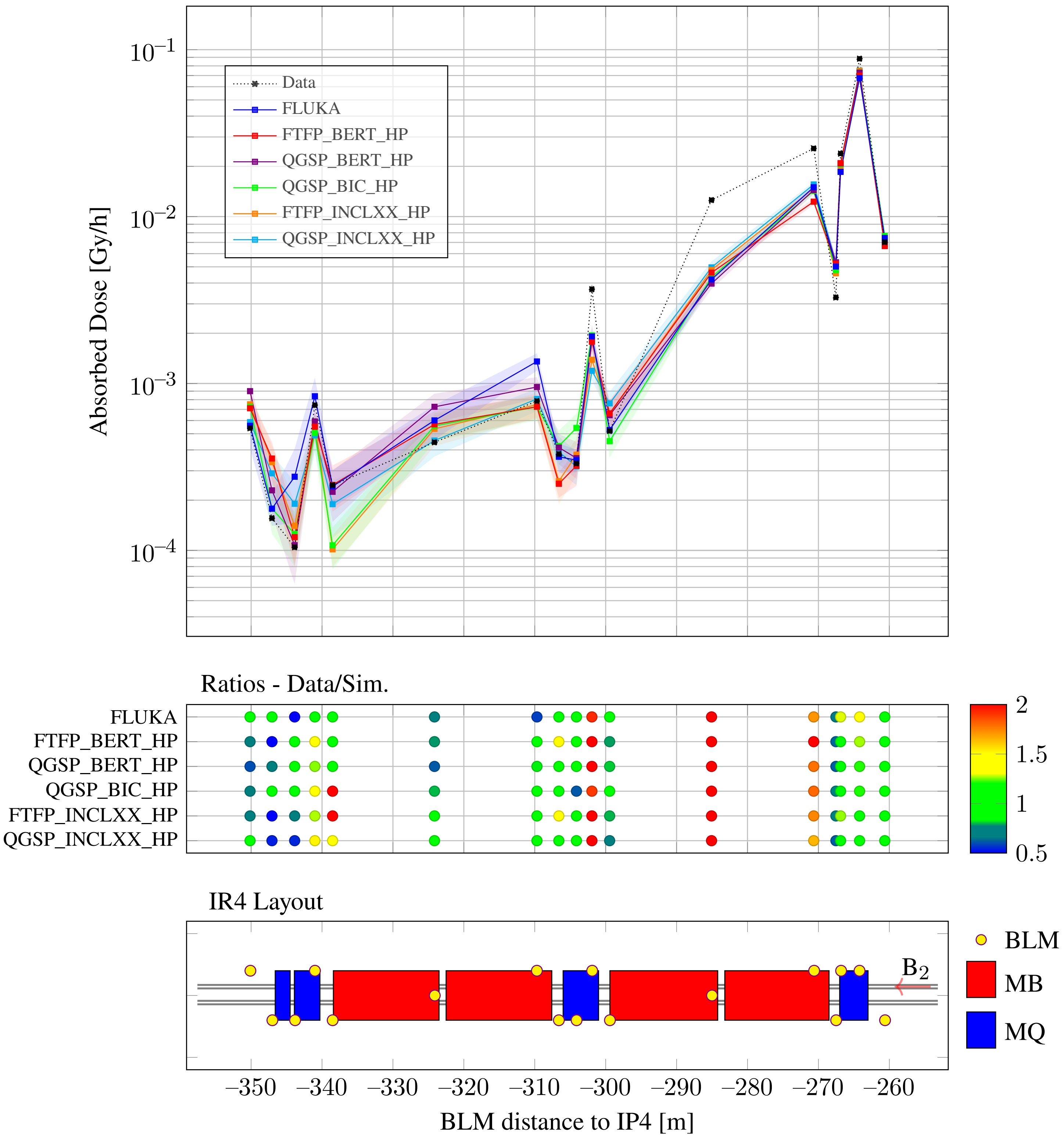

Figure 7.34: Doses in mostly irradiated magnets

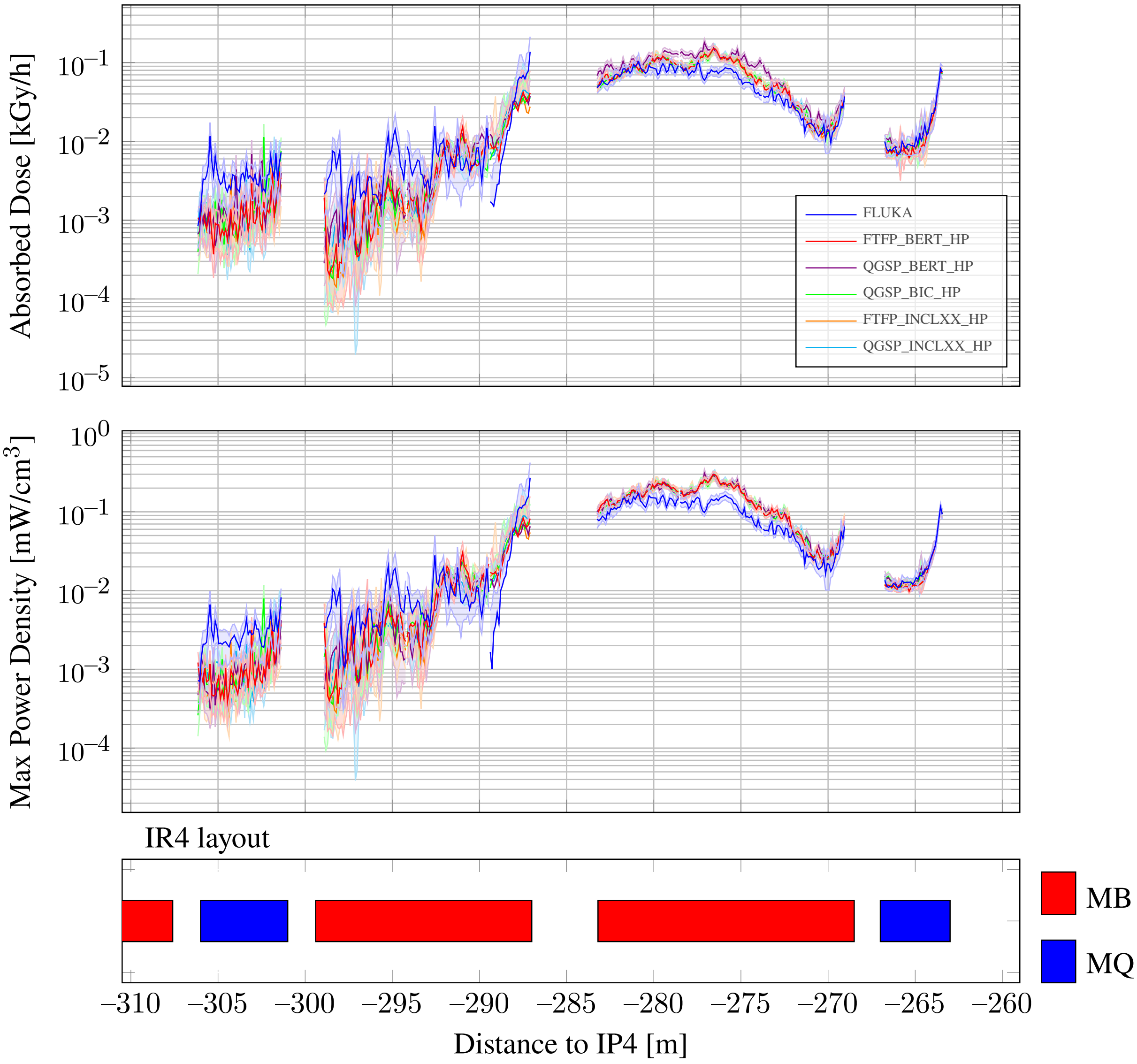

7.6.6 Conclusions

This is the second result of machine protection in complex geometries at high energies presented in this manuscript. Although the energy is reduced to less than 110 GeV when G4 is used, this result remains highly relevant, as it is the first study of quench risk with hadronic models alternative to FLUKA's.

Regarding the BLM benchmarks, all results showed remarkable performance, with a difference not exceeding a factor of two. These cases of greater discrepancy are replicated by all models, i.e., the BLM.(QF7, BA9, QA8, QC8), suggesting that some aspect of the simulation, not associated with the physical models, such as details in the geometry or simplifications in the sampling method, might need improvement.

It was concluded from the simulations with all models that the contributions in the most irradiated magnets, specifically those closest to the BGV, MB.(A8, B8) and MQ.(M7, M8), would not pose any risk of damage due to accumulated dose during the period expected to be used in the HL-LHC era, nor the possibility of quenches. It is important to consider the contributions to them, but in themselves, they do not entail a risk.

7.6.7 Next Steps

- Implement in Moira a routine for the initial inelastic interactions in order not to depend on FLUKA's and to have results purely with G4 models.
- Carry out the simulation at 7 TeV without the need to extrapolate the results from those obtained at 6.5 TeV.
- Again, repeating these simulations with Moira using the FLUKA physics list is necessary for FLUKA v5, and to obtain information that may be relevant for the analysis of the already obtained results.

7.6.8 Acknowledgement

Many thanks again to Daniel Prelipcean, the original author of this study, for the FLUKA results and all the inputs utilised for these complementary results.

7.7 Quench assessment due to IR7 Protons Leakage on IR6 SC Quadrupole Magnets

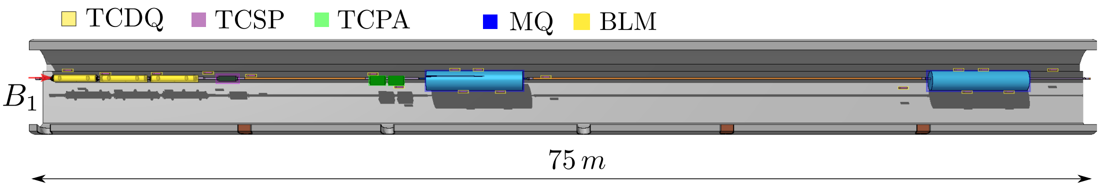

Figure 7.36: Layout of IR6 section under study, created with Flair.

IR6 is the section of the LHC that houses the beam dump system, where the particles are extracted from the machine. This extraction can be caused by certain conditions:

- Normal dump: After a period of collision, the beam degrades and becomes unsuitable for further experiments.
- Accidental dump: Can occur if an event such as a magnet quench or an electronic failures, poses a risk to the equipment or the accelerator's integrity.

IR6 is equipped with a series of collimators designed to absorb particles that may not be extracted as planned, thereby protecting the superconducting magnets that are part of the LSS in IR6. However, those collimators also intercept particles during normal operation of the machine. It is suspected that some of the losses initiated in the betatron cleaning insertion (IR7) induce radiation in IR6. Those outscattered particles could be a risk to the superconducting magnets housed in IR6.

This study analyses the possibility of a quench occurring in the SC magnets of IR6 (see Fig. 7.36), as a result of the mentioned losses in IR7, during the HL-LHC run. The presented results are complementary results to the FLUKA ones performed by Jean-Beaptiste Potoine in 2021-2023 [151], but obtained with Moira using multiple G4 physics lists.

7.7.1 IR6 Extraction System

To carry out the extraction of proton bunches, the following sequence of events is performed, as depicted in Figure 7.37:

1. Initiation of the beam dump.
2. Bunches, after passing through an MQ_5 (SC quadrupole), are horizontally deflected by the fast-pulsed Ejection Dump Kicker magnet (MKD), which is activated during the "abort gap". This refers to a 3µs time frame where no protons are present in the bunch train.
3. The deflected particles pass through another SC quadrupole (MQ_4) and are redirected by a septum magnet (MSD) towards the extraction line.
4. In the extraction line, the particles are dispersed by diluter magnets (MKB) and finally impact a graphite block (TDE) that absorbs all their energy.

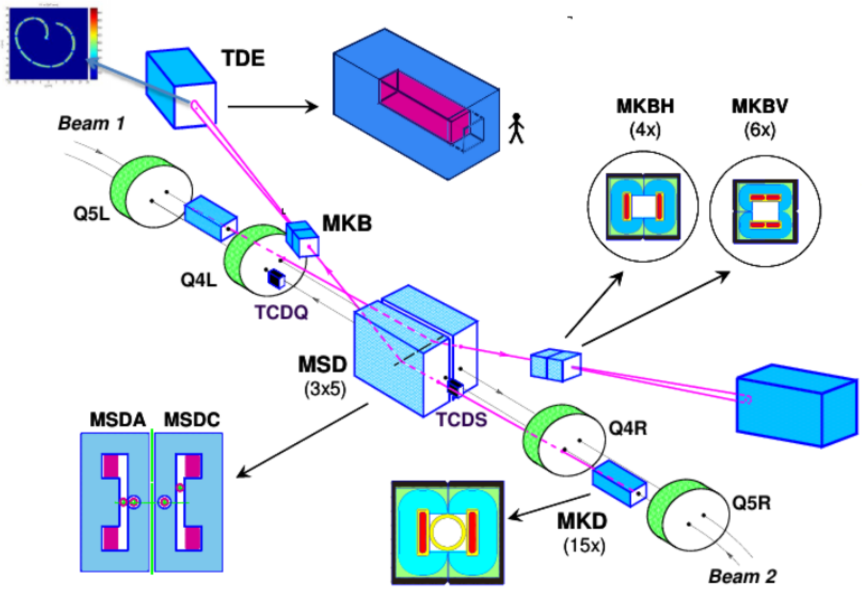

Figure 7.37: IR6 Extraction system. Courtesy [152].

While the above process typically occurs during beam extraction, there are cases where this procedure does not go as planned. This can happen when the MKD is activated at a time outside of the "abort gap", resulting in an "asynchronous beam dump". It is crucial to have an adequate protection system for such events to prevent potential damage to the MSD and SC magnets. This protection system can be observed in Figure 7.38 and consists of:

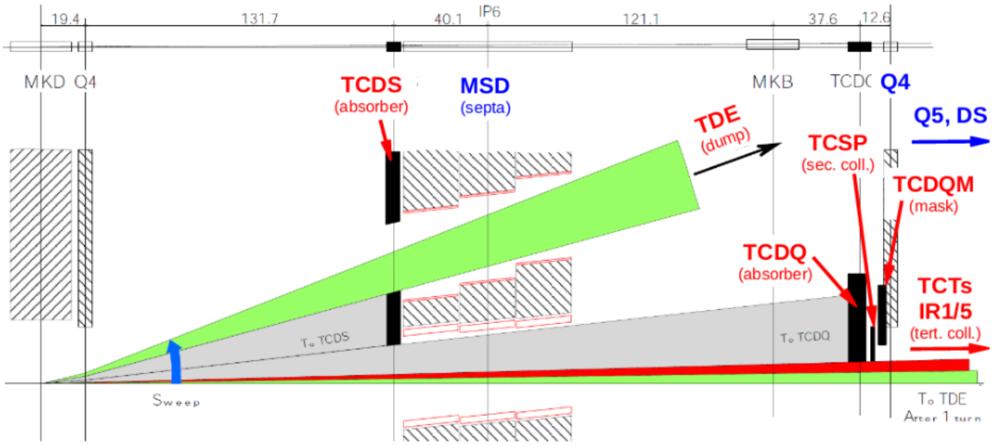

Figure 7.38: Layout of IR6 collimation system. Based from [153].

- Target Collimator Dump Septum (TCDS): Designed to protect the MSD.
- To safeguard the MQ quadrupoles:
  - The Target Collimator Dump Quadrupoles (TCDQs): Collimator covering the side of

the beam in its extracted path, comprising three modules.
- The Target Collimator Secondary Protection (TCSP): A single module, complementing the protection of the TCDQ.
- The Target Collimator Downstream Quadrupole Mask (TCDQM): An immobile collimator, located at the entrance of MQ4, serving as the last line of defence against radiation showers.

These collimators were designed to effectively protect the SC magnets in IR6 against asynchronous beam dumps. However, no studies were performed to quantitatively assess their performances during normal operation. In the studies presented here, an analysis of the energy deposition of particles outscattered from IR7 into the SC magnets of IR6 is performed, assessing the associated risk of quenching during the HL-LHC era.

7.7.2 Geometry of Interest

The introduced figure 7.36 presents the layout of the geometry used for simulations, comprising the following features:

- Approximately 75 m of the LSS in IR6 (Dump region in LHC).
- TCDQ and TCSP collimators (sources of proton losses).
- Two SC Quadrupole Magnets: (MQ_4 and MQ_5).
- 17 Beam Loss Monitors:
  - [4R, 14R, Y4R, Z4R, G4R, A4R, B4R, C4R, D4R, E4R, B5R, A5R, C5R, D5R, E5R, F5R, G5R] located at = [142.7, 145.5, 152.6, 156.6, 164.8, 166.7, 170.7, 171.3, 172.4, 174.0, 177.2, 202.8, 207.1, 207.7, 208.9, 210.7, 213.9] m w.r.t. IP6

7.7.3 Studies & Methodology

The study outlined in this chapter was based on the LHC's design specification guidelines. It states that the collimation system must manage for a few seconds a beam decay of 0.2 h, without causing a quench. This is the beam lifetime (BLT):

Beam Lifetime (BLT)
Interval of time necessary for the initial intensity of the Beam to be reduced to 1/e of its original value.

Considering the beam parameters of protons in HL-LHC, where 2760 bunches with an intensity of 2.3×10^{11} protons per bunch will circulate in the accelerator, a beam life time of 0.2h corresponds to a lost rate of 8.8×10^{11}protons/s in the machine.

This variable quantifies the absolute loss rate in the machine. Those particles lost arises from every section of the LHC:

$$\mathrm{N_{tot}} = \sum_{i=1}^{8} \mathrm{N_{IRi}} \tag{7.7}$$

However, since most of the losses are generated in the IR7 region, It is reasonable to assume that $\mathrm{N_{tot}} \approx \mathrm{N_{IR7}}$.

On the other hand, since most of the primary collimators are located in IR7, some of these first halo beam losses logically end up in the secondary collimators of IR6. In this way, it is assumed that there will be a factor ($\mathrm{f_{IR6}}$) that will account for the protons lost in IR6, which will be a fraction of the total losses in IR7:

$$\boxed{\mathrm{N_{IR6}} \approx \mathrm{f_{IR6}} \times \mathrm{N_{IR7}}} \tag{7.8}$$

Finally, considering the 0.2h BLT scenario:

$$\dot{\mathrm{N}}^{\mathrm{IR6}}_{\mathrm{max}} \approx \mathrm{f_{IR6}} \times \dot{\mathrm{N}}_{\mathrm{max}} \Rightarrow \boxed{\dot{\mathrm{N}}^{\mathrm{IR6}}_{\mathrm{max}} \approx \mathrm{f_{IR6}} \cdot 8.8 \times 10^{11} \mathrm{protons/s}} \tag{7.9}$$

This factor will allow to scale the simulation in IR6 to the maximum allowed number of lost protons in IR6.

The energy deposition on the cold magnets will depends on the impacted collimator. Hence, one should understand the origin of those proton losses, between IR6 collimators, before investigating the energy deposition in the superconducting magnets of IR6. This arises from the impossibility of knowing the number of these losses that end up impacting the TCDQ or TCSP collimators. One can introduce two new factors to take into consideration the relative contribution of each collimators to the loss rate in IR6:

$$\boxed{\mathrm{f_{TCDQ}} + \mathrm{f_{TCSP}} = 1} \tag{7.10}$$

A much more detailed analysis of the different cases selected for this study can be found in the doctoral thesis of the original author of this study [154]. In this manuscript, the description will be limited to describing them, commenting on the context for which they were chosen, and the reason.

7.7.4 Details about the Simulations

The impossibility of knowing the number of losses in each collimator generated the need to carry out two separate simulations, one where all losses were concentrated in the TCDQs, and another where they ended up in the TCSP. Both inputs obtained for SixTrack-FLUKA simulations. In this way, only by imposing a weight through the factors $\mathrm{f_{TCDQ}}$ and ($\mathrm{f_{TCSP}}$), one can derive the BLMs signals in IR6, and the heat loads in the SC quadrupole magnets for each case of interest.

The empirical study performed by the aforementioned author with Run II provided a range of f_{IR6} possible for the HL-LHC design case:

$$f_{IR6} \in [5\times10^{-4} - 2\times10^{-3}] \tag{7.11}$$

On the other hand, three cases of interest were found for the factor f_{TCDQ}:

- $f_{TCDQ} = 0.0$, $f_{TCSP} = 1.0$: Considered as the "worst case" scenario. This is because, as will be seen in the results, the radiation produced in the TCSP is greater than that of the TCDQ.
- $f_{TCDQ} = 0.2$, $f_{TCSP} = 0.8$: This case proved to be the most frequent, the one that was most observed with respect to other possibilities.
- $f_{TCDQ} = 0.8$, $f_{TCSP} = 0.2$: Specific values found during machine development studies (Quench tests [155, 156])

These values were obtained through simulations of the dose deposited in the BLMs. From the experimental measurements of the BLMs, the results of these simulations were adjusted to estimate the values f_{TCDQ} and f_{TCSP} corresponding to each case.

In this way, the following cases will be presented for the quench risk analysis in the SC quadrupole magnets:

Table 7.16: Comparison of Different Cases

Case	f_{IR6}	f_{TCDQ}
Worst Case	2×10^{-3}	0.0
Quench Case	2×10^{-3}	0.8
Operational Case	5×10^{-4}	0.2

7.7.5 Results

The first aspect to note is the BLM benchmarks. Contrary to the previous benchmarks, the discussion presents G4 values in relation to FLUKA. Figure 7.39 shows the dose for impacts on the TCDQ collimators, while figure 7.40 does so for impacts on the TCSP collimator. Initially, the results appear highly consistent across all models, with only a few exceptions that are not overly extreme.

In terms of physical interpretation, the data indicates that when protons impact the TCDQ, the adjacent BLMs register a significantly higher dose of radiation compared to those near the SC quadrupoles. Conversely, when impacts are solely on the TCSP, the neighboring BLMs show similar levels to the previous case ($O10^{-10}$/pr), but the dose in the BLMs of the magnets is about an order of magnitude higher than in the TCDQ scenario. This suggests that the magnets receive more radiation when the source is in the TCSP. Indeed, the TCDQ comprises three larger modules and precedes the TCSP. Therefore, protons impacting the TCDQs are better intercepted than if they initially hit the TCSP, leading to lower doses measured by the BLMs and, consequently, less energy deposited on the superconducting magnets.

Comparing G4 with FLUKA shows the most significant differences in the TCSP scenario at the initial BLMs.(4R, 14R), but these are not deemed representative due to the minimal radiation generated in this region, primarily produced from back-scattering. The associated error in each simulation, for these BLMs is also noteworthy.

The BLM benchmarks indicate that models incorporating FTFP align more closely with FLUKA than those using QGSP, with differences up to 50%. Excluded are the BLM.Y4R and BLM.A4R for TCDQ and TCSP scenarios respectively. These specific instances reveal a significant discrepancy, near factor 2, between G4 and FLUKA results, suggesting a factor beyond the physical models influencing the obtained values.

Having made these observations, despite the shown differences, the results near the magnets are quite consistent across all models. This allows for comparisons of the analyses in figures 7.41 without needing extra scaling factors to estimate the heat loads. These figures demonstrate the energy peaks in the coil of the superconducting quadrupoles, covering the three study cases of interest (see 7.16).

All results indicate similar trends in energy deposition in the magnets, with an increasing deposition in front of the magnet in MQ_4 until it stabilises around one meter away. In contrast, MQ_5 shows a significant energy peak at the magnet's start, likely due to the absorbers at the entrance of MQ_4, which MQ_5 lacks.

It is very peculiar to observe in MQ_4 how the curves associated with FTFP and QGSP bifurcate at a value of a few tenths of a cm, a value that also characterises the inelastic scattering of 7 TeV protons in copper [157]. The graph seems to show that this necessarily has to be due to the nuclear interactions of these protons on the magnet, since the existence of a range where all models coincide suggests that part of the protons must interact in a range where string models act.

Also notable in MQ4 is the difference of about 40% overestimation of all G4 models compared to FLUKA in the first 50 cm of the magnet. This suggests some kind of inconsistency in the Moira simulations, requiring an in-depth analysis to understand if it arises from any geometric error, scoring, primary particles, among other possibilities.

Regarding the rest of the magnet, there is a correspondence between FLUKA and the G4 models, with FLUKA included within the range covered by the latter, which show a difference of 20%. There is a noticeable decrease in FLUKA's power peak with distance, which is not observed in G4, although this fact may not be appreciated with Moira given that the statistical error reached for these simulations is notably higher than that of FLUKA.

Regarding the risk of a quench in MQ_4, in none of the three cases was the value of $38\,\mathrm{mW/cm^3}$ [158] reached by any model, thus producing an extra degree of confidence that MQ_4 is well protected for what will happen during the HL-LHC era.

On the other hand, MQ_5 shows that all models have an equivalent functional form, but with different peak powers at about 10 cm from the front of the magnet for each result. Regarding the G4 models, FTFP, again, shows values higher than QGSP by about 25%-40%, while FLUKA is the result with the highest peak, with greater agreement with the FTFP models, as already observed in the BLM benchmarks.

Regarding the risk of quench in MQ_5, value estimated at $25\,\mathrm{mW/cm^3}$ [158], there is an accompaniment to the results already obtained with FLUKA in the original study. That is, all models predict that a quench should occur if the conditions considered in the "Worst case" and "Quench case" occur, while it is not reached for the "Operational case".

It can be thought that the "Worst case" scenario occurs in a somewhat unreal situation in which all protons in a 0.2h BLT impact the TCSP, while machine development studies have shown that in cases with high loss rates, 90% of these occurred in the TCDQ and it was never observed, even in cases like a quench test in 2023 [159] where the BLM dump thresholds were relaxed, a BLT of less than 17 minutes for just a few seconds before the beam was dumped.

Regarding the "Quench case", similar results, where FLUKA exceeded the quench level by a factor of 2, showed that these studies already predicted a quench in MQ5, but it was not observed experimentally [160]. The results presented here do allow a degree of speculation considering the different models. Although it is always possible to assume that the modelling of the magnets is imperfect and is the reason why what is predicted in FLUKA does not agree with experimental reality, it is possible to consider that these magnets have a high level of detail and think that in reality certain models are overestimating the deposited energy. These models are those of FLUKA and FTFP, which are shown to be around 32% above the quench level. On the other hand, the QGSP models are close to the quench level with a range of ±3%.

Although these cases are highly unlikely to occur in a real situation, what is obtained in the results suggests that protection, similar to that already possessed by MQ_4, would be advisable to reduce this spike in power density in the MQ_5 and thus avoid greater setbacks in the operation of the HL-LHC.

Concluding the last study conducted for this manuscript, Table 7.17 shows the average times to transport a primary particle in the considered geometry. FLUKA shows in this case a much better performance with respect to the G4 models, being faster in a factor 3 to 4; a very significant difference.

	FLUKA [s]	FBERT [s]	QBERT [s]	QBIC [s]	FINCLXX [s]	QINCLXX [s]
TCDQ/TCSP	100	400	400	350	310	300

Table 7.17: Average CPU time per primary particle transported in IR6 study for both cases TCDQ & TCSP.

Figure 7.39: BLMs benchmark IR6 - TCDQ

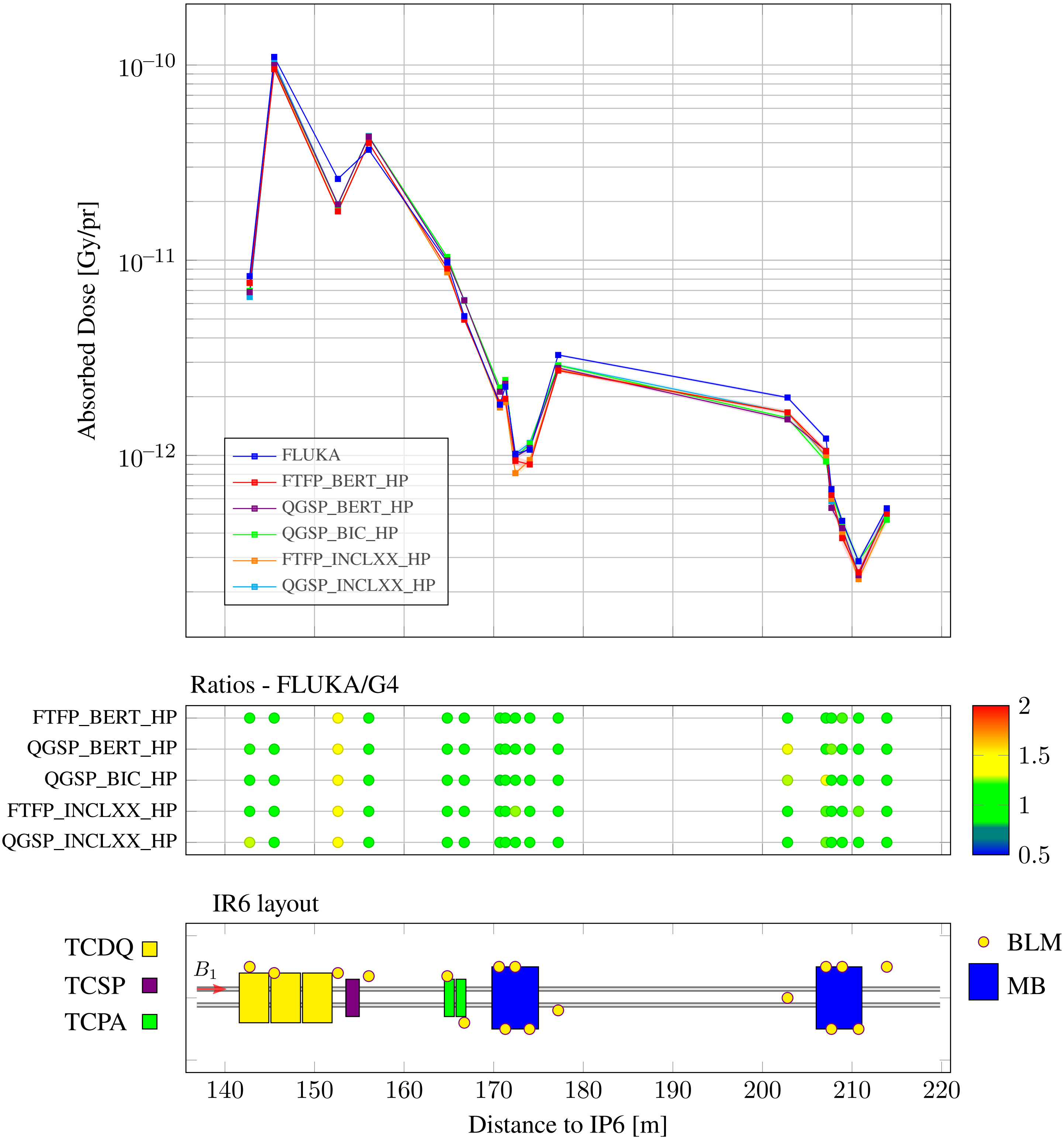

Figure 7.40: BLMs benchmark IR6 - TCSP

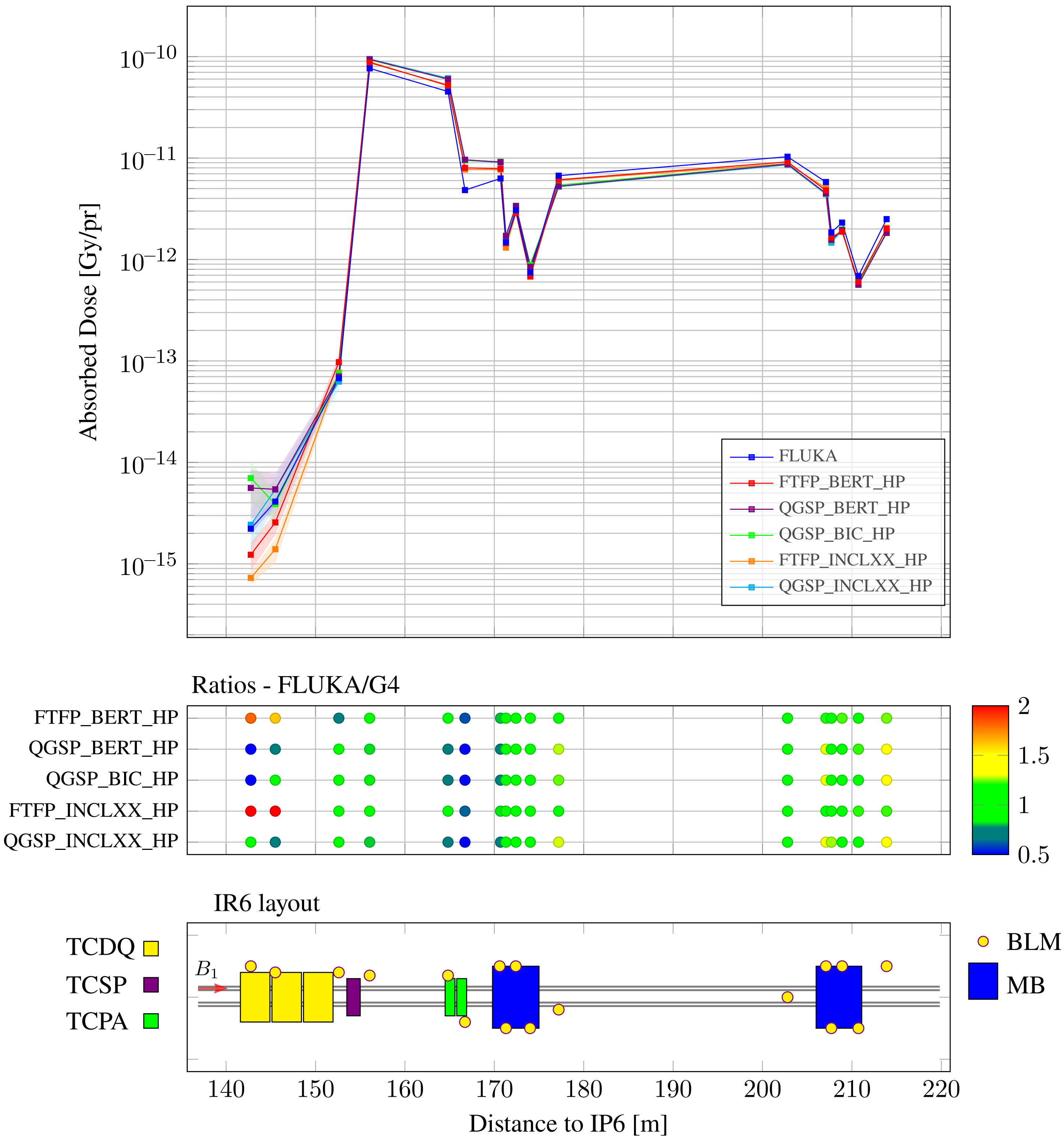

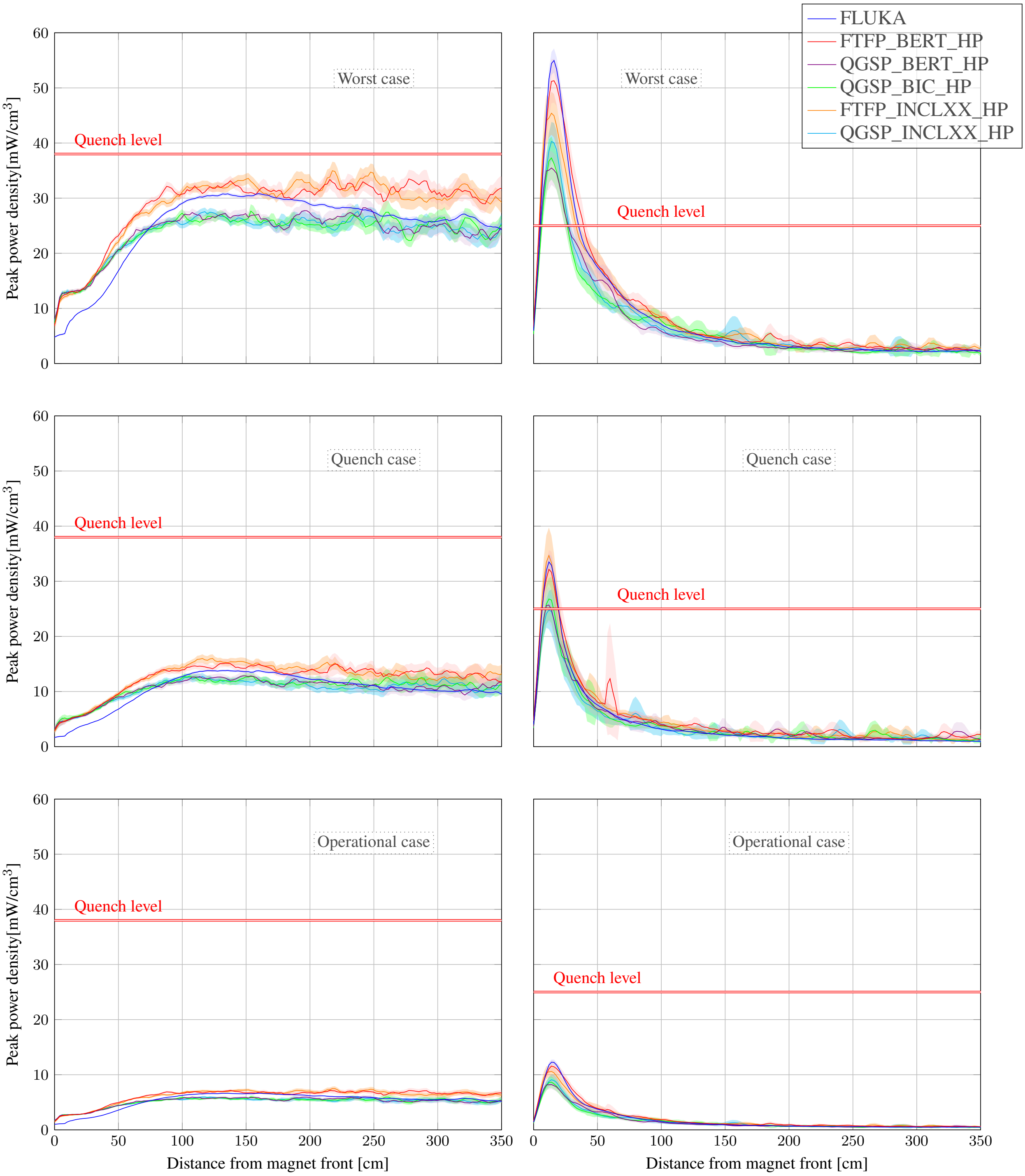

Figure 7.41: Peak power density benchmark in MQ_4 (left) and MQ_5 (right) in IR6 for a 0.2 h HL-LHC BLT between FLUKA and G4 models.

7.7.6 Conclusions

For this last study presented in this manuscript, a machine protection result was again obtained from the IR6 section of the LHC, transporting 7 TeV protons using multiple G4 physical models. Given the peculiar nature of the case, where two "idealised" benchmark cases were carried out with the impact entirely on one collimator or another, comparisons were made between the G4 models and FLUKA, unlike previous studies which used experimental data.

Both benchmarks showed consistent results across all models, except for some specific cases of BLM.(Y4R) in the TCDQ case and BLM.(Z4R) in the TCSP case, where differences of around 50% were observed.

Regarding the risk of quench in the SC quadrupoles, none of the models predict that MQ_4 could have a circumstance of this type in the three cases of interest described. Certainly, the G4 results partially reproduce the behaviour of FLUKA, but the 40% overestimation by all G4 models in the first 50 cm of the magnets suggests some error/inconsistency in the Moira simulations.

The situation is different in MQ_5, where the curves of all the results show equivalent outcomes, with a spike around 10 cm from the front of the magnets, with a noticeable difference between models at this point, with discrepancies ranging from 25% to 40% between them. All models predict a potential risk of quench in the "worst case" and "quench case" scenarios, with the caveat that the QGSP models in this last scenario are very close to the quench level. Nonetheless, what is obtained suggests that, although these cases are very unlikely to occur during the HL-LHC era, it would be advisable to have extra protection at the front of MQ_5, similar to that already present in MQ_4, to absorb some of these protons energy, and thus have confidence that a quench will not occur in any situation.

7.7.7 Next Steps

- Once again, the opportunity to conduct these simulations using the FLUKA physics list in Moira would enable to obtain additional results for comparison with those already achieved. This process is a step forward to fulfil the objectives for the new generation of FLUKA v5.
- Conducting a thorough analysis to identify the source of the observed differences in MQ_4 within the first 50 cm is crucial. While it seems plausible that these discrepancies might be related to Moira's scoring system, they could also stem from more superficial issues. For instance, there might be errors in the input commands used to define factors like position or rotation, or other errors related to the implementation, necessitating a debugging of Moira to pinpoint the exact cause.
- Reducing the statistical errors in G4 simulations could enable a more refined analysis of the results obtained with QGSP near the quench limit. Additionally, it would be beneficial in MQ4 to verify whether there is a decrease in peak power with distance as observed in FLUKA results

7.7.8 Acknowledgement

Infinite thanks to Jean-Baptiste Potoine. His contribution by providing the FLUKA inputs, his always active presence for discussions, and his support in analysing the results were invaluable.

8 Conclusions

Monte Carlo codes for particle transport in matter are fundamental for conducting studies in various fields, from hadronic therapies to shielding evaluations and machine protection. Two of the most important codes currently available are FLUKA and Geant4. As multi-particle and multi-purpose MC codes, they can perform simulations in a wide range of situations, including the aforementioned studies. They are particularly capable of emulating scenarios like the Large Hadron Collider, where particles reach energies in the order of TeV, transported in highly complex geometry. Among these codes, FLUKA stands out for this type of study, not necessarily due to its "better results", but because rather owing to the infrastructure of codes built around FLUKA, such as FEDB, LB, and SixTrack-FLUKA Coupling. Without this infrastructure, carrying out these simulations with G4 or any other MC code would be a Herculean task. On the other hand, dependence on a single MC code is a limitation considering the inherent systematic errors that are part of these codes. Therefore, being able to compare with an alternative code, whose physical models and databases are adequately validated and can be applied in the same study circumstances, can lend to a better quantification of these uncertainties, thus obtaining more conclusive results.

This thesis began by presenting the development of "Moira", an application that allows simulations in the format used in FLUKA, but with the G4 toolkit. The specifics of its creation were detailed, along with its current state, in terms of emulating FLUKA's geometry description, and the analogous FLUKA options it already has for scoring, biasing, production and transport cuts, fields, and the benefits of the Flair graphical interface. The latter is crucial, as it was updated so that all its tools can be used with Moira, but also because of a novel feature that allows converting FLUKA input to Moira. Then, a user can obtain results with both codes in an almost automatic way. Currently, Moira is capable of producing simulations in almost all cases that FLUKA can, as demonstrated in the studies presented in this manuscript.

Regarding the seven produced studies, as this thesis sought to demonstrate, all generated results of interest. This text showed for the first time studies produced with two different MC codes, at very high energies, in very complex and extensive geometries, where the characteristics of the simulations were equivalent in all terms, the only exception being the use of different physical models.

Of these seven studies, two were first presented that were required to the FLUKA.CERN collaboration: the particle production study for the SATIF-15 conference and the SD2 benchmark. Both were simulations with relatively simple geometries, which in themselves did not justify the creation of Moira. Nonetheless, they are a first example of the use of this new development and how necessary it is to have alternative codes to compare results. Regarding the particle production study, it was interesting to observe that for such a simple problem, so many discrepancies could be obtained. The most notable were FLUKA's significant overproduction of photons (related to neutral pions) in the forward direction, as well as differences in protons and neutrons in this same direction, and the peculiar appearance of a "shoulder" with an increase in scattering angle. As for the SD2 benchmark, the great performance of this code for space shielding simulations was demonstrated, due to its precision and efficiency. The results were mostly in remarkable agreement, except for some discrepancies at deeper layers and lower energies. The latter might have been due to the lack of single-scattering models in the MC codes. These two studies demonstrate, by their relative simplicity and varied differences, the importance of being able to perform these types of comparisons, which can now be carried out almost effortlessly by the user, automatically.

The third study is somewhat outside the spectrum of studies that this thesis sought to analyse, which focused on shielding and machine protection, but the ability to perform simulations in a facility as complex as n_TOF was worth demonstrating the type of simulations Moira is capable of performing. This was the first study with five different results obtained with G4 physics, as was the case for the rest of the simulations. The neutron flux results from FLUKA can be differentiated based on the energy range. At medium energies, all models show good alignment with experimental data, with an under/overestimation of 20% depending on the cascade model. For low and high energies, the observed discrepancies suggest the superiority of FLUKA's thermal model and how cascade model dependence significantly modifies the flux at high energies.

The last four studies are all purely associated with machine protection. Starting with the fourth, the estimation of systematic error of each MC code through a BLM benchmark at CHARM provided interesting conclusions. In this first BLM benchmark obtained, Moira, along with G4 physics, showed that the results are on par with those of FLUKA, a fact confirmed by the possession of experimental data. Mostly, the simulations showed the expected results in the various configuration variations of the experimental area, differing mainly in under/overestimation factors depending on the string model. In turn, the agreement between simulations with the addition of the 4^{th} shielding allows inferring deficiencies in the simulation geometry. The results permited to have the physics packages 'calibrated' for future studies of machine protection, mostly focused on radiation to electronic.

The fifth study is totally disruptive, being the first simulation of machine protection studies at multi-TeV energies in very complex geometries using hadronic models alternative to FLUKA. The BLM benchmark performed showed better performance by FLUKA when compared to experimental data. However, since FLUKA was, preliminary, the only code reaching the dose limit in the MQW.C5 magnet coil, this could conclude that the addition of protection for the MQW.C5 magnet was actually not neccessary. The final result, taking into account additional factors in the accumulated dose in the coils of the magnets, showed in all results the need for extra protection for the HL-LHC era, but also confirmed that no more protection would be needed for the MQW.(D5, E5) magnets.

The sixth had the particularity of being the first study of quench risk with hadronic models alternative to those of FLUKA. A very acceptable agreement was observed between the simulations regarding the BLM benchmark. This allows inferring a potential deficiency in the input definition given the low concordance with experimental data observed in the BLM.(QF7, BA9, QA8, QC8). On the other hand, the results allowed confirming that what was predicted by FLUKA is confirmed by the results with Moira, where there would be no real risk of quench, nor in damage from absorbed dose, in the most highly irradiated magnets, during the HL-LHC phase.

Lastly, the seventh study sought to analyse really extreme cases about the potential incidence of leakage protons from IR7 on the superconducting magnets of IR6, these being protons at 7 TeV, in the HL-LHC phase. Despite some particular discrepancies in the exhibited BLM benchmarks, the results achieved among all models were consistent. Moira confirms that there is no quench risk in the MQ_4 magnet for any of the analysed cases, however, the peak power results showed a probable deficiency in Moira's scoring that requires investigation. On the other hand, the MQ_5 showed a possible quench risk by all models in the scenario called "Worst case", that there would be no danger in the "operational case", while the "Quench case" suggests a risk as well. However, the cascade models BERT are very close to the quench level. Although these are cases practically unlikely to occur, what was obtained suggests that it would be advisable to add an absorber, similar to that of MQ_4, to this superconducting quadrupole MQ_5.

As a conclusion to this manuscript, the development of Moira, the results it allows and will allow to achieve, and those that have been obtained for this text, have a relative importance.
Moira and its direct relationship with the development of Flair, and in turn, its future as the basis of a new generation of FLUKA, is a very powerful tool for all kinds of studies requiring MC simulations for particle transport in matter. Its existence allows for clear progress given the simplification its use generates in order to make comparisons between different MC codes. Given the intrinsic limitations in these codes, obtaining simulations with several of them allows the conclusions that can be reached from the results to have more support through the improved quantification of systematic errors. The studies shown in this text allowed the inference of several relevant facts, from potential errors in the setup used in the simulations, confirmations of results already obtained, and even possible unnecessary excesses in terms of shielding. Since machine protection studies always seek to minimise as much as possible the likelihood of greater inconveniences in the operation of the machines at the cost of an expense that may or may not be necessary, being FLUKA the code that showed, in practically all the results, the most "conservative" values, the complementary results ultimately did nothing more than, as already said, confirm these results.

It is also worth mentioning that, although it is advisable to perform this type of comparisons, the data displayed regarding the times necessary to produce these results are also a more than relevant factor for users. Therefore, seeing that in several of the studies a notable difference in the average times required for the transport of a primary particle was observed, becoming up to 4 times (IR6 study) or up to 20 times (n_TOF study), it is essential to optimise the current state of Moira/G4 to reduce them. This does not mean that, in any case, the simulations will require a non-negligible time to be carried out, which is left to the discretion of the user to carry out or not.

Acknowledgements

I would like to start by thanking my supervisors, Mike Seidel and Vasilis Vlachoudis, for this great opportunity to be part of a project that is already innovative but will be part of something much bigger. Thanks to them, I had the chance to advance academically and professionally.

Moreover, a big thanks to the jury, Dr. Ogawa, Dr. Versaci and Dr. Lauchli, as well as the chairman Dr. Mila, who accepted and invested part of their valuable time participating in the defence and reviewing this project.

I would also like to give special thanks to Cesc and Gabi, for their constant support on a day-to-day basis, in terms of work and also on a personal level. Additional gratitude to Philippe for reviewing a big part of this manuscript.

Furthermore, I would like to emphasise the warmth I always received from the Beam-Machine-Interaction section, including colleagues and superiors. Particularly, friends like JB, Mario, Dani, Andreas, with whom I shared many experiences and their beautiful company was always invaluable.

Additionally, I would like to thank other colleagues, but above all, my friends from CERN - Alvaro, Pablo, Miguel, Yago - for their great friendships.

I would not want to forget my friends across the pond - Lu, Nacho, Pau, Fede, Anita, Lufa, Franco, Mati, Agus, Zuvi, Fla - for always welcoming me upon my returns at the end of the year and making me feel at home.

Thanks to the group of Argentinean lawyers in Geneva - Bri, Jime, Nacho, Domi, Agus, Agustin, Romi, Ro, Ceci, Flor, Alan, Magui - for bringing part of my roots to Geneva.

A very special thanks to Kati for all her love and company. A lot of homemade vegan food will come to compensate all these hard times.

Finally, thanks to my family. To my mother, for always being there to listen to me and support me in all my decisions, to my brother whom I miss a lot, and those who could not be here. I hope they would be proud of this achievement.v

A The FTFP_BERT Physics List

Inelastic Models

The **inelastic hadron-nucleus** processes are implemented by Fritiof, Bertini and Precompound models. The interaction of the following particles:

$\mathrm{p}, \mathrm{n}, \pi^+, \pi^-, \mathrm{K}^+, \mathrm{K}^-, \mathrm{K}_\mathrm{L}, \mathrm{K}_\mathrm{S}, \Lambda, \Sigma^+, \Sigma^-, \Sigma^0, \Xi^-, \Xi^0,$ and Ω^-

is handled by Bertini between [0, 6] GeV and FTF between [3 GeV, 100 TeV].

FTF also handles $\overline{\mathrm{p}}$, $\overline{\mathrm{n}}$, $\overline{\mathrm{d}}$, $\overline{\mathrm{t}}$, $\overline{^3\mathrm{He}}$, $\overline{\alpha}$ and anti-hyperons from 0 to 100 TeV/n.

In the overlap of Bertini and FTF there is a random selection of the processes, overlapping the models with a probability decreasing linearly between [3, 6] GeV.

When FTF is used:

- Precompound model invoked to de-excite the remnant nucleus.
- Fermi breakup, neutron, light ion and neutron evaporation called when needed.

If Bertini is used it has its own precompound and de-excitation models, which are simpler.

Inelastic nucleus-nucleus scattering for all incident A:

- Binary cascade (BIC) in [0, 6] GeV/n energy range.
- FTF in [3 GeV/n, 100 TeV/n] energy range.
- Same overlap as FTFP and BERT in h-N interactions.

For baryons and mesons, which includes b- and c- quarks, the FTFP model is used.

The **hadronic interaction of gammas**:

- Bertini below 6 GeV.

- above 3 GeV by the Quark-gluon String (QGS) model.
- Below 200 MeV low-energy model based on de-exitation module is used (?)

Finally, μ, e^- and e^+ interact via transfer of virtual photons, handled by G4MuonVDNuclearModel and G4ElectroVDNuclearModel all energies. (*should explain something of the models).

Inelastic Cross sections

p, n, π's:

- Barashenkov parameterisation below 20 GeV.
- Glauber-Gribov above 20 GeV.

kaons, hyperons and anti-hyperons: Glauber-Gribov

Hadronic gamma interaction cross sections are supplied by G4PhotoNuclearCrossSection which is used at all gamma energies. G4ElectroNuclearCrossSection is used at all energies for e+ and e-, while G4KokoulinMuonNuclearXS is used for μ^+ and μ^- at all energies

Elastic Models

p, n: Chips model [0, 100] TeV. Using Kossov parameterised cross sections.

K^+ and K^-, hyperons, ^2H, ^3H, ^3He, ^4He, $\overline{n}$: G4HadronElastic (based?) model at all energies

π^+, π^-: G4ElasticHadrNucleusHE coherent scattering model for all energies (based on?).

For $\overline{p}$, $\overline{n}$, $\overline{^2H}$, $\overline{^3H}$, $\overline{^3He}$ and $\overline{\alpha}$:

- G4HadronElastic is used from 0 to 100 MeV/n.
- Above 100 MeV/n these particles are handled by the G4AntiNuclElastic model.

For almost all other hadrons the G4HadronElastic model is used for some or all of the energy range.

No elastic scattering model for nuclear projectiles with $A > 4$.

Elastic cross sections

p, n, π's:

- Barashenkov parameterisation below 91 GeV.
- Glauber-Gribov above 91 GeV.

K's, hyperons, anti-hyperons and light ions: G4ComponentGGNuclNuclXsc elastic cross section at all energies.

$\overline{p}$, $\overline{n}$, $\overline{^{2}H}$, $\overline{^{3}H}$, $\overline{^{3}He}$ and $\overline{\alpha}$ use the Glauber model cross section (G4ComponentAntiNuclNuclearXS) at all energies.

Capture, stopping and decay

n: capture G4NeutronRadCapture with G4NeutronCaptureXS cross sections.

μ: capture handled by G4MuonMinusCapture.

π^- and K^- capture at rest is handled by the BertiniCaptureAtRest model which uses the Bertini cascade.

$\overline{p}$, $\overline{d}$, $\bar{t}$, $\overline{^{3}He}$ and $\overline{^{2}H}$ is handled by the FritiofCaptureAtRest model which uses the Fritiof string model.

The decay of long-lived hadrons and leptons is handled by G4Decay. It does not handle the decay of hadronic resonances like deltas, which should be decayed within hadronic models and heavy-flavor particles like D and B mesons or charmed hyperons.

B The EM0 Electromagnetic Package

For each particle type there are several processes, covered from 0 to 100 TeV for all particles. It is recommended to avoid the range below 1keV, where the accuracy is lower.

γ:

- e^-/e^+ pair production: Bethe-Heitler model with Landau-Pomeranchuk-Migda (LPM) effect at high energies (100 GeV?)
- Compton scattering: Klein-Nishina model
- Photo-electric effect: Livermore model
- Rayleight scattering: Livermore model

e^- and e^+:

- Multiple coulomb scattering: Wentzel Urban model [0, 100] MeV, and Wentzel VI model [100 MeV, 100 TeV]. The latter is combined with single Coulomb scattering model applied for large angle scattering.
- Bremsstrahlung: eBremSB model and eBremLPM model, taking account the LPM effect at high energies.
- Ionisation: Moller-Bhabba formulation
- Positron annihilation: eplus2gg model.

μ's:

- Multiple Coulomb Scattering: Wentzel Vi model combined with single scattering model at all energies, and by the eCoulombScattering model at all energies(?).
- Bremsstrahlung: MuBrem model.
- Ionisation:
  - Bragg model [0, 200] keV for μ^+.
  - ICRU73Q0 parameterisation [0, 200] keV for μ^-.
  - Above 200 keV MuBetheBloch model used for both.

  - e^-/e^+ pair production: muPairProduction model handles for μ^+, and μ^-.

π's, K's, p, $\overline{p}$:

- Multiple Coulomb scattering is performed by the WentzelVI model and Coulomb scattering by the eCoulombScattering model.
- Bremsstrahlung is handled by hBrem model.
- e-/e+ pair production by hadrons is implemented by the hPairProduction model.
- Ionisation is handled by several models depending on energy and particle type:
  - For pions below 298 keV, Bragg model ionisation is used for positively charged pions, and the ICRU73Q0 parameterisation is used for negatively charged pions. Above this energy, Bethe-Bloch ionisation is used.
  - For kaons, the same ionisation models are used, but the change from low energy to high energy models occurs at 1.05 MeV.
  - For protons, the Bragg model is used below 2 MeV and the Bethe-Bloch model is used above.
  - For anti-protons, the ICRU73Q0 is used below 2 MeV and Bethe-Bloch is used above.

α and Heavy Ions: Only two EM processes are applied:

- Multiple Coulomb scattering in implemented by the Urban model at all energies.
- For alphas, Bragg ionisation is performed below 7.9 MeV and Bethe-Bloch ionisation is performed above.
- For heavy ions, Bragg is used below 2 MeV/u and Bethe-Bloch is used above.

C Alternative Pre-Defined Electromagnetic Packages in Geant4

EMV (differences with EM0)

- Photons:
  - ApplyCuts option is used to cut out low-energy e^{-} produced by gamma processes
  - No Rayleigh scattering
- Electrons and positrons:
  - Minimal step limitation is used for multiple scattering.
  - Multiple scattering is combined with transportation in G4TransportationWithMsc process.??
- Muons and Generic ions:
  - No nuclear stopping.

EMX (differences with EM0)

- Photons:
  - No Rayleigh scattering
- Electrons and positrons:
  - Minimal step limitation is used for multiple scattering.
  - Multiple scattering is combined with transportation in G4TransportationWithMsc process.??
- Muons and Generic ions:
  - No nuclear stopping.

EMY (differences with EM0)

- Photons:
  - G4BetheHeitler5DModel used in pair production if polarisation activated.
- Electrons and positrons:
  - Urban Model used for msc from 0 to 100 TeV.
  - UseSafety step limitation is used for multiple scattering. Range factor in 0.03.

- Muons:
  - msc handled by Urban model from 0 to 100 TeV.
- Pions, Kaons, protons and anti-p:
  - msc uses Urban model.
- Generic ions:
  - For ionisation the ICRU73/ICRU90 model (G4LinhardSorensenIonModel) is used (Anton did it!) at all energies.

EMZ ($\neq$ EM0)

- Photons:
  - G4BetheHeitler5DModel used in pair production if polarisation activated.
  - Compton Scattering handled by Monarsh University model (G4LowEPComptonModel) below 20 MeV and Klein-Nishina model with Doppler broading effect above 20 MeV.
- Electrons and positrons:
  - msc:
    - from 0 to 100 MeV Goudsmit-Sounderson model
    - UseSafetyPlus step limitation with error free approach near geometry boundaries
    - Range Factor is 0.08
  - Penelope model used for ionisation below 100 keV.
  - The process of e-, e+ pair production by electrons and positrons is also used.
- Muons: Identical
- Protons and light ions:
  - ICRU90 data for the stopping powers are used for water, graphite, and air targets.
- Generic ions:
  - For ionisation the ICRU73/ICRU90 model (G4LinhardSorensenIonModel) is used at all energies.

LIV ($\neq$ EMZ)

- Photons:
  - G4BetheHeitler5DModel used in pair production below 80 GeV and relativistic Bethe-Heitler above.
  - Compton Scattering handled by Livermore below 1 GeV and Klein-Nishina model above.
- Electrons (and positrons ?):
  - Bremsstrahlung:
    - Seltzer-Berger model below 1 GeV and eBremsstrahlungRelModel above.
  - Ionisation uses Livermore model

PEN ($\neq$ EMZ)

- Specific low-energy Penelope models are used for gamma, e- , and e+ below 1 GeV.

GS (≠ EM0)

- Msc of e- and e+ handled by Goudsmit-Sounderson model from 0 to 100 MeV.

LE (≠ EM0)

- Photons:
  - G4BetheHeitler5DModel used in pair production below 80 GeV and relativistic Bethe-Heitler above.
  - Compton Scattering handled by Monarsh University model (G4LowEPComptonModel) below 20 MeV and Klein-Nishina model with Doppler broading effect above 20 MeV.

  For all charged particle and energies G4LowEWentzelVIModel is used for simulation of multiple scattering. The BS generator is used for simulation of bremsstrahlung angular distribution. For protons and alpha ICRU90 data for 3 materials is used. For ion ionisation of ions below 10 MeV/u ICRU73 model (G4IonParametrisedLossModel) is used, above 10 MeV/u the Lindhard-Sorensen model is applied (G4LindhardSorensenIonModel). Additionally, bremsstrahlung and e-/e+ pair production are implemented for ions.

WVI (≠ EM0)

- This configuration is same as in the default G4EmStandardPhysics constructor, except multiple scattering For e-, e+ at all energies G4WentzelVIModel is used for simulation of multiple scattering combined with single elastic at large angles. For ion ionisation of ions below 2 MeV/u the Bragg model is used, above 2 MeV/u the ATIMA model is applied (G4AtimaEnergyLossModel) with ATIMA fluctuation model (G4AtimaFluctuations)..

SS (≠ EM0)

- This physics list uses “standard” GEANT4 electromagnetic physics as built by the G4EmStandardPhysicsSS constructor. This configuration is same as in the default G4EmStandardPhysics constructor, except multiple scattering is not used and only elastic scattering process is applied for all charged particles.

D Alternative Pre-Defined Physics Lists in Geant4

Using the previous physics list (FTFP_BERT), it is possible to detail the composition of the other possible pre-defined physics lists:

- FTFP_INCLXX: INCLXX cascade substitutes the Bertini cascade.
- FTFP_BERT_ATL: Transition between FTF model and Bertini cascade change to [9, 12] GeV.
- FTFP_BERT_TRV:
  - Default EM package to GS.
  - Replaced elastic Chips model for Diffusive model on p, n, pi+, pi-.
  - Diffraction activated.
- FTFQGSP_BERT: QGS fragmentation of strings, instead of Lund string fragmentation.
- FTF_BIC: Binary cascade is used instead of internat FTF cascade for rescaterring of secondary particles within nucleus.
- QGSP_BERT: (≠ FTFP_BERT)
  - Inelastic models: QGS handles p, n, pi's and K's above 12 GeV, FTF in [3, 25] GeV,
  - Inelastic Cross sections: for p, n, pi's the Barashenkov parametrisation used below 91 GeV, and Glauber-Gribov above.
- QGSP_FTFP_BERT: (≠ QGSP_BERT)
  - It is identical
- QGSP_INCLXX (≠ QGSP_BERT)
  - INCLXX cascade substitutes the Bertini cascade.
- QGSP_BIC (≠ QGSP_BERT)
  - Binary cascade replace BERT for n, p interactions between 0 and 6 GeV.
  - Generic Ion elastic process added (G4IonElasticPhysics)
- Shielding (≠ FTFP_BERT_HP)
  - FTFP model not used for baryons and mesons which includes b- and c- quarks?
  - Hadronic interaction of gammas below 200 MeV low-energy model based on de-excitation module is not used??
  - Inelastic Cross sections: for p, n, pi's the Barashenkov parametrisation used below 91

    GeV.
  - For all ions the G4ComponentGGNuclNuclXsc elastic cross section is used.
  - QMD (Quantum Molecular Dynamics) physics for ions.
  - Radioactive decay activated.
- ShieldingM (≠ Shielding)
  - Transition from the Bertini model to the FTF model: from 9.5 to 9.9 GeV
- ShieldingLEND (≠ Shielding)
  - Different configurations of low-energy neutron transport with LEND option.(*see more details)

E Beam Dynamics Overview

For the discussions in the following sections, the focus will be on analysing the dynamics of beams in circular accelerators. They concentrate on detailing the characteristics of linear transverse and linear longitudinal dynamics, introducing as well many relevant concepts associated to the beam.

E.1 Transverse Dynamics

The force that governs the dynamics of a charged particle in a circular accelerator is given by the Lorentz Force:

$$F = q(E + v \times B) \tag{E.1}$$

It provides the force that a particle with charge q, moving at a velocity v, will experience when inside an electromagnetic field. To curve this charged particle, magnetic fields are normally used, while electric fields in the direction of the particle's motion add energy to it.

When the particle is in a homogeneous magnetic field perpendicular to its trajectory, it will follow a circular path if the Lorentz Force is of equal magnitude to the centrifugal force, defined by:

$$F_c = m\frac{v^2}{\rho} \tag{E.2}$$

Where m is the relativistic mass ($m = m_0\ \gamma$), and ρ is the radius of curvature. Equating the mentioned terms, a fundamental result is obtained:

$$\rho = \frac{p}{qB} \tag{E.3}$$

This important equation relates the particle momentum - p -, the particle charge - q -, and the strength of the magnetic field - B -, to the radius of the circle - ρ - that it will generate on its path. This would be the motion of the particle in an ideal trajectory.

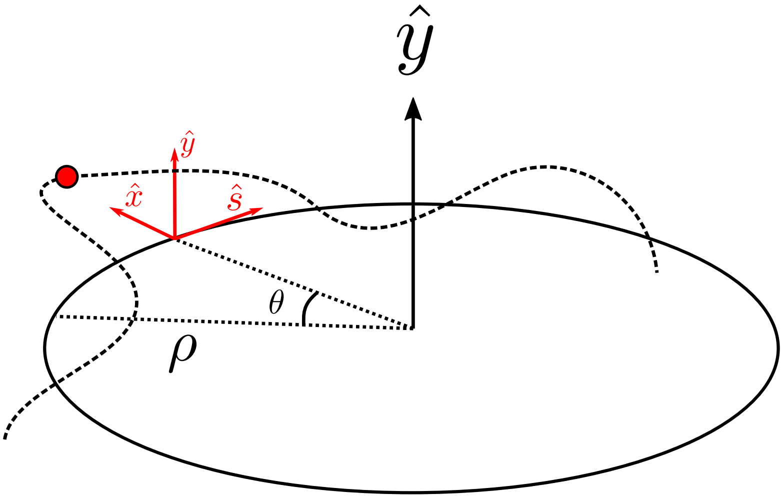

Figure E.1: Frenet-Serret coordinate system

It is very useful to consider the Frenet-Serret coordinate system for analysing the movement of particles through the circular accelerator, as shown in fig E.1. This system accounts for the particles' deviations from the ideal orbit of an accelerator. This system uses three orthogonal axes, placing the origin in the movement of an ideal reference particle, located at point "s" of the accelerator, with the variables x and y expressing the horizontal and vertical deviations of the particle from the point in the ideal orbit. To express the transverse motion equation of a particle in an accelerator composed of dipole magnets and quadrupolar magnets, which are the main elements that make up circular accelerators, they are derived through Hill's equations [161], given by:

$$\begin{gathered} \mathrm{x}''(\mathrm{s}) + \left(\frac{1}{\mathrm{R}^2(\mathrm{s})} - \mathrm{K_x}(\mathrm{s})\right)\mathrm{x}(\mathrm{s}) = 0,\ \ \mathrm{K_x}(\mathrm{s}) = \frac{1}{\rho(\mathrm{s})^2} - \frac{\mathrm{B_1}(\mathrm{s})}{\mathrm{B_0}} \\ \mathrm{y}''(\mathrm{s}) + \mathrm{K_x}(\mathrm{s})\mathrm{y}(\mathrm{s}) = 0,\ \ \mathrm{K_y}(\mathrm{s}) = -\frac{\mathrm{B_1}(\mathrm{s})}{\mathrm{B_0}\,\rho(\mathrm{s})} \end{gathered} \tag{E.4}$$

Where the parameters $\mathrm{B_0}$ and $\mathrm{B_1}$ are related to the effects of dipoles and quadrupoles on the beam. For the transverse direction x (analogue for y), the general form of the solution to these equations is:

$$\mathrm{x}(\mathrm{s}) = \sqrt{\varepsilon_\mathrm{x}\beta_\mathrm{x}(\mathrm{s})}\sin(\varphi(\mathrm{s}) + \varphi_0) \tag{E.5}$$

The result is an oscillatory transverse movement, called *betatron oscillations*, modulated by a periodic function called the *beta function* - $\beta_\mathrm{x}(\mathrm{s})$ -, with the amplitude of these oscillations determined by the *particle emittance* - ε_x -. On the other hand, *the betatron phase* - $\varphi_\mathrm{x}(\mathrm{s})$ - describes the phase advance of the oscillation, which depends on the amplitude of oscillation, as:

$$\varphi(\mathrm{s}) = \int_0^\mathrm{s} \frac{\mathrm{ds}}{\beta(\mathrm{s})} \tag{E.6}$$

Additionally, two very well-known parameters can be defined through β:

$$\alpha_x(s) = -\frac{1}{2}\frac{d\beta_x(s)}{ds} \quad \gamma_x(s) = \frac{1+\alpha_x^2(s)}{\beta_x(s)} \tag{E.7}$$

α, β, and γ are known as the *Twiss parameters*. These are very useful as they allow describing the movement in the phase space (x-x') of the particle beam at any point of the accelerator. Fig. E.2shows how these parameters describe the shape of an ellipse in phase space, associated with the points that the particle can occupy at a given point of the machine. This ellipse takes different shapes along the machine, but its area remains constant. This area depends on the presented parameters in the following way:

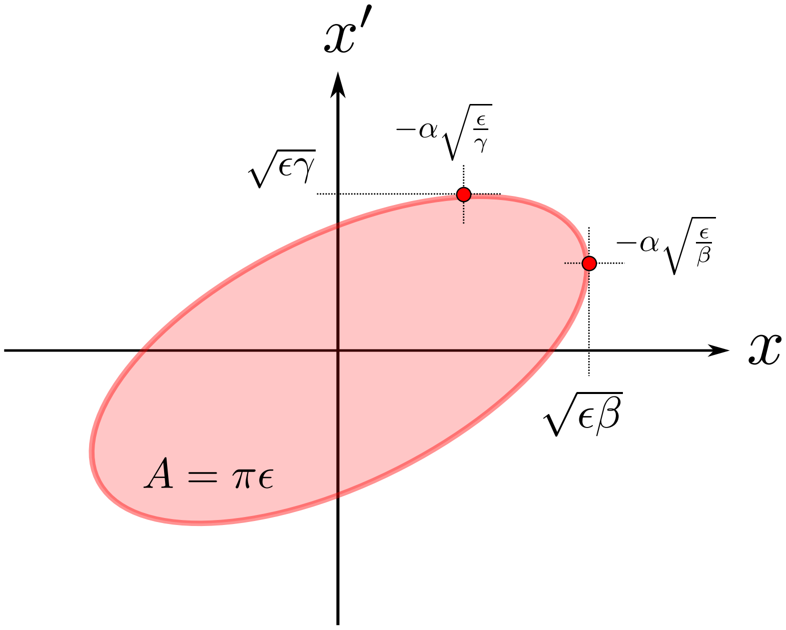

Figure E.2: Ellipse in the phase-space representing the distribution of particles in a point of the accelerator. The Twiss parameters in any point of the accelerator define this ellipse.

$$\frac{\text{AREA}}{\pi} = \varepsilon = \gamma(s)x^2(s) + 2\alpha(s)x(s)x'(s) + \beta(s)x'^2(s) \tag{E.8}$$

For the case of a Gaussian ensemble of particles, which is a common assumption for beam distribution, the parameters ε and β allow for a characterisation of the beam, through the *betatronic rms size* - $\sigma_x(s)$ - and the *betatronic rms divergence* - $\sigma'_x(s)$ -, whose definition is:

$$\sigma_x(s) = \sqrt{\varepsilon_x\beta_x(s)} \quad \sigma'_x(s) = \sqrt{\varepsilon_x\gamma_x(s)} \tag{E.9}$$

A value $\propto \sigma$ is usually used to define the "core" of the beam for an accelerator. Those particles outside of this zone, and located in the tails, are particles that are in the *beam halo*.

E.2 Longitudinal Dynamics

Particles in their transport through the accelerator obtain energy through RF cavities to be accelerated, or to make up the nominal energy of the beam in the machine that they may lose during their journey. These cavities generate an an oscillating voltage defined as follows:

$$V(t) = V_0 \sin(\varphi_s + \omega t) \tag{E.10}$$

Where φ_s is the *synchronous phase*, V_0 is the maximum voltage of the cavity, and ω is a frequency, defined in such a way that it is a multiple of the nominal revolution frequency of the particles through the accelerator. Thus, those particles that are at the nominal energy will obtain a variation in their energy given by:

$$\Delta E = qV_0 \sin(\varphi_s) \tag{E.11}$$

Being, in the ideal case, particles without energy loss, $\varphi_s = 0$. Now, those particles that have a different momentum than the nominal one, will be accelerated or decelerated. In the event that the off-momentum of one these particles is sufficiently small, they will oscillate around the synchronous particle, known as *synchrotron oscillations*. The equation describing the motion of these particles in phase-energy space is:

$$\ddot{\varphi} + \frac{\omega_s^2}{\cos\varphi_s}(\sin(\varphi) - \sin(\varphi_s)) = 0 \tag{E.12}$$

Figure E.3 illustrates the longitudinal movement of the particles represented in their corresponding φ and E. The graph shows two regions, separated by a *separatrix*, which characterises the stable particles within it and the unstable ones that are inevitably lost from the particle bucket.

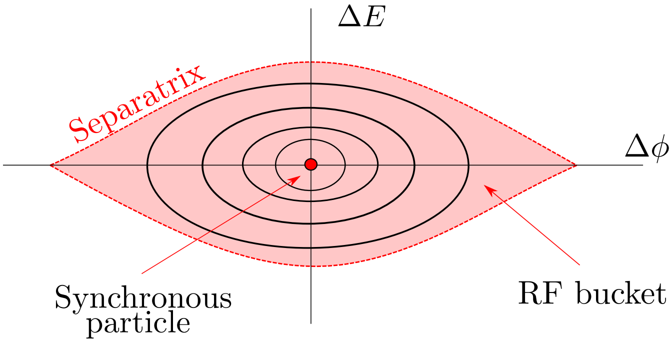

Figure E.3: Longitudinal movement of particles in the energy-phase space

E.3 Dispersion Function

To conclude the discussion in this section, it is interesting to analyse the solution to Hill's equation of motion when considering a deviation in momentum:

$$\delta p = \frac{p - p_0}{p_0} \tag{E.13}$$

By introducing this additional factor and considering only its effects due to magnetic dipoles, the following solution can be derived:

$$x(s) = x_\beta(s) + D(s)\delta p \tag{E.14}$$

This solution consists of the original term without deviation, and the dispersion function - D(s) -. This additional term produces an offset in the reference trajectory relative to the ideal path for particles that have a δp in momentum. A significant result is deduced from this additional factor, associated with an increase in horizontal $\sigma(s)$ due to dispersion:

$$\sigma(s) = \sqrt{\beta(s)\varepsilon + (D(s)\delta p)^2} \tag{E.15}$$

F Proof of Homogeneous Fluence on Target

This chapter demonstrates that a homogeneous fluence distribution is achieved on the target. The scenario under consideration is where the semi-sphere's surface emits according to a cosine-law, and the goal is to assess whether this leads to a uniform fluence distribution at the entire sphere centre.

F.1 Preliminary Definitions and Assumptions

Let $\varphi(r, \vartheta, Z = 0)$ denote the fluence at the centre of the sphere, specifically, the fluence on the first layer of the target. It is established that $\varphi(r, \vartheta, Z = 0)$ is constant for all r within the range $[0, R]$ and ϑ within the range $[0, 360°)$.

F.2 Revolution Symmetry

Given that the surface under consideration is a semi-sphere, it possesses rotational symmetry around the z axis. This implies that any spatial quantity, such as the fluence φ, remains invariant under rotation $R(z)$ around the z axis. Mathematically, this is expressed as:

$$R(z)\varphi(r_0, \vartheta_0) = \varphi(r_0, \vartheta_0)$$

Moreover, for any rotation $R(z)$, it holds that:

$$R(z)\varphi(r_0, \vartheta_0) = \varphi(r_0, \vartheta_1)$$

Therefore, it is deduced that:

$$\varphi(r_0, \vartheta_0) = \varphi(r_0, \vartheta_1)$$

This confirms that for a given radius r_0, the fluence φ is constant for all ϑ.

F.3 Uniformity Across Radii

Next, the uniformity of fluence across different radii is established. Assume, for the sake of contradiction, that $\varphi(\mathrm{r}_0) \neq \varphi(\mathrm{r}_1)$ for two different radii r_0 and r_1 in a semi-sphere. If the semi-sphere is completed to form a full sphere, the combined fluence at the same radius should be the sum of the doses from both semi-sphere. This is formulated as:

$$\varphi_{\mathrm{ss1}}(\mathrm{r}_0) + \varphi_{\mathrm{ss2}}(\mathrm{r}_0) \neq \varphi_{\mathrm{ss1}}(\mathrm{r}_1) + \varphi_{\mathrm{ss2}}(\mathrm{r}_1) \tag{F.1}$$

However, since both are semi-spheres with identical properties, the sum of their doses at a given radius should equal the fluence of the entire sphere. This leads to:

$$\varphi_{\mathrm{sp}}(\mathrm{r}_0) = \varphi_{\mathrm{ss1}}(\mathrm{r}_0) + \varphi_{\mathrm{ss2}}(\mathrm{r}_0) = 2\varphi_{\mathrm{ss}}(\mathrm{r}_0) \neq 2\varphi_{\mathrm{ss}}(\mathrm{r}_1) = \varphi_{\mathrm{ss1}}(\mathrm{r}_1) + \varphi_{\mathrm{ss2}}(\mathrm{r}_1) = \varphi_{\mathrm{sp}}(\mathrm{r}_1) \tag{F.2}$$

This implies $\varphi_{\mathrm{sp}}(\mathrm{r}_0) \neq \varphi_{\mathrm{sp}}(\mathrm{r}_1)$, a contradiction since a uniform fluence distribution is expected in a complete sphere. Hence, the initial assumption is false, and the fluence must be uniform for all radii in a semi-sphere.

Acronyms

BGV Beam Gas Vertex. 131–136, 139
BLM Beam Loss Monitoring. 64, 65

CDF Cumulative Distribution Function. x, 26, 134, 135
CG Combinatorial Geometry. 46, 70, 71
CHARM The CERN High-energy AcceleRator Mixed field facility. ix, xi, 116–118, 120, 121
CLT Central Limit Theorem. vii, 23, 24

DS Dispersion Suppressor. 59

FEDB FLUKA Element DataBase. viii, 53–55

G4 Geant4. viii, 31, 33–36, 38, 46, 67, 89

h-A hadron-nucleus. 10, 12, 48, 84
h-N hadron-nucleon. 10, 12, 48
HL High-Luminosity. 62

IC Ionisation Chambers. 64
INC Intra Nuclear Cascade. 13, 49

LB Line Builder. 54
LHC Large Hadron Collider. iv, viii, xi, 53, 55, 57–62, 64–66
LS2 Long Shutdown 2. x, 124
LSS Long-Straight-Section. 59

MC Monte Carlo. 19–21, 23–25, 27–31, 33, 45, 57, 122, 126

N-N nucleon-nucleon. 11

OO object-oriented. 34, 40

PS Proton Synchrotron. 53, 55, 117

RF radio-frequency. 62, 174

SATIF Shielding Aspects of Accelerators, Targets and Irradiation Facilities. 89–91, 94, 100

SD-2 ShielDose-2. 101, 102, 104, 106–108

SPS Super Proton Synchrotron. 53, 55

Bibliography

[1] James Clerk Maxwell. “A Dynamical Theory of the Electromagnetic Field”. In: *Philosophical Transactions of the Royal Society of London* 155 (1865). 54 pages, pp. 459–512. URL: https://www.jstor.org/stable/108892 (cit. on p. 3).

[2] William Herschel. “XIV. Experiments on the refrangibility of the invisible rays of the sun”. In: *Philosophical Transactions of the Royal Society of London* 90 (1800), pp. 255–283. DOI: 10.1098/rstl.1800.0015 (cit. on p. 3).

[3] Jan Frercks, Heiko Weber, and Gerhard Wiesenfeldt. “Reception and discovery: the nature of Johann Wilhelm Ritter’s invisible rays”. In: *Studies in History and Philosophy of Science Part A* 40.2 (2009), pp. 143–156. DOI: 10.1016/j.shpsa.2009.03.014 (cit. on p. 3).

[4] Wilhelm Konrad Roentgen. “Wilhelm Konrad Roentgen: a new kind of rays”. In: *Journal of Emergency Medicine* 11.6 (Nov. 1993), pp. 743–745. DOI: 10.1016/0736-4679(93)90635-k (cit. on p. 3).

[5] Henri Becquerel. “Sur les radiations émises par phorescence”. French. In: *Comptes Rendus* 122 (1896), pp. 420–421 (cit. on p. 3).

[6] M Skłodowska-Curie. *Traité de radioactivité*. French. Vol. 2. Paris: Gauthier-Villars, 1910 (cit. on p. 3).

[7] A. Lechner. “Particle interactions with matter”. In: *CERN Yellow Report School Proceedings* 5 (2018), p. 47 (cit. on pp. 8, 11, 16).

[8] N. V. Mokhov and F. Cerutti. “Beam–material interactions”. In: *Proc. 2014 Joint International Accelerator School: Beam Loss and Accelerator Protection*. CERN-2016-002. CERN. Newport Beach, CA, USA, Nov. 2014, p. 83. URL: http://dx.doi.org/10.5170/CERN-2016-002 (cit. on p. 8).

[9] P. Sigmund. *Particle Penetration and Radiation Effects*. Berlin: Springer-Verlag, 2006 (cit. on p. 8).

[10] M.J. Berger et al. *XCOM: Photon Cross Section Database (version 1.5)*. http://physics.nist.gov/xcom. [Online; accessed 27-December-2023]. Gaithersburg, MD, 2010 (cit. on p. 8).

[11] Hon. J.W. Strutt. “On the light from the sky, its polarization and colour”. In: *The London, Edinburgh, and Dublin Philosophical Magazine and Journal of Science* 41.271 (1871), pp. 107–120. DOI: 10.1080/14786447108640452 (cit. on p. 8).

[12] Hon. J.W. Strutt. “On the scattering of light by small particles”. In: *The London, Edinburgh, and Dublin Philosophical Magazine and Journal of Science* 41.275 (1871), pp. 447–454. DOI: 10.1080/14786447108640507 (cit. on p. 8).

[13] Arthur H. Compton. “A Quantum Theory of the Scattering of X-rays by Light Elements”. In: *Physical Review* 21.5 (May 1923), p. 483 (cit. on p. 8).

[14] M.J. Berger et al. *ESTAR, PSTAR, and ASTAR: Computer Programs for Calculating Stopping-Power and Range Tables for Electrons, Protons, and Helium Ions (version 1.2.3).* http://physics.nist.gov/Star. [Online; accessed 27-December-2023]. Gaithersburg, MD, 2005 (cit. on pp. 10, 104, 106).

[15] A. Ferrari and P.R. Sala. “The Physics of High Energy Reactions”. In: *Proc. of the Workshop on Nuclear Reaction Data and Nuclear Reactors Physics, Design and Safety*. Ed. by A. Gandini and G. Reffo. Miramare-Trieste, Italy: World Scientific, 15 April-17 May 1996, p. 424 (cit. on pp. 11, 48).

[16] P. D. B. Collins. *An Introduction to Regge Theory and High Energy Physics*. Cambridge Monographs on Mathematical Physics. Cambridge University Press, 1977. DOI: 10.1017/CBO9780511897603 (cit. on p. 12).

[17] E. Fermi. “Zur Quantelung des idealen einatomigen Gases”. In: *Zeitschrift für Physik* 36.11 (Nov. 1926), pp. 902–912. ISSN: 0044-3328. DOI: 10.1007/BF01400221. URL: https://doi.org/10.1007/BF01400221 (cit. on p. 13).

[18] Morgan B. Fox et al. “Investigating high-energy proton-induced reactions on spherical nuclei: Implications for the preequilibrium exciton model”. In: *Physical Review C* (2020). URL: https://api.semanticscholar.org/CorpusID:225066928 (cit. on p. 14).

[19] D.A. Brown et al. “ENDF/B-VIII.0: The 8th major release of the nuclear reaction data library with CIELO-project cross sections, new standards and thermal scattering data”. In: *Nuclear Data Sheets* 148 (2018), p. 1. DOI: 10.1016/j.nds.2018.02.001. URL: https://doi.org/10.1016/j.nds.2018.02.001 (cit. on p. 16).

[20] J. Rowlinson. “The Maxwell–Boltzmann distribution”. In: *Molecular Physics* 103 (Nov. 2005), pp. 2821–2828. DOI: 10.1080/002068970500044749 (cit. on p. 15).

[21] A.J.M. Plompen et al. “The joint evaluated fission and fusion nuclear data library, JEFF-3.3”. In: *European Physical Journal A* 56 (2020), p. 181. DOI: 10.1140/epja/s10050-020-00141-9. URL: http://dx.doi.org/10.1140/epja/s10050-020-00141-9 (cit. on p. 16).

[22] O. Iwamoto et al. “Japanese evaluated nuclear data library version 5: JENDL-5”. In: *Journal of Nuclear Science and Technology* 60 (2023), p. 1. DOI: 10.1080/00223131.2022.2141903. URL: https://doi.org/10.1080/00223131.2022.2141903 (cit. on p. 16).

[23] C. Patrignani et al. “Review of Particle Physics”. In: *Chinese Physics C* 40 (2016). Updated 2017, p. 100001. DOI: 10.1088/1674-1137/40/10/100001. URL: https://doi.org/10.1088/1674-1137/40/10/100001 (cit. on p. 17).

[24] W. Heitler. *The Quantum Theory of Radiation*. Oxford: Clarendon Press, 1954 (cit. on p. 17).

[25] Stanislaw M. Ulam. *Adventures of a Mathematician*. ISBN: 9780684143910. New York: Charles Scribner’s Sons, 1976 (cit. on p. 19).

[26] G. Buffon. “Essai d’arithmétique morale”. In: *Histoire naturelle, générale et particulière* Supplément 4 (1777), pp. 46–123 (cit. on p. 19).

[27] Los Alamos Scientific Laboratory The Atom. *Fermi Invention Rediscovered at LASL*. 1966 (cit. on p. 20).

[28] F. Coccetti. “The Fermiac or Fermi’s Trolley”. In: *IL NUOVO CIMENTO* 39 C (2016), p. 296. DOI: 10.1393/ncc/i2016-16296-7 (cit. on p. 20).

[29] Nicholas Metropolis and Stanislaw Ulam. “The Monte Carlo Method”. In: *Journal of the American Statistical Association* 44.247 (1949), pp. 335–341. ISSN: 0162-1459. DOI: 10.2307/2280232 (cit. on p. 20).

[30] H. H. Goldstine and A. Goldstine. “The Electronic Numerical Integrator and Computer (ENIAC)”. In: *IEEE Annals of the History of Computing* 18.1 (Spring 1996), pp. 10–16. ISSN: ISSN: 1058-6180. DOI: 10.1109/85.476557 (cit. on p. 20).

[31] F. James. “A Review of Pseudorandom Number Generators”. In: *Computer Physics Communications* 60.3 (Oct. 1990), pp. 329–344. DOI: 10.1016/0010-4655(90)90032-V (cit. on p. 24).

[32] Derrick H. Lehmer. “Mathematical Methods in Large-Scale Computing Units”. In: *Proceedings of 2nd Symposium on Large-Scale Digital Calculating Machinery*. 1951, pp. 141–146 (cit. on p. 25).

[33] F. Salvat. *PENELOPE, a code system for Monte Carlo simulation of electron and photon transport*. Tech. rep. DOC(2015)3, 2. NEA/NSC, 2014, pp. 49–100 (cit. on p. 27).

[34] Philippe Schoofs. “Monte Carlo Modeling of Crystal Channeling at High Energies”. CERN-THESIS-2014-131, Presented 18 Mar 2014. PhD. Ecole Polytechnique, Lausanne, 2014 (cit. on p. 28).

[35] Hyung Jin Shim et al. “McCARD: Monte Carlo code for advanced reactor design and analysis”. In: *Nuclear Engineering and Technology* 44 (Mar. 2012). DOI: 10.5516/NET.01.2012.503 (cit. on p. 28).

[36] Alfredo Ferrari et al. “Po-production in lead: A benchmark between Geant4, FLUKA and MCNPX”. In: *arXiv preprint arXiv:1806.03732* (2018). URL: https://doi.org/10.48550/arXiv.1806.03732 (cit. on p. 31).

[37] Leila Mokhtari Oranj et al. “Benchmarking FLUKA, PHITS, MCNPX, and MARS15 codes with product yields of 209Bi(p, x) reactions”. In: *Nuclear Instruments and Methods in Physics Research Section B: Beam Interactions with Materials and Atoms* 462 (Jan. 2020), pp. 154–162. DOI: 10.1016/j.nimb.2019.11.017. URL: https://doi.org/10.1016/j.nimb.2019.11.017 (cit. on p. 31).

[38] Reginald Martin Ronningen, Igor Remec, and Lawrence H. Heilbronn. *Benchmarking Heavy Ion Transport Codes FLUKA, HETC-HEDS MARS15, MCNPX, and PHITS*. Web. 2013. DOI: 10.2172/1082753. URL: https://doi.org/10.2172/1082753 (cit. on p. 31).

[39] N. V. Mokhov et al. “Energy deposition studies for the high-luminosity Large Hadron Collider inner triplet magnets”. In: *Physical Review Special Topics - Accelerators and Beams* 18 (2015), p. 051001. DOI: 10.1103/PhysRevSTAB.18.051001 (cit. on pp. 31, 136).

[40] J. Allison et al. “Recent Developments in Geant4”. In: *Nuclear Instruments and Methods in Physics Research Section A* 835 (2016), pp. 186–225 (cit. on pp. 33, 37).

[41] J. Allison et al. “Geant4 Developments and Applications”. In: *IEEE Transactions on Nuclear Science* 53 (2006), pp. 270–278 (cit. on pp. 33, 34).

[42] S. Agostinelli et al. “Geant4 - A Simulation Toolkit”. In: *Nuclear Instruments and Methods in Physics Research Section A* 506 (2003), pp. 250–303 (cit. on p. 33).

[43] European Organization for Nuclear Research. *Home*. `https://home.cern/`. Accessed: 2024-01-06. 2024 (cit. on p. 33).

[44] High Energy Accelerator Research Organization. *Home*. https://www.kek.jp/. Accessed: 2024-01-06. 2024 (cit. on p. 34).

[45] R. Brun et al. “GEANT3”. In: (Sept. 1987) (cit. on p. 34).

[46] A. Dellacqua et al. *Geant4: an object-oriented toolkit for simulation in HEP*. Tech. rep. CERN/DRDC/94-29. CERN, 1994 (cit. on p. 34).

[47] Simone Giani et al. “GEANT 4: An Object-Oriented Toolkit for Simulation in HEP”. In: *CERN/LHCC* (1998), pp. 98–44 (cit. on p. 34).

[48] G. Cosmo and On behalf of the Geant4 Collaboration. “Geant4 – Towards major release 10”. In: *Journal of Physics: Conference Series* 513 (2 2014), p. 022005. DOI: 10.1088/1742-6596/513/2/022005. URL: https://doi.org/10.1088/1742-6596/513/2/022005 (cit. on p. 34).

[49] Kostas Kordas et al. “GEANT4 for the ATLAS Electromagnetic Calorimeter”. In: *Proceedings of the IXth International Conference on Calorimetry in Particle Physics*. Annecy, France, Oct. 2000 (cit. on p. 34).

[50] Stefan Piperov. *Geant4 validation with CMS calorimeters test-beam data*. 2008. arXiv: 0808.0130 `[physics.ins-det]` (cit. on p. 34).

[51] Farah Hariri et al. “Geant4 Detector Simulations for Future HEP Experiments”. In: *PoS* ICHEP2018 (2019), p. 268. DOI: 10.22323/1.340.0268 (cit. on p. 34).

[52] M.C. Espirito-Santo et al. “GEANT4 applications for astroparticle experiments”. In: *2003 IEEE Nuclear Science Symposium. Conference Record (IEEE Cat. No.03CH37515).* Vol. 3. 2003, 1530–1534 Vol.3. DOI: 10.1109/NSSMIC.2003.1352168 (cit. on p. 34).

[53] L. Archambault et al. “Overview of Geant4 applications in medical physics”. In: Nov. 2003, 1743–1745 Vol.3. ISBN: 0-7803-8257-9. DOI: 10.1109/NSSMIC.2003.1352215 (cit. on p. 34).

[54] P. Paschalis et al. “Geant4 software application for the simulation of cosmic ray showers in the Earth’s atmosphere”. In: *New Astronomy* 33 (2014), pp. 26–37. ISSN: 1384-1076. DOI: https://doi.org/10.1016/j.newast.2014.04.009. URL: https://www.sciencedirect.com/science/article/pii/S1384107614000621 (cit. on p. 34).

[55] Geant4 Collaboration. *Introduction to Geant4 - Release 11.2.* https://geant4-userdoc.web.cern.ch/UsersGuides/IntroductionToGeant4/fo/IntroductionToGeant4.pdf. Accessed: 2024-01-06 (cit. on p. 35).

[56] Geant4 Collaboration. *Geant4 User’s Guide for Application Developers.* https://geant4-userdoc.web.cern.ch/UsersGuides/ForApplicationDeveloper/fo/BookForApplicationDevelopers.pdf. Accessed: 2024-01-07 (cit. on pp. 35–38, 40–42).

[57] Radovan Chytracek et al. “Geometry Description Markup Language for Physics Simulation and Analysis Applications”. In: *Nuclear Science, IEEE Transactions on* 53 (Nov. 2006), pp. 2892–2896. DOI: 10.1109/TNS.2006.881062 (cit. on p. 35).

[58] Geant4 Collaboration. *Geant4 Geometry From Text File (TextGeom).* https://geant4.web.cern.ch/collaboration/working_groups/persistency/docs/textgeom.pdf. Accessed: 2024-01-07 (cit. on p. 35).

[59] N.S. Amelin. *Hadron Formation Time Within the Quark-Gluon String Model.* Tech. rep. JINR–3-36-89. USSR: Joint Institute for Nuclear Research, 1989 (cit. on p. 37).

[60] Geant4 Collaboration. *Geant4 Physics Reference Manual.* https://geant4-userdoc.web.cern.ch/UsersGuides/PhysicsReferenceManual/fo/PhysicsReferenceManual.pdf. Accessed: 2024-01-07 (cit. on p. 37).

[61] B. Andersson, G. Gustafson, and B. Nilsson-Almqvist. “A model for low-pT hadronic reactions with generalizations to hadron-nucleus and nucleus-nucleus collisions”. In: *Nuclear Physics B* 281.1 (1987), pp. 289–309. ISSN: 0550-3213. DOI: https://doi.org/10.1016/0550-3213(87)90257-4. URL: https://www.sciencedirect.com/science/article/pii/0550321387902574 (cit. on p. 37).

[62] Vladimir Uzhinsky. “The Fritiof (FTF) Model in Geant4”. In: 2013. URL: https://api.semanticscholar.org/CorpusID:203392640 (cit. on p. 37).

[63] K.K. Gudima, S.G. Mashnik, and V.D. Toneev. “Cascade-exciton model of nuclear reactions”. In: *Nuclear Physics A* 401.2 (1983), pp. 329–361. ISSN: 0375-9474. DOI: https://doi.org/10.1016/0375-9474(83)90532-8. URL: https://www.sciencedirect.com/science/article/pii/0375947483905328 (cit. on p. 37).

[64] M.P. Guthrie, R.G. Alsmiller, and H.W. Bertini. “Calculation of the capture of negative pions in light elements and comparison with experiments pertaining to cancer radiotherapy”. In: *Nuclear Instruments and Methods* 66.1 (1968), pp. 29–36. ISSN: 0029-554X. DOI: https://doi.org/10.1016/0029-554X(68)90054-2 (cit. on p. 37).

[65] G. Folger, V.N. Ivanchenko, and J.P. Wellisch. “The Binary Cascade”. In: *European Physical Journal A* 21 (2004), pp. 407–417. DOI: 10.1140/epja/i2003-10219-7 (cit. on p. 37).

[66] A. Boudard et al. “New potentialities of the Liège intranuclear cascade model for reactions induced by nucleons and light charged particles”. In: *Phys. Rev. C* 87 (1 Jan. 2013), p. 014606. DOI: 10.1103/PhysRevC.87.014606. URL: https://link.aps.org/doi/10.1103/PhysRevC.87.014606 (cit. on p. 37).

[67] H. Burkhardt et al. “Geant4 standard electromagnetic package for HEP applications”. In: vol. 3. Nov. 2004, 1907–1910 Vol. 3. ISBN: 0-7803-8700-7. DOI: 10.1109/NSSMIC.2004.1462617 (cit. on p. 37).

[68] Geant4 Collaboration. *Geant4 Physics List Guide*. 2023. URL: https://geant4-userdoc.web.cern.ch/UsersGuides/PhysicsListGuide/fo/PhysicsListGuide.pdf (cit. on p. 37).

[69] Makoto Asai et al. “The PENELOPE Physics Models and Transport Mechanics. Implementation into Geant4”. In: *Frontiers in Physics* 9 (2021). DOI: 10.3389/fphy.2021.738735. URL: https://doi.org/10.3389/fphy.2021.738735 (cit. on p. 37).

[70] E. Keil. “The Large European e+e- Collider Project LEP”. In: *IEEE Transactions on Nuclear Science* 28.4 (1981), pp. 3656–3659. DOI: 10.1109/TNS.1981.4331815 (cit. on p. 40).

[71] C. Runge. “Über die numerische Auflösung von Differentialgleichungen”. In: *Mathematische Annalen* 46 (1895), pp. 167–178 (cit. on p. 40).

[72] W. Kutta. “Beitrag zur näherungsweisen Integration totaler Differentialgleichungen”. In: *Zeitschrift für Mathematik und Physik* 46 (1901), pp. 435–453 (cit. on p. 40).

[73] Takuyo Kodama et al. “GAG: GEANT4 Adaptive Graphical User Interface”. In: 1998. URL: https://api.semanticscholar.org/CorpusID:16370944 (cit. on p. 42).

[74] Mark Segal and Kurt Akeley. “The Design of the OpenGL Graphics Interface”. In: (June 2000) (cit. on p. 43).

[75] Laurent Garnier. “Geant4 Qt visualization driver”. In: (Mar. 2009) (cit. on p. 43).

[76] M.A. Reading. *The Inventor Mentor: Programming Object-Oriented 3D Graphics with Open Inventor*. Reading, MA: Addison-Wesley, 1994 (cit. on p. 43).

[77] J. Perl. “HepRep: A Generic Interface Definition for HEP Event Display Representables”. In: *Proceedings of the CHEP 2000 Conference*. SLAC-REPRINT-2000-020, See also: http://heprep.freehep.org. Padova, Italy, Feb. 2000 (cit. on p. 43).

[78] S. Tanaka and M. Kawaguti. “DAWN for Geant4 visualization”. In: *Proceedings of the CHEP ’97 Conference*. Berlin, Germany, Apr. 1997 (cit. on p. 43).

[79] Ayumu Saitoh et al. “gMocren: High-quality volume visualization tool for Geant4 simulation”. In: *2007 IEEE Nuclear Science Symposium Conference Record*. Vol. 1. 2007, pp. 888–891. DOI: 10.1109/NSSMIC.2007.4436470 (cit. on p. 43).

[80] CERN. *The official CERN FLUKA website*. Accessed 23-01-2024]. URL: https://fluka.cern (cit. on p. 45).

[81] CERN FLUKA Team. *FLUKA: A Particle Physics MonteCarlo Simulation Tool*. Online. Accessed: 2024-01-18. 2024. URL: https://fluka.cern/ (cit. on p. 45).

[82] G. Battistoni et al. “Overview of the FLUKA code”. In: *Annals of Nuclear Energy* 82 (2015), pp. 10–18 (cit. on p. 45).

[83] G. Battistoni et al. “The FLUKA atmospheric neutrino flux calculation”. In: *Astroparticle Physics* 19.2 (2003), pp. 269–290. ISSN: 0927-6505. DOI: https://doi.org/10.1016/S0927-6505(02)00246-3 (cit. on p. 46).

[84] Francesco Cerutti. “Machine and radiation protection challenges of high energy/intensity accelerators: the role of Monte Carlo calculations”. In: *EPJ Web of Conferences* 153 (Jan. 2017), p. 03018. DOI: 10.1051/epjconf/201715303018 (cit. on p. 46).

[85] V. Andersen et al. “The application of FLUKA to dosimetry and radiation therapy”. In: *Radiation Protection Dosimetry* 116.1-4 (Dec. 2005), pp. 113–117. DOI: 10.1093/rpd/nci040 (cit. on p. 46).

[86] Giuseppe Battistoni et al. “Applications of FLUKA Monte Carlo code for nuclear and accelerator physics”. In: *Nuclear Instruments and Methods in Physics Research Section B: Beam Interactions with Materials and Atoms* 269.24 (2011). Proceedings of the 10th European Conference on Accelerators in Applied Research and Technology (ECAART10), pp. 2850–2856. DOI: https://doi.org/10.1016/j.nimb.2011.04.028 (cit. on p. 46).

[87] Victor Andersen et al. “The FLUKA code for space applications: Recent developments”. In: *Advances in space research : the official journal of the Committee on Space Research (COSPAR)* 34 (Feb. 2004), pp. 1302–10. DOI: 10.1016/j.asr.2003.03.045 (cit. on p. 46).

[88] CC Chen, RJ Sheu, and SH Jian. “Calculations of neutron shielding data for 10-100 MeV proton accelerators”. In: *Radiation Protection Dosimetry* 116.1-4 Pt 2 (2005), pp. 245–251. DOI: 10.1093/rpd/nci193 (cit. on p. 46).

[89] A. Ferrari and P.R. Sala. “A new model for hadronic interactions at intermediate energies for the FLUKA code”. In: *Proc. MC93 Int. Conf. on Monte Carlo Simulation in High Energy and Nuclear Physics*. Ed. by P. Dragovitsch, S.L. Linn, and M. Burbank. Tallahassee, Florida: World Scientific, 22-26 February 1993, pp. 277–288 (cit. on p. 48).

[90] A. Capella et al. “Dual parton model”. In: *Physics Reports* 236 (1994), pp. 225–330 (cit. on p. 48).

[91] A. Ferrari et al. “Cascade particles, nuclear evaporation, and residual nuclei in high energy hadron-nucleus interactions”. In: *Z. Phys. C* 70 (1996), pp. 413–426 (cit. on p. 48).

[92] S. Roesler, R. Engel, and J. Ranft. “The Monte Carlo Event Generator DPMJET-III”. In: *Proceedings of the Monte Carlo 2000 Conference*. Ed. by A. Kling et al. Lisbon, Portugal: Springer-Verlag Berlin, Oct. 2001, pp. 1033–1038 (cit. on p. 48).

[93] A. Fedynitch. “PhD Thesis”. PhD thesis. 2015. URL: https://cds.cern.ch/record/2231593/files/CERN-THESIS-2015-371.pdf (cit. on p. 48).

[94] H. Sorge, H. Stoecker, and W. Greiner. “Annals of Physics”. In: 192 (1989), p. 266 (cit. on p. 48).

[95] V. Andersen et al. “The FLUKA code for space applications: recent developments”. In: *Advances in Space Research* 34.6 (2004), pp. 1302–1310 (cit. on p. 48).

[96] M. Cavinato et al. “Monte Carlo calculations using the Boltzmann Master Equation theory of nuclear reactions”. In: *Phys. Lett. B* 382 (1996), pp. 1–5 (cit. on p. 48).

[97] Vlachoudis, Vasilis et al. “Recent developments in the point wise neutron treatment for FLUKA v4”. In: *EPJ Web of Conf.* 284 (2023), p. 03021. DOI: 10.1051/epjconf/202328403021. URL: https://doi.org/10.1051/epjconf/202328403021 (cit. on p. 50).

[98] FLUKA Collaboration. *FLUKA User’s Manual*. Access Year. URL: https://flukafiles.web.cern.ch/manual/ (cit. on pp. 50–53).

[99] V. Vlachoudis. “FLAIR: A Powerful But User Friendly Graphical Interface For FLUKA”. In: *Proceedings of the International Conference on Mathematics, Computational Methods & Reactor Physics (MC 2009)*. Saratoga Springs, New York, 2009 (cit. on p. 53).

[100] Michael Evan Rising et al. *MCNP® Code Version 6.3.0 Release Notes*. Tech. rep. LA-UR-22-33103, Rev. 1. Los Alamos, NM, USA: Los Alamos National Laboratory, Jan. 2023. DOI: 10.2172/1909545. URL: https://www.osti.gov/biblio/1909545 (cit. on p. 53).

[101] Tatsuhiko Sato et al. “Recent improvements of the particle and heavy ion transport code system – PHITS version 3.33”. In: *Journal of Nuclear Science and Technology* (). DOI: 10.1080/00223131.2023.2275736 (cit. on p. 53).

[102] A. Mereghetti et al. “The FLUKA Linebuilder and Element Database: Tools for Building Complex Models of Accelerators Beam Lines”. In: *Conference Proceedings C1205201*. 2012, WEPPD071 (cit. on pp. 53, 54).

[103] R. De Maria et al. “SixTrack Version 5: Status and New Developments”. In: *Proceedings of the International Particle Accelerator Conference (IPAC 2019)*. Melbourne, Australia: JACoW, 2019, pp. 3200–3203. DOI: 10.18429/JACoW-IPAC2019-WEPTS043 (cit. on p. 55).

[104] Eleftherios Skordis et al. “FLUKA coupling to Sixtrack”. In: *CERN Yellow Rep. Conf. Proc.* 2 (2020). Ed. by Stefano Redaelli, pp. 17–25. DOI: 10.23732/CYRCP-2018-002.17 (cit. on pp. 55, 124).

[105] Esma Mobs. *The CERN Accelerator Complex in 2019*. General Photo. Complexe des accélérateurs du CERN en 2019. 2019 (cit. on p. 58).

[106] O S Brüning et al. *LHC Design Report*. DOI:10.5170/CERN-2004-003-V-1. 2004 (cit. on p. 59).

[107] G Apollinari et al. *High Luminosity Large Hadron Collider HL-LHC*. en. 2015. doi: 10.5170/CERN-2015-005.1. url: https://cds.cern.ch/record/2120673 (cit. on p. 62).

[108] R Versaci et al. “R2E FLUKA studies for Point 1 and Point 5”. In: (2010). url: https://cds.cern.ch/record/1302276 (cit. on p. 66).

[109] L. Sarchiapone et al. “FLUKA Monte Carlo simulations and benchmark measurements for the LHC beam loss monitors”. In: *Nuclear Instruments and Methods in Physics Research Section A: Accelerators, Spectrometers, Detectors and Associated Equipment* 581.1 (2007). VCI 2007, pp. 511–516. issn: 0168-9002. doi: https://doi.org/10.1016/j.nima.2007.08.038. url: https://www.sciencedirect.com/science/article/pii/S016890020701710X (cit. on p. 66).

[110] L S Esposito, F Cerutti, and E Todesco. “Fluka Energy Deposition Studies for the HL LHC”. In: *Conf. Proc.* C130512 (2013), TUPFI021. url: https://cds.cern.ch/record/1636133 (cit. on p. 66).

[111] Barbara Humann, Francesco Cerutti, and Roberto Kersevan. “Synchrotron Radiation Impact on the FCC-ee Arcs”. In: *JACoW* IPAC2022 (2022), pp. 1675–1678. doi: 10.18429/JACoW-IPAC2022-WEPOST002 (cit. on p. 66).

[112] Daniele Calzolari et al. “Radiation Load Studies for Superconducting Dipole Magnets in a 10 TeV Muon Collider”. In: *JACoW IPAC* 2022 (2022), pp. 1671–1674. doi: 10.18429/JACoW-IPAC2022-WEPOST001. url: https://cds.cern.ch/record/2845834 (cit. on p. 66).

[113] CERN Moira. *Moira by CERN*. Accessed: 15-01-2024. url: https://moira.web.cern.ch/moira/ (cit. on p. 68).

[114] Geant4 Collaboration. *Geant4 10.6 Release Notes*. https://geant4-dev.web.cern.ch/download/release-notes/notes-v10.6.0.html. Accessed: 23-01-2024. 2019 (cit. on p. 70).

[115] Gabrielle Hugo. *FLUKA.CERN Status & Plans Scoring*. https://indico.cern.ch/event/1156193/contributions/5051070/attachments/2517529/4328454/MOIRA_FLUKA++_STATUS.pdf. Accessed: 23-01-2024. September 2022 (cit. on p. 73).

[116] H Vincke and C Theis. “ActiWiz 3 – an overview of the latest developments and their application”. In: *Journal of Physics: Conference Series* 1046.1 (June 2018), p. 012007. doi: 10.1088/1742-6596/1046/1/012007. url: https://dx.doi.org/10.1088/1742-6596/1046/1/012007 (cit. on p. 81).

[117] Ernest Rutherford. *Radio-activity*. University Press, 1905, p. 331 (cit. on p. 81).

[118] Harry Bateman. “The solution of a system of differential equations occurring in the theory of radioactive transformations”. In: *Proc. Cambridge Philos. Soc* 15.pt V (June 1910), pp. 423–427 (cit. on p. 81).

[119] Gabrielle Hugo. *FLUKA.CERN Hadronic Event Generator Interface*. https://indico.cern.ch/event/1156193/contributions/5051331/attachments/2519353/4332076/FLUKA_HADRONIC_GENERATOR_2.pdf. Accessed: 23-01-2024. September 2022 (cit. on p. 84).

[120] "15th International Conference on Nuclear Data for Science and Technology (ND2022)". In: *EPJ Web of Conferences* 284.15 (2023). Published online on 26 May 2023, p. 16006. DOI: 10.1051/epjconf/202328416006. URL: https://doi.org/10.1051/epjconf/202328416006 (cit. on p. 86).

[121] *Shielding Aspects of Accelerators, Target and Irradiation Facilities – SATIF 12 Workshop Proceedings*. NEA/NSC/R(2015)3. Nuclear Energy Agency (NEA). Batavia, Illinois, United States: OECD NEA, Apr. 2014. URL: www.oecd-nea.org (cit. on p. 89).

[122] *Shielding Aspects of Accelerators, Target and Irradiation Facilities (SATIF-13) - Proceedings of the Thirteenth Meeting*. 10-12 October 2016. Nuclear Energy Agency (NEA). Dresden, Germany: OECD Publishing, Paris, Oct. 2016 (cit. on p. 89).

[123] *Shielding Aspects of Accelerators, Targets and Irradiation Facilities (SATIF-14)*. Nuclear Energy Agency (NEA). OECD Publishing, Paris, 2021 (cit. on p. 89).

[124] *SATIF-15*. https://indico.frib.msu.edu/event/19/. [Online; accessed 09-January-2024]. 2022 (cit. on p. 90).

[125] *15th Workshop of Shielding Aspects of Accelerators, Targets and Irradiation Facilities (SATIF-15)*. To be published. 2024 (cit. on p. 93).

[126] *16th Workshop of Shielding Aspects of Accelerators, Targets and Irradiation Facilities (SATIF-16)*. https://www.lnf.infn.it/conference/satif16/index.php. [Online; accessed 09-January-2024]. 2024 (cit. on p. 100).

[127] NASA. *NASA Artemis*. https://www.nasa.gov/specials/artemis/. [Online; accessed 09-January-2024]. 2021 (cit. on p. 101).

[128] NASA. *The Artemis Plan*. https://www.nasa.gov/wp-content/uploads/2020/12/artemis_plan-20200921.pdf. [Online; accessed 09-January-2024]. 2020 (cit. on p. 101).

[129] S. M. Seltzer. *SHIELDOSE, A Computer Code for Space-Shielding Radiation Dose Calculations*. NBS Technical Note 1116. Washington, D.C.: National Bureau of Standards, 1980 (cit. on p. 101).

[130] S. M. Seltzer. *Updated calculations for routine space-shielding radiation dose estimates: SHIELDOSE-2*. NISTIR 5477. Gaithersburg, MD: National Institute of Standards and Technology (NIST), Dec. 1994 (cit. on p. 101).

[131] Steven J. Gentz and Insoo Jun. *Space-Shielding Radiation Dosage Code Evaluation Phase 1: SHIELDOSE-2 Radiation-Assessment Code*. NASA Technical Memorandum NASA/TM20230010640, NESC-RP-21-01718. NASA Langley Research Center; Jet Propulsion Laboratory, 2023. URL: https://ntrs.nasa.gov/api/citations/20230010640/downloads/7-27-23%2020230010640.pdf (cit. on p. 102).

[132] *AZ-93 Product Information*. https://www.aztechnology.com/product/1/az-93. [Online; accessed 09-January-2024] (cit. on p. 108).

[133] *n TOF Facility*. www.cern.ch/ntof. 2022 (cit. on p. 109).

[134] C. Guerrero et al. "Performance of the neutron time-of-flight facility n TOF at CERN". In: *Eur. Phys. J. A* 49 (2013), p. 27 (cit. on p. 109).

[135] N. Colonna, F. Gunsing, and E. Chiaveri. “The Second Beam-Line and Experimental Area at n TOF: A New Opportunity for Challenging Neutron Measurements at CERN”. In: *Nuc. Phys. News* 25.4 (2015), pp. 19–23 (cit. on p. 109).

[136] Vasilis Vlachoudis et al. “On the resolution function of the n_TOF facility: a comprehensive study and user guide”. In: (2021). The document provides an extensive description of the resolution function of n_TOF, methodology of extracting it from the simulated data and how to use it. URL: https://cds.cern.ch/record/2764434 (cit. on pp. 110, 111).

[137] J. Lerendegui-Marco, S. Lo Meo, C. Guerrero, et al. “Geant4 simulation of the n_TOF-EAR2 neutron beam: Characteristics and prospects”. In: *European Physical Journal A* 52 (2016), p. 100. DOI: 10.1140/epja/i2016-16100-8. URL: https://doi.org/10.1140/epja/i2016-16100-8 (cit. on p. 110).

[138] M E Stamati et al. “Preparing Phase 4 of the n_TOF/CERN facility”. In: *Adv. Nucl. Phys.* 28 (2022), pp. 109–111. DOI: 10.12681/hnps.3610. URL: https://cds.cern.ch/record/2861075 (cit. on p. 110).

[139] The n_TOF Collaboration (M. Bacak et al.) In preparation. 2024 (cit. on p. 110).

[140] Daniel Prelipcean. “Comparison between measured radiation levels and FLUKA simulations at CHARM and in the LHC tunnel of P1-5 within the R2E project in Run 2. Vergleich zwischen gemessenen Strahlungswerten und FLUKA-Simulationen bei CHARM undim LHC-Tunnel von P1-5 innerhalb des R2E-Projekts in Run 2”. Presented 29 Jul 2021. Technical University of Munich, 2021. URL: https://cds.cern.ch/record/2777059 (cit. on p. 116).

[141] Daniel Prelipcean et al. “Benchmark Between Measured and Simulated Radiation Level Data at the Mixed-Field CHARM Facility at CERN”. In: *IEEE Transactions on Nuclear Science* 69.7 (2022), pp. 1557–1564. DOI: 10.1109/TNS.2022.3169756 (cit. on p. 116).

[142] J. Mekki et al. “CHARM: A mixed field facility at CERN for radiation tests in ground atmospheric space and accelerator representative environments”. In: *IEEE Transactions on Nuclear Science* 63.4 (Aug. 2016), pp. 2016–2114 (cit. on p. 116).

[143] A. Infantino et al. “Dose gradient assessment at the new CERN CHARM irradiation facility”. In: *Radiation Physics and Chemistry* 155 (Feb. 2019), pp. 225–232 (cit. on p. 116).

[144] Andreas Waets et al. *FLUKA energy deposition studies for IR3 magnets, Presented at Collimation WG 258*. Sept. 2021. URL: https://lhc-collimation.web.cern.ch/meeting_2021.htm (cit. on pp. 123, 126).

[145] Eleftherios Skordis et al. *FLUKA simulations of dose in IR3, Presented at Collimation WG 163*. Sept. 2013. URL: https://lhc-collimation.web.cern.ch/meeting_2013.htm (cit. on p. 124).

[146] James Molson et al. *IR3 simulations as input to energy deposition studies*. July 2021. URL: https://lhc-collimation-upgrade-spec.web.cern.ch/Meetings.php (cit. on p. 124).

[147] Anton Lechner et al. *Recap of previous energy deposition studies in IR3, Presented at Collimation WG 247*. Feb. 2020. URL: https://lhc-collimation.web.cern.ch/meeting_2020.htm (cit. on p. 126).

[148] D. Prelipcean et al. “Radiation levels produced by the operation of the Beam Gas Vertex monitor in the LHC tunnel at IR4”. In: *Proceedings of the International Particle Accelerator Conference*. JACoW Publishing. 2023, pp. 732–735. DOI: 10.18429/JACoW-IPAC2023-THPL082 (cit. on p. 131).

[149] J. Carvalho. “Compilation of cross sections for proton–nucleus interactions at the HERA energy”. In: *Nuclear Physics A* 725 (2003), pp. 269–275. URL: https://www.sciencedirect.com/science/article/pii/S0375947403015975 (cit. on pp. 133, 134).

[150] R. Kersevan and M. Ady. “Recent Developments of Monte-Carlo Codes Molflow+ and Synrad+”. In: *Proceedings of the International Particle Accelerator Conference*. JACoW Publishing. 2019, pp. 1327–1330. DOI: 10.18429/JACoW-IPAC2019-TUPMP037 (cit. on p. 134).

[151] Jean-Baptiste Potoine et al. “Risk of Halo-Induced Magnet Quenches in the HL-LHC Beam Dump Insertion”. In: *12th International Particle Accelerator Conference*. Aug. 2021. DOI: 10.18429/JACoW-IPAC2021-MOPAB002 (cit. on p. 140).

[152] CERN. *LHC Machine Outreach - Beam Dump*. https://lhc-machine-outreach.web.cern.ch/components/beam-dump.htm. Accessed: 2024-01-16. 2024 (cit. on p. 141).

[153] T. Antonakakis et al. “Upgrade of the LHC Beam Dumping Protection Elements”. In: *Conf. Proc. C* 1205201 (2012). Ed. by Vic Suller, pp. 556–558 (cit. on p. 141).

[154] Jean-Baptiste Potoine. “Performance of beam collimation for high-energy colliders.” To be published. PhD. Université de Montpellier, 2023 (cit. on p. 143).

[155] Pascal Hermes, Stefano Redaelli, and Marco D’Andrea. *Analysis of Collimation Quench Test with Protons*. Collimation Upgrade Specification Meeting 158. 2022 (cit. on p. 144).

[156] B. M. Salvachua Ferrando et al. “Collimation Quench Test with 6.5 TeV Proton Beams”. In: (Jan. 2016) (cit. on p. 144).

[157] Valdimir Fortov et al. “Interaction of the CERN Large Hadron Collider (LHC) Beam with Solid Metallic Targets”. In: (Jan. 2004) (cit. on p. 145).

[158] A. Verweij. “QP3 User Manual”. Internal note, unpublished. 2011 (cit. on pp. 145, 146).

[159] P. Hermes et al. *MD 7224: LHC Collimation Quench Test with Protons*. Technical Report CERN-ACC-NOTE-2023-XXX. CH-1211 Geneva, Switzerland: CERN, May 2023 (cit. on p. 146).

[160] A. Lechner et al. “Energy Deposition in IR6 Magnets During Regular and Irregular Beam Losses”. In: (2019) (cit. on p. 146).

[161] M. Martini. *An introduction to transverse beam dynamics in accelerators*. Tech. rep. CERN/PS 96-11. CERN, 1996 (cit. on p. 172).